FERMILAB-THESIS-2023-03

Measurement of Neutrino Oscillations using Neutrino and Antineutrino Beams in the NOvA Experiment

Yibing Zhang

Submitted for the degree of Doctor of Philosophy

University of Sussex

9th March 2023

Declaration

I hereby declare that this thesis has not been and will not be submitted in whole or in part to another University for the award of any other degree.

Signature:

Yibing Zhang

UNIVERSITY OF SUSSEX

Yibing Zhang

Measurement of Neutrino Oscillations using Neutrino and Antineutrino Beams in the NOvA Experiment

Abstract

NOvA is a long-baseline accelerator neutrino oscillation experiment using the NuMI neutrino beam from Fermilab. Its main physics goals are to probe the 3-flavour oscillation parameters: neutrino mass hierarchy, CP-violating phase δ_{cp} and octant of θ_{23} mixing angle by observing electron neutrino appearance and muon neutrino disappearance. Two functionally identical detectors are placed off-axis from the centre of the NuMI beam. The near detector at Fermilab is 100 m underground, and the far detector is located on the surface at Ash River, 810 km away from the beam source. The initial neutrino beam spectra are measured using the near detector data and the oscillation parameters are extracted by fitting the observed data to the predicted neutrino spectrum in the far detector.

This thesis is centered around how to improve the sensitivity of $|\Delta m^2_{32}|$ and θ_{23} measurements in the muon neutrino disappearance analysis. NOvA will take data for about 12 years. The operation of the NOvA experiment for each year costs tens of millions of dollars, thus it is valuable to maximise the sensitivity of the analysis. Three samples of muon neutrino events are studied in this thesis to improve the analysis sensitivities. First, higher energy muon neutrinos are investigated by extending the energy range in NOvA's current standard analysis. Second, for the sample of events used in NOvA's existing analysis, a new energy estimator which has been developed to improve the neutrino energy

resolution is considered. Furthermore, in addition to binning the events as function of energy and hadronic energy fraction, three particle identifiers are introduced to separate neutrino events by signal purity to reduce the effects from backgrounds. Third, an additional lower purity sample of muon neutrino charged current (CC) events that look similar to neutral current events and have not been included in NOvA's existing analyses have been studied.

This thesis reanalyses NOvA's data used in the 2020 analysis, corresponding to an exposure of 13.60×10^{20} protons on target (POT) in the neutrino beam mode recorded from February 6, 2014 to March 20, 2020, and 12.50×10^{20} protons on target in the antineutrino beam mode recorded between June 29, 2016 to February 26, 2019. This thesis has implemented a fit to Asimov fake data, generated where $\sin^2\theta_{23} = 0.59$ and $\Delta m^2_{32} = 2.5 \times 10^{-3}$ eV^2. These sensitivity studies show that the uncertainty range of $|\Delta m^2_{32}|$ at 1 σ in the new analysis is reduced by 5.5% and the significance of maximal disappearance rejection improves by 7.7%, compared to the standard analysis. This is equivalent to adding 11-16% more data. The best fit values of the oscillation parameters from fitting to the far detector (FD) data with the new analysis are found to be $\sin^2\theta_{23} = 0.568^{+0.025}_{-0.043}$ ($\sin^2\theta_{23} = 0.454^{+0.046}_{-0.026}$) and $\Delta m^2_{32} = 2.399^{+0.055}_{-0.070} \times 10^{-3}$ eV^2 (Δm^2_{32} $= -2.427^{+0.055}_{-0.067} \times 10^{-3}$ eV^2) for the normal (inverted) hierarchy. The difference in the best fit for $\sin^2\theta_{23}$ (Δm^2_{32}) between the new analysis and NOvA's 2020 analysis is around 2% (1.4%). The uncertainty range at 1 σ for Δm^2_{32} decrease by 8% (4%) for the normal hierarchy (inverted hierarchy) compared to the standard analysis. The uncertainty range for $\sin^2\theta_{23}$ is close to the standard analysis. This thesis also implements the fit from combining electron neutrino appearance and muon neutrino disappearance. The combined analysis shows that the best fit values are very close to the standard analysis. However, the uncertainty range of Δm^2_{32} at 1 σ is reduced by 3.7% using the new analysis. The maximal disappearance significance is not improved in the new analysis, but the new analysis slightly improves the rejection of the disfavoured octant.

Acknowledgements

It is my pleasure to acknowledge the people who have been playing important roles during my study as a PhD student in the University of Sussex. Pursuing a PhD degree is a challenging experience for me. I have been fortunate to meet so many excellent experts, colleagues, friends and family members. It would not have been possible for me to complete my research work without the support and kind help of these people around me.

First of all, I would like to express my sincere gratitude to my supervisor, Jeff Hartnell, for continuously providing skilful and excellent guidance at every step when I did my research, as well as his great patience and kindness at all times. I hugely appreciate his constant encouragement and useful discussions, that bring me to a wonderful world of experimental particle physics and will be beneficial to my academic career. Jeff also provided me with warm and thoughtful guidance, assistance, and advice that helped me adapt to life abroad. I am extremely grateful for his attentive help .

I really enjoyed working in 4C10 in Pevensey 2, which provided a really awesome research environment full of useful discussions and innovative ideas. I greatly appreciate the discussions and help from my second supervisor Clark Griffith. I would like to thank my senior colleagues Tyler Alion, Alexander Booth, and Diana Mendez, who were always willing to help me with valuable and reliable suggestions when I encountered some difficult technical or physics problems. I would like to thank Wilf Shorrock for giving me a lot of valuable suggestions for my thesis. I am also thankful to Lily Asquith, Pierre Lasorak, Iker de Icaza-Astiz, Brett Mayes, Charlie Mills, Aran Borkum for giving me so much help and all of the answers to so many questions from me.

Thanks to all the NOvA collaboration members for providing me their helpful and valuable suggestions. I am also grateful to have the opportunity to work at Fermilab. Working with so many excellent experts, I have learnt a lot of valuable things about neutrinos and technical skills.

The acknowledgement would not end without thanking all my family members who have given me their loving support. Thank you, Yina and Ke, for always being so hu-

morous, witty, and lovely. I must express my utmost emotions of being deeply moved and grateful to Yili, who has been continuously giving me her deepest love and teaching me knowledge and the principles of being a good person since I was a child. I would like to express my deepest thanks to my mother and my father, whose unwavering support, encouragement, and love have been indispensable throughout my academic journey.

Finally, I would like to acknowledge the financial, technical, and academic support from the University of Sussex. I also thank the China Scholarship Council (CSC) for providing the funding support through my PhD study.

Preface

The main goals of the data analysis of neutrino oscillations in NOvA in this thesis were suggested by my supervisor, Jeff Hartnell.

Chapter 1 is the introduction, introducing the motivation of the thesis.

Chapter 2 presents the theory framework of neutrino physics including the discovery history of neutrinos and neutrino oscillation physics and introduce some representative neutrino oscillation experiments as well as NOvA's latest measurement results.

Chapter 3 describes NOvA's experimental set-up. This chapter describes the source of NOvA's neutrino beam, near and far detectors, data taking process and simulation process.

Chapter 4 presents the general methodology of the NOvA analysis chain. Neutrino event reconstruction, energy reconstruction, event selections and background sources, the extrapolation method from the Near Detector (ND) to the Far Detector (FD), and sources of systematic uncertainties are covered. This chapter is based on the work developed by the NOvA collaboration.

Chapter 5 introduces the sensitivity improvement techniques performed by the author. This chapter discusses several methods that can improve the ν_μ disappearance sensitivities on θ_{23} and $|\Delta m^2_{32}|$ based on NOvA's standard 3-flavour oscillation analysis. The improvement methods and results are from my own work.

Chapter 6 presents the result of using the sensitivity improvement techniques described in Chapter 5 to analyse the far detector data based on my own work. I have modified the code written by other members of the NOvA collaboration to make it suitable for my work to produce some of the plots. All the spectra and oscillation fit results are entirely produced by me.

Chapter 7 summarises and concludes the thesis.

Contents

List of Tables

List of Figures

Chapter 1

Introduction

Neutrinos are one of the important and interesting fields of research in particle physics. The neutrino was first discovered in experiments in 1956 by C. Cowan and F. Reines [1]. Then many types of neutrino oscillation experiments have been designed and constructed. Neutrinos can come from various sources, such as the sun, accelerators, reactors, cosmic rays, radioactive decays in the Earth and supernova explosions [2]. It has been discovered that there are three flavours of neutrinos, electron neutrino ν_e, muon neutrino ν_μ, and tau neutrino ν_τ, which correspond to the three families of the standard model of particle physics.

Neutrinos are massless particles in the Standard Model of particle physics, which is a well-known and successful theory to describe interactions in terms of fundamental particles [3]. The Super-Kamiokande experiment in Japan observed a deficit of muon neutrinos in 1998, which indicated that muon neutrinos were oscillated into tau neutrinos [4]. The SNO experiment in Canada in 2000 [5] confirmed that the solar electron neutrinos can oscillate into other flavours. Neutrino flavour oscillation is a quantum mechanical phenomenon where a neutrino with a specific flavour can be detected as another neutrino flavour after a propagation process. This oscillation only occurs when the neutrinos have mass, and the masses are not all the same. Therefore, the explanation of non-zero neutrino mass requires the new physics beyond the standard model.

For neutrino oscillations, we often consider a standard three-flavour paradigm, which is described by two independent mass-squared splittings, one CP violating phase and three mixing angles. So far, most of the oscillation parameters have been measured well, such as the solar and atmospheric mass-squared differences and mixing angles (i.e., Δm^2_{21}, $|\Delta m^2_{31}|$, θ_{12}, θ_{23}) [6]. However, there are still some unanswered questions. One of the most important goals is to determine whether neutrinos and antineutrinos have the same

behaviour, which leads to a CP violation problem. Measuring the CP violating phase can help explain the asymmetry between matter and antimatter. In addition, it is necessary to determine the ordering of the neutrino mass eigenstates [7] and if θ_{23} is a maximal mixing angle $\pi/4$, which corresponds to a fundamental symmetry between μ and τ flavours [8].

Neutrinos from the Main Injector (NuMI) Off-Axis Neutrino Experiment (NOvA) is a long-baseline neutrino oscillation experiment measuring the 3-flavour oscillation parameters: neutrino mass hierarchy, CP-violating phase δ_{CP} and octant of θ_{23} mixing angle by observing electron neutrino appearance and muon neutrino disappearance [9]. The initial neutrino beam spectra are measured with the 300 tonne near detector, which is 100 m underground at Fermilab. The oscillation parameters are extracted from fitting the observed data to the predicted neutrino spectrum in the 14 kilo-tonne far detector, which is located on the surface in Minnesota, 810 km away from the beam source.

This thesis presents several techniques to improve NOvA's latest 3-flavour oscillation analysis, with a particular focus on the muon neutrino and antineutrino appearance channels. The latest analysis used the datasets with an exposure of 13.6×10^{20} POT in the neutrino beam mode and 12.5×10^{20} POT in the antineutrino beam mode. Sensitivity studies show that the uncertainty range of Δm^2_{32} of the new analysis is reduced by 5.5% and the significance of maximal disappearance rejection improves by 7.7% at a test point where $\Delta m^2_{32} = 2.5 \times 10^{-3}$ eV^2 and $\sin^2\theta_{23} = 0.59$. A new fit to the FD data is also performed using the datasets in neutrino and antineutrino beam modes. The new analysis can also help reduce the uncertainty range of Δm^2_{32} and improve the rejection of the the disfavoured octant.

The structure of the thesis is shown in the Preface.

Chapter 2

Neutrino Physics

2.1 A brief introduction to neutrinos

2.1.1 Discovery of neutrinos

A neutrino is one of the fundamental particles in the Standard Model. It was first postulated and named "neutron" by Wolfgang Pauli in 1930 to explain the continuous energy spectrum in nuclear beta decays, which otherwise violated the energy conservation law [10]. In Pauli's postulate, the new particle has no electric charge and spin 1/2 to satisfy the conservation of the electric charge and the conservation of angular momentum. In 1932, James Chadwick discovered the particle that we now call the neutron, but this is not the particle from Pauli's postulation [11]. The discovered neutron was far too heavy to be Pauli's particle. The name "neutrino" which means "little neutral one" was given by Enrico Fermi who rebuilt the theory of beta decays in 1934 [12]. In Fermi's theory, Chadwick's neutral heavy "neutron" can decay into a proton, an electron and a neutrino (which we now call an electron antineutrino): $n \to p + e^- + \bar{\nu}_e$.

In 1956, Frederick Reines and Clyde Cowan first confirmed they had detected the neutrino using a tank filled with 1400 litres of liquid scintillator. In this experiment, the antineutrinos emitted through beta decay in a nuclear reactor interacted with protons to produce positrons and neutrons via the so-called inverse $\beta-$decay process: $\bar{\nu}_e + p \to n + e^+$. The positron can be observed through the positron-electron annihilation emitting two gamma rays, and later the neutron capture on cadmium can release an additional gamma ray. The technique of the delayed coincidence of these two events provides a signature of the neutrino interaction and substantially reduced the background. Frederick Reines was awarded the 1995 Nobel prize for providing convincing evidence of the existence of neutrinos.

After that, neutrino physics entered into a fast-growing era. Maurice Goldhaber, Lee Grodzins and Andrew Sunyar from Brookhaven National Laboratory in 1958 found that neutrinos have left-handed helicity[1] [13]. In 1962, Lederman, Schwartz and Steinberger first observed muon neutrinos from pion decays produced by a 15 GeV proton beam hitting a beryllium target [14]. When the neutrinos produced in this experiment interacted in the spark chamber downstream, they mainly produced muons. This phenomenon indicated that the existence of at least two generations of the neutrino family.

In the 1960s and 1970s, many scattering experiments were constructed to study the quark structure of hadrons. In 1973, the hadronic [15, 16] and leptonic [17] neutral current interactions with ν_μ and $\bar{\nu}_\mu$ were detected by the Gargamelle neutrino experiment at CERN. These reactions need a neutral carrier particle to mediate the weak nuclear force, and hence provided evidence for the theory of the electroweak unification. In 1975 the SPEAR e^+e^- collider at SLAC observed the τ lepton [18], which indicated the existence of the tau neutrino ν_τ. The tau neutrino was first observed in the DONUT experiment at Fermilab in 2001 [19].

2.1.2 Neutrino oscillation

Neutrino oscillation is a quantum-mechanical phenomenon that neutrinos undergo flavour transitions as they propagate over a distance. It can be described in terms of the relationship between the eigenstates of the weak interaction ν_e, ν_μ and ν_τ, and the mass eigenstates of the free-particle Hamiltonian, ν_1, ν_2 and ν_3. This phenomenon was verified by observed deficits of solar and atmospheric neutrinos.

The sun provides abundant electron neutrinos with energy of the order of 1 MeV, produced from the thermonuclear fusion reactions in the sun's core. The pioneering Homestake experiment in South Dakota in the USA first detected solar neutrinos. The detector of this experiment located 1478 m below the surface. This detector consisted of a steel tank containing 615 tons of tetrachloroethylene (C_2Cl_4). The neutrinos were detected through this process: $\nu_e + {}^{37}\mathrm{Cl} \rightarrow e^- + {}^{37}\mathrm{Ar}$, which is called the Pontecorvo-Alvarez inverse β-decay Cl-Ar reaction. Then the number of neutrinos events can be obtained by counting the radioactive decay of the argon atoms. The Homestake experiment showed the solar neutrino rate was about two thirds less than the prediction by John Bahcall's Standard Solar Model (SSM) [20, 21]. In the 1980s, GALLEX/GNO in Italy and SAGE in Russia,

[1] The helicity h of a particle is defined as the component of spin along the direction of motion: $h = \frac{\vec{S}\cdot\vec{p}}{p}$. For a spin-half fermion, the $h = +1/2$ and $h = -1/2$ states are defined as right-handed and left-handed helicity states, respectively.

which detected solar neutrinos though the interaction $\nu_e + {}^{71}\text{Ga} \rightarrow {}^{71}\text{Ge} + e^-$, found the ratio of neutrino flux to the SSM prediction were 0.60 and 0.52, respectively [22, 23]. The Kamiokande experiment in Japan using a water Cherenkov detector gathered more evidence for the deficit of solar neutrinos and reported the ratio of neutrino flux to the SSM model is 0.54 [24]. These deficits were known as the Solar Neutrino Problem. Data might indicate oscillations, or could be explained by a problem with SSM.

Research for atmospheric neutrinos was mainly from the Super Kamiokande experiment [25], which used an underground water Cherenkov detector. The detector was able to observe interactions from both upward and downward atmospheric neutrinos. In 1998, Super-K reported a 6.2 σ evidence of a zenith angle dependent deficit of muon neutrino events, which provided compelling evidence that missing muon neutrinos were turned into tau neutrinos [4]. In 2001, the Sudbury Neutrino Observatory experiment (SNO) in Ontario, Canada successfully solved the solar neutrino problem. The SNO detector was located 2 km underground and contained 1102 tons of heavy water. The unique design of SNO was that it can detect electron neutrinos, as well as the neutral current interactions of muon and tau neutrinos. It turned out that the electron neutrinos can be oscillated into muon or tau neutrinos when they travel [5]. This result was further supported by the subsequent accelerator neutrino experiments such as K2K [26] and MINOS [27]. Takaaki Kajita from Super-K and Arthur McDonald from SNO were awarded the 2015 Nobel Prize for their work on neutrino oscillations.

2.2 Neutrinos in the Standard Model

2.2.1 Introduction to the Standard Model

The Standard Model (SM) [29, 30, 31] of particle physics is a well-known theoretical framework used to describe the strong, electromagnetic and weak interactions in terms of a set of fundamental particles. The SM is a gauge theory constructed on the local symmetry group $\text{SU}(3)_C \times \text{SU}(2)_L \times \text{U}(1)_Y$, where C, L, Y represents colour, left-handed chirality[2] and weak hypercharge, respectively. Figure 2.1 shows the 17 Standard Model elementary particles including fermions and bosons. The fermions, which are spin 1/2 particles, consist of three generations of quarks and three generations of leptons. Quarks can participate in all interactions, while leptons participate in all the interactions except

[2] A Dirac spinor can be written as the sum of left and right handed chiral components. The chiral projection operators, P_L and P_R project out left and right-handed chiral particle states, respectively. Only in the ultra-relativistic limit, the helicity eigenstates are the same as the chiral eigenstates.

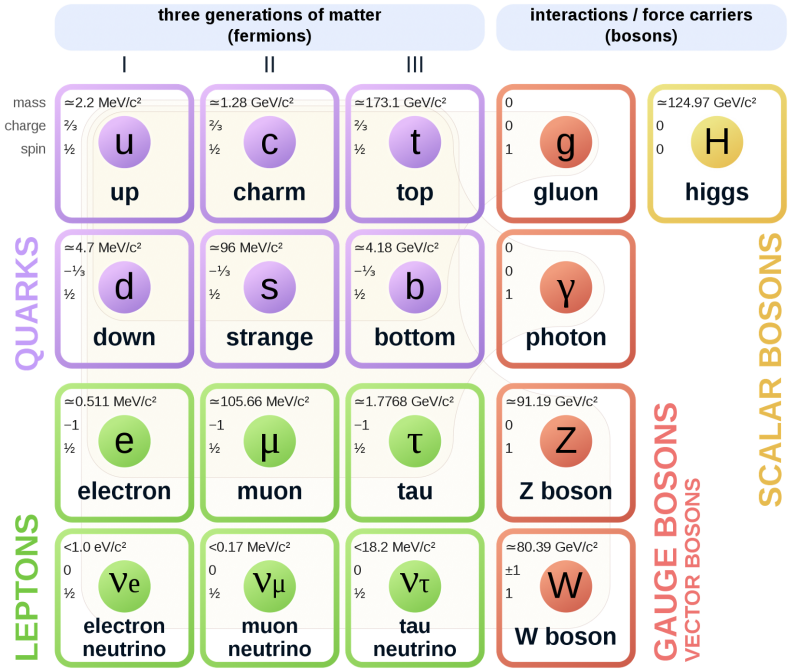

Figure 2.1: Elementary particles of the Standard model [28].

strong interactions. Each quark or lepton has a corresponding anti-particle, and the anti-particle has opposite values for all the quantum numbers. The gauge bosons which are integer spin (0 or 1) particles are the mediators of the strong, electromagnetic and weak interactions.

The strong interaction is a SU(3) gauge theory, and it involves the quarks with different colours (red, green or blue)[3] and eight gluons. Quarks are always confined in bound states, which are called hadrons. Hadrons have two types, mesons and baryons. Mesons are bound states of a quark and an antiquark, while baryons are bound states of three quarks. Four gauge bosons, including the massless photon, the massive $W^{\pm}$ and Z, which are related to the three generators of $\mathrm{SU}(2)_L$ and one generator of $\mathrm{U}(1)_Y$, mediate electroweak interactions. The last discovered particle in the SM family is the Higgs boson, by which the mass is generated[4]. In 2012, CERN announced the discovery of the Higgs boson [32].

2.2.2 Weak interactions

The electromagnetic and weak forces are described under an $\mathrm{SU}_L(2) \times \mathrm{U}(1)$ gauge group. The symmetry group $\mathrm{SU}(2)_L$ is related to weak isospin and the symmetry group $\mathrm{U}(1)_Y$ is

[3] An antiquark can carry anti-red, anti-green or anti-blue.

[4] This mechanism can not generate neutrino masses. A fermion obtains mass through the interaction involving a left-handed fermion, a right-handed fermion, and the Higgs field. However, only left-handed neutrinos were observed.

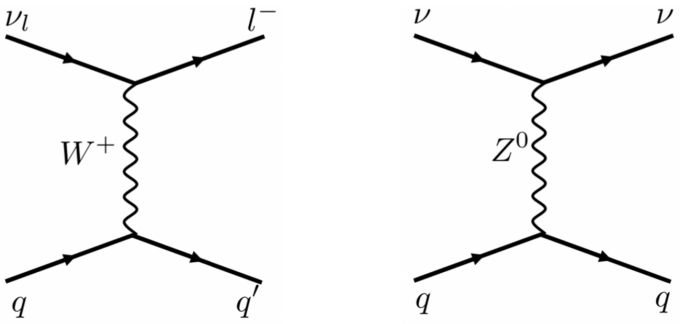

(a) Charged Current (b) Neutral Current

Figure 2.2: Feynman diagrams for examples of the CC and NC interactions. Left shows the process of the interaction between a neutrino and a quark. The neutrino with flavour ℓ is absorbed and the lepton of flavour ℓ is emitted, and the W^+ transfer the charge to the quark. Right shows the neutral current interaction, where the neutrino scatters off the quark, interacting via the Z^0 boson.

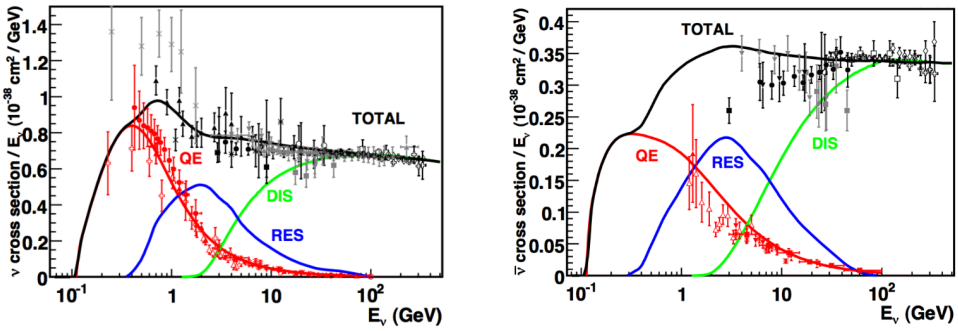

Figure 2.3: Cross section vs. energy for neutrinos on the left and antineutrinos on the right. Points with error bars shows measurement data, and the curves show the models. Quasi-elastic (QE) scattering, resonance production (RES), and deep inelastic scattering (DIS) have contributions in this energy region. Taken from [33].

called hypercharge. Under $SU(2)_L$, left-handed fermions are doublets while right-handed fermions are singlets. After symmetry breaking, $W^{\pm}$ and Z acquire masses and act as the mediators of the weak force, and the photon remains massless. Quarks and charged leptons obtain their masses by interacting with the Higgs field through Yukawa interactions. Neutrinos are massless in the SM, since there are no right-handed neutrinos. The weak force acts on the flavour of both hadrons and leptons over a very short range, and the electromagnetic force only exists between particles that have electric charges and works with a long range. Neutrinos are electrically neutral and colourless, thus they only participate in weak interactions.

There are two types of weak interactions introduced for neutrinos in the Standard Model. The neutrino couples to $W^{\pm}$ bosons in the Charged Current (CC) interactions and to the Z^0 boson in the Neutral Current (NC) interaction. The charged weak current j_W^{μ} is given by

$$j_W^{\mu} = 2 \sum_{\alpha=e,\mu,\tau} \bar{\nu}_{L,\alpha} \gamma^{\mu} l_{\alpha L}, \tag{2.1}$$

and the neutral current j_Z^{μ} can be expressed as

$$j_Z^{\mu} = 2 \sum_{\alpha=e,\mu,\tau} g_L^{\nu} \bar{\nu}_{\alpha L} \gamma^{\mu} \nu_{\alpha L} + g_L^f \bar{l}_{\alpha L} \gamma^{\mu} l_{\alpha L} + g_R^f \bar{l}_{\alpha R} \gamma^{\mu} l_{\alpha R}, \tag{2.2}$$

where $\nu_{\alpha L(R)}$ and $l_{\alpha L(R)}$ represent the left (right) neutral and charged leptonic fields, respectively, and g_L^{ν}, g_L^f and g_R^f are the fermion left and right handed couplings. Then the leptonic charged-current weak interaction Lagrangian is expressed as

$$L_{CC} = -\frac{g}{2\sqrt{2}} (j_W^{\mu} W_{\mu} + j_W^{\mu,\dagger} W_{\mu}^{\dagger}), \tag{2.3}$$

and the leptonic neutral-current weak interaction Lagrangian is expressed as

$$L_{NC} = -\frac{g}{2\cos\theta_W} j_Z^{\mu} Z_{\mu}, \tag{2.4}$$

where W_{μ} and Z_{μ} are the heavy gauge boson fields, g is the weak coupling constant, and θ_W is the Weinberg angle. Figure 2.2 shows the examples of these two types of interaction. In the charged current case, neutrinos can be converted to their partner lepton via the $W^{\pm}$ boson. The electrically charged lepton with the same flavour as the neutrino flavour can be detected by the detector, thus the incoming neutrino flavour can be identified. In the case of NC interaction, the force is mediated by the electrically neutral Z boson, so there is no transfer of electric charge. Figure 2.3 shows the cross sections for different interaction types as a function of energy. The V-A theory, which is a universal theory of weak interaction, shows that the weak CC interaction is stronger than the NC counterpart.

There are several ways neutrinos interact with a target nucleus or electron, and neutrino interactions can be further classified into several types:

- **Neutrino-electron elastic scattering** Neutrinos and antineutrinos can interact with electrons via the elastic scattering process $\nu_\alpha(\bar{\nu}_\alpha) + e^- \rightarrow \nu_\alpha(\bar{\nu}_\alpha) + e^-$ with $\alpha = e, \mu, \tau$. In the case of $\alpha = e$, at tree level, both NC and CC interactions can contribute to the process, while in the case of $\alpha = \mu, \tau$ only the NC interaction contributes.

- **Neutrino-electron quasielastic scattering** Muon neutrinos with enough energy to produce a μ can interact with electrons though the quasielastic charged-current process $\nu_\mu + e^- \rightarrow \nu_e + \mu^-$. Tau neutrinos can have a similar interaction.

- **Quasielastic reactions on nucleons** For CC interactions, a neutrino scatters off a nucleon and emits a lepton: $\nu_l + n \rightarrow l^- + p$, $\bar{\nu}_l + p \rightarrow l^+ + n$ with $l = e, \mu, \tau$. The NC interactions happen via $\nu_l + n(p) \rightarrow \nu_l + n(p)$, $\bar{\nu}_l + n(p) \rightarrow \bar{\nu}_l + n(p)$, where the outgoing lepton is the neutrino.

- **Resonant production** Neutrinos with enough energy can excite a nucleon to a baryon resonance N*, then the N* typically decays to a nucleon and a single pion. The CC interaction occurs through $\nu_\mu + N \rightarrow \mu^- + \pi + N'$, and the NC interaction occurs through $\nu_\mu + N \rightarrow \nu_\mu + \pi + N$, where $N, N' = n, p$ and π represents $\pi^\pm$, π^0.

- **Coherent pion production** Neutrinos can coherently scatter from the entire nucleus and transfer a small amount of energy to the nucleus. This low-Q^2 (Q is the four momentum transfer) process causes no nuclear recoil and produces a forward scattering pion. The NC interactions are $\nu_l + A \rightarrow \nu_l + A + \pi^0$, $\bar{\nu}_l + A \rightarrow \bar{\nu}_l + A + \pi^0$, and CC interactions are: $\nu_l + A \rightarrow l^- + A + \pi^+$, $\bar{\nu}_l + A \rightarrow l^+ + A + \pi^-$ in which A is the nucleus with atomic number equal to A.

- **Deep inelastic scattering** Neutrinos and antineutrinos with high energy scatter directly off quarks. NC interactions are $\nu_l(\bar{\nu}_l) + N \rightarrow \nu_l(\bar{\nu}_l) + X$, and CC interactions are $\nu_l(\bar{\nu}_l) + N \rightarrow l^-(l^+) + X$, where N=p, n and X represents a set of hadrons.

- **Meson exchange current interaction (MEC)** Neutrinos interact with a correlated pair of nucleons in a nucleus, resulting in multiple nucleons in the final state. "2 particle-2 hole (2p-2h)" interaction as a particular MEC process is often considered. In a 2p2h interaction, neutrinos interacts with two nucleons in a nucleus, leading to a 2-nucleon emission [34].

2.2.3 Neutrino Mass

As described in Section 2.2.1, the origin of neutrino masses is still a mystery beyond the Standard Model. When the right-handed neutrinos are introduced, a Dirac neutrino mass can be created by the Higgs mechanism that applies to quarks and charged leptons. The mass term of the Lagrangian of a Dirac neutrino is given as

$$L_{Dirac} = m\bar{\psi}\psi = m\bar{\psi}_L\psi_R + m\bar{\psi}_R\psi_L, \tag{2.5}$$

where ψ_L and ψ_R are the left-handed and right-handed chiral components of the neutrino field. This model is called the minimally extended Standard Model, where the asymmetry between the lepton and quark sector in the SM because of the absence of the right-handed neutrinos is eliminated [2]. The right handed neutrino is usually called sterile neutrinos because they can't participate in weak interactions.

Another way is to express the mass by a Majorana mass term, which only needs the left-handed component

$$L_{Majorana} = \frac{1}{2}(m\bar{\psi}_L\psi_R^C + m\bar{\psi}_R^C\psi_L) = \frac{1}{2}(m\bar{\psi}_L C\bar{\psi}_L^T + m\psi_L^T C^\dagger\psi_L), \tag{2.6}$$

where ψ represents the neutrino, C is the charged conjugation matrix. Here the neutrino is assumed to be the same as the antineutrino. However, Majorana masses violate total lepton number conservation by two units $\Delta L = 2$, which is beyond the SM.

2.3 Neutrino oscillations in vacuum

Neutrinos interact with matter by the weak interaction in three flavour eigenstates, ν_e, ν_μ and ν_τ. However, neutrinos propagate in vacuum in mass eigenstates, ν_1, ν_2 and ν_3. Each of the flavour states can be written as a superposition of the mass states and vice-versa. For example, a neutrino of the weak flavour α can be expressed as a linear combination of the mass eigenstates as follows:

$$|\nu_\alpha\rangle = \sum_{i=1}^{3} U_{\alpha i}^* |\nu_i\rangle, \tag{2.7}$$

where $U_{\alpha i}^*$ is the element of the unitary Pontecorvo-Maki-Nakagawa-Sakata (PMNS) matrix describing the conversion relation between the flavour eigenstate α and the mass eigenstate i.

In general, the standard parameterisation of the PMNS matrix is conventionally ex-

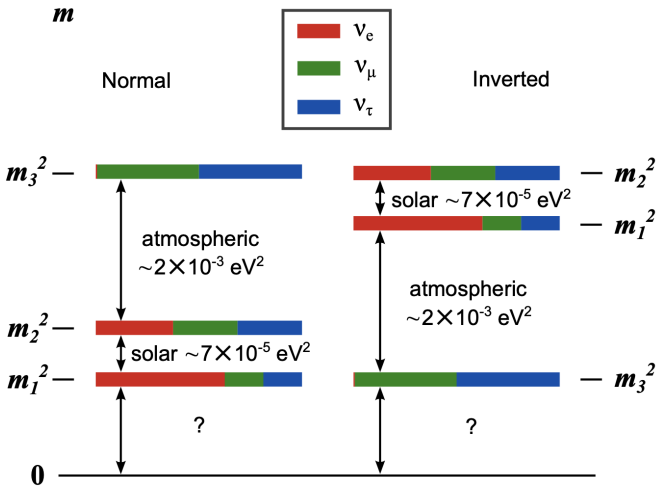

Figure 2.4: Neutrino mass hierarchy.

pressed as

$$U = \begin{pmatrix} U_{e1} & U_{e2} & U_{e3} \\ U_{\mu 1} & U_{\mu 2} & U_{\mu 3} \\ U_{\tau 1} & U_{\tau 2} & U_{\tau 3} \end{pmatrix} \tag{2.8}$$

$$= \begin{pmatrix} c_{13}c_{12} & c_{13}s_{12} & s_{13}e^{-i\delta} \\ -c_{23}s_{12} - s_{13}s_{23}c_{12}e^{i\delta} & c_{23}c_{12} - s_{13}s_{23}s_{12}e^{i\delta} & c_{13}s_{23} \\ s_{23}s_{12} - s_{13}c_{23}c_{12}e^{i\delta} & -s_{23}c_{12} - s_{13}c_{23}s_{12}e^{i\delta} & c_{13}c_{23} \end{pmatrix} \begin{pmatrix} e^{i\frac{\alpha_1}{2}} & 0 & 0 \\ 0 & e^{i\frac{\alpha_2}{2}} & 0 \\ 0 & 0 & 1 \end{pmatrix} \tag{2.9}$$

$$= \begin{pmatrix} 1 & 0 & 0 \\ 0 & c_{23} & s_{23} \\ 0 & -s_{23} & c_{23} \end{pmatrix} \begin{pmatrix} c_{13} & 0 & s_{13}e^{-i\delta} \\ 0 & 1 & 0 \\ -s_{13}e^{i\delta} & 0 & c_{13} \end{pmatrix} \begin{pmatrix} c_{12} & s_{12} & 0 \\ -s_{12} & c_{12} & 0 \\ 0 & 0 & 1 \end{pmatrix} \begin{pmatrix} e^{i\frac{\alpha_1}{2}} & 0 & 0 \\ 0 & e^{i\frac{\alpha_2}{2}} & 0 \\ 0 & 0 & 1 \end{pmatrix}, \tag{2.10}$$

where θ_{ij} represents three mixing angles, $c_{ij} = \cos\theta_{ij}$, $s_{ij} = \sin\theta_{ij}$, δ is the CP violating phase and the other two phases show the two Majorana phases. The first term called the 23 sector in Equation 2.10 is associated most strongly with atmospheric neutrino oscillations, involving the mixing angle θ_{23} and the largest mass splitting differences Δm^2_{32} and Δm^2_{31}. In the middle term, which is also called the 13 sector, the value of Δm^2_{31} is approximately close to the atmospheric mass splitting, and the angle θ_{13} is measured to be non-zero by the reactor neutrino experiments. The last sector called the 12 sector is associated with solar neutrino oscillations with the mixing angle θ_{12} and the squared mass splitting difference Δm^2_{21}.

So far neutrino oscillation experiments have measured Δm^2_{21}, θ_{12}, and θ_{13} with high precision. In the atmospheric sector it is difficult to determine the sign of Δm^2_{32}. This

problem is known as neutrino mass hierarchy, which is depicted in Figure 2.4. The positive Δm^2_{32} corresponds to the case of normal hierarchy (NH), where ν_3 is the heaviest mass eigenstate. In the inverted hierarchy (IH) case, the sign of Δm^2_{32} is negative and ν_3 is the lightest mass eigenstate. It is very important to determine whether $\theta_{23} = 45°$ or not. From Equation 2.8 to Equation 2.10, $U_{\mu 3} = U_{\tau 3} = \frac{1}{2}c_{13}$, which means the third mass eigenstate has equal contributions of muon and tau neutrino eigenstates. This is also corresponding to a lepton universality of symmetry [8], thus whether θ_{23} is 45° or not really matters. A non-maximal value of θ_{23} gives rise to octant degeneracy problem (i.e. lower octant: $\theta_{23} < 45°$ or higher octant: $\theta_{23} < 45°$). Finally, the value of the CP violation phase is one of the important goals for neutrino oscillation experiments, as solving this problem can help explain the asymmetry of matter and antimatter in the universe.

In Equation 2.7, the massive neutrino states $|\nu_k\rangle$ are eigenstates of the Hamiltonian,

$$\hat{H}|\nu_k\rangle = E_k|\nu_k\rangle, \tag{2.11}$$

with energy eigenvalues

$$E_k = \sqrt{\vec{p}^2 + m_k^2}. \tag{2.12}$$

The massive neutrino states evolve in time as plane waves

$$|\nu_k(t)\rangle = e^{-iE_k t}|\nu_k\rangle. \tag{2.13}$$

Assuming a neutrino is created with a flavour α at time $t = 0$, the time evolution of this state is given by

$$|\nu_\alpha(t)\rangle = \sum_k U^*_{\alpha k} e^{-iE_k t}|\nu_k\rangle. \tag{2.14}$$

Because of the unitarity relation

$$U^\dagger U = 1 \quad (\sum_k U_{\alpha k} U^*_{\beta k} = \delta_{\alpha\beta}), \tag{2.15}$$

the massive states can be written in terms of flavour states

$$|\nu_k\rangle = \sum_\alpha U_{\alpha k}|\nu_\alpha\rangle. \tag{2.16}$$

Substituting Equation 2.16 into Equation 2.14, $|\nu_\alpha(t)\rangle$ can be written as

$$|\nu_\alpha(t)\rangle = \sum_{\beta=e,\mu,\tau} (\sum_k U^*_{\alpha k} e^{-iE_k t} U_{\beta k})|\nu_\beta\rangle. \tag{2.17}$$

Then the amplitude of $\nu_\alpha \to \nu_\beta$ as a function of time t is

$$A_{\nu_\alpha \to \nu_\beta}(t) \equiv \langle \nu_\beta | \nu_\alpha(t)\rangle = \sum_k U^*_{\alpha k} U_{\beta k} e^{-iE_k t}. \tag{2.18}$$

The oscillation probability is then given by

$$P_{\alpha\beta}(L,E) = |A_{\nu_\alpha \to \nu_\beta}(t)|^2 = \sum_{k,j} U^*_{\alpha k} U_{\beta k} U_{\alpha j} U^*_{\beta j} e^{-i(E_k - E_j)t}. \tag{2.19}$$

Since ultrarelativistic neutrinos propagate close to the speed of light, it is reasonable to assume $t = L$ and $E = p$, where L is the distance between the source and the detector, E is the neutrino energy and p is the neutrino momentum. Using a binomial expansion, we find

$$E_i \simeq p + \frac{m_i^2}{2p} \simeq E + \frac{m_k^2}{2E}, \tag{2.20}$$

thus

$$E_k - E_j \simeq \frac{\Delta m^2_{kj}}{2E}, \tag{2.21}$$

where $\Delta m^2_{jk} = m^2_j - m^2_k$. Then the oscillation probability in Equation 2.18 can be approximated by

$$P_{\alpha\beta}(L,E) = \sum_{k,j} U^*_{\alpha k} U_{\beta k} U_{\alpha j} U^*_{\beta j} \exp(-i\frac{\Delta m^2_{kj} L}{2E}). \tag{2.22}$$

It is easy to see the propagation distance and neutrino energy affects the oscillation phase

$$\phi_{jk} = -\frac{\Delta m^2_{kj} L}{2E}, \tag{2.23}$$

where Δm^2_{jk} as a constant also affects the phase. The oscillation amplitude is determined by the elements of the matrix U, which are constant values. Therefore the values of the squared mass differences and the parameters in U can be measured through neutrino oscillation experiments. If $L = 0$, the oscillation probability can be written as

$$P_{\nu_\alpha \to \nu_\beta}(L = 0, E) = \delta_{\alpha\beta}. \tag{2.24}$$

From the square of the Equation 2.15, the real and imaginary parts of $U_{\beta k} U^*_{\alpha k} U^*_{\beta j} U_{\alpha j}$ can be separated as below

$$\sum_k |U_{\alpha k}|^2 |U^2_{\beta k}| = \delta_{\alpha\beta} - 2 \sum_{k>j} R[U^*_{\alpha k} U_{\beta k} U_{\alpha j} U^*_{\beta j}]. \tag{2.25}$$

Therefore, the probability can be written as

$$\begin{aligned} P(\nu_\alpha \to \nu_\beta) = \delta_{\alpha\beta} &- 4 \sum_{k>j} R[U^*_{\alpha k} U_{\beta k} U_{\alpha j} U^*_{\beta j}] \sin^2(\tfrac{\Delta m^2_{kj}}{4E} L) \\ &+ 2 \sum_{k>j} I[U^*_{\alpha k} U_{\beta k} U_{\alpha j} U^*_{\beta j}] \sin(\tfrac{\Delta m^2_{kj}}{2E} L). \end{aligned} \tag{2.26}$$

For the antineutrino oscillations, under the assumption of CPT invariance, the probability can be given as

$$P(\bar{\nu}_\alpha \to \bar{\nu}_\beta) = P(\nu_\beta \to \nu_\alpha). \tag{2.27}$$

In sum, all neutrino oscillation patterns can be calculated by the PMNS matrix based on the energy and distance travelled by the neutrino. Two neutrino oscillation channels $\nu_\mu \to \nu_\mu$ and $\nu_\mu \to \nu_e$ that are used in NOvA will be discussed below.

The $\nu_\mu \to \nu_\mu$ channel is usually called ν_μ disappearance, since some initial muon neutrinos disappear after a propagation distance. Starting from Equation 2.26, the muon disappearance probability can be written as

$$P_{\mu\mu} = 1 - 4\sum_{k>j} |U_{\mu i}|^2 |U_{\mu j}|^2 \sin^2(\frac{\Delta m^2_{ij}}{4E} L), \tag{2.28}$$

where the imaginary term of Equation 2.26 is zero. Since current experimental results show that θ_{13} is small compared to other mixing angles, $\sin\theta_{13} \sim 0$ and $\cos\theta_{13} \sim 1$, and then the PMNS elements

$$|U_{\mu 1}|^2 \approx \sin^2\theta_{12}\cos^2\theta_{23}, \tag{2.29}$$

$$|U_{\mu 2}|^2 \approx \cos^2\theta_{12}\cos^2\theta_{23}, \tag{2.30}$$

$$|U_{\mu 3}|^2 \approx \sin^2\theta_{23}. \tag{2.31}$$

Therefore the probability in Equation 2.28 can be approximately written as

$$\begin{aligned} P_{\mu\mu} &= 1 - 4(|U_{\mu 1}|^2|U_{\mu 2}|^2\sin^2(\Delta_{21}) + |U_{\mu 2}|^2|U_{\mu 3}|^2\sin^2(\Delta_{32}) + |U_{\mu 1}|^2|U_{\mu 3}|^2\sin^2(\Delta_{31})) \\ &\approx 1 - 4(c_{23}^2 s_{12}^2 c_{23}^2 c_{12}^2\sin^2(\Delta_{21}) + c_{23}^2 c_{12}^2 s_{23}^2\sin^2(\Delta_{32}) + c_{23}^2 s_{12}^2 s_{23}^2\sin^2(\Delta_{31})) \\ &\approx 1 - 4\cos^2\theta_{23}\sin^2\theta_{23}\sin^2(\Delta_{23}) \\ &= 1 - \sin^2 2\theta_{23}\sin^2(\Delta_{23}). \end{aligned} \tag{2.32}$$

where $c_{ij} = \cos\theta_{ij}$, $s_{ij} = \sin\theta_{ij}$ and $\Delta_{ij} = \frac{\Delta m^2_{ij} L}{4E}$. Experimental results have shown that Δm^2_{31} is about 30 times larger than Δm^2_{21}, which allows the approximation $\Delta m^2_{32} \simeq \Delta m^2_{31}$. For a given neutrino energy, the wavelength for $\sin^2\Delta_{21}$ term is 30 times that of the $\sin^2\Delta_{31}$ oscillation term. At the NOvA experiment, only the short wavelength component matters. Therefore, the term proportional to $\sin^2\Delta_{21}$ has been ignored. From this probability it is clear that muon neutrino disappearance can be used to measure the mixing angle θ_{23} and mass splitting $|\Delta m^2_{32}|$, but not the θ_{23} octant and the sign of Δm^2_{32}.

The channel $\nu_\mu \to \nu_e$ is called ν_e appearance where some ν_e appear from the initial ν_μ. Starting from Equation 2.26, the oscillation probability of $\nu_\mu \to \nu_e$ is approximated as

$$P_{\mu e} = P_{\text{atm}} + P_{\text{sol}} + 2\sqrt{P_{\text{atm}}P_{\text{sol}}}(\cos\Delta_{32}\cos\delta_{\text{CP}} \mp \sin\Delta_{32}\sin\delta_{\text{CP}}) \tag{2.33}$$

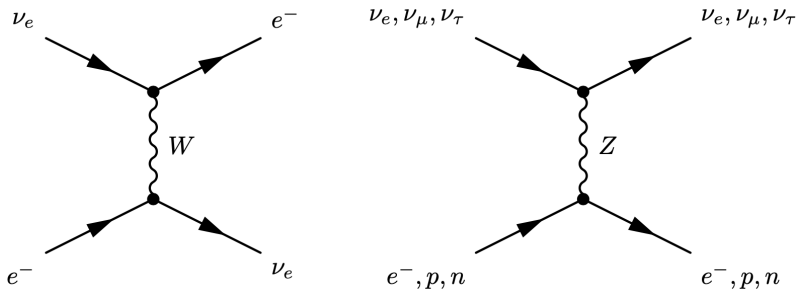

Figure 2.5: Feynman diagrams for the coherent forward elastic scattering processes. The left process generate the charged-current potential V_{cc} via W exchange and the right process generate the neutral-current potential V_{NC} via Z exchange.

with

$$P_{\text{atm}} = \sin^2\theta_{23}\sin^2 2\theta_{13}\sin^2\Delta_{31} \tag{2.34}$$

and

$$P_{\text{sol}} = \cos^2\theta_{23}\cos^2\theta_{13}\sin^2 2\theta_{12}\sin^2\Delta_{21}, \tag{2.35}$$

where the $-$ is for neutrinos and $+$ for antineutrinos [35].

2.4 Neutrino Oscillations in Matter

When neutrinos propagate in matter, the interactions between neutrinos and this matter modify the mixing and oscillation. Neutrinos are mainly affected by effective potentials generated by the coherent interactions with the matter by coherent forward elastic charged-current and neutral-current scatterings. The Feynman diagrams of CC and NC scatterings are shown in Figure 2.5. The coherent forward scattering occur via NC interactions with protons, neutrons, electrons, and CC interactions with electrons.

Because the mass of the W boson is much greater than the neutrinos, the matter effect can be described by introducing an additional potential V_{MSW} into neutrino Hamiltonian:

$$H = H_0 + V_{MSW}, \tag{2.36}$$

where $H_0 = Udiag(E_1, E_2, E_3)U^\dagger$ corresponds to the vacuum Hamiltonian, in which E_i are the energy eigenvalues in vacuum, and

$$V_{\text{MSW}} = \sqrt{2}G_F \begin{pmatrix} N_e + N_n/2 & & \\ & N_n/2 & \\ & & N_n/2 \end{pmatrix}, \tag{2.37}$$

where G_F represents the Fermi constant, N_e represents the electron number density in the matter, and N_n denotes the number density of neutrons. The NC contributions from protons and electrons are cancelled since these particles have equal numbers [2]. The index "MSW" stands for Stanislav Mikheyev, Alexei Smirnov and Lincoln Wolfenstein, who first introduced matter effects in neutrino oscillations [36, 37, 38].

Now the neutrino oscillation probability in matter can be derived. First, the new Hamiltonian in Equation 2.36 is diagonalised, creating a new mixing matrix $\tilde{\mathrm{U}}$ and new energy eigenvalues $\tilde{E}_j = (p_j^2 + \tilde{m}_j^2)^{1/2}$, where $\tilde{m}_j$ represents the effective neutrino masses in matter. Second, with replacing U and m_j by $\tilde{U}$ and $\tilde{m}_j$ in Equation 2.19, the probability in matter can be calculated. In this calculation, the flavour diagonal contributions to V_{MSW} are cancelled, since only energy differences are relevant. Finally, a simplified matter potential

$$V_{\mathrm{MSW}} = \sqrt{2} G_F N_e U^{\dagger} diag(1,0,0) U \tag{2.38}$$

can be used as a substitute for Equation 2.37.

When considering matter effects, the $\sqrt{P_{\mathrm{atm}}}$ and $\sqrt{P_{\mathrm{sol}}}$ in Equation 2.33 are given by

$$\begin{aligned} \sqrt{P_{\mathrm{atm}}} &= \sin\theta_{23} \sin 2\theta_{13} \frac{\sin(\Delta_{31} \mp aL)}{\Delta_{31} \mp aL} \Delta_{31}, \\ \sqrt{P_{\mathrm{sol}}} &= \cos\theta_{23} \sin 2\theta_{12} \frac{\sin(aL)}{(aL)} \Delta_{21}, \end{aligned} \tag{2.39}$$

where $a = \frac{G_F N_e}{\sqrt{2}}$, and the $-$ is for neutrinos and the $+$ for antineutrinos [35]. The $\sqrt{P_{\mathrm{atm}}}$ contains $\sin^2\theta_{23}$, thus the electron neutrino appearance channel has the sensitivity to the θ_{23} octant. The matter effect provides sensitivity to the neutrino mass hierarchy. If δ_{CP} is equal to 0 or π, the probability becomes the same for neutrinos and antineutrino in vacuum, which means that CP is conserved. If δ_{CP} takes any other value, this means CP is violated. Therefore δ_{CP} can be tested by comparing the probabilities of $\nu_\mu \to \nu_e$ and $\bar{\nu}_\mu \to \bar{\nu}_e$.

2.5 Neutrino Oscillation Experiments

2.5.1 The 12 sector measurement

In the 12 sector, reactor and solar neutrino experiments contribute to the measurement of Δm^2_{21} and θ_{12}. The Sun is an intense source, producing electron neutrinos by the thermonuclear fusion reactions in its core. There are two groups of reactions: the pp chain and the CNO cycle. The result of the two reaction groups can be treated as the overall reaction

$$4\ p + 2\ e^- \to {}^4\mathrm{He} + 2\ \nu_e + 26.73\ \mathrm{MeV}. \tag{2.40}$$

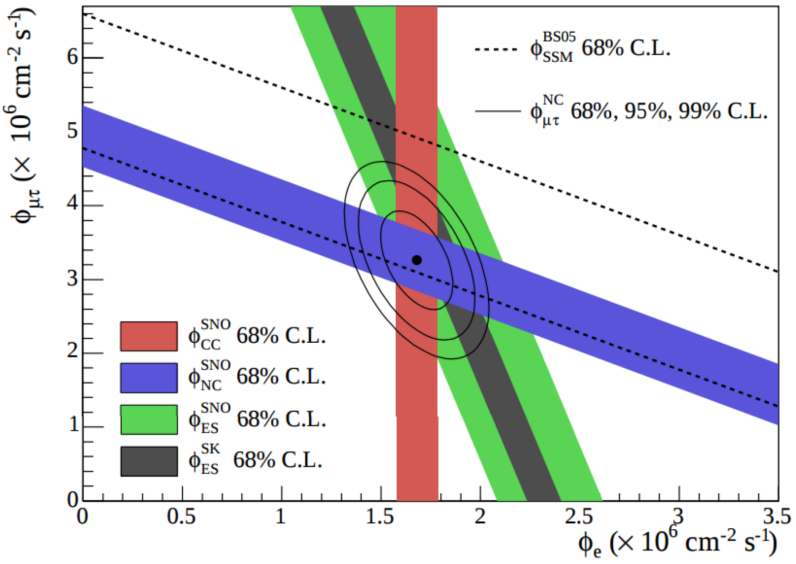

Figure 2.6: Flux of ν_μ and ν_τ versus flux of ν_e measured by SNO [39]. Fluxes measured by CC, NC and ES interactions are shown in red, blue, and green bands, respectively. The grey band shows the measurement of ES by Super-Kamiokande [40]. The band enclosed by the dashed lines represent the total predicted solar neutrino flux. The black point represents the best fit point of ϕ_e from the CC flux and $\phi_{\mu\tau}$ from the NC-CC difference with 68%, 95%, and 99% C.L. contours included.

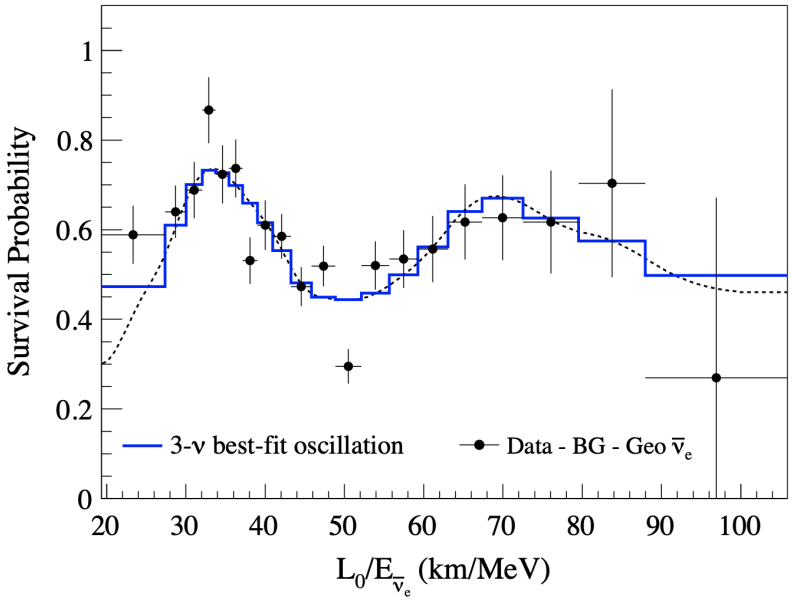

Figure 2.7: Ratio of the observed events to the prediction with no oscillations versus the baseline divided by the neutrino energy in KamLAND. Black points shows the observed data. The blue histogram shows the 3-flavour fit to the data. The dashed black curve shows the best-fit survival probability. Taken from [41].

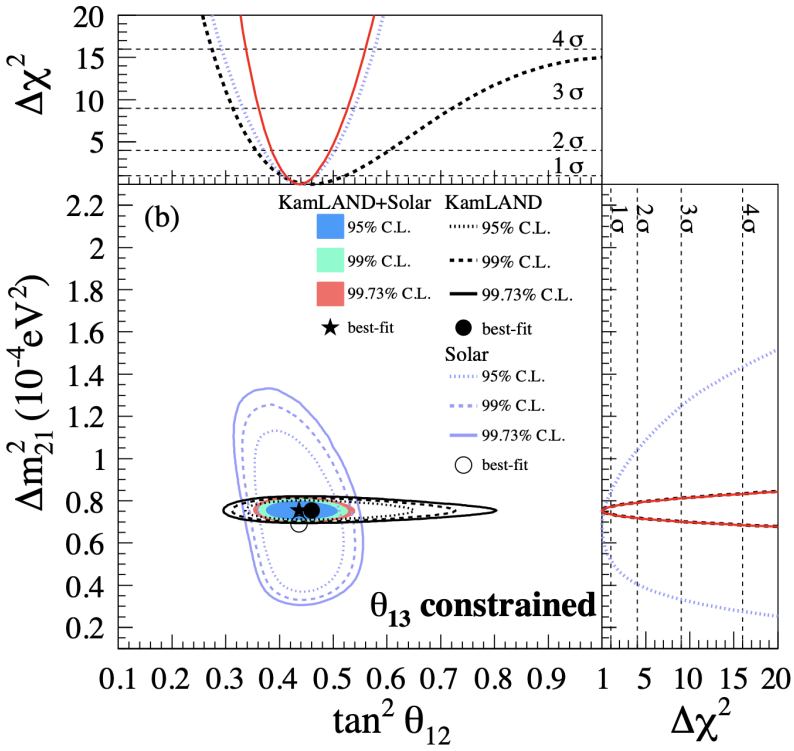

Figure 2.8: Allowed regions of Δm^2_{21} vs. $\tan^2\theta_{12}$ in KamLAND. The black (blue) contours show the constraints from KamLAND (solar experiments). The combination analysis of these two experiments is shown in the shaded regions. Figure taken from [41].

Most solar neutrinos have energies below 0.5 MeV, but the neutrino energy spectrum can extend up to about 20 MeV. As presented in Section 2.1.2, a deficit in the observed ν_e flux compared to expectations was first reported by solar neutrino experiments. In 2002, the SNO experiment confirmed that the missing ν_e change flavour as they travel [5]. The SNO experiment used the below three interactions to detect solar neutrinos

$$\begin{aligned} &\text{CC} : \nu_e + d \to p + p + e^-, \\ &\text{NC} : \nu_x + d \to p + n + \nu_x, \\ &\text{ES} : \nu_x + e^- \to \nu_x + e^-, \end{aligned} \tag{2.41}$$

with $x = e, \mu, \tau$. The charged-current (CC) interaction on deuterium is used to measure the spectrum of electron neutrinos. The neutral-current (NC) on deuterium is used to find the total flux of all active neutrinos which have the same cross section. The elastic scattering (ES) reaction on electrons is a mixture of CC and NC interactions. SNO observed 2176 ± 78 CC events, 2010 ± 85 NC events, and 279 ± 26 ES events, corresponding to the measured fluxes

$$\begin{aligned} \phi_{CC} &= (1.68 \pm 0.06^{+0.08}_{-0.09}) \times 10^6 \text{ cm}^{-2} \text{ s}^{-1}, \\ \phi_{NC} &= (4.94 \pm 0.21^{+0.38}_{-0.34}) \times 10^6 \text{ cm}^{-2} \text{ s}^{-1}, \\ \phi_{ES} &= (2.35 \pm 0.22 \pm 0.15) \times 10^6 \text{ cm}^{-2} \text{ s}^{-1}. \end{aligned} \tag{2.42}$$

The ratio $\frac{\phi_{CC}}{\phi_{NC}} = 0.340 \pm 0.023^{+0.029}_{-0.031}$ can be explained as about two thirds of the electron neutrinos are converted to ν_μ or ν_τ when they arrive on earth. Futhermore, these fluxes can be expressed by the fluxes of ν_e, ν_μ and ν_τ as

$$\begin{aligned} \phi_{CC} &= \phi_e, \\ \phi_{NC} &= \phi_e + \phi_{\mu\tau}, \\ \phi_{ES} &= \phi_e + \frac{\sigma_\mu^{ES}}{\sigma_e^{ES}} \phi_{\mu\tau} = \phi_e + 0.1553 \phi_{\mu\tau}, \end{aligned} \tag{2.43}$$

where ϕ_e represents the flux of ν_e, $\phi_{\mu\tau}$ represents the total flux of ν_μ and ν_τ, σ_e^{ES} represents the cross section of electron neutrinos, and σ_μ^{ES} represents the cross section of ν_μ. The resulting values for the flux of ν_μ and ν_τ are $\phi_{\mu\tau}^{NC} = (3.26 \pm 0.25^{+0.40}_{-0.35}) \times 10^6$ cm^{-2} s^{-1} and $\phi_{\mu\tau}^{ES} = (4.36 \pm 1.52^{+0.90}_{-0.87}) \times 10^6$ cm^{-2} s^{-1}. Figure 2.6 shows the flux of $\nu_{\mu\tau}$ versus the flux of ν_e. These measurements demonstrate that ν_μ and ν_τ fluxes are about twice the ν_e flux, implying flavour transitions. In addition, the NC flux that measures all active species in the solar flux is consistent with the total ν_e flux predicted from the SSM.

The precision measurement of Δm^2_{21} was provided by the reactor experiment Kamioka Liquid scintillator AntiNeutrino Detector (KamLAND). KamLAND can detect electron antineutrinos from 53 reactors in Japan, with a small contribution from the rest of the world. The oscillation distances vary from 80 km to 800 km. The detector is a spherical

ballon with a diameter of 13 m filled with liquid scintillator. The electron antineutrinos are detected by the inverse neutron decay process $\bar{\nu}_e + p \to n + e^+$. To allow θ_{12} and Δm^2_{21} to be measured, the probability is approximately expressed as

$$P(\bar{\nu}_e \to \bar{\nu}_e) \approx 1 - \sin^2 2\theta_{12} \sin^2(1.27\Delta m^2_{21} L/E). \tag{2.44}$$

Figure 2.7 shows the ratio of the observed ν_e spectrum to the no oscillation expectation and the best fit oscillation survival probability. Figure 2.8 shows the measurement results published by KamLAND in 2013. Combining the KamLAND and solar experiments gives tight constraints on θ_{12} ($\tan^2\theta_{12} = 0.436^{+0.029}_{-0.025}$) and Δm^2_{21} ($\Delta m^2_{21} = 7.53^{+0.18}_{-0.18} \times 10^{-5}\text{eV}^2$).

2.5.2 The 23 sector measurement

The 23 sector refers to the parameters θ_{23} and Δm^2_{32}, which were first measured in the atmospheric neutrino experiments. Atmospheric neutrinos are produced by cosmic rays interacting with the atmosphere. The main production process is

$$\begin{aligned} &p + \text{Atomic Nucleus} \to \pi^\pm + \text{Further Hadrons}, \\ &\pi^\pm \to \mu^\pm + \overset{(-)}{\nu}_\mu, \\ &\mu^+(\mu^-) \to e^+(e^-) + \bar{\nu}_\mu(\nu_\mu) + \nu_e(\bar{\nu}_e). \end{aligned} \tag{2.45}$$

Therefore the initial atmospheric neutrino flux consists of ν_e, $\bar{\nu}_e$, ν_μ, $\bar{\nu}_\mu$. The Super-Kamiokande experiment in Japan provided the first compelling evidence for neutrino oscillations in 1998 [42]. Super-Kamiokande detects neutrinos through the Cherenkov radiation emitted by the charged particles produced by neutrino interactions. The detector can clearly distinguish electron neutrinos and muon neutrinos, but it can not distinguish neutrinos from antineutrinos. In addition, tau neutrinos were not identified well in the detector, since the final state particles of tau neutrino interactions are very messy and complex.

The flux of upward going muon neutrinos is significantly less than the expectation assuming no neutrino oscillations, and the flux of downward going muon neutrino and electron neutrino events agree with the expectation without oscillations. The observation result can be explained by the two-flavour oscillation $\nu_\mu \to \nu_\tau$ with the probability

$$P(\nu_\mu \to \nu_\tau) = \sin^2 2\theta_{23} \sin^2(1.27\Delta m^2_{32} L/E). \tag{2.46}$$

Oscillations of ν_μ into ν_τ have been confirmed by long-baseline accelerator neutrino experiments, such as K2K and MINOS. Accelerator neutrino beams will be described in detail in Chapter 3. The very first long baseline neutrino oscillation experiment was

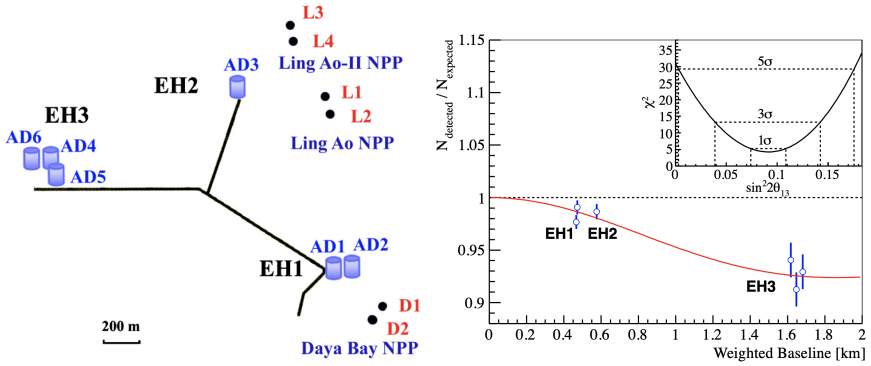

Figure 2.9: Left: Layout of the Daya Bay experiment. The black dots D1, D2, L1, L2, L3 and L4 represent six reactors. There are six antineutrino detectors (ADs), labeled as AD1, AD2, AD3, AD4, AD5, and AD6, placed in three different experimental halls (EHs), which are used to measure neutrinos with different baselines. Right: Ratio of the number of observed neutrino events and the prediction assuming no oscillations in Daya Bay's 2012 analysis. Each blue point represents the data from one detector and the red curve shows the oscillation probability at the best fit. The error bar is the uncorrelated uncertainty for each detector. The inset plot shows the χ^2 versus $\sin^2 2\theta_{13}$. Plots are taken from [46].

the K2K experiment in Japan, which ran from 1999 to 2004 [26]. K2K produced a muon neutrino beam from a proton synchrotron and the its oscillation baseline was 250 km. Two detectors were used to detect the $\nu_\mu \to \nu_\mu$ survival and $\nu_\mu \to \nu_e$ oscillation. A near detector measured the flux and a far detector measured neutrino oscillations. It concluded that at 4.3 σ confidence level there had been a disappearance of muon neutrinos and measured the mass squared splitting Δm^2_{32} is between 1.9 and 3.5 $\times$ 10^{-3} eV^2 at the 90% C.L. with a best-fit value of 2.8 $\times$ 10^{-3} eV^2.

The MINOS experiment began to observe neutrino data in 2005 and used neutrinos from the NuMI beamline at Fermilab. It consisted of a near detector and a far detector, separated by a baseline of 735 km away. These two functionally identical detectors used steel-scintillator, sampling calorimeters which are made of alternating planes of magnetised steel and plastic scintillators. MINOS reported their latest measurements in 2020: $\sin^2\theta_{23} = 0.43^{+0.20}_{-0.04}$ and $|\Delta m^2_{32}| = 2.4^{+0.80}_{-0.09} \times 10^{-3}$ eV^2 [43].

There are several other accelerator neutrino oscillation experiments using various detectors or beamline designs, such as NOvA, T2K [44], and DUNE (Deep Underground Neutrino Experiment) [45].

2.5.3 The 13 sector measurement

Reactor neutrino experiments have been used to measure θ_{13} and Δm^2_{31} in the 13 sector. Fisson reactors produce a source of electron antineutrinos though beta decays. In general, there are four main fission isotopes: ^{235}U, ^{238}U, ^{239}Pu and ^{241}Pu. The Cowan-Reines experiment in 1956 first detected reactor antineutrinos. The Double-Chooz experiment in France observed an antineutrino flux deficit in 2011 that gave an indication of a non-zero value of the mixing angle $\sin^2 2\theta_{13}$ [47]. In 2012, the Daya Bay experiment in China reported a 5.2 σ evidence of θ_{13} being non-zero [46]. The RENO experiment in Korea soon after also observed a non-zero θ_{13} with a significance of 4.9 σ [48]. So far θ_{13} has become the most precisely known mixing angle with the contributions from Daya Bay, RENO and Double-Chooz. The non-zero θ_{13} along with non-zero θ_{12} and θ_{23} allows CP violation to occur and δ_{cp} to be measured.

The reactor neutrino experiments above have a baseline of about 1 km and an average energy about 4 MeV. The oscillation probability which is expressed as a good approximation allowing θ_{13} to be measured is given as

$$P(\bar{\nu}_e \to \bar{\nu}_e) \approx 1 - \sin^2 2\theta_{13} \sin^2\left(\frac{1.267\Delta m^2_{31} L}{E}\right), \tag{2.47}$$

where $\Delta m^2_{31} = \Delta m^2_{32} \pm \Delta m^2_{21}$, E is the neutrino energy in MeV, and L is the distance between the neutrino source and the detector in metres.

The electron antineutrinos produced by reactors are usually detected though the inverse beta decay process: $\bar{\nu}_e + p \to n + e^+$. The neutrino energy can be expressed by

$$E_\nu = E_e + T_n + m_n - m_p \approx E_e + 1.293 \text{ MeV}, \tag{2.48}$$

where T_n is the recoil kinetic energy of the neutron, which is small and can be ignored for a MeV scale antineutrino, E_e is the energy of the positron, and m_p and m_n are the masses of proton and neutron, respectively. The threshold neutrino energy of the reaction is $E_{thr} \approx m_n - m_p + m_e \approx 1.804$ MeV. The final state positron annihilates immediately with an electron and the total visible energy $E_e + m_e$ can be detected by scintillator detectors. The neutrino events can be identified by the coincidence of the prompt positron signal with the delayed signal produced by the nuclear capture of the neutron through the process Gd+$n \to$ Gd+γ.

In Figure 2.9, the left diagram shows the layout of Daya Bay experiment and the right plot shows the observed number of neutrino events compared to the no oscillations prediction in each detector. A 6% rate deficit was observed in EH3 compared to other EHs,

showing strong evidence of a non-zero θ_{13}. The red curve shows the best-fit oscillation probability. The inset plot shows the χ^2 as a function of $\sin^2 2\theta_{13}$. In 2018, Daya Bay released the latest precision measurement for θ_{13} using 1958 days of data collection, obtaining $\sin^2 2\theta_{13} = 0.0856 \pm 0.0029$ and $\Delta m^2_{32} = (2.471^{+0.068}_{-0.070}) \times 10^{-3}$ eV^2 assuming the normal hierarchy and $\Delta m^2_{32} = -(2.575^{+0.068}_{-0.070}) \times 10^{-3}$ eV^2 assuming the inverted hierarchy [49].

2.6 Current status of the NOvA Experiment

This section presents the latest results from the neutrino oscillation analysis in NOvA. Details about NOvA will be described in the next several chapters. NOvA's 2020 results use an exposure of 13.60×10^{20} and 12.50×10^{20} protons on target (POT) with the beam in neutrino mode and antineutrino mode respectively.

Figure 2.10 shows the reconstructed muon neutrino spectra. There were 211 candidates in FHC and 105 candidates in RHC mode. Figure 2.11 shows the reconstructed electron neutrino spectra. The number of electron neutrinos is less than the number of muon neutrinos at the FD. There were 82 and 33 candidates observed in FHC and RHC respectively. NOvA's 2020 result obtained the best fit values $\sin^2\theta_{23} = 0.57^{+0.04}_{-0.03}$, $\Delta m^2_{32} = (2.41 \pm 0.07) \times 10^{-3}$ eV^2, and $\delta_{cp} = 0.82\ \pi$. The lower octant of θ_{23} is disfavoured at 1.2 σ and the inverted hierarchy is disfavoured at 1 σ. The 1, 2, 3 σ contours in $\sin^2\theta_{23} - \Delta m^2_{23}$ and $\sin^2\theta_{23} - \delta_{cp}$ are shown in Figure 2.12.

2.7 Current Status of the Neutrino Experiments

Measurements of neutrino oscillation parameters have made great progress through various neutrino experiments. Δm^2_{21} with its sign and θ_{12} have been measured precisely by solar neutrino experiments and KamLAND. Atmospheric sector neutrino experiments such as SuperK, T2K [50], MINOS and NOvA measured Δm^2_{23} and θ_{23}. The reactor experiments Daya Bay, RENO and Double Chooz have measured θ_{13} with a small uncertainty. However, some remaining issues in neutrino physics still exist, such as θ_{23} octant, the mass hierarchy, and the value of the CP violation phase. T2K's most recent analysis found a best fit value of $\delta_{\rm CP} = -1.97^{+0.97}_{-0.70}$ and excluded the CP-conserving values of $\delta_{\rm CP}$ of 0 and π at the 90% C.L. [51]. The results also preferred the normal hierarchy and upper octant, with best fit at $\sin^2\theta_{23} = 0.56^{+0.01}_{-0.03}$ and $\Delta m^2_{32} = 2.487^{+0.05}_{-0.05} \times 10^{-3}$ eV^2 [52]. The latest global best fit values of these parameters are listed in Table 2.1. NOvA, T2K and next generation (such as DUNE [53] and Hyper-K [54]) experiments aim to push the measurements of neutrino

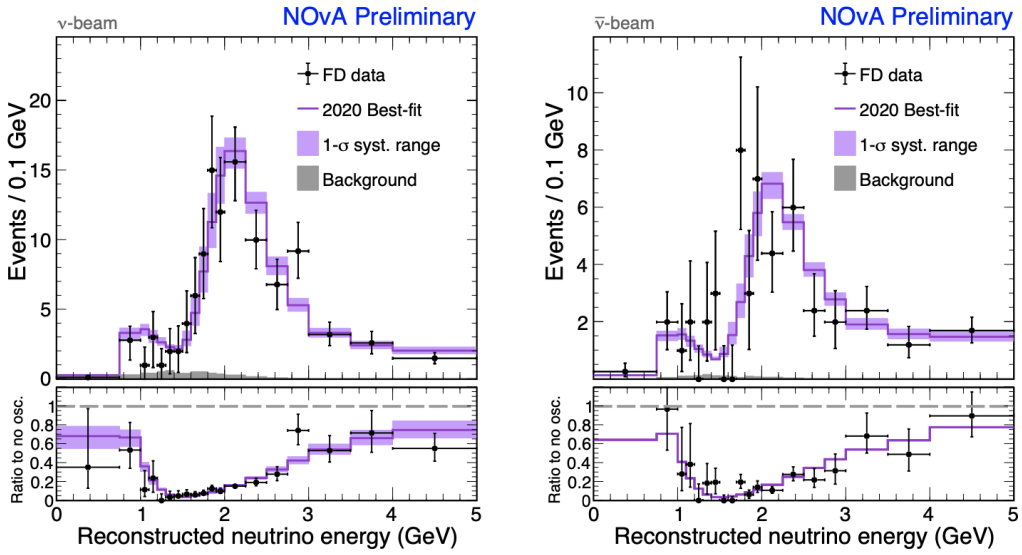

Figure 2.10: Reconstructed muon neutrino energy spectra at the FD. The neutrino mode FHC and antineutrino mode RHC are shown in the left and right panels respectively. The ratio to no oscillations for both data and the best fit prediction are also shown below the spectra.

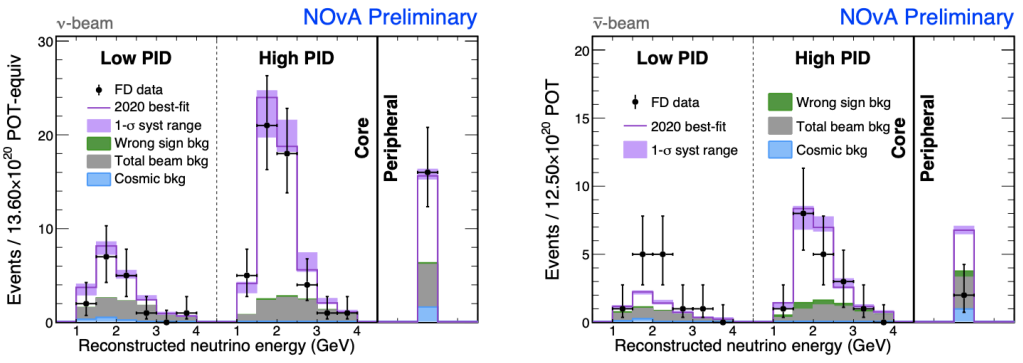

Figure 2.11: Reconstructed electron neutrino energy spectra at the FD. The Neutrino mode FHC and antineutrino mode RHC are shown in the left and right panels respectively.

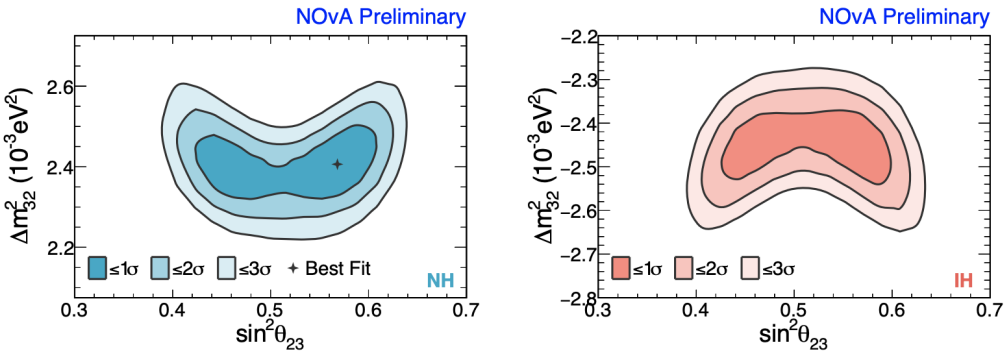

(a)

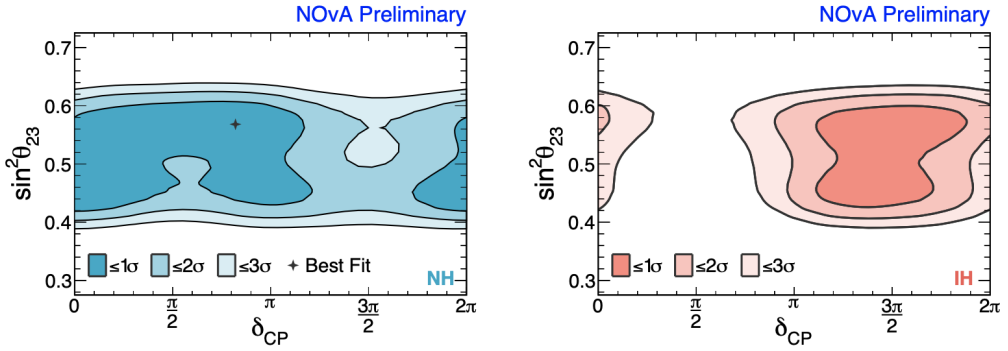

(b)

Figure 2.12: 1 σ, 2 σ and 3 σ contours in $\sin^2\theta_{23}$ - Δm^2_{23} and $\sin^2\theta_{23}$ - δ_{cp} in NH and IH in NOvA's 2020 analysis.

		Normal Ordering (best fit)		Inverted Ordering ($\Delta\chi^2 = 2.7$)	
		bfp $\pm 1\sigma$	3σ range	bfp $\pm 1\sigma$	3σ range
without SK atmospheric data	$\sin^2\theta_{12}$	$0.304^{+0.013}_{-0.012}$	$0.269 \to 0.343$	$0.304^{+0.013}_{-0.012}$	$0.269 \to 0.343$
	$\theta_{12}/^\circ$	$33.44^{+0.78}_{-0.75}$	$31.27 \to 35.86$	$33.45^{+0.78}_{-0.75}$	$31.27 \to 35.87$
	$\sin^2\theta_{23}$	$0.570^{+0.018}_{-0.024}$	$0.407 \to 0.618$	$0.575^{+0.017}_{-0.021}$	$0.411 \to 0.621$
	$\theta_{23}/^\circ$	$49.0^{+1.1}_{-1.4}$	$39.6 \to 51.8$	$49.3^{+1.0}_{-1.2}$	$39.9 \to 52.0$
	$\sin^2\theta_{13}$	$0.02221^{+0.00068}_{-0.00062}$	$0.02034 \to 0.02430$	$0.02240^{+0.00062}_{-0.00062}$	$0.02053 \to 0.02436$
	$\theta_{13}/^\circ$	$8.57^{+0.13}_{-0.12}$	$8.20 \to 8.97$	$8.61^{+0.12}_{-0.12}$	$8.24 \to 8.98$
	$\delta_{\rm CP}/^\circ$	195^{+51}_{-25}	$107 \to 403$	286^{+27}_{-32}	$192 \to 360$
	$\frac{\Delta m^2_{21}}{10^{-5}\ \text{eV}^2}$	$7.42^{+0.21}_{-0.20}$	$6.82 \to 8.04$	$7.42^{+0.21}_{-0.20}$	$6.82 \to 8.04$
	$\frac{\Delta m^2_{3\ell}}{10^{-3}\ \text{eV}^2}$	$+2.514^{+0.028}_{-0.027}$	$+2.431 \to +2.598$	$-2.497^{+0.028}_{-0.028}$	$-2.583 \to -2.412$
		Normal Ordering (best fit)		Inverted Ordering ($\Delta\chi^2 = 7.1$)	
		bfp $\pm 1\sigma$	3σ range	bfp $\pm 1\sigma$	3σ range
with SK atmospheric data	$\sin^2\theta_{12}$	$0.304^{+0.012}_{-0.012}$	$0.269 \to 0.343$	$0.304^{+0.013}_{-0.012}$	$0.269 \to 0.343$
	$\theta_{12}/^\circ$	$33.44^{+0.77}_{-0.74}$	$31.27 \to 35.86$	$33.45^{+0.78}_{-0.75}$	$31.27 \to 35.87$
	$\sin^2\theta_{23}$	$0.573^{+0.016}_{-0.020}$	$0.415 \to 0.616$	$0.575^{+0.016}_{-0.019}$	$0.419 \to 0.617$
	$\theta_{23}/^\circ$	$49.2^{+0.9}_{-1.2}$	$40.1 \to 51.7$	$49.3^{+0.9}_{-1.1}$	$40.3 \to 51.8$
	$\sin^2\theta_{13}$	$0.02219^{+0.00062}_{-0.00063}$	$0.02032 \to 0.02410$	$0.02238^{+0.00063}_{-0.00062}$	$0.02052 \to 0.02428$
	$\theta_{13}/^\circ$	$8.57^{+0.12}_{-0.12}$	$8.20 \to 8.93$	$8.60^{+0.12}_{-0.12}$	$8.24 \to 8.96$
	$\delta_{\rm CP}/^\circ$	197^{+27}_{-24}	$120 \to 369$	282^{+26}_{-30}	$193 \to 352$
	$\frac{\Delta m^2_{21}}{10^{-5}\ \text{eV}^2}$	$7.42^{+0.21}_{-0.20}$	$6.82 \to 8.04$	$7.42^{+0.21}_{-0.20}$	$6.82 \to 8.04$
	$\frac{\Delta m^2_{3\ell}}{10^{-3}\ \text{eV}^2}$	$+2.517^{+0.026}_{-0.028}$	$+2.435 \to +2.598$	$-2.498^{+0.028}_{-0.028}$	$-2.581 \to -2.414$

Table 2.1: Three-flavor oscillation parameters obtained from the fit to global data. $\Delta m^2_{3\ell} \equiv \Delta m^2_{31} > 0$ for normal hierarchy and $\Delta m^2_{3\ell} \equiv \Delta m^2_{32} < 0$ for inverted hierarchy. Table taken from [6].

oscillations to the next stage.

Chapter 3

The NOvA Experiment

NOvA is an experiment designed to study neutrino oscillations with the appearance channel ν_μ ($\bar{\nu}_\mu$)$\rightarrow\nu_e$ ($\bar{\nu}_e$) and disappearance channel ν_μ ($\bar{\nu}_\mu$)$\rightarrow\nu_\mu$ ($\bar{\nu}_\mu$) using a proton-accelerator produced neutrino beam. It is a long-baseline experiment consisting of two functionally identical detectors. Its physics motivations are probing the neutrino mass hierarchy, δ_{cp} phase and the octant of θ_{23} mixing angle.

3.1 NOvA Beam

NOvA's neutrino beam is provided by the Neutrinos at the Main Injector (NuMI) beam facility at Fermi National Accelerator Laboratory (Fermilab) in the United States. NuMI is part of the Fermilab accelerator complex that is shown in Figure 3.1. The neutrino-generating process starts from high energy protons. In the Linear accelerator (Linac), 750 keV H^- ions are accelerated to 400 MeV and then sent to the Booster through a thin carbon foil. Two electrons are stripped from each H^- ion when the ions pass through the foil. The Booster, which is a rapid-cycling synchrotron, accelerates the resulting proton beam to 8 GeV at a rate of 15 Hz. The protons are then transferred to the Recycler, which performs a "slip-stacking" process[1] and then extracts the beam to the Main Injector that can accelerate protons to 120 GeV. The Recycler and the Main Injector, which share the same enclosure, are currently the largest acceleration machines in use at Fermilab. The Main Injector is built at the bottom of the enclosure, with the Recycler 47 inches above it.

[1] Slip-stacking is the process of injecting pairs of batches (a batch is the output of one Booster cycle, which contains 84 bunches.) into the Recycler and then merging the pairs to form double-intensity batches. The Recycler is capable of slip-stacking up to twelve booster batches, which leads to six double-intensity batches for extraction to the Main Injector.

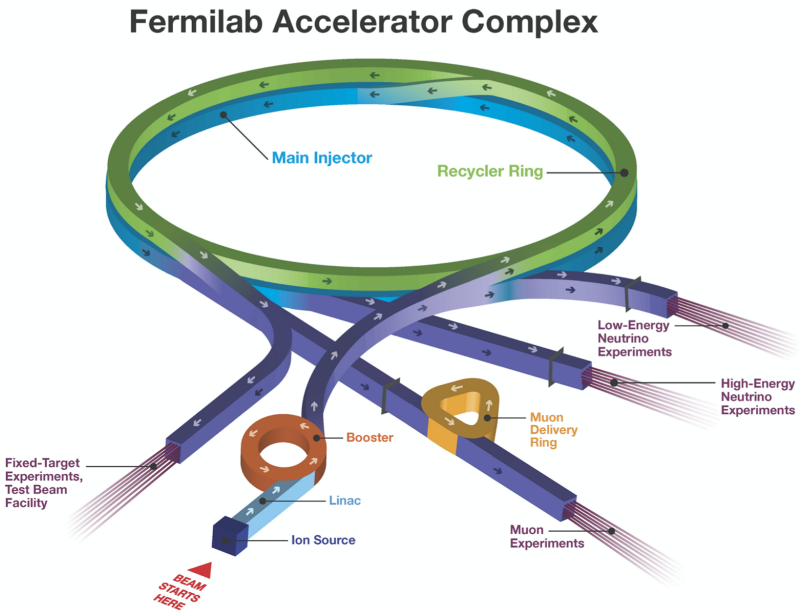

Figure 3.1: Diagram of the Fermilab accelerator complex, composed of the linac, booster, recycler and main injector. The accelerated protons are directed into the NuMI beam facility to produce neutrinos. Taken from [55].

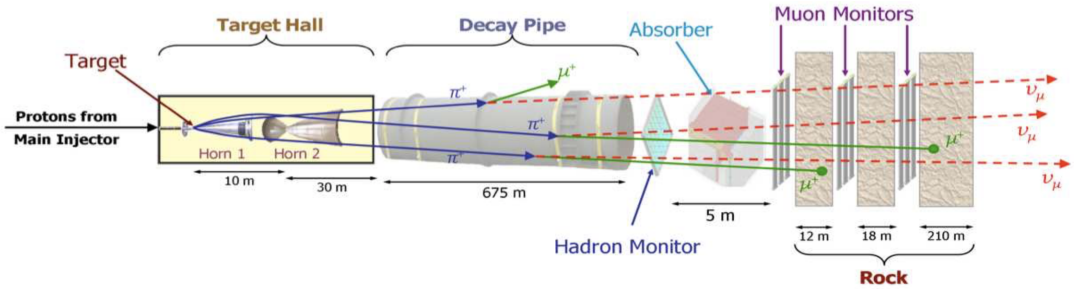

Figure 3.2: Schematic diagram of the NuMI beam facility, consisting of the target, horns, decay pipe, hadron absorber and the muon shield. Taken from [55].

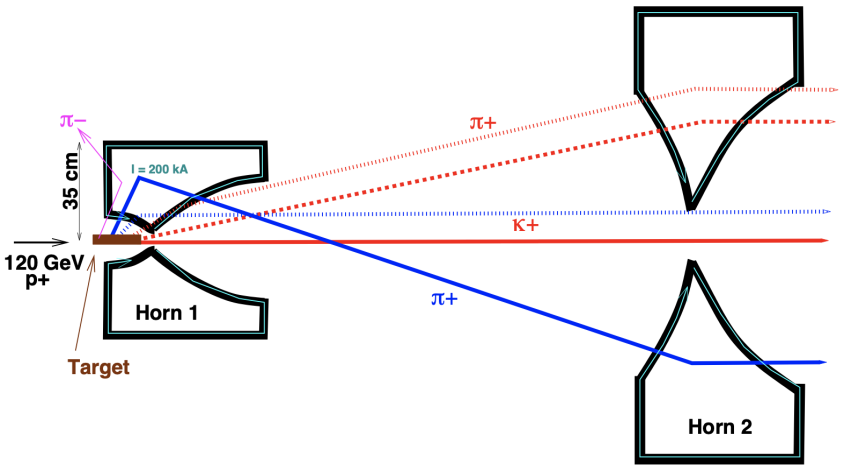

Figure 3.3: Schematic drawing of the NuMI focusing horns which are pulsed in "forward" mode. Hadrons produced by the NuMI target are focused by these pair of magnetic horns. Taken from [55].

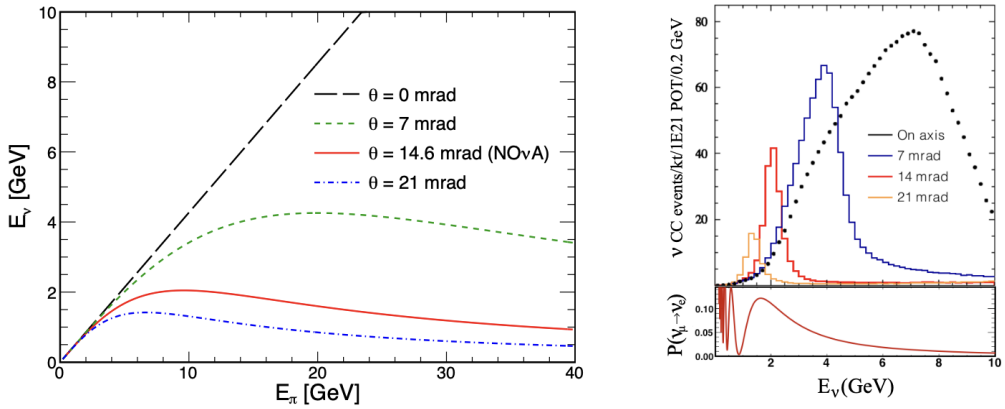

Figure 3.4: Left: The neutrino energy versus pion energy for different off-axis angles. Right: The ν_μ spectrum expected at the FD with different off-axis angles. Taken from [9].

Figure 3.2 shows a diagram of the NuMI beam facility composed of the target, horns, decay pipe, hadron absorber and muon shield. The Main Injector can transfer about 5×10^{13} protons to the NuMI graphite target in 10 μs spills every 1.33 s. The secondary beam produced from the target including charged pions and kaons is focused by two parabolic magnetic horns, Horn 1 and Horn 2, which are shown in Figure 3.3. These horns consist of cylindrical shaped outer conductors and parabolic-shaped inner conductors that create magnetic fields to act as lenses. The focal length of the lens is proportional to the momentum of the particle. Two polarity modes of the horns can be set by changing the current direction to reverse the magnetic field. The "forward" horn current mode (FHC) focuses mesons with positive charges, π^+ and K^+, which then decay into mostly muon neutrinos. The "reverse" horn current (RHC) mode produces muon antineutrinos by selecting particles π^- and K^-. Some opposite sign mesons that are very parallel to the beam direction can also pass through the centre of the horn necks, producing the backgrounds which are called "wrong-sign contamination".

After passing through the horns, the hadron beam enters into a 2 m diameter decay pipe filled with 0.9 atm helium. The pipe is 675 m long, which approximately corresponds to the decay length of a 10 GeV pion. The pions and kaons decay through $\pi^{\pm} \rightarrow \mu^{\pm} + \nu_{\mu}(\bar{\nu}_{\mu})$, $\mathrm{K}^{\pm} \rightarrow \mu^{\pm} + \nu_{\mu}(\bar{\nu}_{\mu})$. Decays of pions, kaons and secondary muons can give rise to an intrinsic electron neutrino component of the beam. Muon decay is the dominant intrinsic beam background in a low energy range below 3 GeV, while decays of K^+ and K_L are the dominant source in the energy above 5 GeV.

The decay pipe is followed by a hadron absorber used to reduce the remaining particles such as protons, mesons, neutrons or electrons produced upstream. The muon shield is solid dolomite rock, responsible for eliminating the remaining muons. The flux of hadrons is monitored by a hadron monitor at the end of the pipe, and the muons are monitored by a muon monitor after the absorber. Neutrinos are produced spill by spill using the protons in the Main Injector.

3.1.1 Off-axis beam design

Both NOvA detectors are located 14.6 mrad off the central NuMI beam axis. This off-axis technique is based on a feature of relativistic hadron decay kinematics which provides a narrow-band neutrino beam and reduces the background. In the two body decay process of the pions, ignoring the mass of the neutrino, the neutrino energy E_{ν} and flux ϕ in the lab frame of reference can be described approximately at a small angle as

$$E_\nu = \frac{(1 - \frac{m_\mu^2}{m_{\text{meson}}^2})E_{\text{meson}}}{1 + \gamma^2\theta^2}, \tag{3.1}$$

$$\phi = (\frac{2\gamma}{1 + \gamma^2\theta^2})^2 \frac{A}{4\pi z^2}, \tag{3.2}$$

where E_{meson} is the energy of the decaying mesons like pions and kaons, m_{meson} is the rest mass of the meson like the pion or muon, θ is the angle between the pion direction and the neutrino direction, γ is the Lorentz boost of the meson, and ϕ is the flux intercepted by the detector area A at distance z. From this equation, it can be known that the beam has a narrow neutrino energy range for a wide range of initial meson energies for small off-axis angles. In NOvA, the off-axis angle is 14.6 mrad off the NuMI beam axis so that the energy of the neutrino beam peaks around 2 GeV. Figure 3.4 shows the neutrino energy as a function of pion energy and the ν_μ spectrum expected at the FD, for different off-axis angles. There are some benefits of choosing this off-axis angle. First, about four times more neutrinos are produced at 2 GeV than the on-axis case. This helps with the ν_e appearance measurement since the maximum oscillation probability of $\nu_\mu \rightarrow \nu_e$ is near 2 GeV. Second, the narrow energy range reduces background events. In the ν_e appearance measurement, high energy neutral-current events can be misidentified as the ν_e charged-current events through the decay process $\pi^0 \rightarrow \gamma + \gamma$. The departing neutrino takes away some of the energy out of the detector and leaves an event topology similar to a ν_e CC event, which is a background source that is hard to reject. The high energy NC events are significantly reduced by producing an energy spectrum with a narrow band. In addition, the off-axis is able to reduce the intrinsic ν_e background in the neutrino beam from muon or kaon decays, since the spectrum of these events is broader than the ν_e signal spectrum.

3.2 NOvA Detectors

NOvA has two detectors. The near detector at Fermilab is 100 m underground, shielded from a great number of cosmic rays, and the far detector is located near Ash River, Minnesota, 810 km away from the beam source. These two functionally identical detectors are designed to reduce the effects of systematic uncertainties. The geographical locations of them are shown in Figure 3.5. The neutrino intensity and the number of neutrino interactions at the near detector is much bigger than the far detector since it is close to the NuMI source.

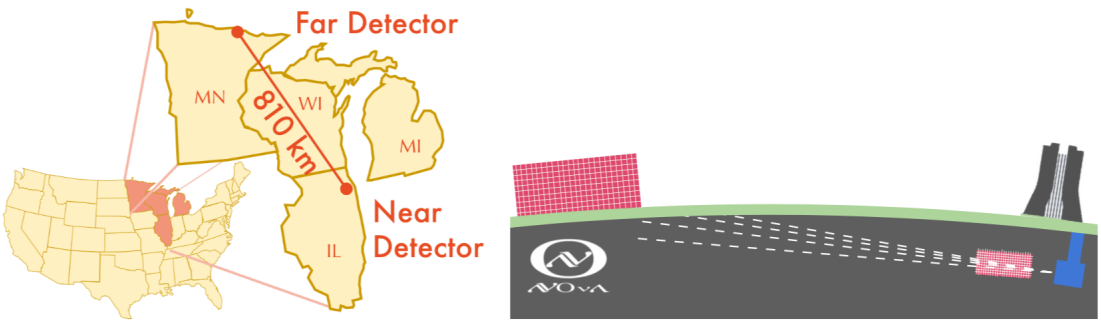

Figure 3.5: Locations of the near and far detectors. Both detectors are placed at the off-axis angle of 14 mrad. The neutrino beam produced at Fermilab travels 810 km through the earth before it arrives at the far detector. Taken from [56].

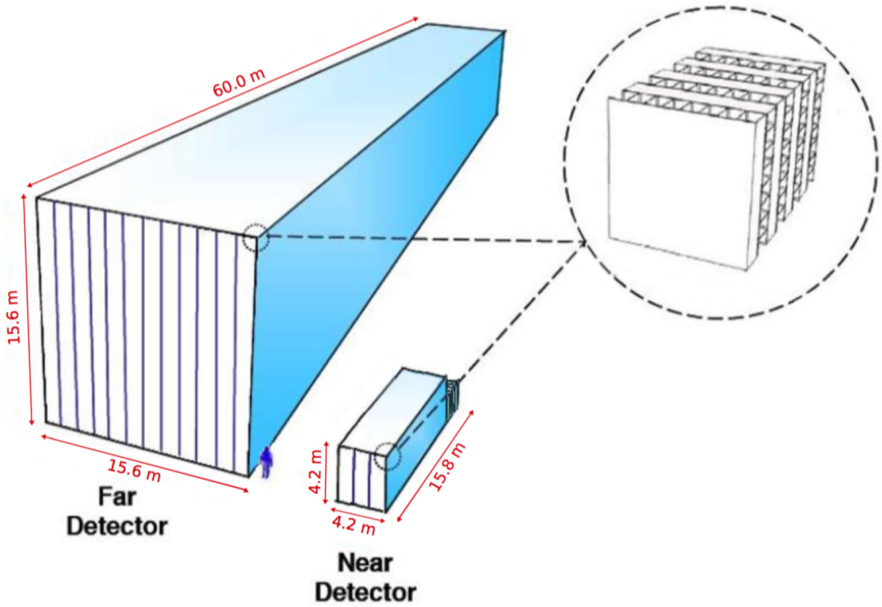

Figure 3.6: Schematics showing the sizes of the detectors and the components inside the detector. The far detector is 14 ktons, and the near detector is only 300 tons as the neutrino intensity at the near detector is much bigger than the far detector. Taken from [9].

Figure 3.7: Left: diagram of a cell. Right: photograph of one PVC extrusion. Taken from [57].

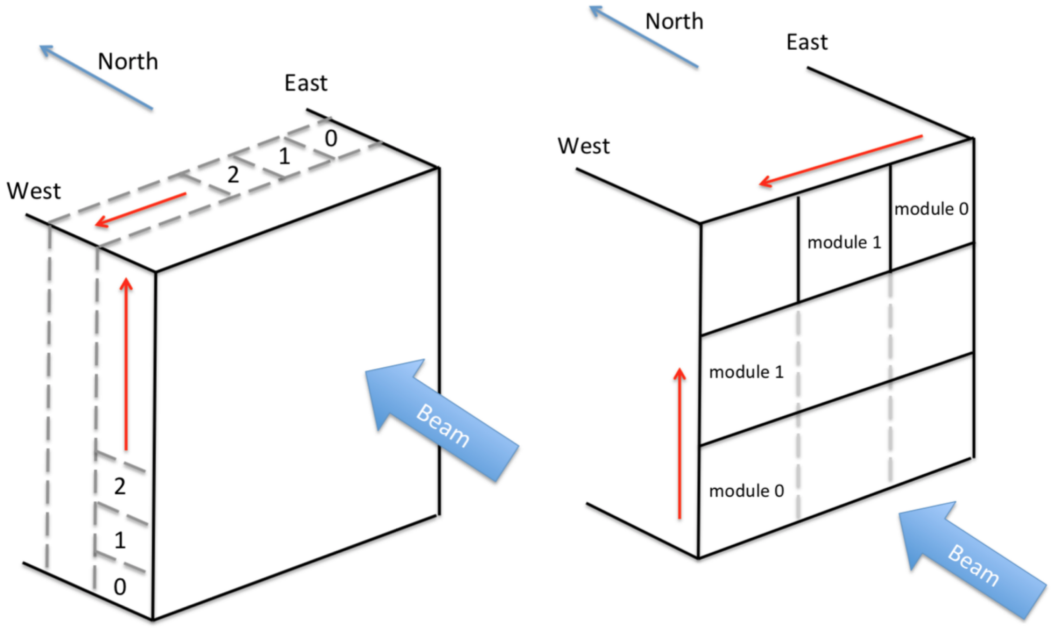

Figure 3.8: Left: diagram showing how the cells are arranged in the ND. Right: diagram showing how the modules are arranged. The number shows the index of the cell or module. Taken from [58].

Figure 3.9: Photographs of the near detector, composed of the active region and the muon catcher. Left: the front of the detector. Right: the downstream end of the detector is the muon catcher. Taken From [59].

3.2.1 Detector Assembly

Figure 3.6 shows the sizes of the two detectors and the structure inside the detector. The detectors consist of Polyvinyl Chloride (PVC) units which are called cells, each of which is filled with organic liquid scintillator and fitted with a wavelength shifting (WLS) fibre. The WLS fibre with a diameter of 0.7 mm is used to collect and transmit the light produced in the liquid scintillator. To reconstruct the three-dimensional track of a particle, the orientations of the cells in two adjacent planes are orthogonal. The horizontal cells are called "Y view" and the vertical cells are called "X view". A group of 16 cells are produced using an extrusion process, and two extrusions make up a module. Figure 3.7 shows the diagram of a cell and the photograph of an extrusion. Figure 3.8 shows the arrangements of the cells and modules and their numbering scheme.

3.2.1.1 Near Detector

The underground near detector contains two parts, the fully active upstream section and the muon catcher. The active part consists of 20,192 cells making up 192 planes. Each cell in the active region has a cross section of 3.6 cm by 5.6 cm as the FD cell and a length of 3.9 m. 24 alternating planes glued together form a unit called a block, and 64 alternating planes form a diblock. Thus the ND has 3 diblocks in total and 3 modules for each plane. In order to contain the full muon track, the near detector is constructed with a muon catcher that is 1/3 less than the main part in height and consists of 22 alternatively orthogonal PVC planes. Between every two PVC planes is a thick steel plane that is used

Figure 3.10: Photograph of the NOvA far detector. Taken From [59].

to absorb energy from the muons so that they will be fully contained in the detector. Therefore, more muons can be included in the analysis with the help of the muon catcher. Figure 3.9 shows the photographs of the upstream side and the muon catcher side of the ND.

3.2.1.2 Far Detector

The FD comprises 896 planes including 344,064 cells. Each cell has the same cross section of 3.6 cm by 5.6 cm as the ND and a length of 15.2 m. 32 alternating planes glued together form a unit called a block, and two neighbouring blocks form a diblock. Thus the FD has 14 diblocks in total and 12 modules for each plane. Figure 3.10 shows the photograph of the FD.

3.2.2 Liquid Scintillator

The chemical composition of the liquid scintillator is displayed in Table 3.1. The mineral oil that serves as the solvent makes a contribution of 94.63% to the total liquid mass. Then the scintillant pseudocumene contributing 5.23% of the liquid mass can emit light with a spectrum of the wavelength peaked at 375 nm. PPO and bis-MSB are the wave shifter, which can shift the scintillation light to 400 nm-450 nm to fulfill the absorption requirement of the wavelength-shifting fibres. In addition, in oder to keep the scintillator transparent Vitamin E is added as the antioxidant.

Component	Purpose	Mass fraction %
mineral oil	solvent	94.63
pseudocumene	scintillant	5.23
PPO	waveshifter	0.14
bis-MSB	waveshifter	0.0016
stadis-425	anti-static agent	0.0010
Vitamin E	antioxidant	0.0010

Table 3.1: Composition of the liquid scintillator [60].

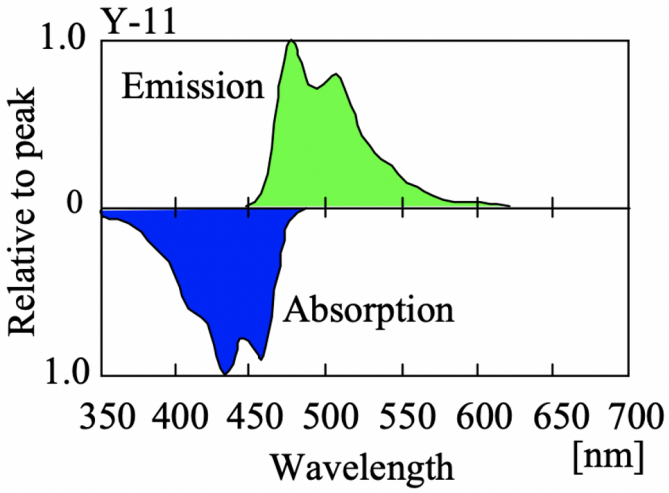

Figure 3.11: Absorption and emission spectra of the K27 dye dissolved in styrene monomer. Taken From [9].

3.3 Data Taking Process

3.3.1 Optical fibres

As mentioned before, each detector cell contains one looped wavelength-shifting (WLS) optical fibre that is used to collect and transmit light. The looped fibre design can help yield more light than a single fibre with a nonreflecting end. The pulses of light traveling to the two ends of the fibre are then collected by a pixel on the photo-sensor. To achieve total internal reflection, the fibre core is made of polystyrene (refractive index n=1.59) mixed with the fluorescent dye, R27, coated with two lower refractive index layers made of acrylic (n=1.49) and fluorinated-polymer (n=1.42) [9]. The dye R27 can shift the wavelength of scintillation light from 400 - 450 nm to 490 - 550 nm. As shown in Figure 3.11, there is an overlap of the absorption and emission spectra for the dye, so the light emitted below

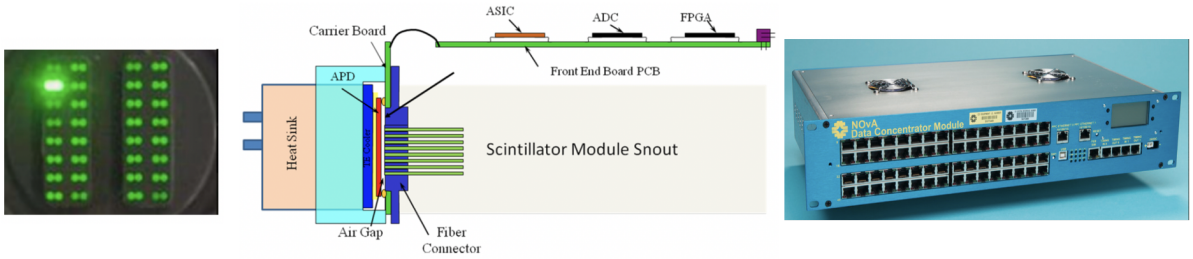

Figure 3.12: (a): ends of 32 WLS fibres from a module interface with an APD. (b) each APD is connected to the Front End Board (FEB), on which there are an Analogy to digital converter (ADC), an Application Specific Integrated Circuit (ASIC) and a Field Programmable Gate Array (FPGA). (c): the photograph of a Data Concentrator Module (DCM). Taken from [61].

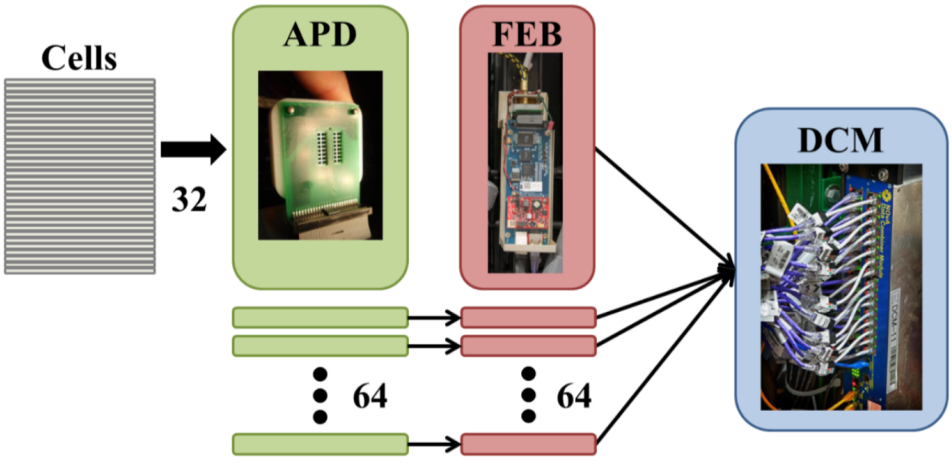

Figure 3.13: Architecture of NOvA Data acquisition system (DAQ) [9].

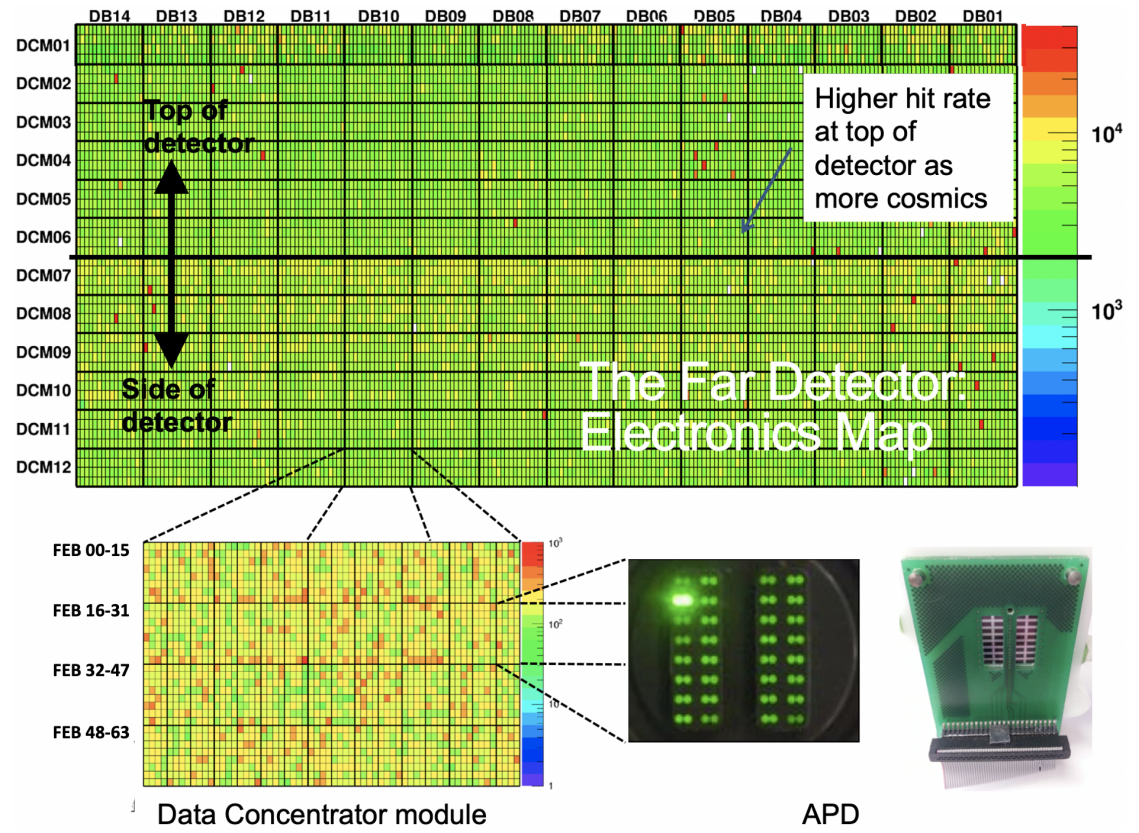

Figure 3.14: Example of the hit rate map of FEBs in the far detector. The FEBs are grouped electronically into the Data Concentrator Modules (DCM)s. DB represents dib-lock. Taken from [61].

around 500 nm is severely attenuated. An energy deposition in a NOvA cell is measured by two light pulses with two different propagation distances. The attenuation effect is modelled by a double-exponential function and corrected in detector calibration.

3.3.2 Photodetector and Electronics

The photo-sensor used by NOvA is an Avalanche Photo-Diode (APD) with 32 pixels. It is designed to fit both ends of the looped fibre onto the same APD pixel to maximize light collection. APDs convert the optical signals from the detector module into photo-electrons (PE). The PE signal is amplified and then passed to a Front End Board (FEB) through a short ribbon cable. The FEBs, each of which connects to one APD, are used to digitise the signals above a threshold[2] and add a time stamp to the signals. Each FEB carries an

[2]Lots of hits from electronic noise can be seen even without any charged particles going through the detector. A threshold is referred to as the minimum level for energy deposited in order to remove the false signals from this noise. The FPGA on the FEB uses this value to determine whether hits should be kept and sent to DAQ.

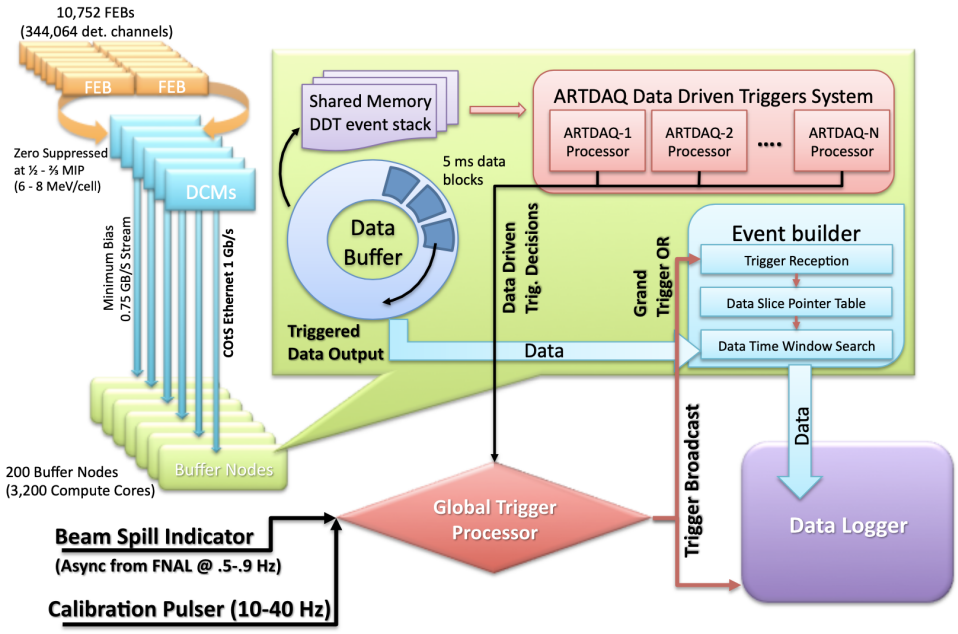

Figure 3.15: Data acquisition system for the FD. The ND is a similar one. Taken from [62].

Analog to Digital Converter (ADC), which converts the shaped analog signals into digital signals; an Application Specific Integrated Circuit (ASIC), performing pulse shaping; and a Field Programmable Gate Array (FPGA), which uses a digital signal processing algorithm to extract the time and amplitude of signals from the APD. The signals from up to 64 FEBs then pass to a Data Concentrator Module (DCM) that is a hardware module able to take input from up to 64 FEBs. Each DCM only communicates with FEBs in the same diblock and in the same view. For each diblock, the FD has six DCMs numbered 1-6 for the vertical view on the top of the detector and six DCMs numbered 7-12 for the horizontal view on the side of the detector. For each diblock, the ND has 2 DCMs for the vertical view on the top of the detector and 2 DCMs for the horizontal view on the side of the detector. Please note that some ND DCMs communicate with less than 64 FEBs. Figure 3.12 shows that fibres from 32 cells from one PVC module map onto the 32 pixels of each APD. A summary of the readout chain from the cell channels to DCMs is illustrated by Figure 3.13. Figure 3.14 shows the electronics map for the FD. As mentioned in Section 3.2.1.2, the FD has 14 diblocks , each of which has 12 DCMs. This map shows the hit rate for every FEB.

Figure 3.15 shows the data acquisition system for the FD. The DCMs collect data from FEBs during 50 μs time windows, called microslices or a data packet. Each microslice is sent to Buffer Nodes via Ethernet that hold our data for about 10 minutes until the trigger system (The trigger system will be described in Section 3.3.4), Global Trigger, works out

if they should be triggering and then written to disk by DataLogger or rejected.

3.3.3 Timing system

NOvA needs to correlate the beam spill information with the neutrino hits in both the ND and FD. This correlation is performed by a timing and synchronisation system which is applied to both the ND and FD sites as well as the accelerator complex at Fermilab [63]. The timing system is able to make sure all cell readouts of the ND and FD can be aligned in time, because even small errors in the timing correction could result in incorrect reconstruction of neutrino events.

The timing system uses a Master Timing Distribution Unit (MTDU) that is connected to an external precise Global Positioning System (GPS) antenna. The MTDU drives slave TDUs (STDUs), each of which synchronises each kiloton of detector mass and drives the timing for a number of DCM readouts. Each DCM in turn sends out the timing information to a set of 64 FEBs. To obtain correct neutrino event reconstructions, these different readout regions should be both internally synchronised (all frontend boards in a region) and globally synchronised with each other. The system also includes a loopback system to perform timing calibration and determine device to device propagation delays. The MTUD at Fermilab is connected to the accelerator complex network. When a beam is produced at Fermilab, it decodes the accelerator time stamp into NOvA time, and the spill information is transferred to the detectors after the flight time of neutrinos in the earth is corrected.

3.3.4 Triggers

Three kinds of triggers exist in NOvA: clock triggers, signal triggers and data-driven triggers [64]. For clock triggers, there is a specific time interval in which the data is stored. For signal triggers, the trigger system receives an external signal upon which data is stored for a determined time interval. For data-driven triggers (DDTs), when the data satisfies specific conditions, the system will store data from the time period in which the behaviour occurs.

- **Clock triggers** NuMI data trigger: stores readouts in a 550 μs period centred around the 10 μs beam spill window. In this time interval, neutrino signals and cosmic ray signals are contained.
- **Signal triggers** Cosmic data trigger: this stores readouts at 10 Hz for 550 μs in the far detector. This data is used to estimate the cosmic background and calibrate

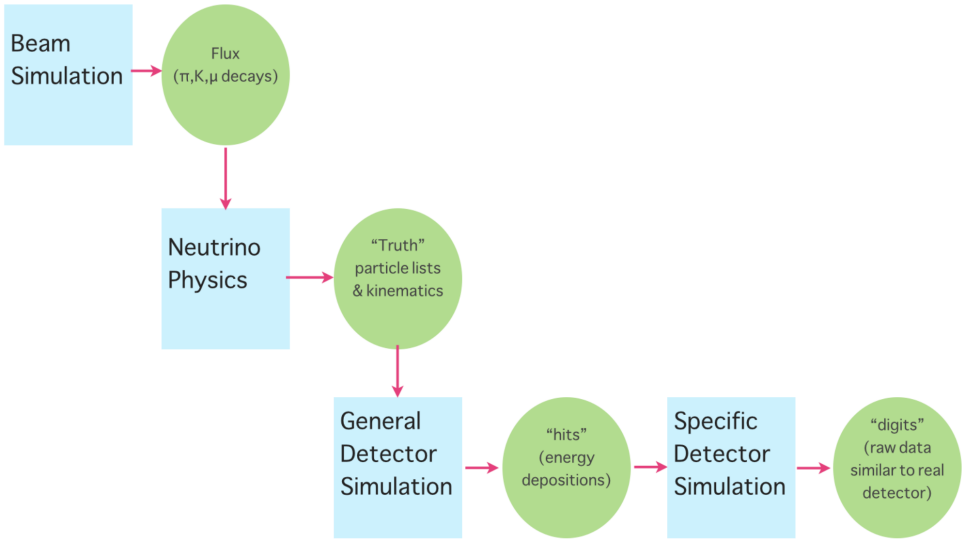

Figure 3.16: Flowchart of the simulation chain in NOvA. Taken from [66].

the detector.

- **Data-driven triggers** (1) DDActivity trigger: this trigger stores readouts activity in the ND for a configurable time period. The stored readouts are used for the ND calibration and evaluation of the running conditions independent of beam activity. (2) DDEnergy trigger: readouts are stored when the total deposited charge in a 50 μs period in the detector exceeds some threshold. (3) SuperNova Early Warning System (SNEWS) trigger: it takes long readout on the order of seconds when receiving an alert of potential supernovae signals from the SuperNova Early Warning System [65].

3.4 Simulation

Neutrino oscillation analysis relies on Monte Carlo (MC) simulations, which are performed by a number of different software packages. The simulation main stages can be categorized as beam flux prediction, neutrino interaction and simulation of detector response. The simulation chain is shown in Figure 3.16.

3.4.1 Beam Flux Simulation

The NOvA simulation uses the G4 package [68] to simulate the hadron production within the target. The propagation of the hadrons in the beamline is simulated by GEANT4 [69] that is used to simulate the geometry of the beamline including the target, horns and decay pipe. The output flux files are generated separately for both FHC and RHC modes for the ND and FD. These files contain the information about the flavour, direction,

	ND, FHC(%)	ND, RHC(%)	FD, FHC(%)	FD, RHC(%)
ν_μ	93.765	6.602	94.116	6.613
$\bar{\nu}_\mu$	5.299	92.495	4.927	92.922
ν_e	0.814	0.170	0.840	0.155
$\bar{\nu}_e$	0.123	0.733	0.116	0.759

Table 3.2: Simulated flux composition integrated between [1, 5] GeV neutrino energy without oscillations for the ND and FD. Taken from [67].

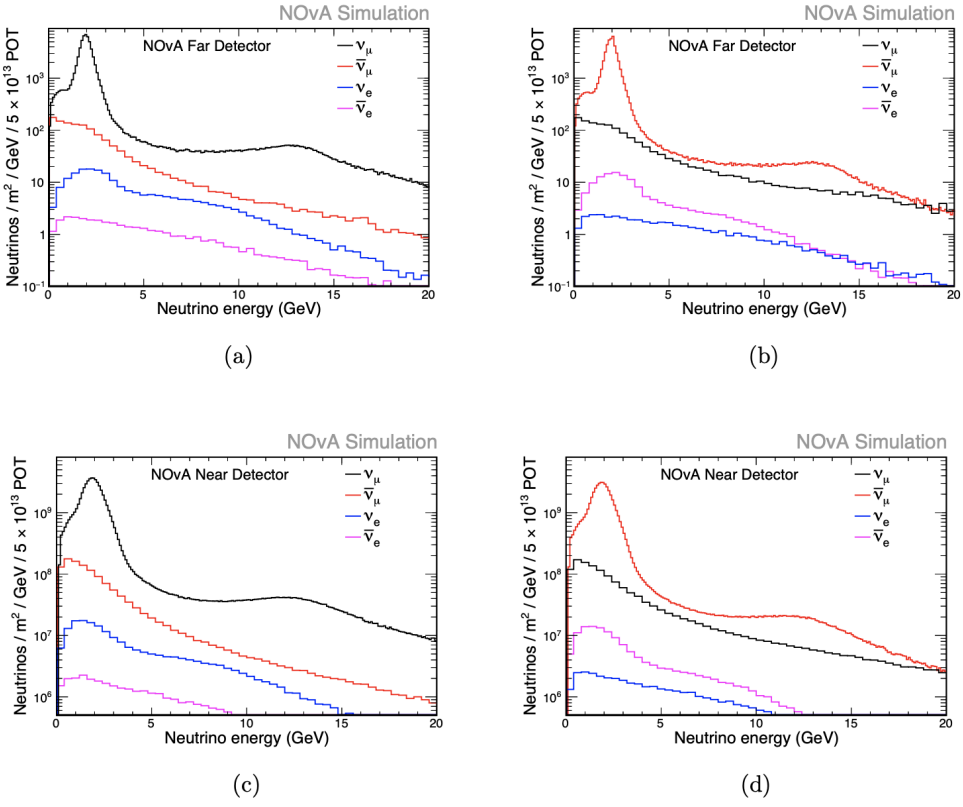

Figure 3.17: ν_μ and ν_e components of the NuMI flux at the ND and FD in the FHC (left) and RHC (right) beam modes assuming no oscillations. Taken from [67].

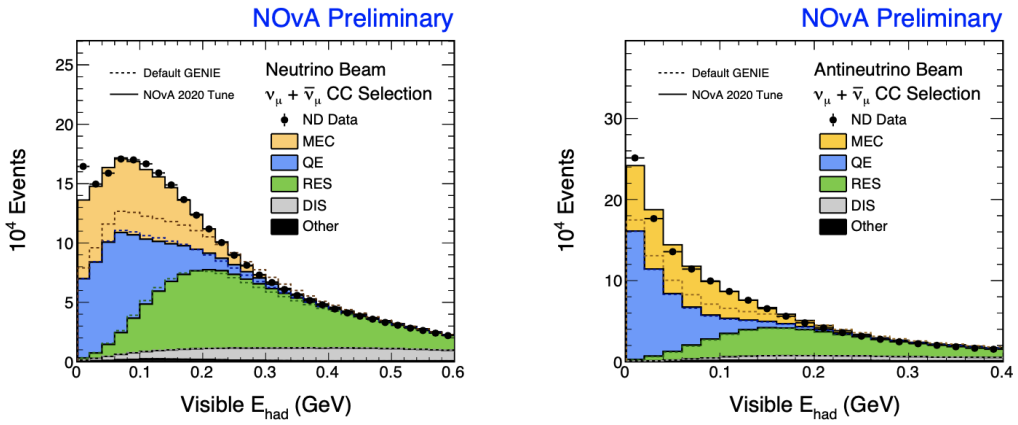

Figure 3.18: Distributions of reconstructed visible hadronic energy in FHC and RHC beam modes in the ND. The stacked histograms represent different MC interaction components. The black solid histogram shows the total events using NOvA tune. The default GENIE are shown by the dashed black histograms. Taken from [71].

energy, decay point and momentum of each neutrino as well as the ancestor that produces the neutrino. The hadron production is corrected by the Package to Predict the Flux (PPFX) [70] using constraints from external hadron production experiments. PPFX also constrains the uncertainties related to hadron production.

For the FD, there are three types of flux files: nonswap, fluxswap, and tau, which are described as follows

- **Nonswap** The NuMI beam flux at the FD assuming no oscillations.
- **Fluxswap** The ν_μ (ν_e) component in the NuMI flux is replaced by the ν_e (ν_μ) component.
- **Tau** All neutrinos in the NuMI beam are replaced by tau neutrinos.

We are able to obtain the neutrino flux with any flavour with the assumption of oscillations by reweighting the above files. Figure 3.17 shows the predicted ν_μ and ν_e spectra below 20 GeV at the ND and FD. In the 1 to 5 GeV neutrino energy region, the predicted flux composition is shown in Table 3.2.

3.4.2 Neutrino Interaction Simulation

The second step is to simulate neutrino interactions in the detectors. The Generates Events for Neutrino Interaction Experiments (GENIE) package [72, 73] is used to simulate the neutrino-nuclear interactions in the NOvA detectors. The input files for GENIE are the neutrino flux and detector geometry files. GENIE utilises theoretical models and cross

section data to simulate neutrino interactions with the material. Some corrections based on external and the ND data as well as theory are applied to the default GENIE configuration. The Valencia model [74] is used for CC MEC mediated 2p2h events. The MEC interaction rate is increased about 20% which is obtained from a fit of this model to the ND data in the space of reconstructed visible hadronic energy versus the three momentum transfer. For the Quasi-elastic interaction, a nuclear physics model that involves a Fermi gas model with corrections from the Random Phase Approximation (RPA) is used [75, 76]. Figure 3.18 shows the distributions of reconstructed visible hadronic energy of events passing the ν_μ CC selection before and after the corrections at the ND.

An important background for the FD comes from interactions of cosmic rays. Cosmic ray data is overlaid with the simulation of NuMI beam events. The Cosmic RaY (CRY) generator is used to simulate the cosmic rays for energy calibration in the FD [77].

3.4.3 Detector Simulation

The simulation of detector response is an important process in the simulation chain. Detector simulation deals with modelling the scintillation light production and transport, particle energy depositions and conversion to electrical signals. This process is done by two steps: photon transport and electronic readout.

GEANT creates energy deposits that are converted to the photons which scatter, reflect, and are absorbed by the fibre. The algorithm takes the information of the measured scintillator response in NOvA detectors, PVC reflectivity, and the measured absorption spectrum of the fibre. Each side of the looped fibre obtains half the collected photons. The lost light in the fibre is modelled based on the average light attenuation measured in the fibre.

The simulation of electronic readout starts from the number of photoelectrons recorded by the APDs and simulates this to transform the raw signal to digitised data.

Chapter 4

NOvA Analysis Methodology

4.1 Analysis Software

NOvA's Common Analysis Format Analysis (CAFAna) software framework [78] has been developed to plot basic histograms, extrapolate nominal and systematically shifted predictions and compute the fit to the data in oscillation analysis. CAFAna is constructed based on the data analysis framework ROOT [79] that provides histogram classes. The analysis in NOvA uses Common Analysis Format (CAF) files [80] which contains data structures, such as lists of reconstructed events, POT information and truth information for MC.

4.2 Event Reconstruction

The main goal of event reconstruction is to search for electron or muon neutrino candidates. A general process begins with recording the hit produced by scintillation light in each cell. Each cell hit contains the information of the plane number, the cell number, the charge in terms of the ADC counts, which is digitised from the APD signal and hit time information. As shown in Figure 4.1, to reconstruct a three dimensional event, information from two dimensional reference systems, the X-Z plane that is the top view of the detector and the Y-Z plane that is the side view of the detector, are combined.

All hits can be classified into two categories: signal hits and noise hits. Signal hits are the results of interactions from charged particles passing through the cell. Noise hits come from the electronics, and they are generally uncorrelated by time and do not deposit energy. Separating hits into sets of correlated groups, called clusters, is referred to as "slicing". The goal is to separate noise hits from signal hits into clusters coming from the

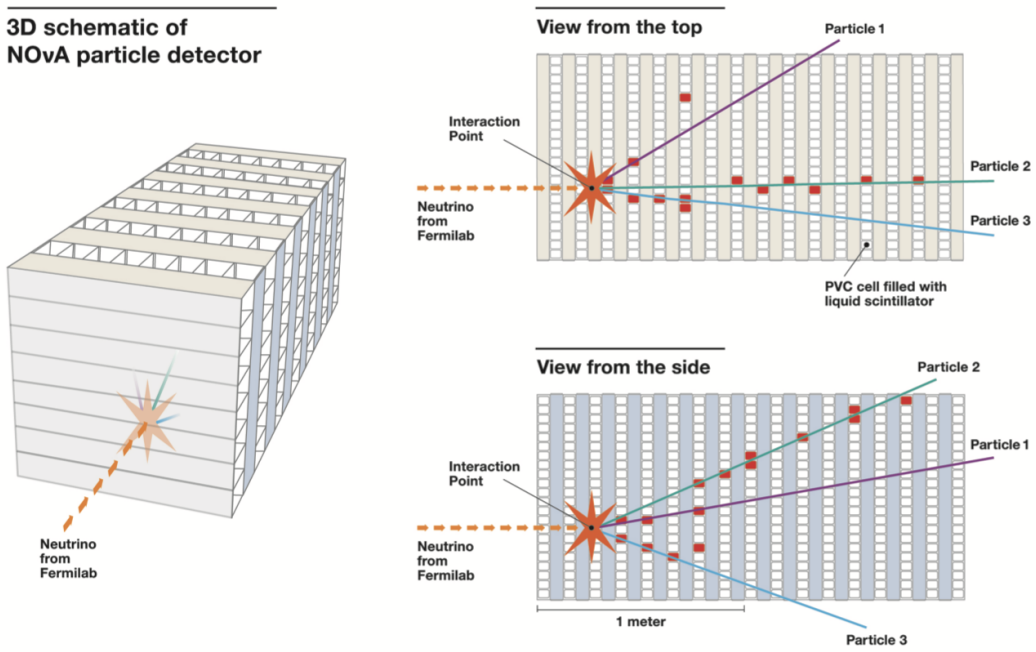

Figure 4.1: Diagram of the structure of the NOvA detector. Combining the top and side detector views allows for a 3D track reconstruction. Taken from [81].

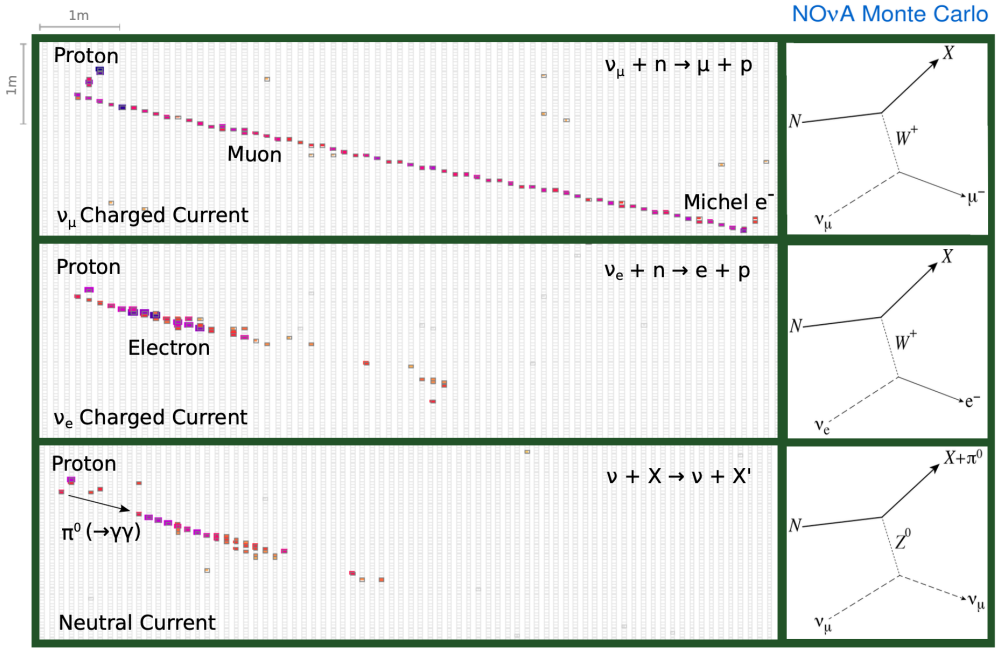

Figure 4.2: Event topologies of ν_μ CC, ν_e CC and NC interactions generated from the NOvA simulation. Taken from [82].

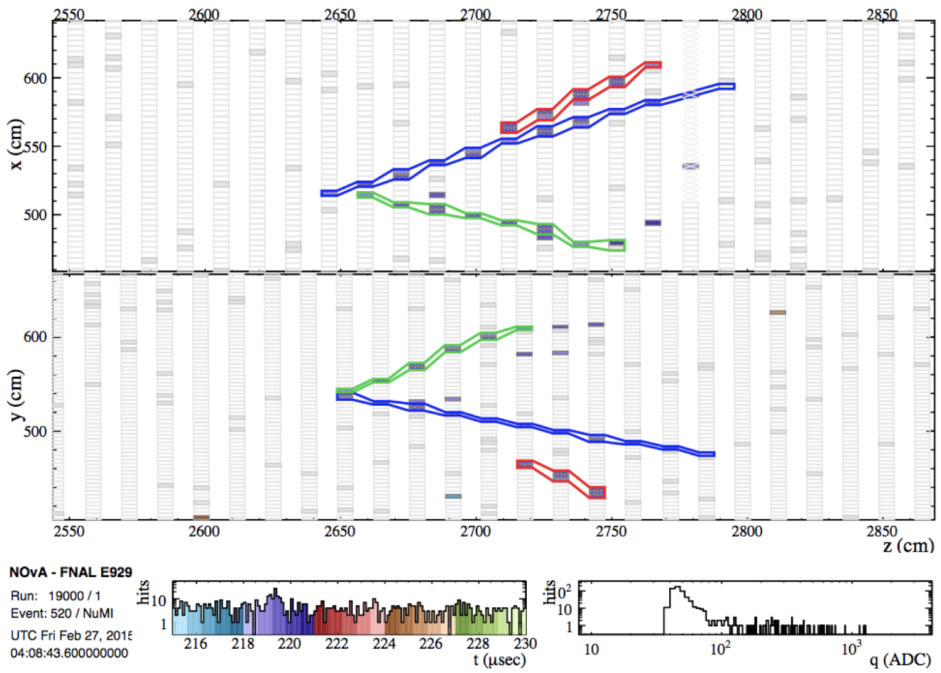

Figure 4.3: Tracks reconstructed by the NOvA Kalman tracker in the FD simulation. Individual reconstructed tracks are shown in different colours. The XZ and YZ views are shown in the top and bottom halves of the figure respectively. Taken from [83].

same physical source (one slice[1] per neutrino interaction, or cosmic ray). In NOvA, three typical types of interactions: ν_μ charged current (ν_μ CC), ν_e charged current (ν_e CC) and neutral current (NC) interactions, with different topologies, are shown in Figure 4.2. Muons are heavy (more than 200 times the mass of an electron). When muon bumps into the molecules in the liquid scintillator, they leave long and straight tracks in the detector. The pattern of an electron is much messier than that of a muon, and is identified by an electromagnetic (EM) shower. The original electron undergoes Bremstralung and then that gamma pair produces e^+ and e^- then they both Bremstralung and produce gammas that also pair produce again and so on. Finally, the energy of all created photons and electrons is absorbed through ionization loss. In NC interactions, neutrinos are the outgoing leptons carrying energies that can not be detected by the detector. In the NOvA experiment, neutral current events are important backgrounds. NC events that produce a charged pion might mimic the signature of ν_μ CC events, which can be rejected by the particle identification algorithms generally. The difference between a NC event with a π^0 and ν_e CC is harder to identify, except the case like the NC interaction in Figure 4.2, where there is a gap between the vertex and the start point of the shower.

[1] A slice refers to a collection of correlated hits clustered in space and time to form a potential event candidate.

4.2.1 Kalman tracker

The Kalman tracker [83] is a technique to reconstruct the tracks of individual particles that deposit energy in the detector in individual slices using the Kalman filter algorithm [84]. This technique can help identify muon neutrinos and muon antineutrinos, as it is typically used to identify particles like muons that have narrow and straight tracks and do not produce electromagnetic and hadronic showers.

The function of the Kalman tracker here is to find all possible tracks by sorting out the hits in a slice. The first step is to obtain all possible track seeds that are formed by two hits that are separated by less than four cells. The pairs of hits are assumed on the same track and used to estimate the position of the track. The next step, called the propagation process, starts from the downstream end of the detector, where particle tracks are the most separated from each other, toward the upstream direction. The adjacent hits can be added to the track if they only change the track's χ^2 by an acceptable value. The calculation of the χ^2 is weighted in a way that favours adjacent hits with small angular deviations. The reconstruction process is performed in the XZ and YZ detector views separately, and then the 3-dimensional track is reconstructed by matching the two 2D tracks. Figure 4.3 shows an example of reconstructed tracks at the far detector using the Kalman tracker.

4.2.2 Cosmic tracker

The Cosmic tracker [85] based on a window tracking algorithm is used to reconstruct the tracks of the cosmic ray muons in the NOvA detectors. The Window Tracking Algorithm has been developed taking into account the fact that the muons undergo multiple Coulomb scatterings in the detector that makes a muon change its direction. Nonetheless, we can still assume that muons follow a straight line trajectory over small portions of the track.

The algorithm evaluates each detector view independently before creating a three dimensional track. The algorithm starts with setting an initial window of n planes in the z-direction. A straight line fit to the hits in that window is performed and those hits consistent with that line are added to a two dimensional track. The window then slides one plane along the z-direction and any hits that are consistent with the line corresponding to the first window are added to the track. A new straight line fit is done to the hits in the downstream $n-1$ planes from the previous window and the hits added for the new plane in the current window. The window then slides one plane down again and the hits in that new plane are evaluated to determine if they are consistent with the previous line. The process repeats itself until all planes in one slice have been evaluated.

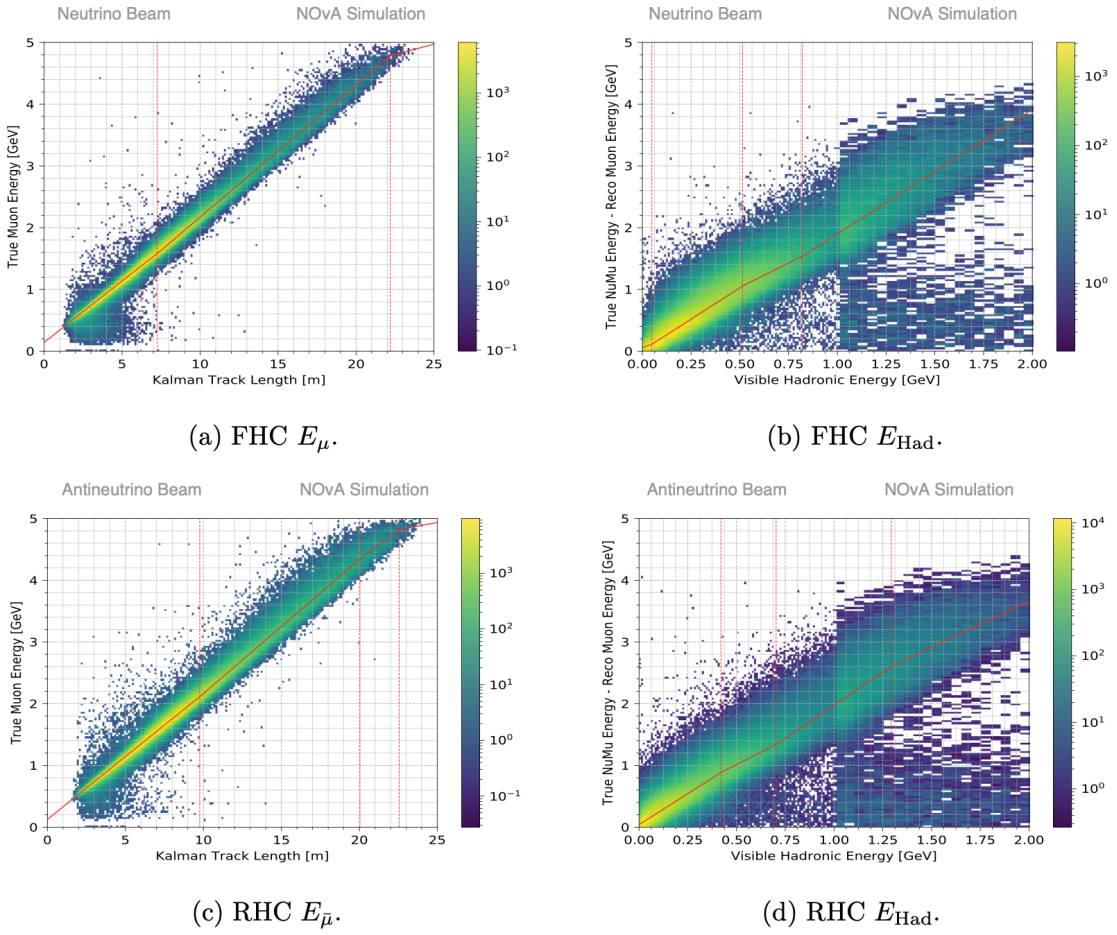

(a) FHC E_{μ}.

(b) FHC E_{Had}.

(c) RHC $E_{\bar{\mu}}$.

(d) RHC E_{Had}.

Figure 4.4: Piece-wise linear fits used to estimate the muon (left) and hadronic (right) energy for the FHC (top) and RHC (bottom) modes at the FD. The red lines The dashed vertical red lines shows the boundaries between different straight line fits. The solid red lines show the linear fit results. Taken from [86].

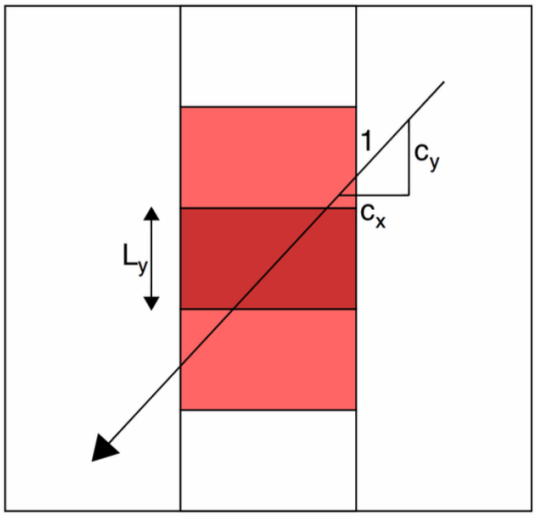

Figure 4.5: Diagram of a tricell hit. The tricell hit (dark red) is selected when each of its neighbour cells (light red) is hit [87].

4.3 Energy reconstruction

For the ν_μ and $\bar{\nu}_\mu$ CC events, the total energy of the neutrino $E_{\nu(\bar{\nu})}$ is calculated by

$$E_{\nu(\bar{\nu})} = E_{\mu(\bar{\mu})} + E_{had}, \tag{4.1}$$

where $E_{\mu(\bar{\mu})}$ is the muon (antimuon) energy estimated by the muon track length and E_{had} is the hadronic energy estimated by summing the visible calibrated energy of all hits from the hadronic system. Figure 4.4 shows the linear fits to the distributions of true muon energy versus muon track length and the difference value between true neutrino energy and reconstructed muon energy versus the reconstructed visible hadronic energy in the FD simulation. The hadronic energy has a resolution of about 30%, that is much bigger than the muon energy resolution of about 4%. In the 2020 3-flavour analysis, the ν_μ and $\bar{\nu}_\mu$ energy resolutions were 9% and 8% respectively at the FD [86].

4.3.1 Calorimetric energy calibration

The calorimetric energy calibration used to estimate the hadronic energy uses cosmic ray muons because their energy loss by ionization is well understood from the Bethe-Bloch curve. The tracks used for calibration are selected by applying quality cuts to remove those with badly reconstructed positions, and only tricells are selected. Tricell hits shown in Figure 4.5 require a perfect hit to be sandwiched by two hits on both adjacent same-plane cells, in order to get a precise path length. The calibration work consists of two parts: relative and absolute calibration. First of all, the following concepts below are very important for calibration:

- PE: uncorrected number of photoelectrons
- PE/cm: number of photoelectrons per unit path length which can be calculated as PE divided by path length in a cell.
- PEcorr: the corrected photoelectrons (PE).
- PEcorr/cm: a corrected detector response per path length unit (i.e. PECorr divided by path length in a cell).
- trueE: true energy deposited in a cell (MeV).
- trueE/cm: true energy deposited per path length unit in a cell (MeV/cm).

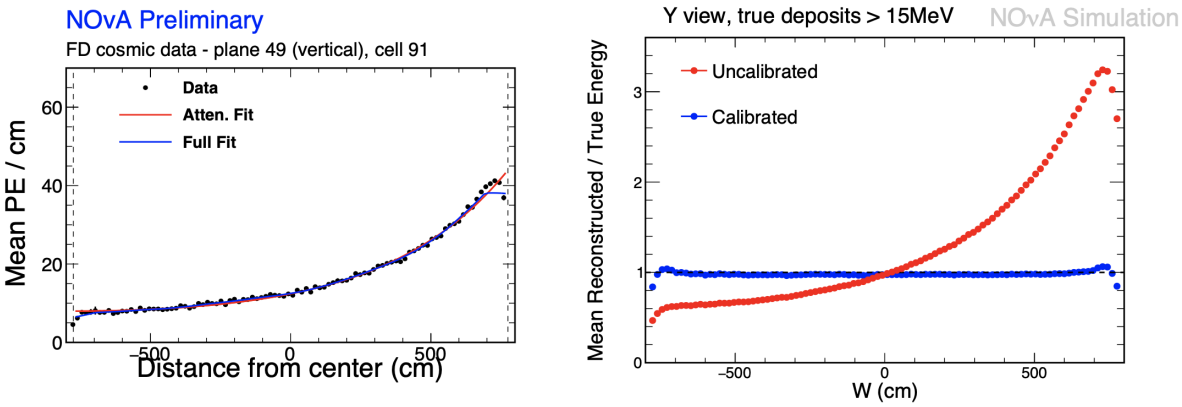

(a) (b)

Figure 4.6: Left: The mean value of PE/cm as a function of the hit position W with respect to the cell centre in a single horizontal cell using the FD. Positions with high W values are close to the readout. The solid lines shows the attenuation fits to the cosmic data. Right: The mean value of the ratio between reconstructed and true energy as a function of the hit position from the FD simulation. The red and blue distributions show the uncalibrated and calibrated scenarios respectively. Taken from [88].

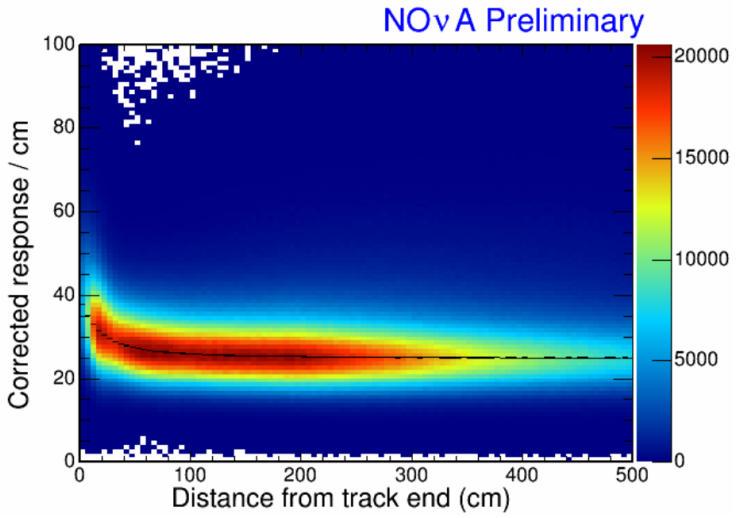

Figure 4.7: Distribution of corrected PE/cm as a function of distance from the end of the track, for tricell hits in selected stopping muon tracks. Each black point shows the mean of a fit made to the peak in each distance slice. The black curve shows the mean of a fit to the peak of the corrected detector response at particular distances from the track end. Hits in between 100 cm and 200 cm, where the response is most uniform, are used to set the energy scale. Taken from [89].

4.3.1.1 Relative Calibration

The goal of the relative calibration is to ensure the detector response is independent of the position of the hit. This is also a process to obtain the corrected photoelectrons PECorr from the original photoelectrons PE at the cell level. There are several main stages in the relative calibration :

- Threshold effect: a threshold is applied to signals. If a signal's PE value is above this threshold, it is counted as a hit. However, the number of photoelectrons produced on the readout follows a Poisson distribution. We discard hits that fall below threshold so we essentially mask the left hand side of a distribution of hit values. The remaining distribution consequently has a higher mean. This can cause an overestimation of a light-level and bias the real hit energies to lower values after the attenuation correction. In order to obtain the best estimate of the total energy deposited in scintillator, we have to account for the threshold effect when correcting for the attenuation.

- Shadowing effect: it is also called self-shielding effect. The FD is very large, thus the overburden of the top part of the detector alters the cosmic spectrum seen by the bottom part. This results in a 10% variation across the detector, mostly in the vertical direction. The shadowing correction flattens the energy deposition rate of particles used for calibration to the constant Minimum Ionizing Particle (MIP) value throughout the whole detector.

- Attenuation effect: light is attenuated while traveling through the fibre. The attenuation calibration corrects for the attenuation of light when the light travels through the optical fibre in the NOvA cell. The purpose of the attenuation calibration is to provide constants such that the energy deposited in the detector and recorded by an APD can be expressed in comparable units, wherever the deposition is. More specifically, the energy deposit PECorr is independent of the distance from the APD which read out the signal. Figure 4.6 illustrates the process of the attenuation correction at the FD. An attenuation correction function is obtained by fitting to the real cosmic data and will be able to provide corrections for any hits.

4.3.1.2 Absolute calibration

The absolute calibration aims to obtain a scale factor to convert the detector response to energy deposition in GeV using tricell hits. The Bethe-Bloch equation predicts the rate of

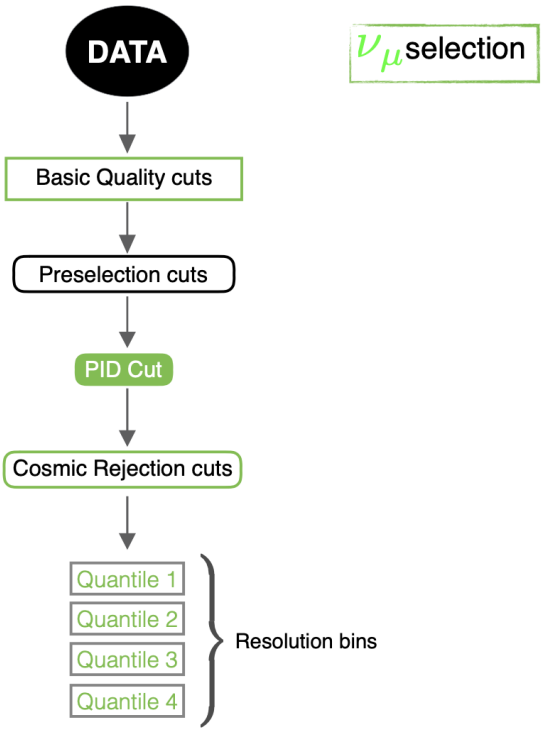

Figure 4.8: Flowchart of the selection of muon neutrino candidates in the FD [90].

energy loss as a muon goes through a type of material. Figure 4.7 illustrates this process. Only the deposits in the 100 cm to 200 cm window away from the end of the muon track are selected, because that region dE/dx is close to the stable minimum ionizing. The conversion factor can be expressed as

$$\text{Calorimetric energy scale} = \frac{\text{MEU}_{true}}{\text{MEU}_{reco}}, \tag{4.2}$$

where MEU_{true} and MEU_{reco} represents the mean values of the true energy and PECorr/cm per path length respectively.

4.4 Event selections and backgrounds

NOvA has an on-the-surface far detector and an underground near detector. The dominant background source is from the NC and cosmic ray events. Figure 4.8 shows the selection flow for $\nu_\mu(\bar{\nu}_\mu)$ selection, which includes data quality selection, containment selection, cosmic rejection cuts and particle identification (PID) selection. These four stages will be described in detail in the following subsections.

4.4.1 Data quality selection

The data quality cuts, which work on the run, subrun and spill information, are the primary selection criteria for candidates of neutrinos and antineutrinos. The goal of this selection is to remove slices that can't satisfy basic reconstructions. This selection considers the following general factors: the number of hits within a slice, number of cosmic tracks identified, muon likelihood score and the number of planes within a slice.

4.4.2 Containment cut

The motivation of the containment cuts is to ensure the selected events are totally inside the detectors to make good reconstruction. Events that enter the detectors from outside sometimes deposit energy at the detector edges, so the containment cuts can also reject some cosmic and rock events. The charged-current ν_μ candidates at the ND must pass several cuts. First, the interaction must be within the ranges: -180 < X , Y < 180 cm, and 40 < Z < 1525 cm. Second, the event vertex is not allowed to locate in the muon catcher. Third, a projected track must have at least five planes projected forwards from the end point and at least ten planes projected backwards from the start point to the edge of the detector. The selection of charged-current ν_μ candidates at the FD is different from the ND. First, neutrino events that are closer than 60, 12, 16, 12, 18 and 18 cm from the top, bottom, east, west, front and back detector edges are rejected, respectively. Second, the events must not contain hits in the front two or back three detector planes. Third, a projected track must have at least six planes projected forwards from the end point and at least seven planes projected backwards from the start point to the edge of the detector.

4.4.3 Particle identification selectors

Apart from the above basic cuts, three kinds of machine learning algorithms also help do the particle identification in the NOvA analyses. Reconstruction Muon Identification (ReMId) is used to score a track's muon likelihood, Convolutional Visual Network (CVN) scoring muon neutrino likelihood is a kind of neural network image classifier, and the cosmic Boosted Decision Tree (BDT) scores the likelihood that a slice is not caused by a cosmic event.

Reconstructed Muon Identifier (ReMId):

ReMId is a k-Nearest Neighbor (kNN) [92] classifier used to identify the muon in an event. The classifier uses Kalman track candidates and scores them based on four reconstructed variables: dE/dx likelihood, scattering likelihood, total track length and non-hadronic

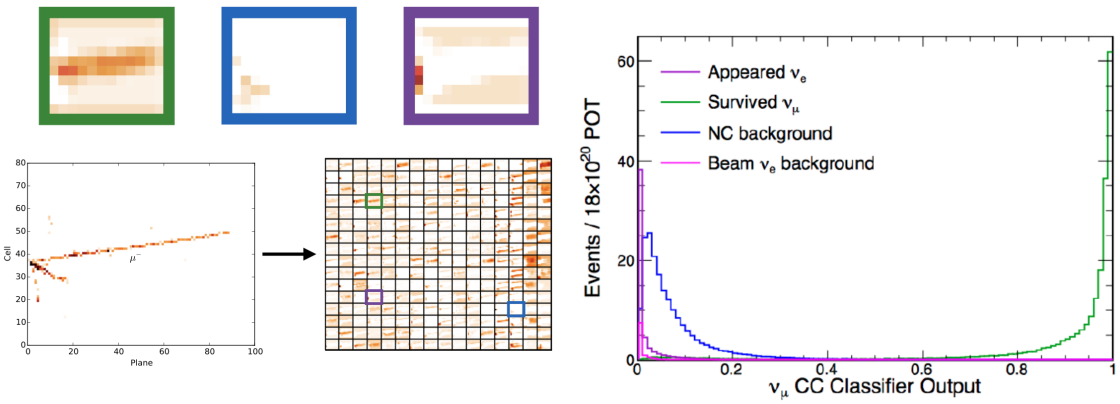

Figure 4.9: Left: Example of ν_μ identification. The three top images show that CVN can identify features such as a muon track (green), electromagnetic showers (blue) and hadronic activity (purple). The bottom left figure panel shows a neutrino interaction in the y-z view. The 256 feature maps are extracted from the event. Right: The distribution of CVN$_{\nu_\mu}$ in the FD simulation. Distributions of ν_μ, appeared ν_e, NC and intrinsic beam background are shown in green, purple, blue and pink respectively. Taken from [91].

plane fraction. The deposited energy per unit path length dE/dx of a muon is different from the one for a pion that can lose energy via hadronic scattering in addition to ionization. The dE/dx log-likelihood is calculated by comparing the dE/dx distribution against the muon hypotheses and returns a likelihood score. Similarly, the scattering likelihood calculates the deviations in the particle trajectory from a straight line. Although the muon track can have a slight curvature through multiple soft scattering and occasionally Coulomb scattering, that effects can be neglected safely. The variable track length considers the fact that hadronic showers are more likely to contain multiple short tracks, rather than single, longer tracks. The fourth variable is the non-hadronic plane fraction, which counts the planes those have energy outside of the track that are excluded from the dE/dx likelihood calculation. The simulation signal and background events are trained by the kNN algorithm which determines the four dimensional distance between the Kalman tracks in the candidate event and the simulated tracks. A track closer to signal-like obtains a higher score. The most muon-like of the tracks is considered as the muon candidate. NOvA's 2020 selection cut for ν_μ required events with ReMId>0.30.

Convolutional Visual Network (CVN):

CVN [91] is an event classification method based on a machine learning algorithm known as a convolutional neural network (CNN). This classifier is combined with the ReMId classifier in order to select muon neutrino events for the disappearance analysis in NOvA.

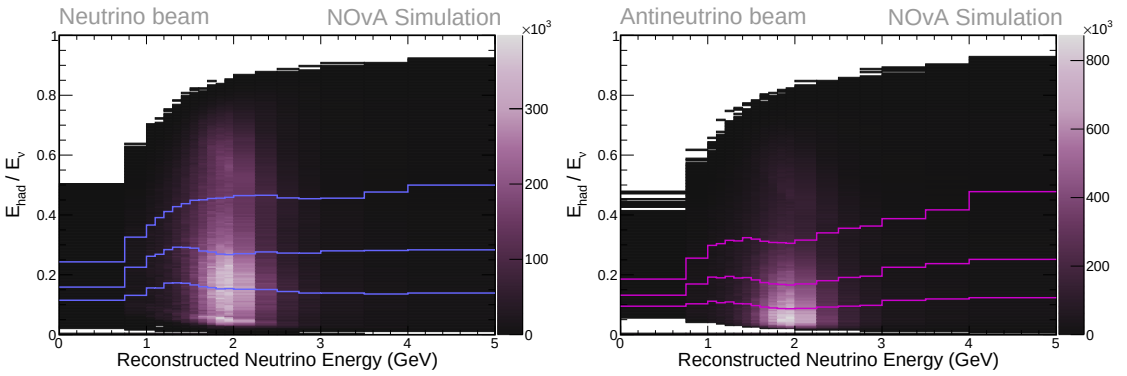

Figure 4.10: Distributions of hadronic energy fraction vs. reconstructed neutrino energy for selected muon neutrino and antineutrino events in the FD simulation without oscillations. The blue (pink) lines are boundaries used to divide the sample into four quartiles in each energy bin for the FHC (RHC) mode. Taken from [95].

It identifies neutrino interactions based on their topology and does not require track or vertex reconstruction. The algorithm takes the images of the event in both two detector views. Each cell is treated as a pixel in the image, and each pixel has an intensity that is proportional to the calibrated charge. The classifier is trained with simulated events and cosmic ray data. CVN was developed using the Caffe framework [93], with an architecture inspired by GoogleNet [94]. Figure 4.9 shows an example of a ν_μ identification, by which CVN is able to identify features from an event, such as a muon track, electromagnetic showers and hadronic activity. In NOvA, separate trainings are implemented for ν_μ CC, ν_e CC, NC and cosmic events. The score for an event is in the (0,1) range, in which the closer to 1 the more likely the event is a muon neutrino. The ν_μ CVN PID output is also shown in Figure 4.9. In the latest NOvA's 2020 analysis, the ν_μ selection required CVN>0.80.

ν_μ cosmic rejection BDT (CosPID or CosRej):

The ν_μ analysis uses a Boosted Decision Tree (BDT) for cosmic rejection. Like CVN and ReMId, this BDT also works as a particle identifier that uses the information from the cosmic and Kalman tracks, as well as the ReMId and CVN cosmic scores. The BDT is trained with Monte Carlo simulations and cosmic trigger for data. Several reconstructed variables are included in the training: angle between the lepton and the neutrino, length of the muon track, verticality of the muon, distance of the track from each detector wall, fraction of hits in the track, and the fraction of the track momentum transverse to the beam direction. The output score is between 0 (cosmic-like) and 1 (ν_μ-like). A BDT score greater than 0.45 was applied in NOvA's 2020 selection.

4.5 Analysis Binning at the FD

4.5.1 Quartile bins

As mentioned in Section 4.3, the reconstructed energy of ν_μ CC events is the sum of the muon energy and the hadronic energy. The hadronic energy resolution is 30% which is the dominant limiting factor for the muon neutrino energy resolution, since muon energy resolution is a small value of 4%. Therefore, ν_μ events with a small amount of hadronic energy are more likely to have better resolution compared to those with a large amount of hadronic energy. For this reason, the ν_μ disappearance analysis in NOvA, both the ND and FD events are split into four separate subsamples: quartile 1, quartile 2, quartile 3, and quartile 4, by hadronic energy fraction that is the ratio of the hadronic energy to the total neutrino energy E_{had}/E_{Total}. Each quartile sample has 25% of the events. Quantile 1 is a set of events with the best energy resolution that has a small hadronic energy fraction, while Quartile 4 has the worst resolution. Another advantage of this binning method is that ν_μ CC events with a small hadronic fraction are more likely to be identified as signal events, leading to a suppression of the backgrounds. In summary, quartile 1 has the best resolution and the fewest background events. Using quartile 1 we can reconstruct a best energy spectrum that is used to measure oscillation parameters. Figure 4.10 shows the distributions of the hadronic energy fraction against reconstructed neutrino energy in both FHC and RHC modes from the FD simulation without oscillations.

4.5.2 Energy binning

In the muon neutrino disappearance channel, θ_{23} determines the amplitude of the dip in the oscillation probability and Δm^2_{32} determines the dip position in the (1, 2) GeV region. For this reason, a binning with non-constant bin widths is used in NOvA's current official analysis. The bins between 1 and 2 GeV are narrower, and wider at high energy, where fewer events are obtained and the impact of oscillation parameters is small. There are 19 reconstructed neutrino energy bins in total. The bin edges are set at (0, 0.75, 1, 1.1, 1.2, 1.3, 1.4, 1.5, 1.6, 1.7, 1.8, 1.9, 2, 2.25, 2.5, 2.75, 3, 3.5, 4, 5) GeV [96].

4.6 Extrapolation Method

To obtain a prediction of the FD spectrum with less systematic uncertainty, we use a method of data-driven corrections which selects the candidate events from the near detector real data and then apply the extrapolation. CAFAna provides the function to

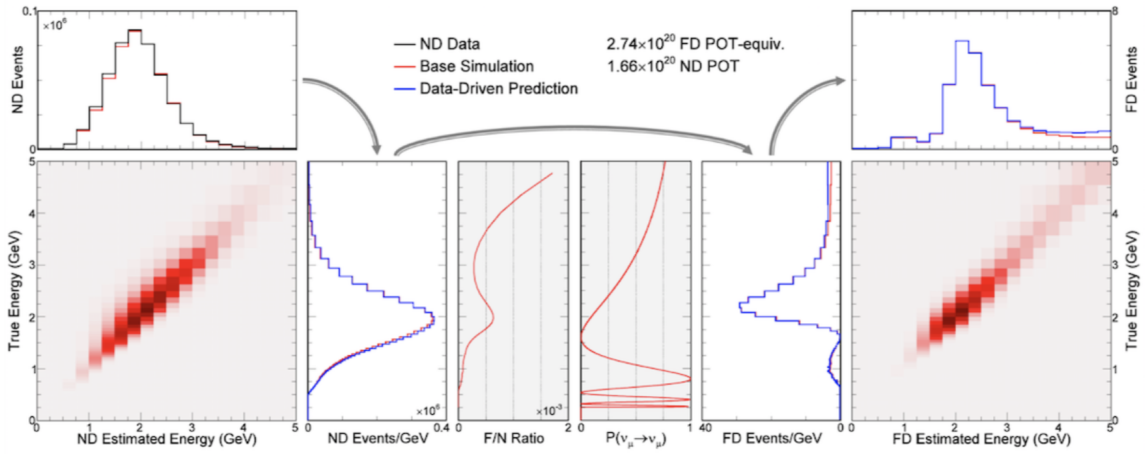

Figure 4.11: Diagram showing the process of getting FD predictions from the ND real data: (1) A matrix is used to convert the ND spectra from reconstructed to true energy, (2) The far detector true spectrum is obtained according to the oscillation probability and far/near detector ratios. (3) A true-to-reconstructed energy matrix is applied to the spectra to obtain the final prediction at the FD. Taken from [97].

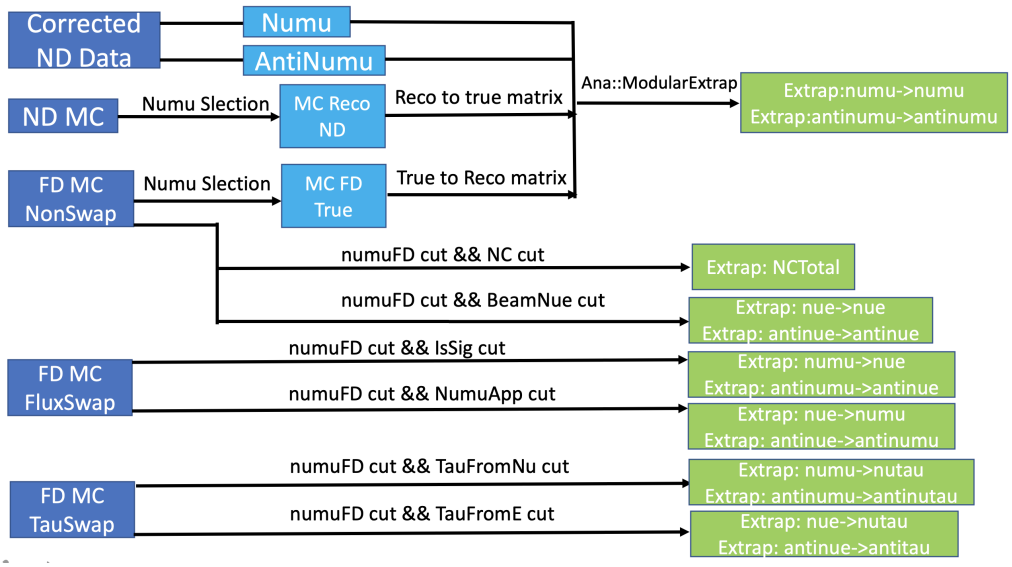

Figure 4.12: Diagram describing the extrapolation process for the ν_μ and $\bar{\nu}_\mu$ disappearance analysis. In the CAFAna framework the ModularExtrapolation class is used for this extrapolation. This modular takes the ND decomposition results and computes the matrices to convert reconstructed energy to true energy (or true to reconstructed). The blue boxes represent different kinds of input ND and FD files. The green boxes represents the signal events and backgrounds we obtained.

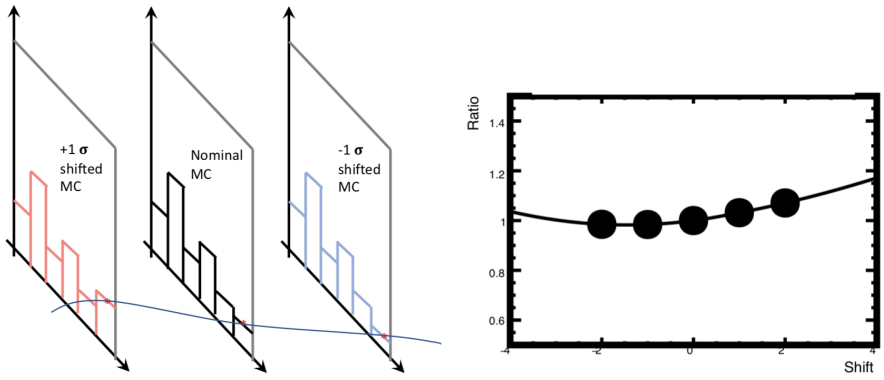

Figure 4.13: The left plot shows the spectra after adding a systematic uncertainty. The right plots shows an example of systematic interpolation. The X-axis is a systematic shift in the uncertainty σ of the systematic. The Y-axis is the ratio of the shifted prediction to the nominal prediction. The black points are fit by an interpolation function. Taken from [98].

extrapolate near detector to the far detector. Figure 4.11 shows the process of getting the FD predicted reconstructed spectrum from the ND reconstructed spectrum. The first step of the extrapolation process uses the near detector real data. The near detector background is calculated from simulation. Then we use a matrix which converts the reconstructed energy spectrum to the true energy spectrum. Then after applying an *unoscillated/oscillated* factor on the true spectrum one can get the far detector true spectrum. Finally, we can get the predicted reconstructed energy spectrum by applying the far detector conversion matrix on the scaled spectrum. A diagram showing the whole picture of extrapolation, is drawn in Figure 4.12. It should be noted that it is possible to obtain the FD prediction only using the MC simulation of the FD. This is referred to as a "no extrapolation" method. The following is how to compute the signal events and backgrounds.

- **Signal** There are two channels in the muon neutrino disappearance analysis: $\nu_\mu \to \nu_\mu$ and $\bar{\nu}_\mu \to \bar{\nu}_\mu$. The goal of the numu extrapolation is to compute the FD predicted reconstructed spectrum $F_{S_\mu}^{Pred}(B_j^\mu)$, where S_μ indicates that ν_μ selection has been applied, B_j^μ are the bins of the reconstructed variable of the ν_μ analysis, indexed by j. Therefore the term $N_{\alpha,S_\mu}^{Pred}(E_i^T)$ is the true energy spectrum at the the near detector, which can be computed as

$$N_{\alpha,S_\mu}^{Pred}(E_i^T) = \sum_k \frac{N_{\alpha,S_\mu}^{Data}(B_k^\mu) \times N_{\alpha,S_\mu}^{MC}(E_i^T, B_k^\mu)}{N_{\alpha,S_\mu}^{MC}(B_k^\mu)}, \tag{4.3}$$

where α is the neutrino flavour, E^T and B_μ indicate a true and reconstructed energy respectively, "Pred" indicates it is a predicted spectrum by the data-driven method, and N indicates the near detector. MC indicates a quantity computed directly from Monte-Carlo files. This operation is equivalent to the application of a reconstructed-to-true matrix. The predicted spectrum at the ND is then extrapolated to the FD. The predicted ν_μ at the FD can be written as

$$F^{Pred}_{\alpha\to\alpha,S_\mu}(E_i^T, B_j^\mu) = \frac{N^{Pred}_{\alpha,S_\mu}(E_i^T) \times F^{MC}_{\alpha\to\alpha,S_\mu}(E_i^T, B_j^\mu)}{N^{MC}_{\alpha,S_\mu}(E_i^T)}, \tag{4.4}$$

where F means the far detector. The oscillation probability are computed from the flavor transition mode, central value of the true-energy bin, and the neutrino-oscillation parameters. Here the F^{Pred} term is constructed by assuming no oscillations, and then is independent of the neutrino-oscillation parameters. Finally, the probability is applied and the FD prediction in bins of reconstructed energy is computed by summing across true energy bins :

$$F^{Pred}_{S_\mu}(B_j^\mu) = \sum_{\alpha\to\beta}\sum_i F^{Pred}_{\alpha\to\beta,S_\mu}(E_i^T, B_j^\mu) P_{\alpha\to\beta}(E_i^T), \tag{4.5}$$

where E_i^T represents the true-energy bins, indexed by i and P is an oscillation probability.

- **Background** Backgrounds to the ν_μ analysis at the FD include two sources. First is the beam background, which is predicted to be small from simulations. The main beam background is the neutral current. For this reason, all the beam backgrounds are trivially derived from the FD Monte-Carlo:

$$F^{Pred}_{\alpha\to\beta,S_\mu}(E_i^T, B_j^\mu) = F^{MC}_{\alpha\to\beta,S_\mu}(E_i^T, B_j^\mu). \tag{4.6}$$

  Second, there are some backgrounds arising from cosmic interactions. To estimate this background, the selection cuts for muon neutrino candidates are applied to the data from the cosmic trigger. Then the histograms are scaled down by the ratio of the livetime in cosmic data to the livetime in NuMI beam data.

4.7 Systematic uncertainties

Sources of systematic uncertainties in NOvA can be divided into a few categories: detector calibration, neutrino cross section, detector response, normalisation and energy scale, lepton reconstruction and flux uncertainties. Table 4.1 lists the definitions of systematic uncertainties used in the muon neutrino disappearance analysis. These uncertainties

Systematic category	Systematic uncertainty description
Detector Calibration	Calibration (Absolute calibration)
	CalibShape (Calibration shape)
	RelativeCalib (Relative calibration)
	CalibDrift (Calibration drift)
Neutrino Cross Sections	genie_small_pc{00-11}
	MaCCRES (Nuclear form factor parameter)
	MaNCRES (Nuclear form factor parameter)
	MvCCRES (Nuclear form factor parameter)
	MvNCRES (Nuclear form factor parameter)
	MECShape2020Nu (MEC 2020(q_0, $\|\vec{q}\|$) response neutrinos)
	MECShape2020AntiNu (MEC 2020(q_0, $\|\vec{q}\|$) response antineutrinos)
	MECInitStateNPFrac2020AntiNu (MEC initial state np fraction, antineutrinos)
	MECInitStateNPFrac2020Nu (MEC initial state np fraction, neutrinos)
	MECEnuShape2020AntiNu (MEC E_ν shape, antineutrinos)
	MECEnuShape2020Nu (MEC E_ν shape, antineutrinos)
	ZExpAxialFFSyst2020_EV1 (CCQE z-exp eigenvector shift 1)
	ZExpAxialFFSyst2020_EV2 (CCQE z-exp eigenvector shift 2)
	ZExpAxialFFSyst2020_EV3 (CCQE z-exp eigenvector shift 3)
	ZExpAxialFFSyst2020_EV4 (CCQE z-exp eigenvector shift 4)
	ZNormCCQE (CCQE z-exp normalisation)
	RPAShapeenh2020 (RPA shape: higher-Q^2 enhancement (2020))
	RPAShapesupp2020 (RPA shape: low-Q^2 suppression (2020))
	LowQ2RESSupp2020 (RES low-Q^2 suppression)
	DISvnCC1pi_2020 (DIS events producing 1 pion)
	hNFSI_MFP_2020 (hN FSI mean free path)
	hNFSI_FateFracEV1_2020 (hN FSI fate fraction eigenvector 1)
Detector Response	Light_Level_ND (ND light level)
	Light_Level_FD (FD light level)
	Cherenkov (Cherenkov light)
Near-Far Uncorr.	NormHornCorr (Correlated normalisation)
	NormFHC2020 (FHC normalisation)
	NormRHC2020 (RHC normalisation)
	cosmicScale (Cosmic background scale)
Neutron Uncertainty	NeutronEvisPrimariesSyst2018 (Neutron visible energy systematic)
Beam Flux	ppfx_hadp_beam_pc{00-04} (Flux component 00-04)
Lepton Reconstruction	UnCorrNDMuEScaleSyst2020 (ND muon energy scale uncorrelated)
	UnCorrMuCatMuESyst2020 (Muon catcher muon energy scale uncorrelated)
	PileupMuESyst2020 (ND neutron pile-up)
	CorrMuEScaleSyst2020 (Muon energy scale correlated)
	UnCorrFDMuEScaleSyst2020 (FD muon energy scale uncorrelated)
	LeptonAngleSystNDXZ2020 (Lepton angle systematic ND XZ)
	LeptonAngleSystNDYZ2020 (Lepton angle systematic ND YZ)
	LeptonAngleSystFDXZ2020 (Lepton angle systematic FD XZ)
	LeptonAngleSystFDYZ2020 (Lepton angle systematic FD YZ)

Table 4.1: Description of systematic uncertainties in this thesis. Left column shows the name of each systematic category while the right column shows the corresponding systematic uncertainties including the shorthand and a description.

can be also separated into correlated and uncorrelated types. Correlated systematics apply to both detectors, and uncorrelated (relative) ones are different between the detectors. Each shifted ND prediction is then translated to the FD using the Far/Near extrapolation technique. This helps to cancel detector correlated uncertainties such as beam flux and neutrino cross section uncertainties due to the functionally identical detectors. Systematic uncertainties fall into three categories by how they are evaluated:

- Reweighted events: these systematics are handled by simply filling spectra with different weights for different event types. Examples: beam flux, cross section.
- Recomputed events: these systematics are computed by recalculating reconstructed energy after adjusting the values of selected CAF branches. Examples: muon energy, neutron systematic uncertainty.
- Completely re-simulated events: sometimes the effect of a systematic uncertainty is more complicated than a simple adjustment, so we go all the way back and make new simulations with the effect applied during this process. Examples: calibration, light-level, calibration shape.

For the first two cases, we can just start with the nominal MC, and "shift" each event as we make the new prediction. For the third scenario, we simulate new art files, then make new CAFs out of those, and finally make the new predictions out of the new CAFs. For each systematic, we make a whole new set of FD predictions like Figure 4.11. As is shown in Figure 4.13 for each bin in reconstructed energy, we generate a polynomial fit between $+1\sigma$, nominal, and -1σ predictions. This allows us to generate a predicted FD spectra for a shift of any size. If repeating this for all systematic uncertainties, we can make predictions for any oscillation parameters as well as for any systematic shift, and can therefore fit everything.

4.7.1 Beam flux uncertainty

The flux uncertainties are constructed to deal with the production and propagation of hadrons in the NuMI facility. The hadron production is derived from the PPFX (Package to Predict the Flux) framework, which constrains the hadron production models for the NuMI beam using external constraints. These PPFX weights are reduced into a set of uncorrelated weights via principal component analysis (PCA) [99]. Uncertainty in the process of transport includes the target position, the size of the beam spot, the position and current of the horns in the beam line.

4.7.2 Detector Response

The light produced in the cell of the detector has two sources: the scintillation light and the Cherenkov radiation. The light production model describes the number of photons which are transmitted by fibres. The detector response systematic uncertainties account for uncertainties in the light production model both from the light level and the Cherenkov radiation.

4.7.2.1 Light Level

The light level model is changed independently for the ND and FD due to different sizes of the two detectors. In the ND, the light production is shifted $\pm 10\%$ in both X and Y views, while in the FD it is shifted $\pm 16\%$ in the X view and an inverse $\mp 6\%$ in the Y view. With the light level model changed, the absolute calibration constants are counter adjusted to match the original energy response.

4.7.2.2 Cherenkov

The Cherenkov systematic uncertainty in the light model deals with the 5% data/MC discrepancy in the dE/dx of protons. The light level model related to the Cherenkov light is changed to reduce the discrepancy to $<1\%$, but keep the detector response to muons the same. Since the Cherenkov light response is related to the mineral oil, and the ND and FD oils are similar, the effect is treated as fully correlated between the two detectors. Since this shift has one direction, only the $+1$ σ uncertainty is evaluated.

4.7.3 Detector Calibration

4.7.3.1 Calibration Energy Scale

The overall energy response uncertainty is determined from the disagreement between data and MC for the candidate protons in the ND. This discrepancy is at the 5% which is greater than other samples, such as the beam muons, the Michel electron candidates and the π^0 candidates. It is difficult to confirm if the data-MC discrepancy exits in the FD because of the lack of statistics. For this reason, both "absolute" (fully correlated: the ND and the FD are shifted in the same direction) and "relative" (fully uncorrelated: the ND and the FD are shifted in opposite directions) energy scale uncertainties were included in order to cover the possibilities.

4.7.3.2 Calibration Shape

The energy response at the ends of the cells is different from the middle, but the calibration can not account for this difference perfectly [100]. A systematic uncertainty named "calibration shape" cover differences between reconstructed and true energies for events close to the detector edges. This systematic is treated as fully correlated between the ND and the FD.

4.7.3.3 Calibration Drift

In the FD, the number of reconstructed hits in the candidate events is seen to decrease at a rate of about 0.24% per year [101, 102]. This is probably because the ageing of scintillator and the detector electronics result in a reduced light yield. To account for this, the modelled light production is reduced with a gradient of 4.5% per year to match the reduction of the number of hits. In addition, a corresponding increase in the absolute calibration constant is appropriately shifted to match the original energy response. Since this systematic uncertainty has one direction, only the $+1$ σ shift file is made.

4.7.4 Neutron

The detector response to fast neutrons, around 1MeV or more of kinematic energy, is not modelled well with the neutron model [103]. This discrepancy will mostly affect the $\bar{\nu}_\mu$ analysis since the hadronic activity of the $\bar{\nu}_\mu$ events often consists of neutron activity. A notable excess of neutron candidate prongs at low energy (below 20 MeV) is observed in simulation compared to the data in neutron rich samples of $\bar{\nu}_\mu$ candidates. To cover this discrepancy, the neutron systematic uncertainty is developed by scaling the contribution of neutrons with a true visible energy below 20 MeV to the hadronic energy.

4.7.5 Muon Energy Scale

The reconstruction of muon tracks is very important to reconstruct the muon energy. The systematic uncertainty on the muon track length consists of five components which are shown below [104]:

- FD uncorrelated error (0.15%)
- ND uncorrelated error (0.13%)
- ND uncorrelated muon catcher error (0.48%)

- Correlated error between FD/ND/muon-catcher (0.74%, 0.74%, 0.13%)
- ND only neutron pileup error (0.46 cm in main detector, 1.3 cm in the muon-catcher)

The three uncorrelated uncertainties between the ND and the FD are dominated by uncertainties in the mass accounting of the detector. The fourth is a correlated uncertainty that is driven by uncertainties in the Fermi density effect and differences in muon range as calculated by GEANT and others [105]. The final uncertainty is designed to address a problem from slow neutrons that are not accurately simulated in MC in the main ND detector and the muon catcher [106]. It has been found that over the course of the beam spill, slow neutrons from early in the beam spill produce excess hits near the end of the beam spill. This results in neutrino events that occur near the end of the beam spill having a higher reconstructed muon track.

4.7.6 Cross section systematics

Most neutrino cross section and final state interaction (FSI) uncertainties are from weight parameters provided the GENIE simulation. These weight parameters are applied to the simulated neutrino interactions based on truth quantities. The uncertainties account for theoretical models and data from NOvA and other experiments. The details of the systematic uncertainties are from Ref. [107].

- **Quasi-Elastic Scattering:** GENIE provides some uncertainty parameters which act on the z-expansion axial form factor model. The normalisation parameter adjusts the total number of events by $+20/-15\%$. Other correlated parameters adjust the shape of the model. NOvA has developed independent weight functions. Long-range interactions between nucleons can affect on the kinematic for QE interactions. Due to this effect, the low Q^2 cross section is suppressed and the high Q^2 cross section is enhanced.
- **Meson Exchange Currents:** there are three types of uncertainties applied to MEC interactions. First, the uncertainty related to neutrino energy comes from comparing several theoretical models to the Valencia model. The updated new models are scaled to match Valencia model at 10 GeV. Then the ratios of the different predictions from new models to the Valencia model define an envelope that gives an energy dependent uncertainty. Second, the fit of the new MEC model to the NOvA ND data is re-performed under two variations of the remaining non-MEC MC: one where the base model is shifted to be more QE-like, resulting in a more RES-like MEC; and one in

which the base model is more RES-like, resulting in a more QE-like MEC. Third, the fraction of nucleon pairs, np or nn (pp) for neutrinos (antineutrinos), in MEC events in the model used is

$$\frac{np}{np + nn(pp)} = 0.69(0.66)^{+15\%}_{-5\%}. \tag{4.7}$$

for neutrinos and antineutrinos.

- **Resonant Production:** The new GENIE model for RES is more suppressed at low Q^2 than the previous version, but there is a small disagreement between data and simulation. An uncertainty is introduced in NOvA to cover more or less suppression. A lot of Q^2 forms come from other experiments and theories were considered. Finally, a parameterization from the MINOS experiment, which applied a functional weight of the form to CC RES to account for disagreement in low-Q^2, was chosen to constrain the allowed range.

- **Deep Inelastic Scattering:** In GENIE, the normalisation uncertainty for DIS interactions is 50% when the hadronic invariant mass W is less than 2 GeV. According to the data constraints, NOvA has applied the 50% uncertainty below a hadronic invariant mass of 3 GeV. Above 3 GeV, the uncertainty decreases linearly from 50% at W = 3 GeV to 5% at W = 5 GeV.

- **Final-state interactions:** NOvA uses the hN FSI model that does not associate GENIE uncertainties. A set of weights were developed using GENIE variations that alter the probability of pions participating in different categories of re-interactions ("fate fractions"). The probabilities were determined from studies of T2K, which used a similar model. Finally, four uncertainties have been developed for NOvA's analysis: one for the pion mean free path (30% variation from the new central value), and three correlated variations in pion absorption (up to 40% variation), pion charge exchange (up to 20%), and pion quasi-elastic scattering (up to 30%) cross sections.

4.7.7 Normalisation

The normalisation uncertainty can be divided into the "correlated normalisation" and the "uncorrelated normalisation". The correlated normalisation has a value of 0.82%, which is obtained from a sum in quadrature of uncertainties in the FD mass and a quantified failure mode in the detector simulation [108]. 0.72% and 0.90% in FHC and RHC respectively. Uncertainty on POT is 0.55% for both FHC and RHC.

4.8 Parameter sensitivities

After obtaining the observed data distributions and predictions we can do the oscillation parameter fit. The parameters are measured in NOvA by fitting the predicted energy spectra to the spectra observed data in the FD with a frequentist statistical method. Suppose the NOvA experiment divides the range of observation into N bins. The outcome is reported with the number of observed events in each bin n_i. With the assumption that the number of events in each bin follows a Poisson distribution, the likelihood function is

$$L(\boldsymbol{\mu}, \boldsymbol{n}) = \prod_i \frac{e^{(-\mu_i)}\mu_i^{n_i}}{n_i!}, \tag{4.8}$$

where μ_i and n_i are the number of predicted events calculated by a model and observed in data in the i^{th} bin of a spectrum, respectively. We let $\boldsymbol{m}$ be the true (unknown) vector of $\boldsymbol{n}$ and then define a likelihood ratio $\lambda = L(\boldsymbol{\mu};\boldsymbol{n})/L(\boldsymbol{m};\boldsymbol{n})$, which is used to examine the goodness of fit of the model. Then $-2ln\lambda$ asymptotically obeys a chi-square distribution [109]:

$$\chi^2 = -2ln\lambda = -2lnL(\boldsymbol{\mu};\boldsymbol{n}) + 2lnL(\boldsymbol{m};\boldsymbol{n}). \tag{4.9}$$

Since we estimate the true values $\boldsymbol{m}$ by $\boldsymbol{n}$, then the χ^2 can be written as

$$\chi^2 = -2ln\lambda = 2\sum_{i=1}^{N}[\mu_i - n_i + n_i ln\frac{n_i}{\mu_i}]. \tag{4.10}$$

In the NOvA experiment, μ_i depends on the oscillation parameters $\boldsymbol{\theta}$=(δ_{cp}, Δm^2_{31}, θ_{23}, θ_{13}, Δm^2_{21}, θ_{12}) and systematical uncertainty parameters $\boldsymbol{\xi}$, and then can be expressed as $\mu_i(\boldsymbol{\theta},\boldsymbol{\xi})$. For each ξ in $\boldsymbol{\xi}$ we have the mean value $<\xi_\alpha>=\hat{\xi_\alpha}$ and the uncertainty σ_α^ξ. Consider ξ at the same level as θ , we can add their information to χ^2 and then get the final form of χ^2

$$\chi^2(\theta,\xi) = \sum_{i=1}^{N}\frac{[\mu_i(\theta,\xi) - n_i]^2}{\sigma_i^2} + \sum_\alpha \frac{(\xi_\alpha - \hat{\xi_\alpha})^2}{(\sigma_\alpha^\xi)^2}. \tag{4.11}$$

The values of the parameters $(\boldsymbol{\theta},\boldsymbol{\xi})$ that minimise the above χ^2 are called the "best fit" values. The confidence intervals are calculated by

$$\Delta\chi^2 = \chi^2 - \chi^2_{min}, \tag{4.12}$$

which is an equation to get the sensitivity with a set of parameters.

Chapter 5

Analysis Improvements

This chapter presents approaches which aim to improve the sensitivity of $|\Delta m^2_{32}|$ and $\sin^2\theta_{23}$ measurements in the muon neutrino disappearance analysis. First, higher energy ν_μ are investigated by extending the energy range in NOvA's current standard analysis. Second, some ν_μ CC events that look similar to neutral current events, which have not been included in NOvA's existing analyses have been evaluated. Third, a new energy estimator, which has been developed to improve the neutrino energy resolution, is evaluated. Fourth, for the sample of events used in NOvA's existing analysis, in addition to binning the events as a function of energy and hadronic energy fraction, three particle identifiers, CVN, CosPID and ReMId are introduced to separate neutrino events by signal purity and reduce the impact of backgrounds. Lastly, the combinations of subsets of these approaches is evaluated.

5.1 Metric to Quantify Analysis Improvement

First of all, it is necessary to define the metric used to quantify the sensitivity improvement to the neutrino oscillation parameters before introducing different analysis methodologies. In this chapter the "standard analysis" corresponds to NOvA's 2020 3-flavour analysis with a neutrino dataset of 13.6×10^{20} POT in FHC and an antineutrino dataset of 12.5×10^{20} POT in RHC [110]. The "standard sample" corresponds to the sample selected through the official cuts. The new analysis methodologies will be compared to this standard analysis. Before doing an oscillation fit to the real FD data, we need to fit a simulated far detector spectrum to an oscillated analogue for data (i.e. fake data) which is used to understand the physics reach. The simplest type of fake data is so-called "Asimov" [111] fake data, which is high statistics MC scaled down to match the exposure of the data and

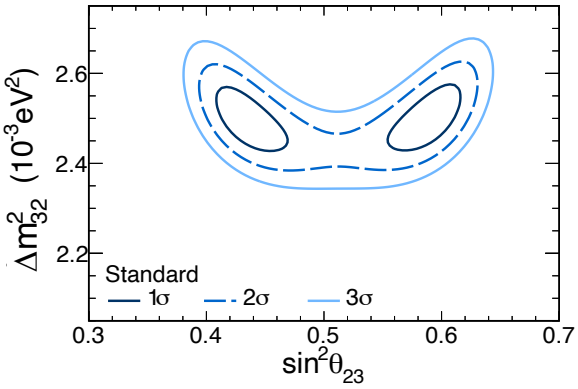

Figure 5.1: Sensitivity contour of constant $\Delta\chi^2$ in the Δm^2_{32} versus $\sin^2\theta_{23}$ space in the standard analysis without systematic uncertainties for Asimov fake data. The best fit values are $\sin^2\theta_{23} = 0.59$ and $\Delta m^2_{32} = 2.5 \times 10^{-3}$ eV^2.

with a particular set of oscillation parameters applied. All sensitivity contours obtained in this chapter are plotted using the "Asimov" approach, assuming the normal hierarchy. Each analysis improvement will be evaluated at a test point where $\sin^2\theta_{23} = 0.59$ and $\Delta m^2_{32} = 2.5 \times 10^{-3}$ eV^2 in the space of Δm^2_{32} versus $\sin^2\theta_{23}$. When searching for sensitivity improvements, in order to reduce the amount of computing resources and time, the $\Delta\chi^2$ is calculated without systematic uncertainties and with a non-extrapolation method which uses only the FD simulation. There are two reasons why the simplified method is used. First, the statistical uncertainty is still the dominant uncertainty at the current stage. Second, the cross section tuning has already accounted for the differences of data and MC, and this tuning is applied to the far detector. This allows for quick comparison between the new analysis method and NOvA's standard analysis, since a large number of analysis methodologies will be investigated. Figure 5.1 shows sensitivity contours of constant $\Delta\chi^2$ in the Δm^2_{32} versus $\sin^2\theta_{23}$ space in the standard analysis. Figure 5.2 and Figure 5.3 show the Gaussian significance $\sqrt{\Delta\chi^2}$ as a function of $\sin^2\theta_{23}$ and Δm^2_{32} respectively in the standard analysis. In Figure 5.2, the $\sqrt{\Delta\chi^2}$ value at $\sin^2\theta_{23} = 0.51$, close to the maximal disappearance point, rather than the maximal mixing point $\sin^2\theta_{23} = 0.5$, will be compared to the new analysis. In Figure 5.3 the uncertainty range at 1 σ for Δm^2_{32} shown by the black line will be used to quantify the new analysis methods. Finally, those methods that give the best sensitivity improvements using the simplified metric described above will be picked and then combined to study the sensitivity improvement with all systematic uncertainties.

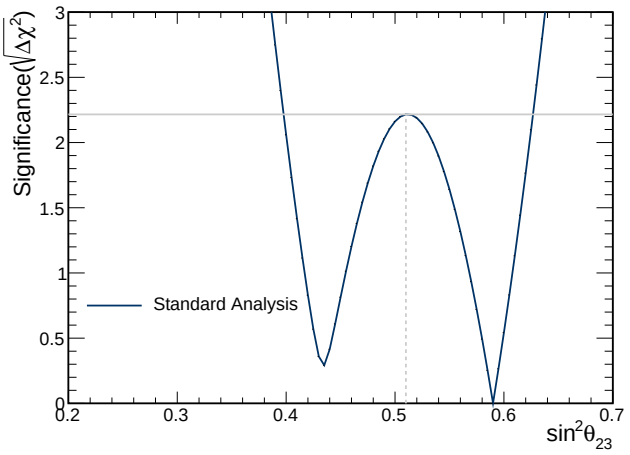

Figure 5.2: Gaussian significance $\sqrt{\Delta\chi^2}$ as a function of $\sin^2\theta_{23}$ in the standard analysis without systematic uncertainties. The $\sqrt{\Delta\chi^2}$ value at $\sin^2\theta_{23} = 0.51$ will be compared to new analysis methodologies.

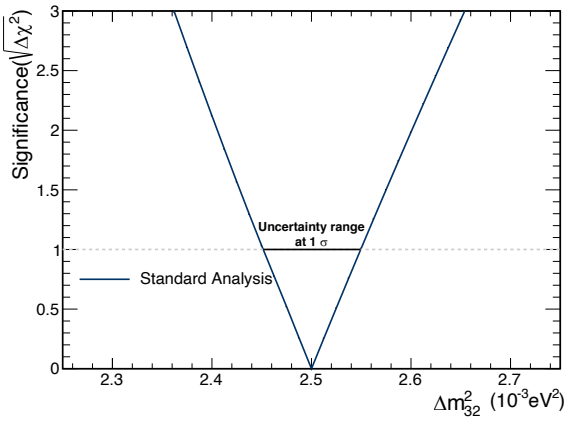

Figure 5.3: Gaussian significance $\sqrt{\Delta\chi^2}$ as a function of Δm^2_{32} in the standard analysis without systematic uncertainties. The uncertainty range at 1 σ for Δm^2_{32} shown by the black line will be used to quantify the new analysis methods.

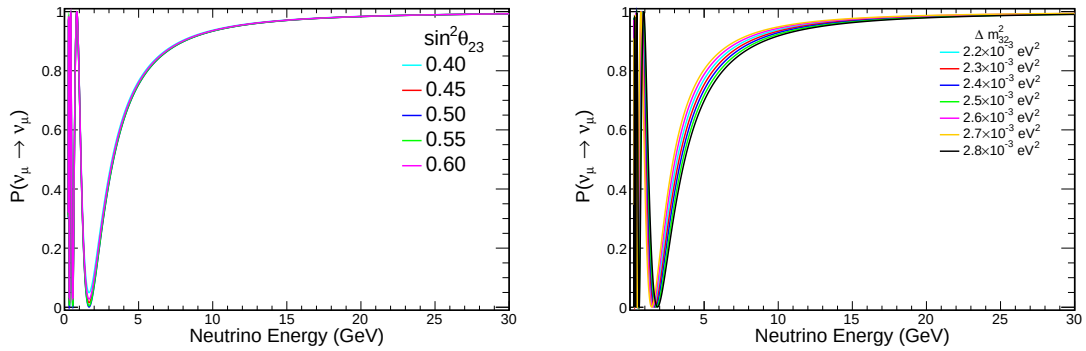

Figure 5.4: Oscillation probabilities in the 0 to 30 GeV energy region for the muon neutrino disappearance channel. $\Delta m^2_{32} = 2.5 \times 10^{-3}$ eV^2 for the left plot, and $\sin^2\theta_{23} = 0.5$ for the right plot. Different values of Δm^2_{32} or $\sin^2\theta_{23}$ are shown in different colours.

5.2 Searching for Sensitivity Gains

5.2.1 High energy event sample

NOvA's standard analysis methodology in the muon disappearance channel utilises neutrino events below 5 GeV. This section discusses the effects of high energy events in the 5 to 20 GeV region on the oscillation parameter extraction.

Figure 5.4 presents the effects of Δm^2_{32} and $\sin^2\theta_{23}$ on oscillation probabilities in the 0 to 30 GeV energy region. This figure shows Δm^2_{32} affects the probability distinctly below 20 GeV, while $\sin^2\theta_{23}$ has a small effect for the high energy region above 5 GeV. Figure 5.5 shows how Δm^2_{32} impacts the predicted reconstructed energy distribution at the FD by comparing $\Delta m^2_{32} = 2.6 \times 10^{-3}$ eV^2 and $\Delta m^2_{32} = 2.3 \times 10^{-3}$ eV^2. In the 5 - 20 GeV region, there are 187.1 and 189 events in the $\Delta m^2_{32} = 2.6 \times 10^{-3}$ eV^2 case and $\Delta m^2_{32} = 2.3 \times 10^{-3}$ eV^2 respectively. Furthermore, Figure 5.6 illustrates the tiny effect of the high energy region by the distribution of Poisson log-likelihood as a function of the reconstructed energy bin. The log-likelihood is calculated by comparing the prediction using $\Delta m^2_{32} = 2.6 \times 10^{-3}$ eV^2 to the prediction using $\Delta m^2_{32} = 2.3 \times 10^{-3}$ eV^2 with Equation 4.10 in Section 4.8, and $\sin^2\theta_{23} = 0.5$ has not been changed in the two cases. The integral of the log-likelihood over all bins is 41.2 and the integral of log-likelihood over the 5 to 20 GeV is 0.11. Thus, high energy range in 5 GeV to 20 GeV has a very tiny impact on the precision measurements. In NOvA's official oscillation analysis, a relatively narrow energy range of neutrinos below 5 GeV is used. Extending the energy range to a broad one can be an important check of the beam and detector performance, even though the higher energy sample is not able to help with the extraction of oscillation parameters.

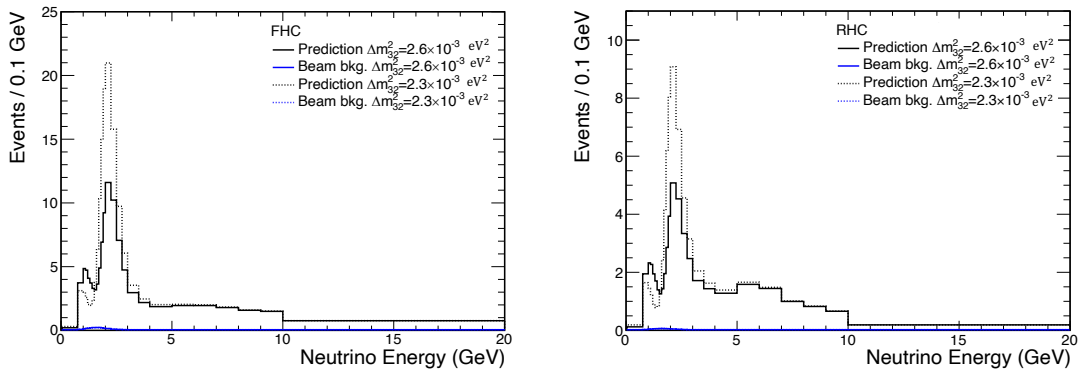

Figure 5.5: Events vs. reconstructed neutrino energy in the 0 to 20 GeV energy region at the FD in FHC and RHC without extrapolation. The dashed histogram is made with $\Delta m^2_{32} = 2.3 \times 10^{-3}$ eV^2 and the solid histogram is made with $\Delta m^2_{32} = 2.6 \times 10^{-3}$ eV^2. $\sin^2\theta_{23} = 0.5$ in both histograms. Predictions and beam backgrounds are shown in black and blue, respectively.

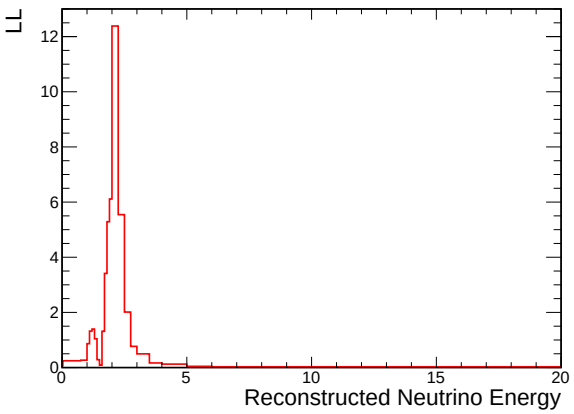

Figure 5.6: Log-likehood distribution from comparison between $\Delta m^2_{32} = 2.6 \times 10^{-3}$ eV^2 and $\Delta m^2_{32} = 2.3 \times 10^{-3}$ eV^2 in the 0 to 20 GeV energy region at the FD using FHC and RHC data without extrapolation. Here $\sin^2\theta_{23} = 0.5$ in both case, and only statistical uncertainties are considered.

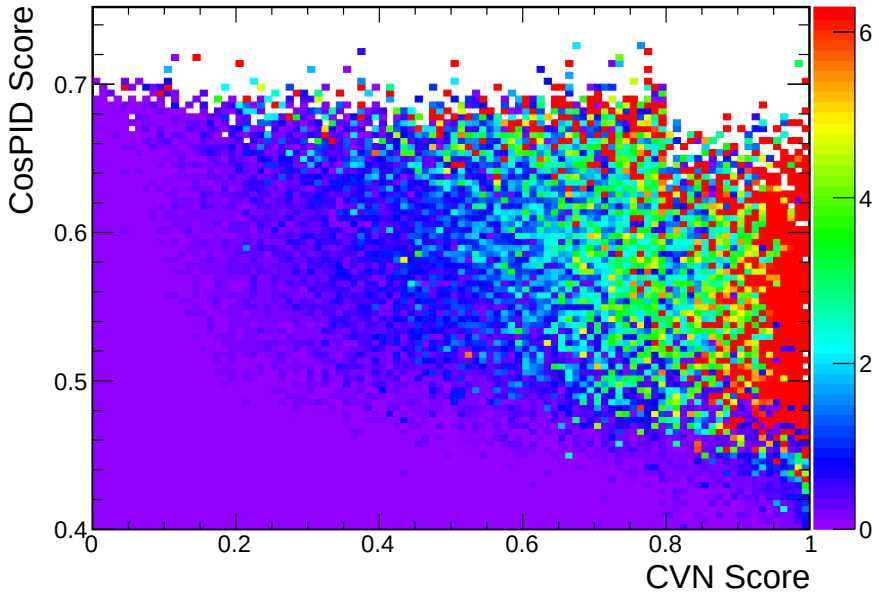

Figure 5.7: Ratio of signal to background events in the CosPID vs. CVN space with the low PID sample in the FHC mode.

A comparison of distributions of the high energy events for MC and data will be shown in Chapter 6.

5.2.2 Adding low PID samples of events

Another method to improve the sensitivity is to add in a low PID sample of events to the ν_μ analysis. There are some ν_μ CC events that can't be identified with high purity and in the NOvA standard analysis these are thrown away. These events typically look similar to neutral current events. However, there is some information that can be included to help

Subsample Index	CVN	CosPID
PID A	[0.99, 1]	[0.4, 0.8]
PID B	[0.93, 0.99]	[0.42, 0.8]
	[0.85, 0.93]	[0.45, 0.8]
PID C	[0.65, 0.85]	[0.47, 0.8]
	[0.40, 0.65]	[0.63, 0.80]
PID D	[0.40, 0.65]	[0.47, 0.63]

Table 5.1: Cuts applied to get the 4 subsamples of the low PID sample for both FHC and RHC at the FD. These cuts are applicable to the ND with the exception of the cosmic rejection score CosPID.

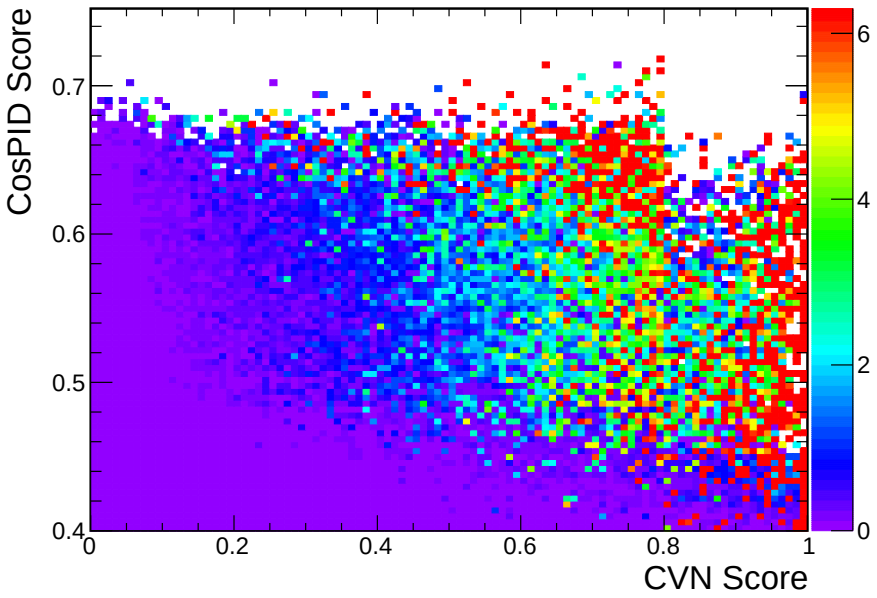

Figure 5.8: Ratio of signal to the background events in the CosPID vs. CVN space with the low PID sample in the RHC mode.

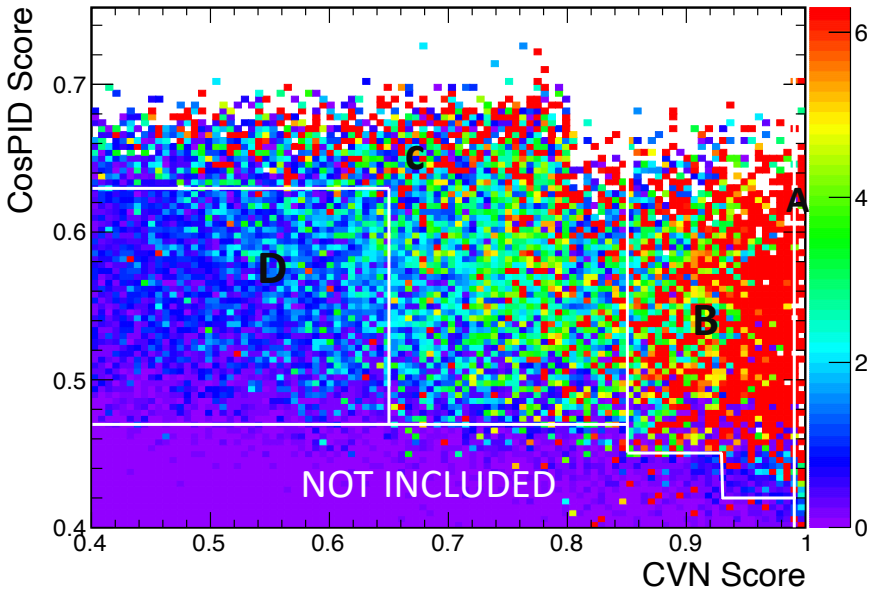

Figure 5.9: Ratio of signal to background events in the CosPID vs. CVN space in the low PID sample for events with CVN > 0.4 events in the FHC mode. The low PID sample is divided into 4 subsamples by signal purity.

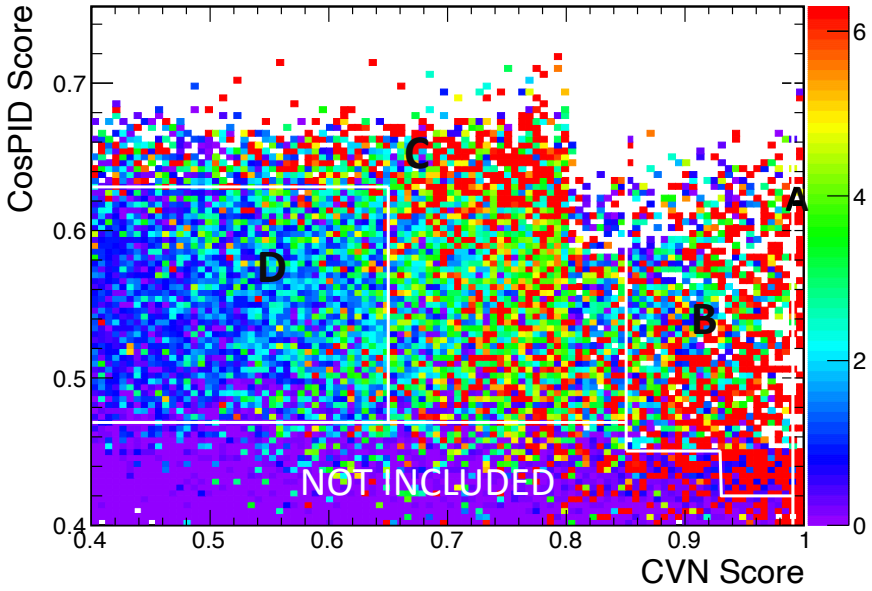

Figure 5.10: Ratio of signal to background events in the CosPID vs. CVN space in the low PID sample for events with CVN > 0.4 events in the RHC mode. The low PID sample is divided into 4 subsamples by signal purity.

	Max. disappearance (σ)	Uncertainty range at 1 σ for Δm^2_{32} (10^{-5} eV^2)
Standard analysis	2.216	9.797
low PID sample added	2.237	9.668
Sensitivity improvement	0.95%	1.32%

Table 5.2: Sensitivity improvement due to adding the low PID sample compared to the standard analysis.

	Maximal disappearance (σ)	Uncertainty range at 1 σ for Δm^2_{32} (10^{-5} eV^2)
Standard analysis	2.216	9.797
Implement the LSTM estimator in the standard analysis	2.312	9.481
Sensitivity improvement	4.32%	3.23%

Table 5.3: Sensitivity improvement when using the LSTM EE in the standard analysis.

separate signals from backgrounds. Many reconstruction variables were tested to separate signal events from the backgrounds. The best four variables are CVN (see 4.4.3), CosPID (see 4.4.3), MuonCVN (CVN on the muon prong[1]) and KalPtP (transverse momentum fraction of the muon). In order to use as few bins as possible for the new sample, the two most significant variables, CVN and CosPID, are considered. NOvA's standard sample includes those events passing the particle identification cuts CVN > 0.85, CosPID > 0.45 and ReMId > 0.3 as well as the basic quality cuts and containment cuts. The low PID sample investigates those events satisfying the basic quality cuts and the containment cuts but failing the particle identification cuts. Since this sample includes a lot of backgrounds, the most important thing is to separate the signal events. Figure 5.7 and Figure 5.8 show the distribution of the ratio of signal to background in the CosPID versus CVN space in FHC mode and RHC mode respectively. Considering that the events with CVN < 0.4 have a very low signal purity, it is reasonable to exclude those events. Figure 5.9 and Figure 5.10 show how the sample is divided into 4 subsamples based approximately on the signal purity. It should be noted that the same cut boundaries are used in the FHC and RHC. In the low CosPID regions the purity distribution in RHC is slightly different from the FHC. However, there are only a tiny number of events in that region, thus changing the boundary will not make a significant difference. Table 5.1 shows the corresponding cut boundaries of CVN and CosPID. Table 5.2 shows the sensitivity improvement from the low PID sample.

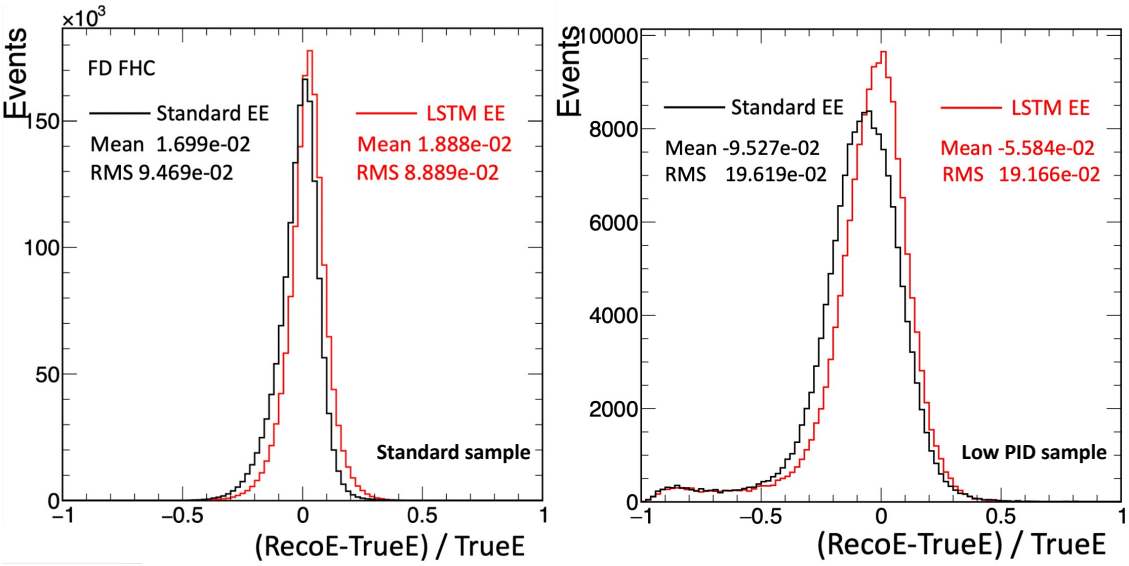

Figure 5.11: Comparison of the FD FHC muon neutrino energy resolution histograms (RecoE-TrueE)/TrueE between Standard EE and LSTM EE. In terms of RMS, LSTM EE has better energy resolution than the Standard EE: 8.9% (19.2%) vs. 9.5% (19.6%) in the standard (low PID) sample.

	Maximal disappearance (σ)	Uncertainty range at 1 σ for Δm^2_{32} (10^{-5} eV^2)
Standard analysis	2.216	9.797
Add low PID sample with LSTM EE based on the standard analysis	2.239	9.653
Sensitivity improvement	1.47%	1.03%

Table 5.4: Sensitivity improvement when adding the low PID sample with the LSTM EE applied.

5.2.3 Long Short-Term Memory (LSTM) ν_μ Energy Estimator

There have been some studies investigating the effects of ν_μ energy resolution on the sensitivity [112]. These studies indicate that the sensitivity improvement from using a better energy estimator corresponds to accumulating 20−40% of extra data. The official analysis currently uses the standard muon neutrino energy estimator (standard EE). The standard EE first takes Kalman track length and estimates muon energy from it. Then it takes detector calorimetric response of the hadronic activity and estimates the hadronic energy component of the ν_μ CC event. In the final step it sums the resulting muon and hadronic components to get the reconstructed ν_μ energy.

A limitation of this standard energy estimator is that it uses just two reconstructed variables as inputs, while it ignores information contained in multiple prong level variables (e.g. prong CVN values, prong BPF[2] variables, and other information about the event topology, etc.). To address these issues, a new energy estimator that uses both slice and prong level inputs to an LSTM neural network has been developed. The new LSTM energy estimator (LSTM EE) uses 3 different types of inputs: slice level, 2d and 3d prong level variables. As Figure 5.11 shows, the LSTM EE is able to predict ν_μ energy better than the standard EE. Table 5.3 shows sensitivity improvements when replacing the standard EE with LSTM EE in the standard analysis. Table 5.4 shows sensitivity improvements when adding a low PID sample with LSTM EE based on the standard analysis. It can be seen the LSTM EE performs well in improving the sensitivity.

Variable	Sensitivity improvement for Δm^2_{32}	Sensitivity improvement at max. disappearance
HadNHit	2.12%	4.25%
KalPtP	2.03%	4.20%
KalCosNumi	1.88%	3.89%
HadEPerNHit	1.81%	3.51%
KalTrkNPlaneGapFrac	2.09%	3.27%
NPng2d	1.73%	3.18%
NCellsEdge	1.27%	2.32%
kBPFBestMuonStartX	1.18%	2.15%
KalmanTrkStartX	1.16%	2.13%

[1] A prong is a collection of hits which correspond to a single particle candidate, coming from the vertex.

[2] BPF stands for Break Point Fitter, which is a NOvA tracking algorithm incorporating momentum reconstruction.

CVN	1.14%	2.06%
KalmanTrkStartY	1.14%	2.01%
kBPFBestMuonStartY	1.11%	1.98%
kBPFBestMuonStopX	1.09%	1.89%
kBPFBestMuonStopY	1.10%	1.88%
KalmanTrkEndX	1.07%	1.87%
KalNPlaneGapLength	1.01%	1.81%
KalmanTrkEndY	1.05%	1.80%
NumuHadCalE	0.82%	1.78%
kBPFBestMuonStopZ	1.02%	1.75%
KalmanTrkEndZ	1.01%	1.74%
kBPFBestMuonStartZ	1.00%	1.74%
KalmanTrkStartZ	1.00%	1.72%
ReMId	0.99%	1.20%
CosPID	0.97%	1.86%
MuEPerNHit	0.81%	1.43%
KalNhitLength	0.77%	1.42%
KalTrkCalE	0.85%	1.31%
NumuHadTrkE	0.67%	1.31%
KalTrkOverlapE	0.67%	1.31%
KalTrkNPlaneGap	0.61%	1.28%
scatLL	0.64%	1.25%
HadEFrac	0.58%	1.19%
KalTrkLength	0.91%	1.12%
nonHadPlaneFrac	0.60%	1.02%
KalTrkCalEPerNHit	0.51%	0.93%
MuE	0.78%	0.91%
NumuHadVisE	0.43%	0.83%
NPng3d	0.54%	0.81%
dedxLL	0.44%	0.72%
HadE	0.39%	0.71%
kNKalman	0.09%	0.16%

Table 5.5: A summary of sensitivity improvements with new binning as a function of energy and a new variable at the FD. The energy binning is the current NOvA binning, and the new variable uses 50 bins with constant bin widths.

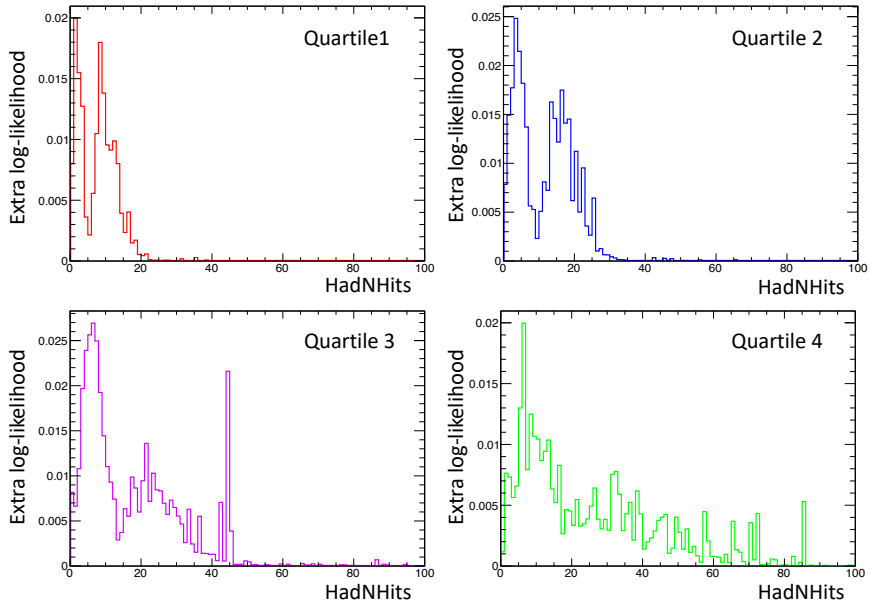

Figure 5.12: Extra log-likelihood as a function of HadNHits bin. The log-likehood is calculated from comparison between $\Delta m^2_{32} = 2.6 \times 10^{-3}$ eV^2 and $\Delta m^2_{32} = 2.3 \times 10^{-3}$ eV^2 at fixed $\sin^2\theta_{23} = 0.50$ in FHC.

5.2.4 Optimization based on the standard sample

As mentioned in Section 5.1, the standard sample refers to the analysis sample selected using NOvA's official cuts. This section discusses how to include more information from other variables in the analysis. A reconstructed neutrino event involves many variables which might help distinguish signals from backgrounds or classify the events by energy resolution. To evaluate the sensitivity improvement of each variable, binning the events as a function of neutrino energy plus another reconstructed variable was implemented. Table 5.5 shows the summary of sensitivity improvement values with the new binning involving another variable compared to the standard analysis. The definitions of those variables can be found in Appendix B. It can be seen the number of hits associated with the hadronic shower (HadNHits) has a highest performance in improving the sensitivity of Δm^2_{32} by 2.12% and the maximal mixing rejection by 4.25%. This variable is related to the hadronic energy thus it might help bin the sample by the energy resolution.

5.2.4.1 Investigation of the HadNHits binning

As presented in Table 5.5, HadNHits is the most powerful variable to improve the sensitivity when it is divided into 50 bins. But that is too many for computational reasons. This section investigates how to reduce the number of HadNHits bins. One way to determine

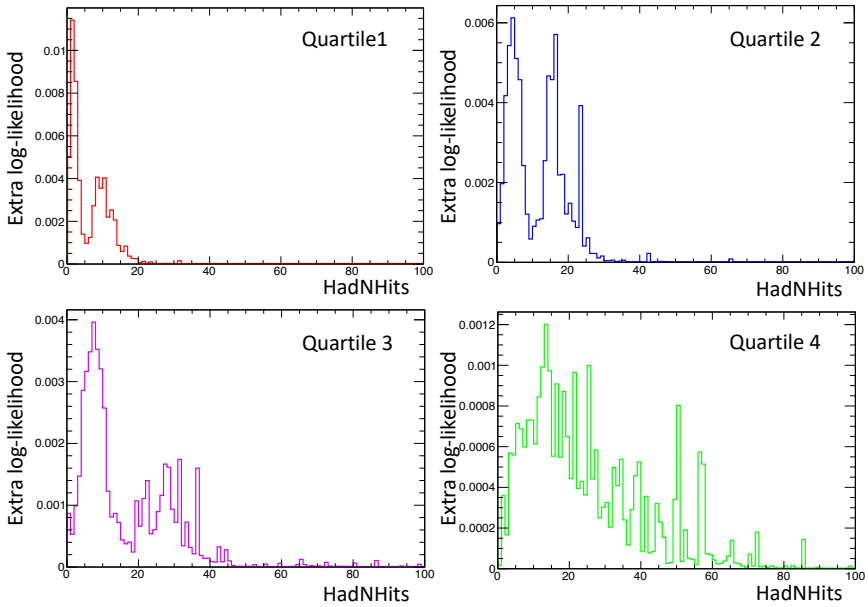

Figure 5.13: Extra log-likelihood as a function of HadNHits bin. The log-likehood is calculated from comparison between $\sin^2\theta_{23} = 0.5$ and $\sin^2\theta_{23} = 0.59$ at fixed $\Delta m^2_{32} = 2.5 \times 10^{-3}$ eV^2 in FHC.

	Quartile 1	Quartile 2	Quartile 3	Quartile 4
HadNHits bin 1	[7, 14]	[0, 7]	[0, 11]	[5, 40]
HadNHits bin 2	Others	Others	Others	Others

Table 5.6: HadNHits bin boundaries when 2 bins are used.

which bins are important is to quantify how much extra log-likelihood (extra log-likelihood refers to the log-likelihood difference between the new binning and the standard binning) each individual HadNHits bin contributes compared to the standard binning analysis. First, the distribution of HadNHits is divided into 100 bins. But they are combined into two HadNHits bins. When considering the i-th bin, the events for the i-th bin are put in the first bin and the other 99 bins are put into the second bin, which is defined as *binning method i*. Then, the log-likelihood difference between, for example, $\Delta m^2_{32} = 2.3\times10^{-3}$ eV^2 and $\Delta m^2_{32} = 2.6 \times 10^{-3}$ eV^2 with that 2-bin binning is calculated and compared with the standard analysis (which is effectively all 100 bins condensed down to 1 bin). In this way, the extra log-likelihood is defined as the log-likelihood difference between the 2-bin case and standard analysis.

Figure 5.12 and Figure 5.13 shows the distributions of extra log-likelihood from comparison between $\Delta m^2_{32} = 2.6 \times 10^{-3}$ eV^2 and $\Delta m^2_{32} = 2.3 \times 10^{-3}$ eV^2 and comparison

	Quartile 1	Quartile 2	Quartile 3	Quartile 4
HadNHits bin 1	(1,4)	(1,7)	(3,9),[44,45]	(5,14)
HadNHits bin 2	(7,14)	(13,19)	[17,29]	[0,5],[14,50)
HadNHits bin 3	Others	Others	Others	Others

Table 5.7: HadNHits bin boundaries when 3 bins are used.

	Quartile 1	Quartile 2	Quartile 3	Quartile 4
HadNHits bin 1	[0, 4]	[0, 7]	[0, 11]	[0, 5]
HadNHits bin 2	[7,14]	(13,20]	(15, 32]	(5, 30]
HadNHits bin 3	(4, 7],(14, 20]	(7, 13], (20, 30]	(30, 60]	Others
HadNHits bin 4	Others	Others	Others	Others

Table 5.8: HadNHits bin boundaries when 4 bins are used.

	Quartile 1	Quartile 2	Quartile 3	Quartile 4
HadNHits bin 1	[0, 4]	[0, 7]	[0, 11]	[0, 5]
HadNHits bin 2	(4, 7]	(7,13]	(11, 19]	(5, 14]
HadNHits bin 3	(7, 14]	(13, 19]	(19, 32]	(14, 30]
HadNHits bin 4	(14, 20]	(19, 30]	(32, 46]	(30, 60]
HadNHits bin 5	Others	Others	Others	Others

Table 5.9: HadNHits bin boundaries when 5 bins are used.

	Quartile 1	Quartile 2	Quartile 3	Quartile 4
HadNHits bin 1	[0, 1]	[0,1]	[0,3]	[0, 5]
HadNHits bin 2	(1, 4]	(1,7]	(3, 11]	(5, 14]
HadNHits bin 3	(4, 7]	(7,13]	(11, 19]	(14, 26]
HadNHits bin 4	(7,14]	(13,19)	(19, 32]	(26, 45]
HadNHits bin 5	(14, 20]	(19,25)	(32, 46]	(45, 60]
HadNHits bin 6	Others	Others	Others	Others

Table 5.10: HadNHits bin boundaries when 6 bins are used.

	Δm^2_{32} improvement at 1σ	Improvement at max. disappearance
2 HadNHits bins	0.20%	0.40%
3 HadNHits bins	1.14%	2.24%
4 HadNHits bins	1.36%	2.77%
5 HadNHits bins	1.55%	3.10%
6 HadNHits bins	1.67%	3.36%
50 HadNHits bins	2.12%	4.25%

Table 5.11: Sensitivity improvements from using the HadNHits binning in the standard sample. The improvement values are obtained by comparing to the standard analysis.

	Quartile 1	Quartile 2	Quartile 3	Quartile 4	All quartiles
Signal	50.64	49.34	50.51	52.60	203.09
Beam bkg.	0.37	0.43	0.70	2.24	3.74
Cosmic bkg.	0.35	0.35	0.84	3.43	4.97
Total prediction	51.36	50.12	52.05	58.27	211.80
$\frac{\text{Total bkg.}}{\text{Total prediction}}$	1.4%	1.56%	2.96%	9.73%	4.29%

Table 5.12: Event counts in both FHC and RHC at the FD with no extrapolation, with $\sin^2\theta_{23} = 0.59$ and $\Delta m^2_{32} = 2.5 \times 10^{-3}$ eV^2.

between $\sin^2\theta_{23} = 0.5$ and $\sin^2\theta_{23} = 0.59$ respectively. In these plots, the x-axis bin i show the *binning method i*. Table 5.6 to 5.10 show the binning methods according to the distributions of extra log-likelihood when HadNHits is divided from 2 bins to 6 bins. Table 5.11 shows the sensitivity improvements with these binning methods.

5.2.4.2 Investigation of the PID binning

This section discusses how to improve sensitivity by reducing the effects from backgrounds. Table 5.12 summarises the predicted compositions of the FD FHC sample for each individual quartile and the combination of all the quartiles. It can be found that the 3rd and 4th quartile samples contains 85% of backgrounds. To understand the effects from backgrounds, one effective way is to remove all the backgrounds using truth information and then calculate the sensitivity. Table 5.13 shows the improvement due to removing all backgrounds. It can be seen that the analysis when backgrounds are removed has 3.23%

[3]The ReMId does not use the same bin size as CosPID and CVN, since the ratio distribution fluctuates dramatically when using a small bin size.

	Maximal disappearance (σ)	Uncertainty range at 1 σ for Δm^2_{32} (10^{-5} eV^2)
Standard analysis	2.216	9.797
Remove backgrounds	2.327	9.481
Sensitivity improvement	5.02%	3.23%

Table 5.13: Sensitivity improvement when removing all backgrounds.

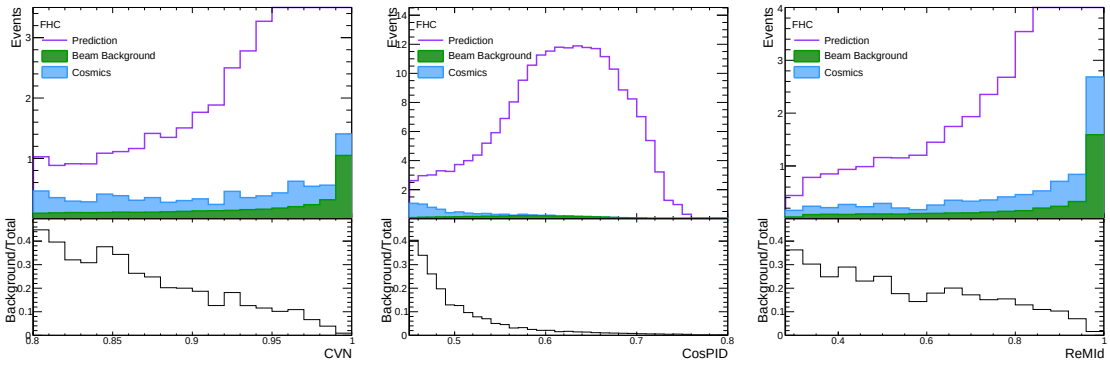

Figure 5.14: Distributions of CVN, CosPID, ReMId[3]for the combination of all the four quartiles in FHC in the FD standard sample.

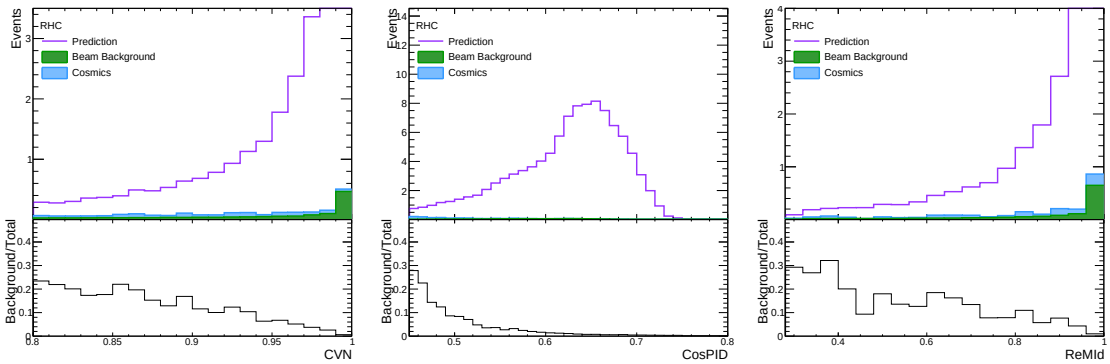

Figure 5.15: Distributions of CVN, CosPID, ReMId for the combination of all the four quartiles in RHC in the FD standard sample.

Name of cut set	Subsample name	Ratio: $\frac{\text{Background}}{\text{Prediction}}$	Cut values	Sensitivity improvement at max. disappearance	Sensitivity improvement for Δm^2_{32}
PID-a	High purity	Ratio<=0.01	CVN>= 0.99 or CosPID>= 0.68	1.79%	0.74%
	Middle purity	0.01 <Ratio<0.05	Other events		
	Low purity	Ratio>=0.05	CVN<= 0.98 or CosPID<= 0.56 or ReMId<= 0.96		
PID-b	High purity	Ratio<=0.01	CVN>= 0.99 or CosPID>= 0.68	2.0%	0.92%
	Middle purity	0.01 <Ratio<0.10	Other events		
	Low purity	Ratio>=0.10	CVN<= 0.97 or CosPID<= 0.52 or ReMId<= 0.92		
PID-c	High purity	Ratio<=0.01	CVN>= 0.99 or CosPID>= 0.68	**2.21%**	**1.09%**
	Middle purity	0.01 <Ratio<0.15	Other events		
	Low purity	Ratio>=0.15	CVN<= 0.93 or CosPID<= 0.49 or ReMId<= 0.8		
PID-d	High purity	Ratio<=0.01	CVN>= 0.99 or CosPID>= 0.68	2.16%	1.11%
	Middle purity	0.01 <Ratio<0.2	Other events		
	Low purity	Ratio>=0.2	CVN<= 0.89 or CosPID<= 0.49 or ReMId<= 0.52		
PID-e	High purity	Ratio<=0.01	CVN>= 0.99 or CosPID>= 0.68	2.17%	1.02%
	Middle purity	0.01 <Ratio<0.25	Other events		
	Low purity	Ratio>=0.25	CVN<= 0.88 or CosPID<= 0.48 or ReMId<= 0.42		
PID-f	High purity	Ratio<=0.01	CVN>= 0.99 or CosPID>= 0.68	2.06%	0.97%
	Middle purity	0.01 <Ratio<0.30	Other events		
	Low purity	Ratio>=0.30	CVN<= 0.86 or CosPID<= 0.47 or ReMId<= 0.36		
PID-g	High purity	Ratio<=0.01	CVN>= 0.99 or CosPID>= 0.68	1.87%	0.82%
	Middle purity	0.01 <Ratio<0.35	Other events		
	Low purity	Ratio>=0.35	CVN<= 0.82 or CosPID<= 0.46 or ReMId<= 0.32		

Table 5.14: Sensitivity improvements from using different PID binnings in FHC. a-g represents different sets of cuts applied to get high purity, middle purity, and low purity samples. The PID-c is chosen for the analysis in this thesis. These cuts are applicable to the ND with the exception of the cosmic rejection score CosPID.

Name of cut set	Subsample name	Ratio: $\frac{\text{Background}}{\text{Prediction}}$	Cut values	Sensitivity improvement at max. disappearance	Sensitivity improvement for Δm^2_{32}
PID-a	High purity	Ratio<=0.01	CVN>= 0.99 or CosPID>= 0.68	1.54%	0.61%
	Middle purity	0.01 <Ratio<0.05	Other events		
	Low purity	Ratio>=0.05	CVN<= 0.97 or CosPID<= 0.53 or ReMId<= 0.96		
PID-b	High purity	Ratio<=0.01	CVN>= 0.99 or CosPID>= 0.68	**1.85%**	**0.81%**
	Middle purity	0.01 <Ratio<0.10	Other events		
	Low purity	Ratio>=0.10	CVN<= 0.94 or CosPID<= 0.49 or ReMId<= 0.72		
PID-c	High purity	Ratio<=0.01	CVN>= 0.99 or CosPID>= 0.68	1.76%	0.79%
	Middle purity	0.01 <Ratio<0.15	Other events		
	Low purity	Ratio>=0.15	CVN<= 0.88 or CosPID<= 0.48 or ReMId<= 0.44		
PID-a	High purity	Ratio<=0.01	CVN>= 0.99 or CosPID>= 0.68	1.60%	0.71%
	Middle purity	0.01 <Ratio<0.20	Other events		
	Low purity	Ratio>=0.20	CVN<= 0.83 or CosPID<= 0.47 or ReMId<= 0.44		
PID-a	High purity	Ratio<=0.01	CVN>= 0.99 or CosPID>= 0.68	1.53%	0.66%
	Middle purity	0.01 <Ratio<0.25	Other events		
	Low purity	Ratio>=0.25	CosPID<= 0.46 or ReMId<= 0.49		

Table 5.15: Sensitivity improvements from using different PID binnings in RHC. a-g represents different sets of cuts applied to get high purity, middle purity, and low purity samples. The PID-b is chosen for the analysis in this thesis. These cuts are applicable to the ND with the exception of the cosmic rejection score CosPID.

	Max. disappearance (σ)	Uncertainty range at 1 σ for Δm^2_{32} (10^{-5} eV^2)
Standard analysis	2.216	9.797
Signal-separating method	2.262	9.696
Sensitivity improvement	2.07%	1.03%

Table 5.16: Sensitivity improvement from using the PID binning in the standard sample.

and 5.02% better sensitivity for Δm^2_{32} and maximal mixing rejection respectively at 1 σ than the standard analysis.

One approach is to separate neutrino events by signal purity using the three particle identifiers CVN, CosPID and ReMId (see Section 4.4.3). Figure 5.14 and Figure 5.15 shows the distribution of individual identifiers as well as the ratio between background and the total prediction in each bin in FHC and RHC, respectively. It is clear to see that the ratio between the background to the total prediction decreases with the increase of particle identification score in all the three plots. We can get a very high pure bin with a ratio less than 0.01 in the CVN>=0.99 range or CosPID<= 0.68[4]. Considering the computing time of adding lots of bins, only three PID bins are introduced, with events separated into high purity, middle purity and the worst purity samples. Table 5.14 and Table 5.15 show the sensitivity improvements using different binning methods by the ratio of background to total events for FHC and RHC respectively. For the FHC sample, the method PID-c is adopted and for the RHC sample, the method PID-b is adopted. Table 5.16 shows the sensitivity improvement with the PID binning in the standard sample.

5.2.4.3 Comparison between the PID binning and HadNHits binning

This section compares the HadNHits binning and PID binning with standard EE and LSTM EE. To investigate the sensitivity improvements for individual quartiles, the log-likelihood is calculated from comparing two Δm^2_{32} values (2.3×10^{-3} eV^2 vs. 2.6×10^{-3} eV^2) or two $\sin^2\theta_{23}$ (0.50 vs. 0.59) values for each hadronic quartile respectively. Figure 5.16 shows the log-likelihood improvement for each quartile using the HadNHits binnings with different bin numbers and PID binning, when using the standard EE. It can be seen that the HadNHits binning has advantage in quartile 1, quartile 2 and quartile 3 when the bin

[4]The ReMId cut is not applied in the high purity selection, because the sensitivity improvement will decrease with ReMId.

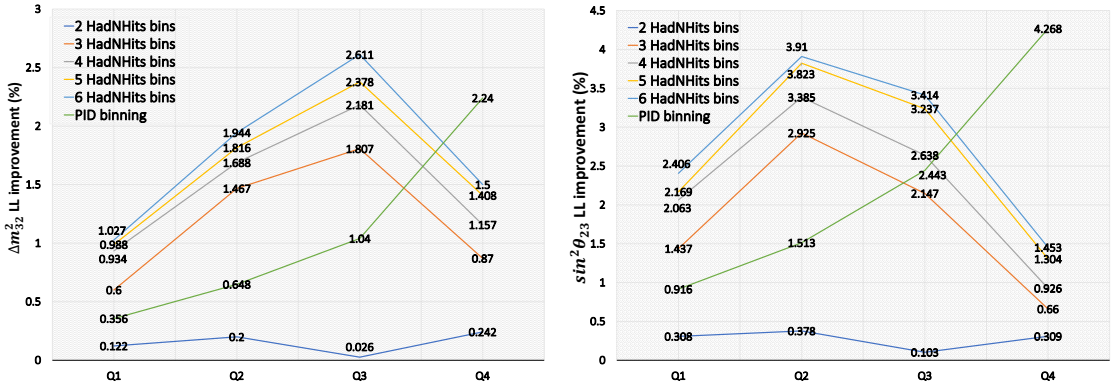

Figure 5.16: Comparison between HadNHits binnings from 2 bins to 6 bins and PID binning using the standard estimator. Left: the log-likelihood improvement in percentage calculated from comparison between $\Delta m^2_{32} = 2.3 \times 10^{-3}$ eV^2 vs. 2.6×10^{-3} eV^2 for each quartile. Right: the log-likelihood improvement in percentage calculated from comparison between $\sin^2\theta_{23} = 0.5$ vs. $\sin^2\theta_{23} = 0.59$ for each quartile.

number is greater than 2 and the PID binning has advantage in quartile 4.

Figure 5.17 shows a comparison of log-likelihood improvements for each quartile using the PID binning and HadNHits binning, when using the LSTM EE. It can be seen that the PID binning can provide a better sensitivity compared to 6 HadNHits bins in the standard sample when using LSTM. This also suggests that there might be an overlap between LSTM and HadNHits in improving the sensitivity. That is because HadNHits is a variable from the hadronic part thus it is related to the energy resolution. Therefore the PID binning combined with the LSTM EE will be applied to a new analysis. There are two reasons for getting rid of the HadNHits method. First, the HadNHits binning does not help a lot when using the LSTM estimator. Second, it is important to avoid too many bins, though the combination of HadNHits and PID methods could gain more improvements.

5.2.5 Energy binning

So far, different methods including low PID sample, LSTM, and PID binning have been chosen to improve the sensitivity. The final investigation for sensitivity improvement is to explore if a finer energy binning can help. NOvA's standard analysis uses the energy binning shown in Section 4.5.2, which has 19 bins.

For the standard sample, a finer energy binning should not contain too many more bins since the PID and hadronic energy quartile bins already contribute a lot of bins. For this reason, the first step is to test a finer binning including constant bin width of

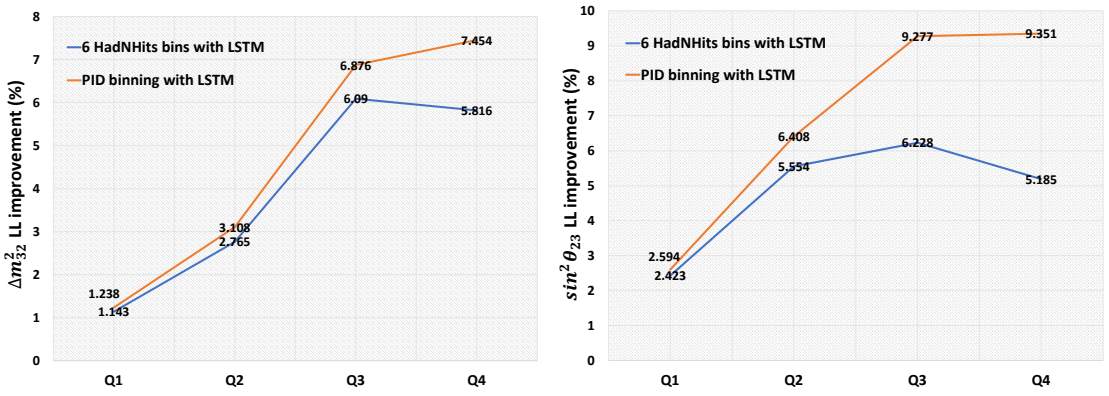

Figure 5.17: Comparison of Log-likelihood improvement in percentage for each hadronic energy fraction quartile between 6 HadNHits bins in orange and PID binning in blue using the LSTM estimator. Left: the log-likelihood improvement calculated from comparison between $\Delta m^2_{32} = 2.3 \times 10^{-3}$ eV^2 vs. 2.6×10^{-3} eV^2. Right: the log-likelihood improvement calculated from comparison between $\sin^2\theta_{23} = 0.5$ vs. $\sin^2\theta_{23} = 0.59$.

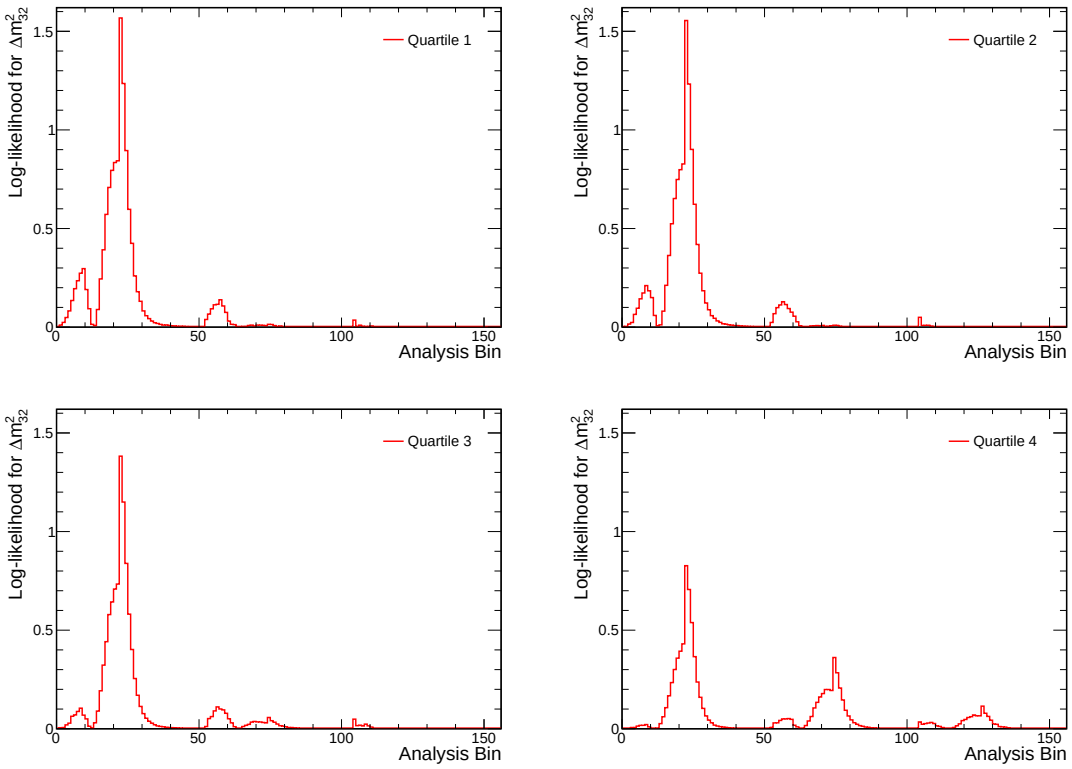

Figure 5.18: Log-likehood distribution from comparison between $\Delta m^2_{32} = 2.6 \times 10^{-3}$ eV^2 and $\Delta m^2_{32} = 2.3 \times 10^{-3}$ eV^2 for each quartile for the standard sample in the new analysis method but using 52 energy bins at the FD using FHC. Here $\sin^2\theta_{23} = 0.5$ in both case, and only statistics is considered. The first 52 bins shows the first bin of the PID bins, bins 53-104 correspond to PID bin 2 and bins 105-156 correspond to PID bin 3.

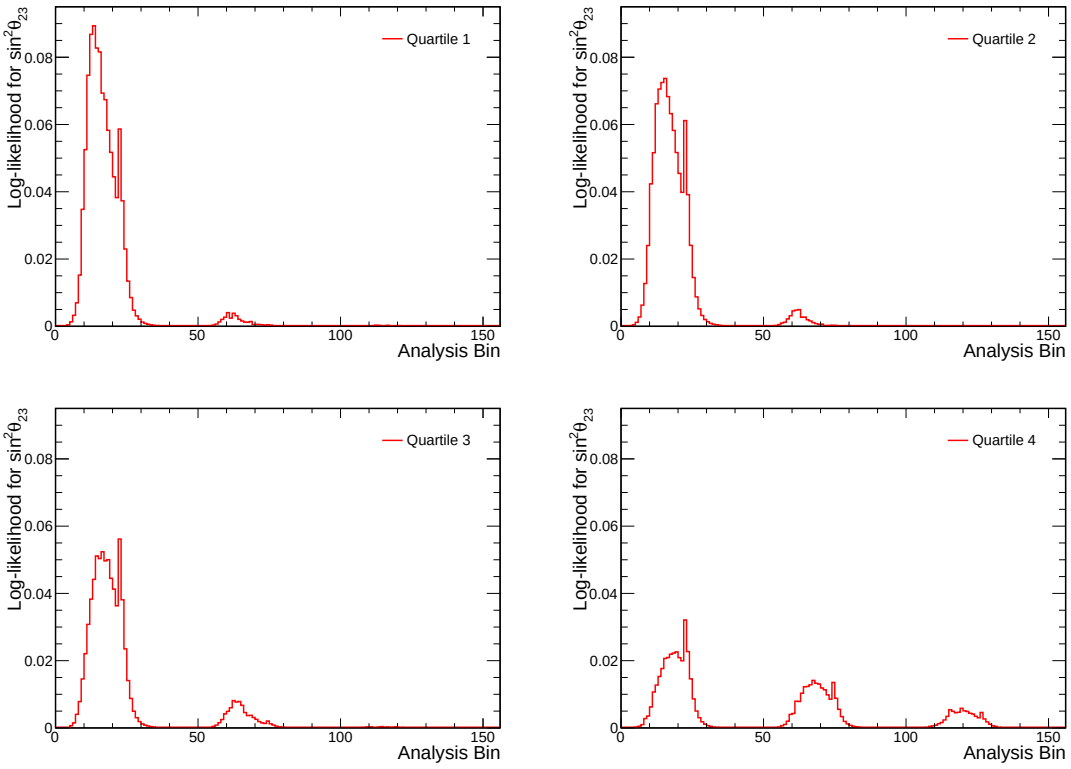

Figure 5.19: Log-likehood distribution from comparison between $\sin^2\theta_{23} = 0.5$ vs. $\sin^2\theta_{23} = 0.59$ for each quartile for the standard sample with the new analysis method but using 52 energy bins at the FD using FHC. Here $\Delta m^2_{32} = 2.5 \times 10^{-3}$ eV^2 in both case, and only statistics is considered. The first 52 bins shows the first bin of the PID bins, bins 53-104 correspond to PID bin 2 and bins 105-156 correspond to PID bin 3.

	Sensitivity improvement at max. disappearance	Sensitivity of Δm^2_{32} improvement
Official energy binning (with PID binning)	2.07%	1.03%
28 energy bins (with PID binning)	3.01%	1.42%
30 energy bins (with PID binning)	3.07%	1.53%
33 energy bins (with PID binning)	3.09%	1.55%
40 energy bins (with PID binning)	3.09%	1.56%
52 energy bins (with PID binning)	3.09%	1.57%

Table 5.17: Sensitivity improvement from using fine energy binnings and PID binning in the standard sample. The standard energy estimator is used.

	Sensitivity improvement at max. disappearance	Sensitivity of Δm^2_{32} improvement
Official energy binning (with PID binning)	6.78%	3.66%
28 energy bins (with PID binning)	7.30%	4.01%
30 energy bins (with PID binning)	7.90%	4.19%
33 energy bins (with PID binning)	7.91%	4.21%
40 energy bins (with PID binning)	7.91%	4.23%
52 energy bins (with PID binning)	7.91%	4.23%

Table 5.18: Sensitivity improvement from using fine energy binnings and PID binning in the standard sample. The LSTM energy estimator is used.

0.05 GeV in the 1-2 GeV region and constant bin width of 0.1 GeV in the 2.0-5.0 GeV. Figure 5.18 shows the distribution of Poisson log-likelihood difference from comparison between $\Delta m^2_{32} = 2.6 \times 10^{-3}$ eV^2 and $\Delta m^2_{32} = 2.3 \times 10^{-3}$ eV^2 as a function of the analysis bin in the FHC, while Figure 5.19 shows the distribution of Poisson log-likelihood from comparison between $\sin^2\theta_{23} = 0.5$ vs. $\sin^2\theta_{23} = 0.59$ as a function of the analysis bin in each quartile in the FHC. The RHC plots are not shown because the RHC has a similar behaviour as FHC. The second step is to reduce bins as much as possible based on the 52 binning. The bins in the 3.7-5 GeV region can be merged into one bin since the contribution from that region is very tiny. This merge results in 40 bins with the following boundaries in GeV: (0, 0.75, 1.05, 1.10, 1.15, 1.20, 1.25, 1.30, 1.35, 1.40, 1.45, 1.50, 1.55, 1.60, 1.65, 1.70, 1.75, 1.80, 1.85, 1.90, 1.95, 2.0, 2.1, 2.2, 2.3, 2.4, 2.5, 2.6, 2.7, 2.8, 2.9, 3.0, 3.1, 3.2, 3.3, 3.4, 3.5, 3.6, 3.7, 5). In a similar way, based on the 40 bins, merging the bins in the 3.3-3.7 GeV and bins in 3.0-3.3 GeV and 2.7-3.0 GeV generates 33 bins (0, 0.75, 1.05, 1.10, 1.15, 1.20, 1.25, 1.30, 1.35, 1.40, 1.45, 1.50, 1.55, 1.60, 1.65, 1.70, 1.75, 1.80, 1.85, 1.90, 1.95, 2.0, 2.1, 2.2, 2.3, 2.4, 2.5, 2.6, 2.7, 3.0, 3.3, 3.7, 5). Doing a further reduction obtains a binning with 30 bins (0, 0.75, 1.05, 1.10, 1.15, 1.20, 1.25, 1.30, 1.35, 1.40, 1.45, 1.50, 1.55, 1.60, 1.65, 1.70, 1.75, 1.80, 1.85, 1.90, 1.95, 2.0, 2.1, 2.2, 2.3, 2.4, 2.6, 2.8, 3.3, 3.8, 5.0). This section will not further reduce the number of bins, since the bins below 2.6 GeV contribute an obvious effect to sensitivity. Table 5.17 shows a comparison of sensitivity among 52 bins, 40 bins, 33 bins, 30 bins and the official energy binning, with the standard energy estimator. Table 5.18 shows the same thing but with the LSTM energy estimator. In this table, all the energy binning methods are compared to the standard analysis. From the table, it can be seen that although a finer energy binning might provide a better sensitivity, 30 is a better choice to avoid too many bins.

For the low PID sample, a finer energy binning with 100 bins of constant bin width has been attempted. This finer binning in combination with the LSTM EE improves the sensitivity by 1.05% for $\sin^2\theta_{23}$ and 1.53% for Δm^2_{32}. Comparing these numbers to those in Table 5.4, the improvement is not significant. Hence, in the remainder of the thesis, the current official energy binning will be used for the low PID sample.

5.2.6 Summary of Analysis Improvement Methods and their Combination

Section 5.2.1 through Section 5.2.5 has represented different methods that were investigated to improve the sensitivity of the ν_μ disappearance channel. First, the investigation on

	Analysis method	Sensitivity improvement at max. disappearance	Sensitivity of Δm^2_{32} improvement
Standard energy estimator	Add low PID sample	0.95%	1.32%
	PID binning in std. sample	2.07%	1.03%
	PID binning in std. sample; fine energy binning in std. sample	3.07%	1.53%
	PID in std. sample; fine energy binning in std. sample; add low PID sample	4.0%	2.79%
LSTM estimator	Add low PID sample	1.47%	1.03%
	Only replace the std. EE with LSTM in std. analysis	4.32%	3.23%
	PID binning in std. sample	6.78%	3.72%
	PID binning in std. sample; fine energy binning in std. sample	7.9%	4.19%
	PID in std. sample; fine energy binning in std. sample; add low PID sample	8.85%	5.48%

Table 5.19: A summary of sensitivity improvements with different improvement methods.

the high energy sample illustrates the tiny sensitivity improvement from including the 5 GeV to 30 GeV neutrinos and so that event sample can be ignored. Second, Section 5.2.3 has shown that the LSTM energy estimator is worth investigating since it has a better energy resolution than the standard energy estimator. Third, Section 5.2.4 discusses how to improve the sensitivity of the standard sample. The goal of this section is to include information from other reconstructed variables based on the current analysis binning. For the standard sample, variable HadNHits provides a good performance in improving sensitivities. Binning events by signal purity using multiple particle identifiers (PID binning) also provides improved sensitivity, even if a CVN, ReMId or CosPID on their own are not able to improve the sensitivity significantly. After comparing the HadNHits and PID binning with the standard EE and LSTM EE, it was found that the PID binning combined with the LSTM provides the best improvement. Table 5.19 summarises the analysis improvement of each analysis methodology. As can be seen, PID binning, the low PID sample and the LSTM energy estimator combined provide the greatest sensitivity improvement and will be applied to the new analysis.

5.3 Full sensitivity calculations

This section presents the results of full sensitivity calculations with the optimised "new analysis". The following new components are added: an additional low PID sample, the new energy estimator LSTM in both the standard and low PID sample, PID binning in the standard sample, and a new energy binning in the standard sample discussed in Section 5.2. It should be noted that the sensitivity results in Section 5.2 only used the FD simulation files to save computing time since we need to investigate a lot of methods. However this section uses the extrapolation method which uses real ND data to predict the FD predictions. Furthermore, the oscillation fit results obtained by applying all the systematic uncertainties will be compared to the standard analysis.

5.3.1 Sensitivity in Oscillation Parameter Space

This section show the comparison of sensitivity for the standard analysis and the new analysis with and without accounting for systematic uncertainties. Figure 5.20 shows the contour of constant $\Delta\chi^2$ in the Δm^2_{32} versus $\sin^2\theta_{23}$ space when only considering the statistical uncertainty. The $\Delta\chi^2$ is obtained by global minimum χ^2 subtracted from the minimum χ^2 at that fit point in the oscillation parameter space. The minimum χ^2 is close to zero when using the fake data. The $\Delta\chi^2$ for each point in the 2D surface is calculated by changing the values of Δm^2_{32} and $\sin^2\theta_{23}$ while profiling for the other oscillation parameters. It can be seen the constraints on Δm^2_{32} and $\sin^2\theta_{23}$ are tighter when using the new analysis. Figure 5.21 and Figure 5.22 show the 1D Gaussian significance $\sqrt{\Delta\chi^2}$ separately for Δm^2_{32} and $\sin^2\theta_{23}$, respectively. In the 1D plot of significance versus Δm^2_{32}, the uncertainty range at 1 σ for the new analysis has shrunk 6.1% compared to the standard analysis. In Figure 5.22, the 1D plot of significance for $\sin^2\theta_{23}$ shows the new analysis increases the rejection of maximal disappearance from 2.26 σ to 2.48 σ, corresponding to an improvement of 9.7%. Figure 5.23, Figure 5.24 and Figure 5.25 show similar sensitivity comparison contours and 1D significance curves but with systematic uncertainties also included. In these plots, systematic uncertainty parameters are profiled over. Similar to the case without systematic uncertainties, the constraints in the contour plot are tighter with the new analysis. From the 1D plots, the uncertainty range at 1 σ for Δm^2_{23} is 5.5% smaller than the standard analysis, and new analysis improves the significance at maximal disappearance point by 7.7% with systematics. In brief, the sensitivity improvements of the new analysis are slightly changed when doing a full sensitivity calculation that includes both extrapolation and systematic uncertainties.

5.3.2 Systematic Uncertainty

Section 4.7 has introduced a lot of systematic uncertainty sources which are applied in the oscillation fit. The effect of a systematic uncertainty on the parameter measurement is calculated according to the difference between two separate fits. The first method only takes the statistical uncertainty into account, while the second method considers both the statistical and systematic uncertainties. The systematic uncertainty on the parameter measurement is obtained from subtraction in quadrature between two fit values of the oscillation parameter at the 68% C.L. boundary. The systematic uncertainties are classified into seven categories: Detector Calibration, Neutrino Cross Section, Detector Response, Near-Far Uncorrelation, Neutron Uncertainty, Beam Flux, and Lepton Reconstruction. As shown before, the new energy estimator LSTM has been adopted into the new analysis methodology in this thesis. However, the LSTM estimator hasn't covered the energy calibration, muon energy uncertainty and neutron uncertainties in a proper way. In order to make a comparison between the new analysis and the 2020 NOvA analysis, this thesis has developed new corresponding systematic uncertainties for the LSTM estimator, which are shown as follows:

- **Energy Uncertainty:** this change consists of the "correlated" (the ND and FD are shifted in the same direction) and "uncorrelated" (the ND and the FD are shifted in opposite directions) uncertainties. In order to approach the shift of the official calibration, the hadronic energy from the LSTM estimator is shifted by $\pm 5\%$.

- **Muon uncertainty:** the muon energy uncertainty is simplified to be just a correlated 1% shift.

- **Neutron Uncertainty:** this uncertainty is obtained according to how much it changes the standard energy variables. If the standard hadronic energy changes by $x\%$ for a particular event then the LSTM hadronic energy is changed by $x\%$.

The contribution of each systematic uncertainty and all systematic uncertainties on the parameter measurements can be quantified. Figure 5.26 and Figure 5.27 show the effect of each systematic category for both the standard and the improved analysis on the measurement of Δm^2_{32} and $\sin^2\theta_{23}$, respectively. Figure 5.28 and Figure 5.29 show the effect of each individual systematic uncertainty on the measurement of Δm^2_{32} and $\sin^2\theta_{23}$ respectively. One of the important goals of making these plots is to examine the new systematic uncertainties for the LSTM estimator, including the calibration uncertainty

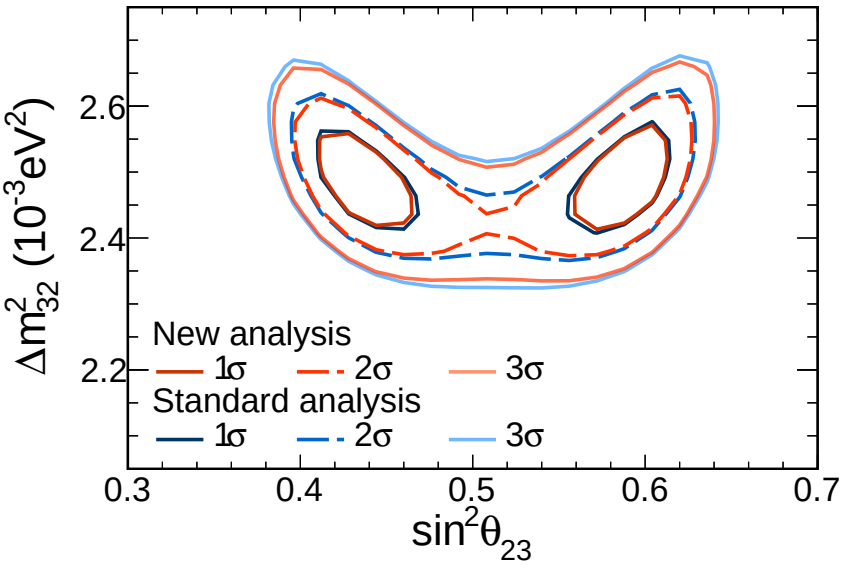

Figure 5.20: The 1σ, 2σ and 3σ contours in Δm^2_{32} vs. $\sin^2\theta_{23}$ without considering systematic uncertainties.

(classified into "Detector Calibration"), muon energy uncertainty (classified into "Lepton Reconstruction") and neutron uncertainty ("Neutron Uncertainty").

Figure 5.26 and Figure 5.27 show the comparison of systematic uncertainty between the new analysis and the standard analysis. In both cases, "Detector Calibration" and "Neutron Uncertainty" have larger effects on $\sin^2\theta_{23}$ and Δm^2_{32} than other systematic uncertainties. In the uncertainty plot for Δm^2_{32}, the new analysis and the standard analysis have a comparable size in the total systematic error. For the $\sin^2\theta_{23}$ chart, the calibration is smaller than the standard analysis. This difference might come from the increase of analysis bins. The total systematic uncertainty is slightly smaller than the standard analysis. The new systematic uncertainties seem to work well although there are some differences. Finally, it also can be seen that, as expected, the new analysis methodology decreases the effects of the statistical uncertainty. This comes from the new energy estimator, that improves the energy resolution, binning method, that reduces the background effects and the additional low PID sample, that provides more signal events.

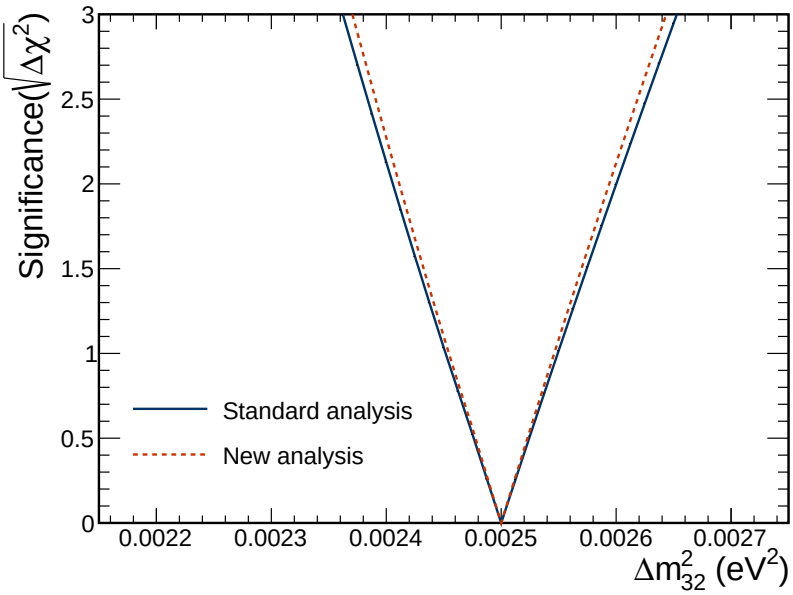

Figure 5.21: Significance plotted as a function of Δm^2_{32} for the true value $\Delta m^2_{32} = 2.5 \times 10^{-3}$ eV^2 without systematic uncertainties. Blue curve shows the standard analysis, while the red curve shows the new analysis methods.

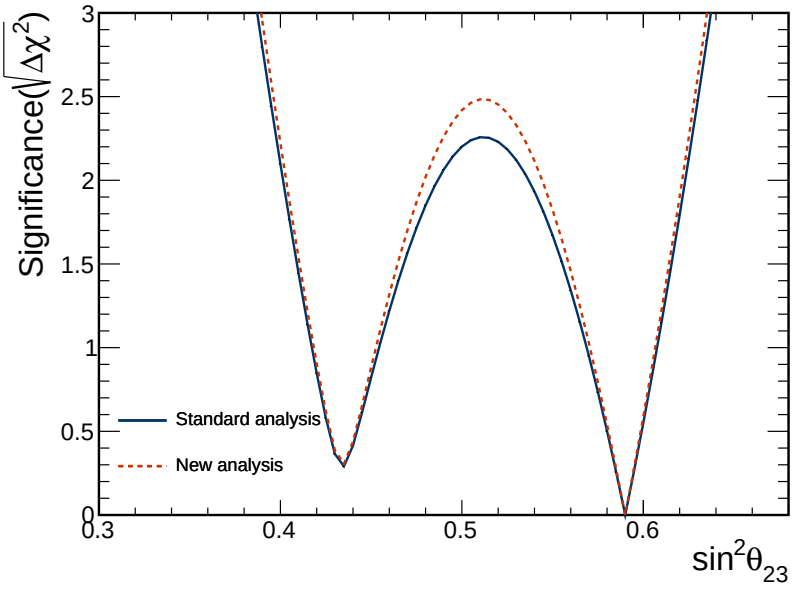

Figure 5.22: Significance plotted as a function of $\sin^2\theta_{23}$ for the true value $\sin^2\theta_{23} = 0.59$ without systematic uncertainties. Blue curve shows the standard analysis, while the red curve shows the new analysis methods.

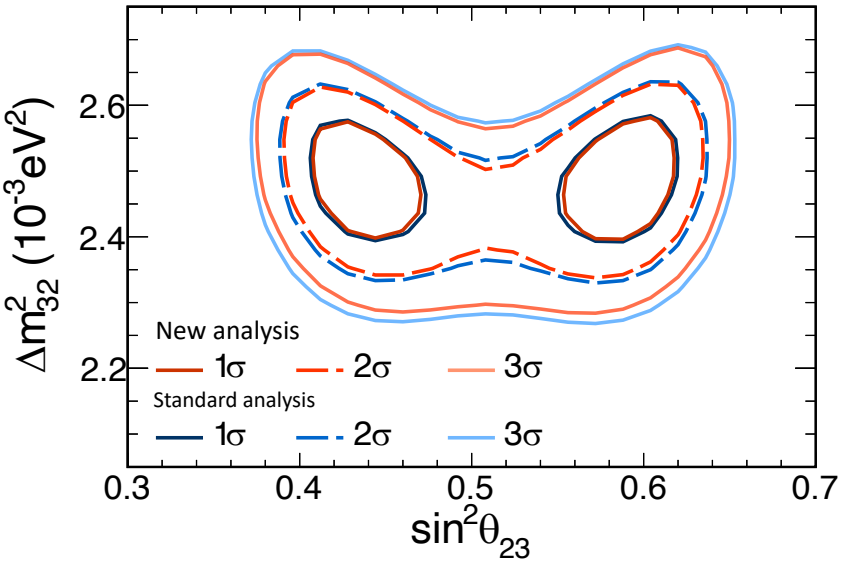

Figure 5.23: The 1σ, 2σ and 3σ contours in Δm^2_{32} vs. $\sin^2\theta_{23}$ with considering all the systematic uncertainties.

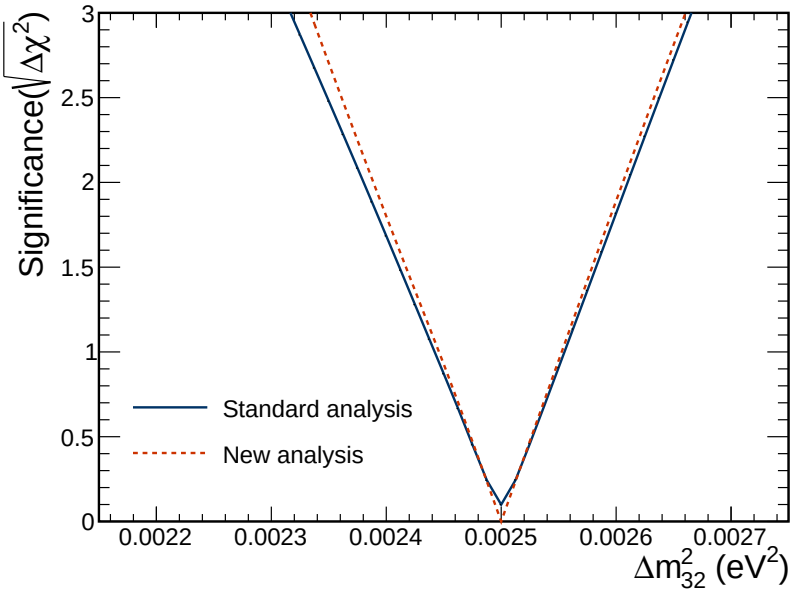

Figure 5.24: Significance plotted as a function of Δm^2_{32} for the true value $\Delta m^2_{32} = 2.5 \times 10^{-3}$ eV^2 with all systematic uncertainties included. Blue curve shows the standard analysis, while the red curve shows the new analysis methods.

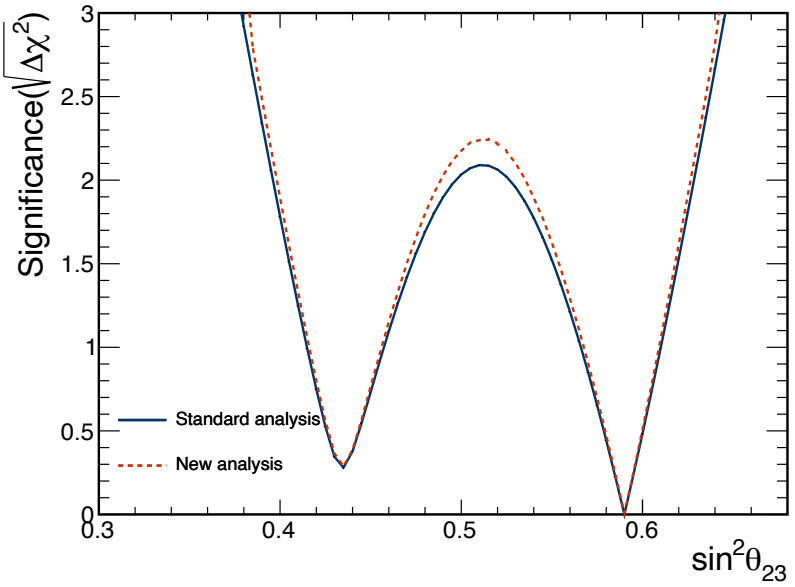

Figure 5.25: Significance plotted as a function of $\sin^2\theta_{23}$ for the true value $\sin^2\theta_{23} = 0.59$ with all systematic uncertainties included. Blue curve shows the standard analysis, while the red curve shows the new analysis methods.

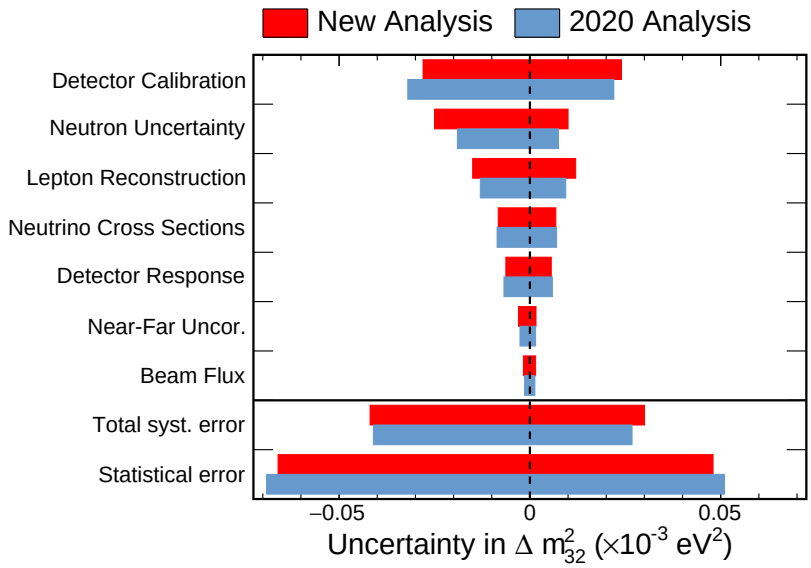

Figure 5.26: The simulated contribution of each category of systematic uncertainty and statistical uncertainty on Δm^2_{32}. The new analysis (red) is compared to the standard analysis (blue).

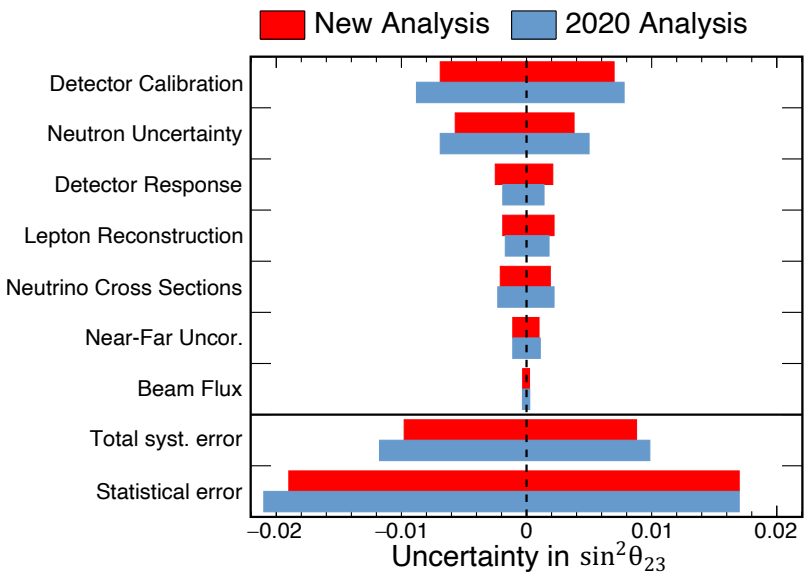

Figure 5.27: The simulated contribution of each category of systematic uncertainty and statistical uncertainty on $\sin^2\theta_{23}$. The new analysis (red) is compared to the standard analysis (blue).

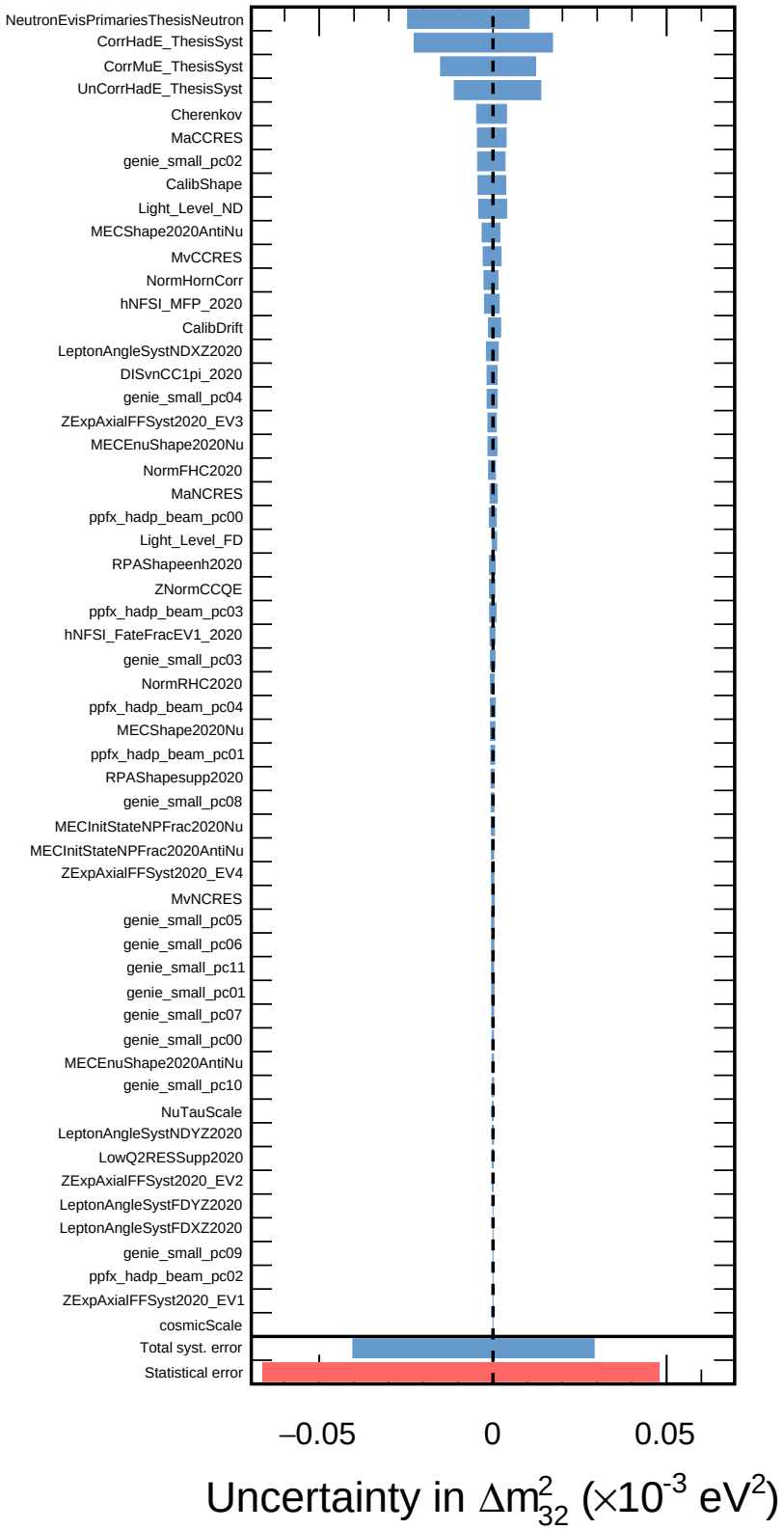

Figure 5.28: Simulated contributions of each systematic uncertainty and statistical uncertainty on Δm^2_{32} in the new analysis.

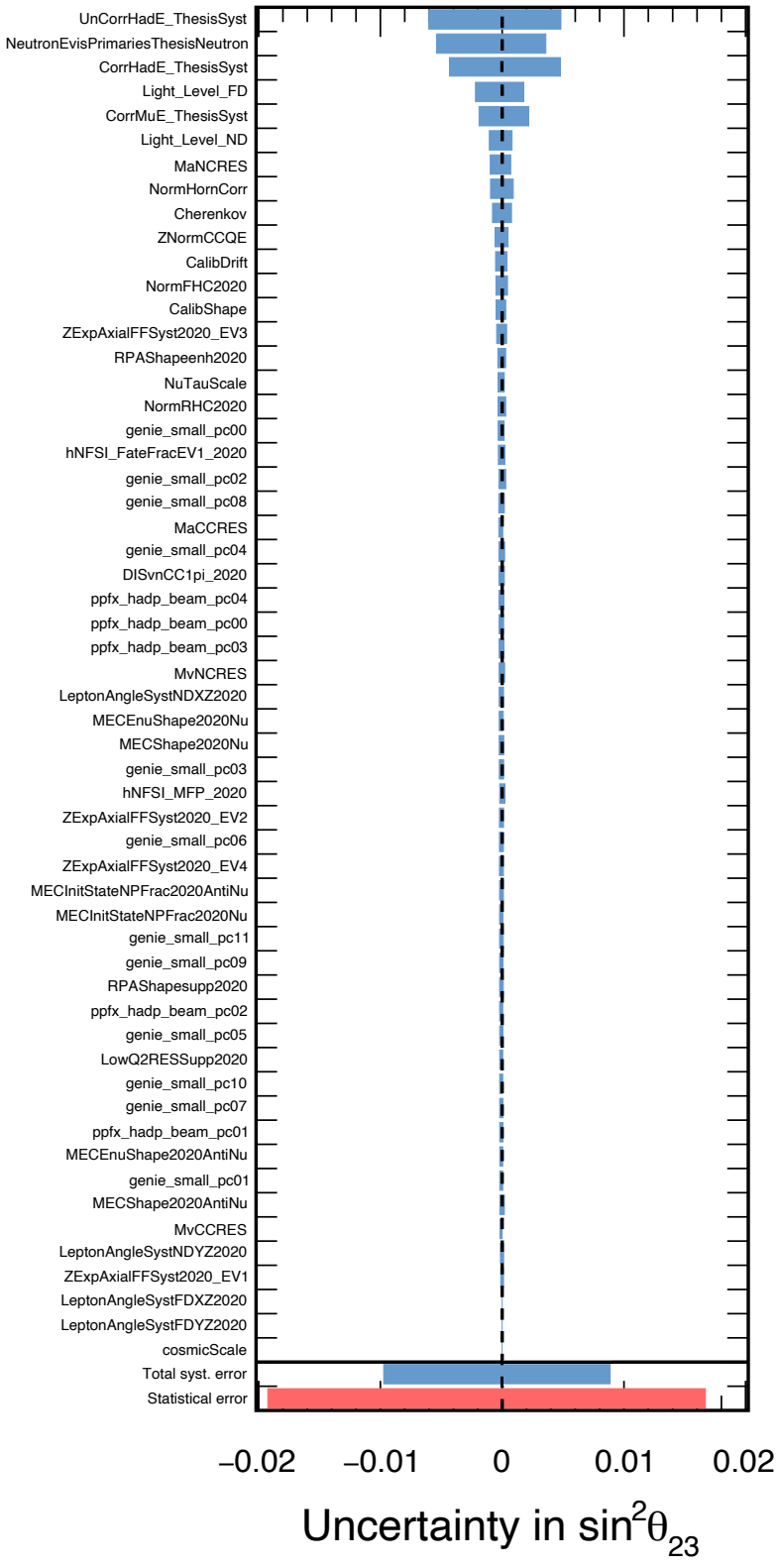

Figure 5.29: Simulated contributions of each systematic uncertainty and statistical uncertainty on $\sin^2\theta_{23}$ in the new analysis.

Chapter 6

Results

This chapter presents the results from an improved analysis of ν_μ and $\bar{\nu}_\mu$ disappearance with NOvA's 2020 dataset. The improvements presented in Chapter 5 based on the basic analysis methodology presented in Chapter 4 are used. In this analysis, the oscillation parameters are extracted through a new fit of the far detector data performed with the above improvement methods. The dataset used for this analysis corresponds to an exposure of 12.50×10^{20} protons on target (POT) in the antineutrino beam mode recorded between June 29, 2016 to February 26, 2019, and 13.60×10^{20} protons on target (POT) in the neutrino beam mode recorded between February 6, 2014 to March 20, 2020.

This chapter shows the comparison of the near detector data and simulation in Section 6.1. Distributions of several variables are chosen to verify the agreement between data and MC in the ND in the standard and low PID samples. Section 6.2 presents the best fit values of oscillation parameters and systematic uncertainties, tables of event counts, spectra in different variables for the FD and oscillation parameter constraint contours in $\Delta\chi^2$ space.

6.1 Studies at the Near Detector

It is significant and necessary to verify the agreement between data and MC at the near detector before doing the oscillation fit at the far detector. This section only shows the near detector distributions of some representative reconstructed variables related to energy: reconstructed neutrino energy, reconstructed muon energy, reconstructed hadronic energy, hadronic energy fraction. The distributions of other variables, CVN muon identification score, ReMId muon identification score, $\cos\theta_{\text{NuMI}}$ (where θ_{NuMI} is the angle of the muon track with respect to the beam direction), transverse momentum, transverse momentum

fraction, Kalman track length, number of hits of the Kalman track and number of hits in slice, will be shown in Appendix B.

In the standard sample, as shown in Table 5.14 and Table 5.15 in Chapter 5, the selected candidates at the ND are split into 12 sub-samples (four quartile bins times three particle identification bins). Figure 6.1 and Figure 6.2 show the distributions of muon neutrino and antineutrino energy respectively. For each sub-sample plot, to match the data, the MC is scaled by a factor in percentage up or down shown on the plot using an area normalisation. These plots effectively show the systematic uncertainties that affect the shape of the distributions. The systematic uncertainties relating to normalisation are applied during the extrapolation process. Figure 6.3 through Figure 6.8 show the ND distributions of those variables related to energy listed above. Distributions of other variables as an important cross check are shown in Figure B.1 through Figure B.16 in Appendix B. In these plots, both data and MC are normalised to one to make all the distributions are visible. It can be seen that the MC and data have a good agreement. The slight disagreements in Quartile 2 PID 1 in the neutrino energy plot and Quartile 3 PID 1 in the antineutrino energy plot are acceptable. In addition, the signal and background distributions behave as expected. In the Quartile 1 sample, which includes the best resolution events, PID 1 has much more events than PID 2 and PID 3. The Quartile 2 and Quartile 3 samples have a similar behaviour. However, in the Quartile 4 sample, which has the worst energy resolution, PID 2 and PID 3 have more events than PID 1. It also can be seen that most of the backgrounds come from the Quartile 4 sample.

In the low PID sample, Figure 6.9 through Figure 6.12 in this section and Figure B.17 through Figure B.24 in Appendix B show the distributions of the variables of interest. As illustrated in Table 5.1 in Chapter 5, the selected candidates in the low PID sample is split into 4 sub-samples according to the CVN values. All the plots show a good agreement between the MC and data. These plots indicate the sample with high CVN values has less background than the sample with low CVN values.

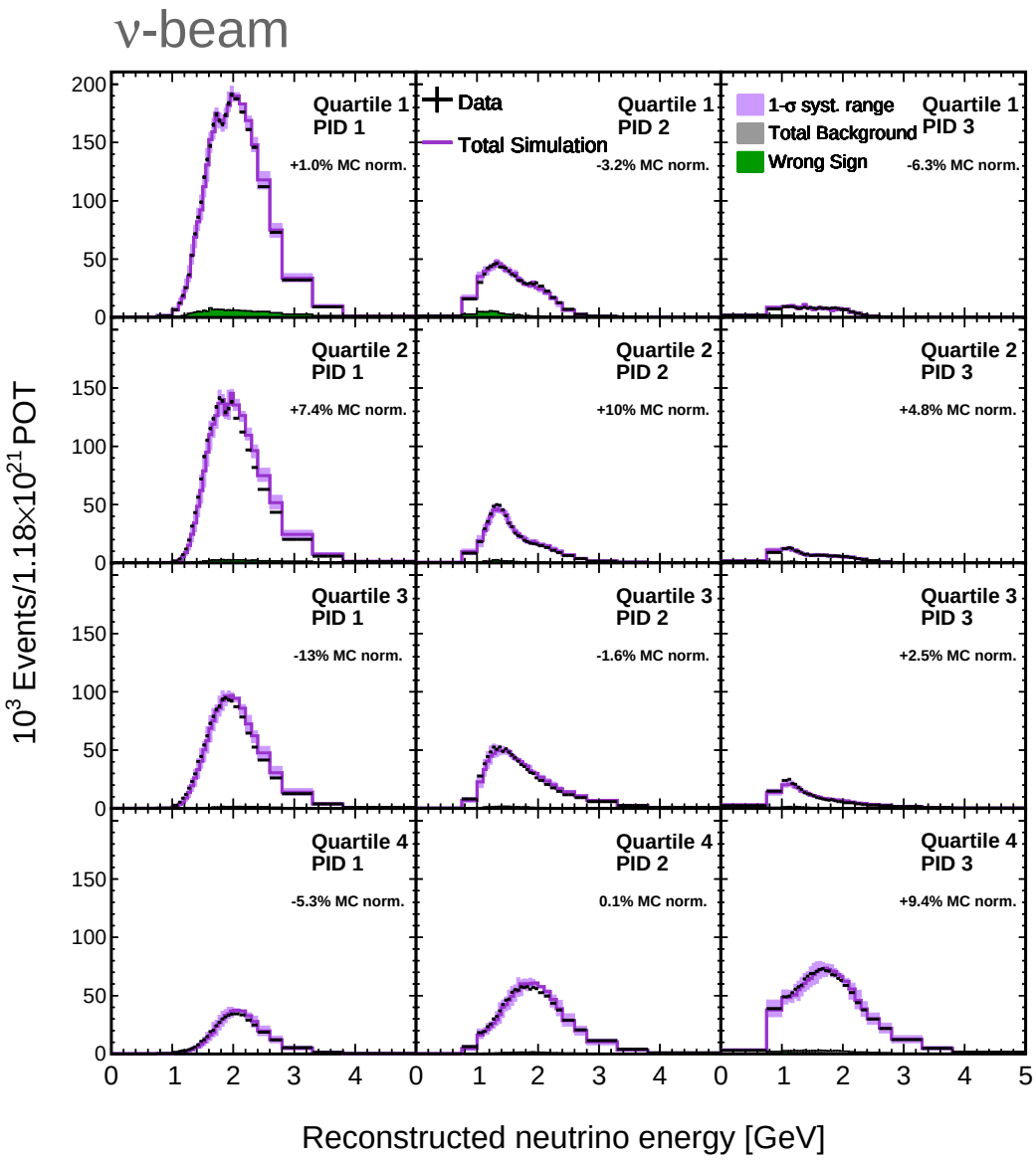

Figure 6.1: Distribution of the reconstructed neutrino energy in data (black) compared to the area-normalised MC total prediction (purple) with the systematic shape uncertainty band (purple shaded region) in the standard ν_μ candidate sample at the ND in FHC. The wrong sign and total background are shown in green and grey respectively by stacked histograms. The MC is scaled by a factor in percentage up or down to match the data.

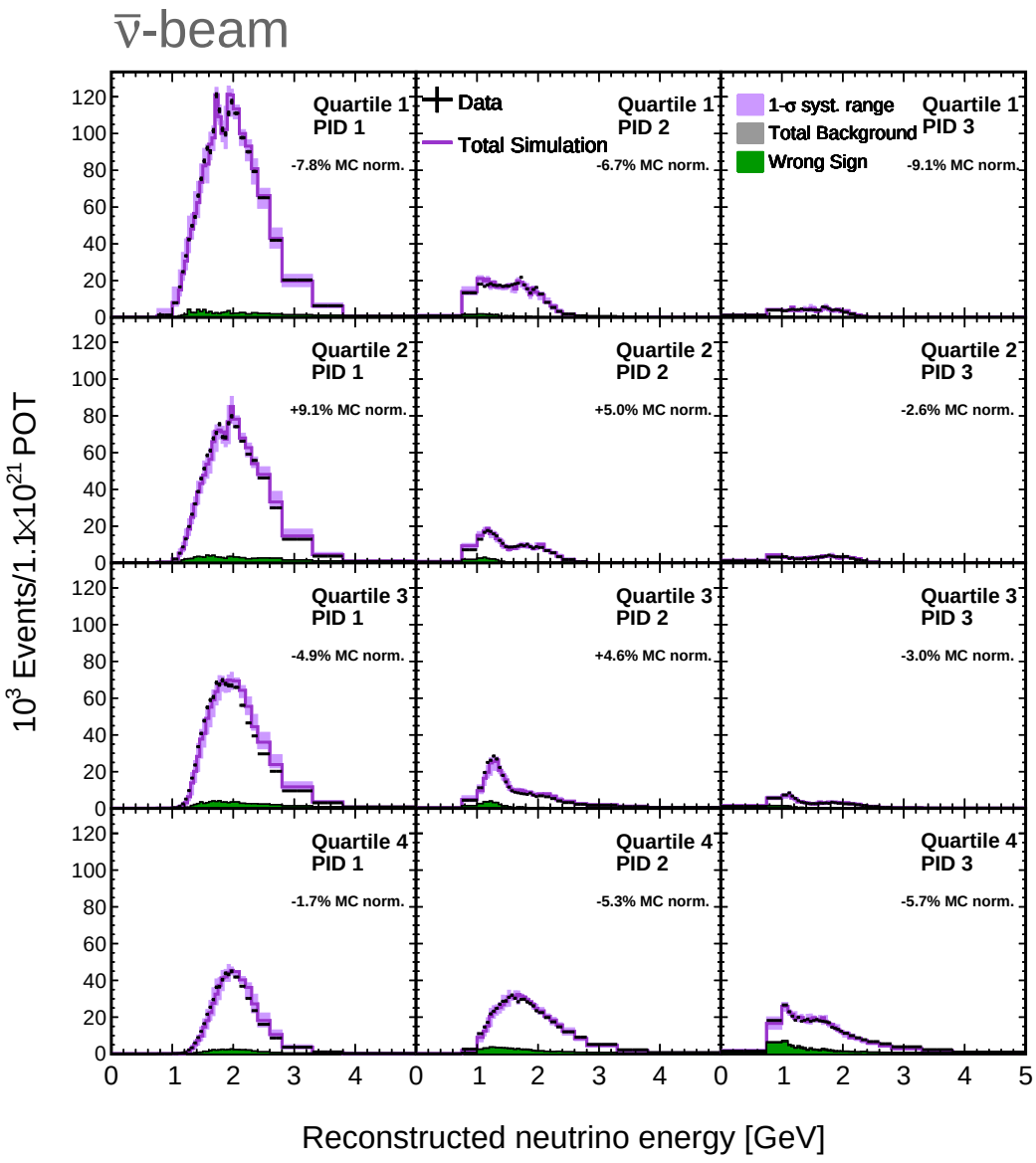

Figure 6.2: Distribution of the reconstructed neutrino energy in data (black) compared to the area-normalised MC total prediction (purple) with the systematic shape uncertainty band (purple shaded region) in the standard ν_μ candidate sample at the ND in RHC. The wrong sign and total background are shown in green and grey respectively by stacked histograms. The MC is scaled by a factor in percentage up or down to match the data.

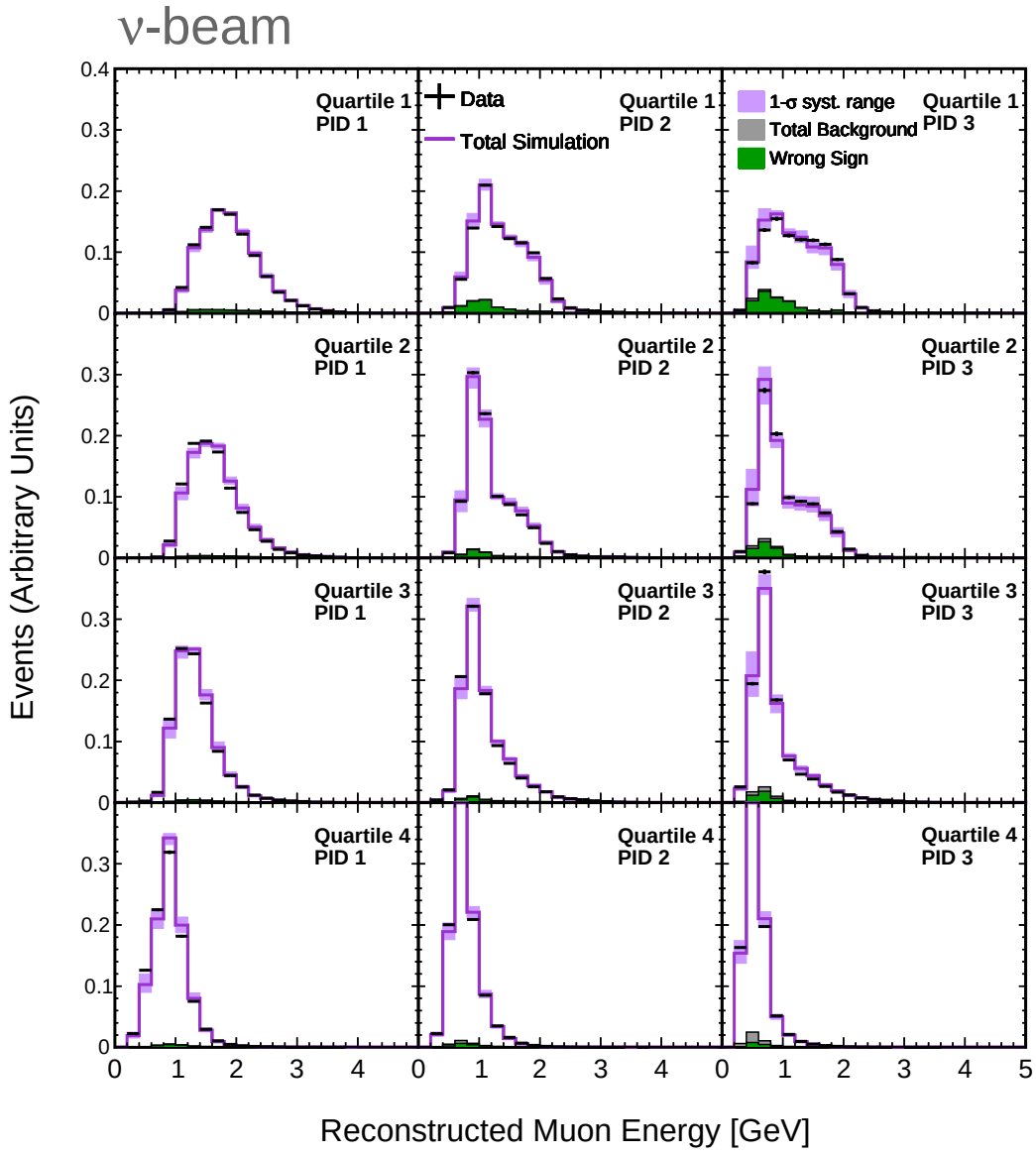

Figure 6.3: Distribution of the reconstructed muon energy in data (black) compared to the MC total prediction (purple) with the systematic shape uncertainty band (purple shaded region) in the standard ν_μ candidate sample at the ND in FHC. The wrong sign and total background are shown in green and grey respectively by stacked histograms. Both data and MC are normalised to one.

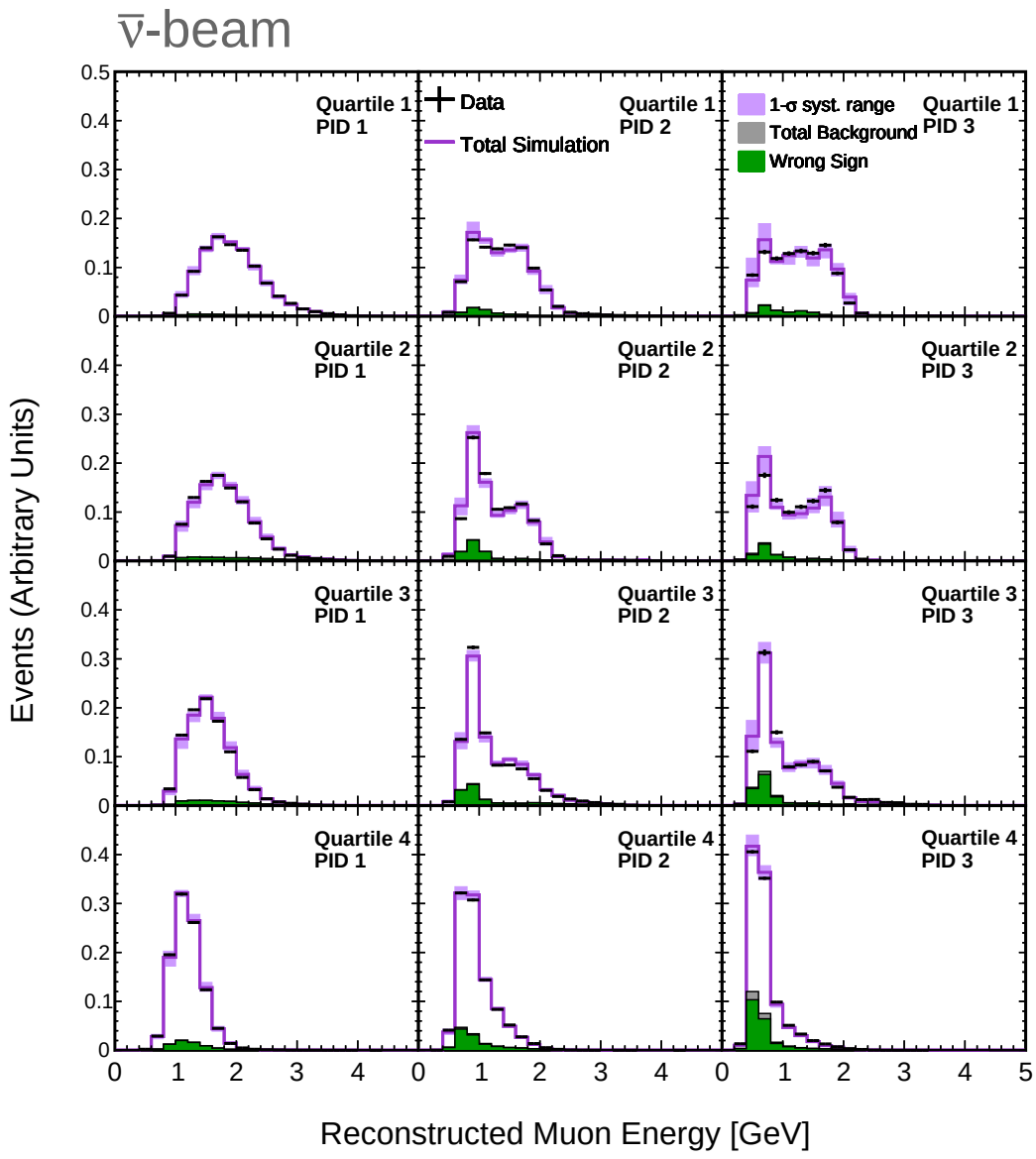

Figure 6.4: Distribution of the reconstructed muon energy in data (black) compared to the MC total prediction (purple) with the systematic shape uncertainty band (purple shaded region) in the standard ν_μ candidate sample at the ND in RHC. The wrong sign and total background are shown in green and grey respectively by stacked histograms. Both data and MC are normalised to one.

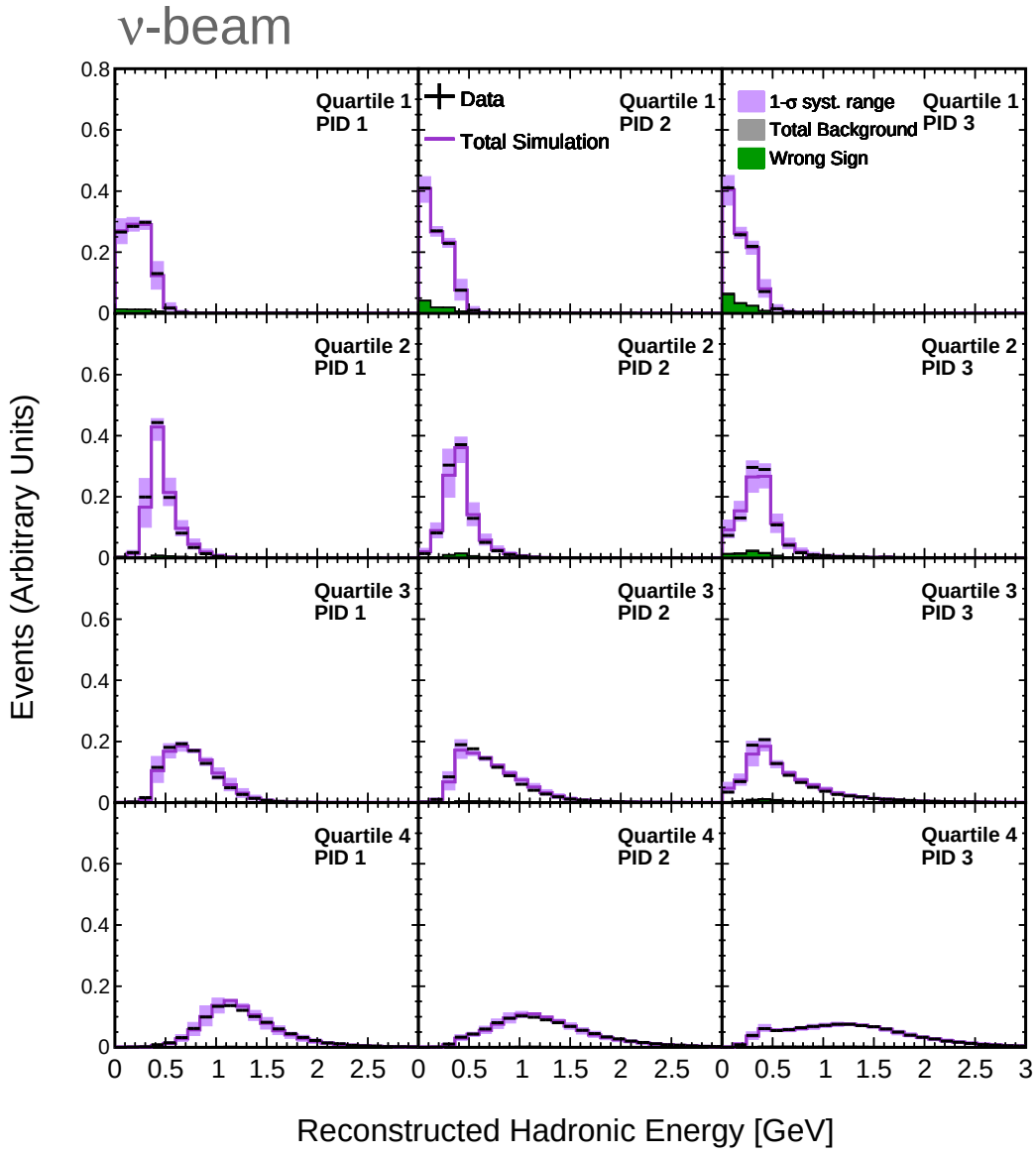

Figure 6.5: Distribution of the reconstructed hadronic energy in data (black) compared to the MC total prediction (purple) with the systematic shape uncertainty band (purple shaded region) in the standard ν_μ candidate sample at the ND in FHC. The wrong sign and total background are shown in green and grey respectively by stacked histograms. Both data and MC are normalised to one.

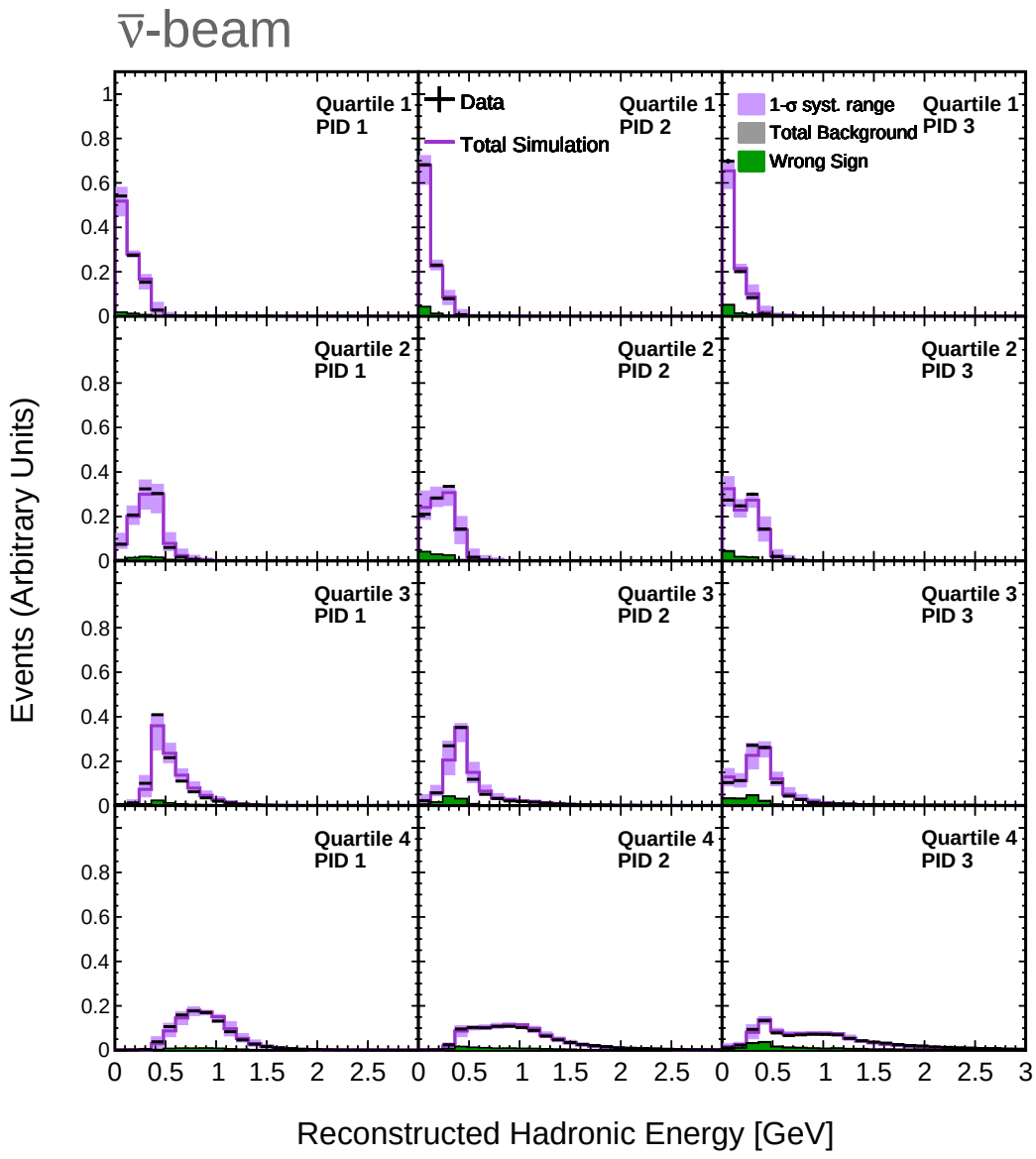

Figure 6.6: Distribution of the reconstructed hadronic energy in data (black) compared to the MC total prediction (purple) with the systematic shape uncertainty band (purple shaded region) in the standard ν_μ candidate sample at the ND in RHC. The wrong sign and total background are shown in green and grey respectively by stacked histograms. Both data and MC are normalised to one.

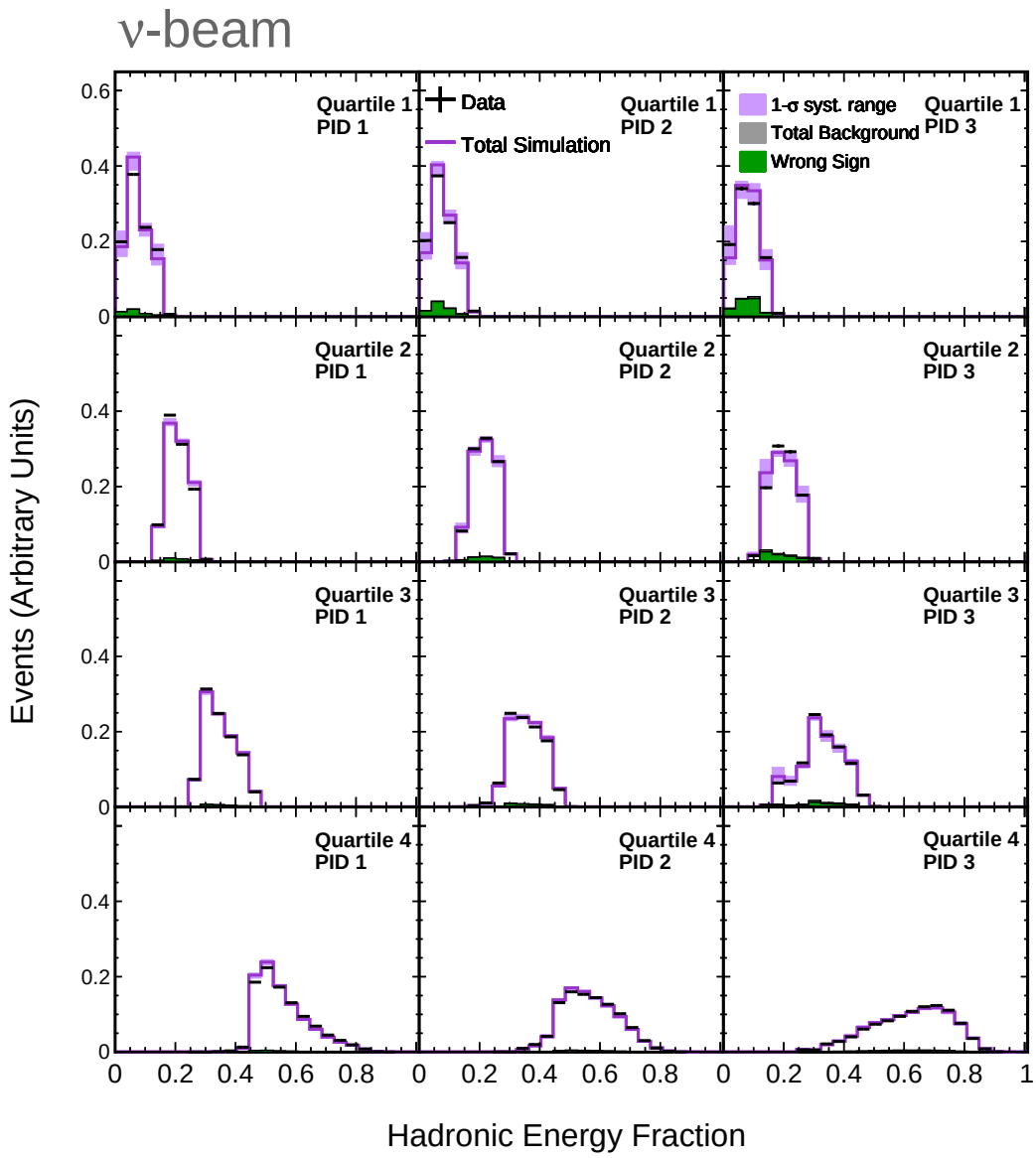

Figure 6.7: Distribution of the hadronic energy fraction in data (black) compared to the MC total prediction (purple) with the systematic shape uncertainty band (purple shaded region) in the standard ν_μ candidate sample at the ND in FHC. The wrong sign and total background are shown in green and grey respectively by stacked histograms. Both data and MC are normalised to one.

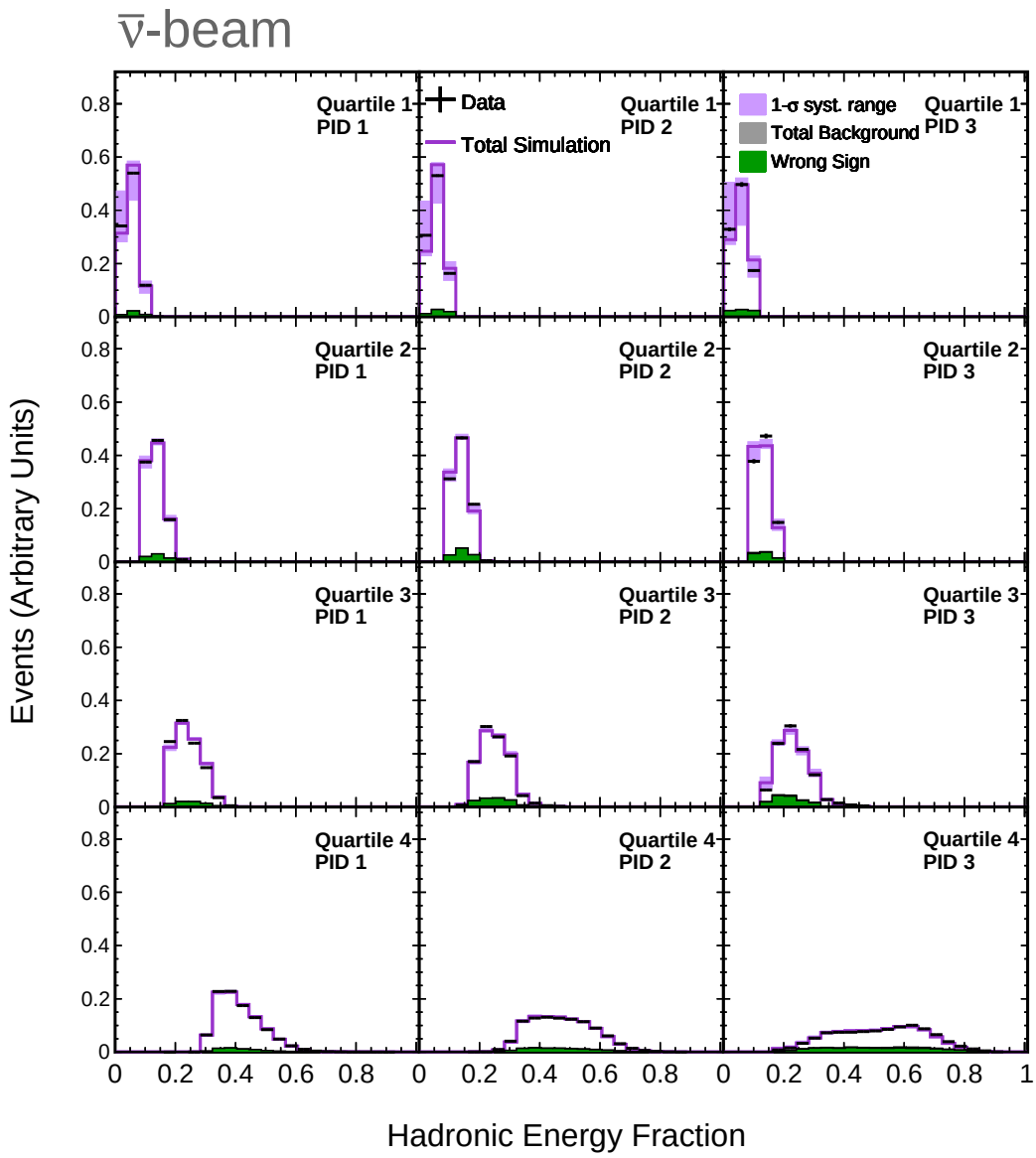

Figure 6.8: Distribution of the hadronic energy fraction in data (black) compared to the MC total prediction (purple) with the systematic shape uncertainty band (purple shaded region) in the standard ν_μ candidate sample at the ND in RHC. The wrong sign and total background are shown in green and grey respectively by stacked histograms. Both data and MC are normalised to one.

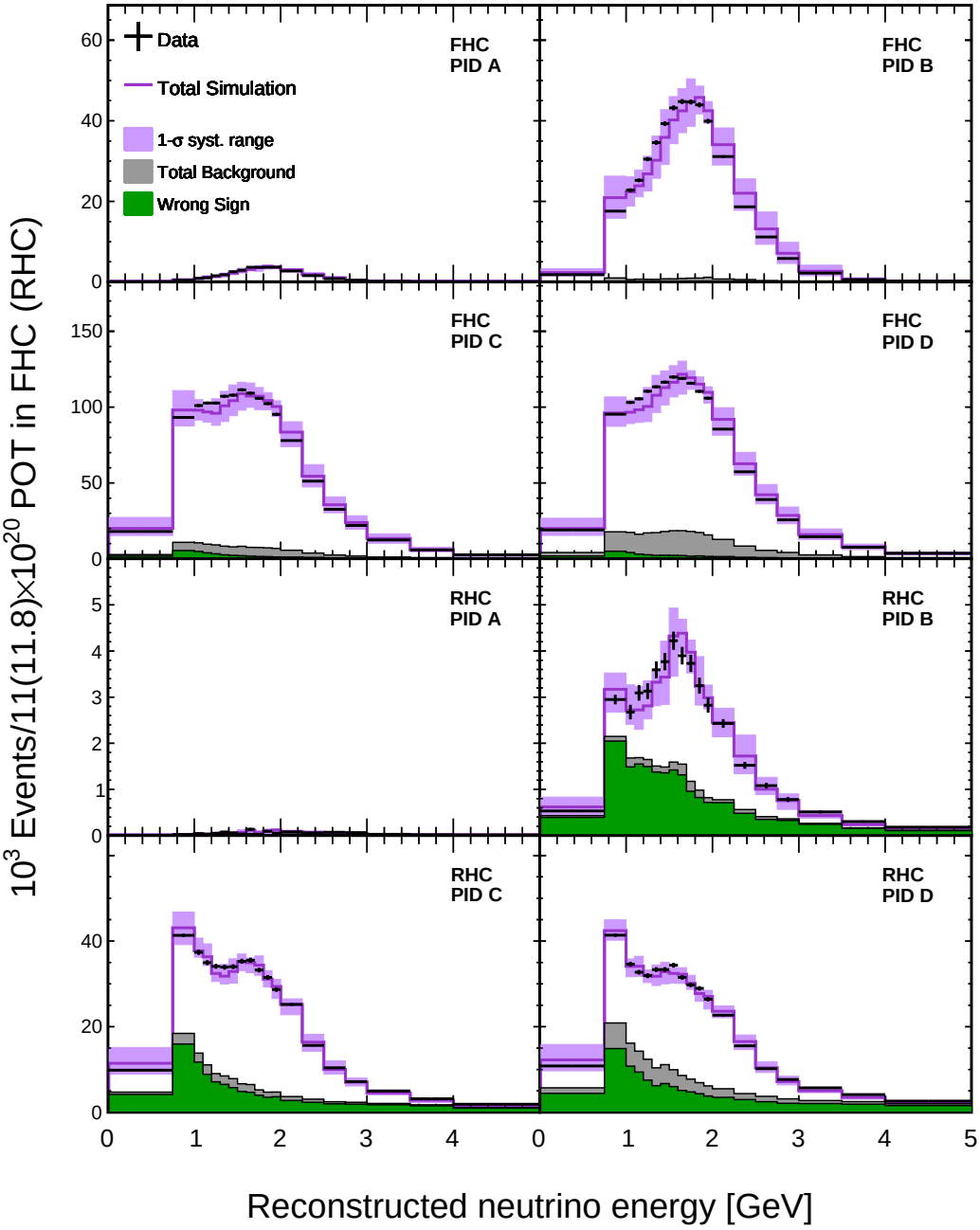

Figure 6.9: Distribution of the reconstructed neutrino energy in data (black) compared to the area-normalised MC total prediction (purple) with the systematic shape uncertainty band (purple shaded region) in the low PID ν_μ candidate sample at the ND. The wrong sign and total background are shown in green and grey respectively by stacked histograms.

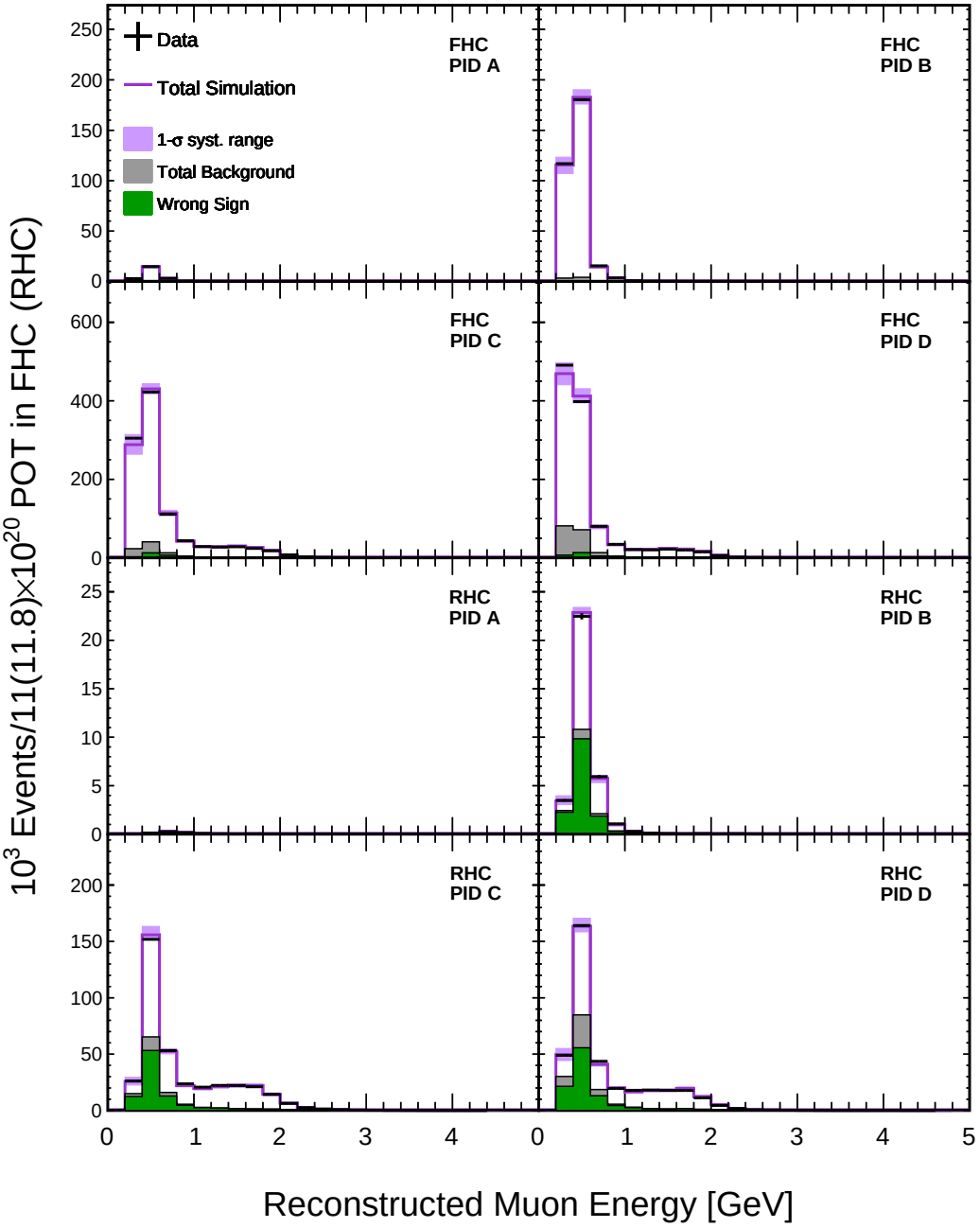

Figure 6.10: Distribution of the muon energy in data (black) compared to the area-normalised MC total prediction (purple) with the systematic shape uncertainty band (purple shaded region) in the low PID ν_μ candidate sample at the ND. The wrong sign and total background are shown in green and grey respectively by stacked histograms.

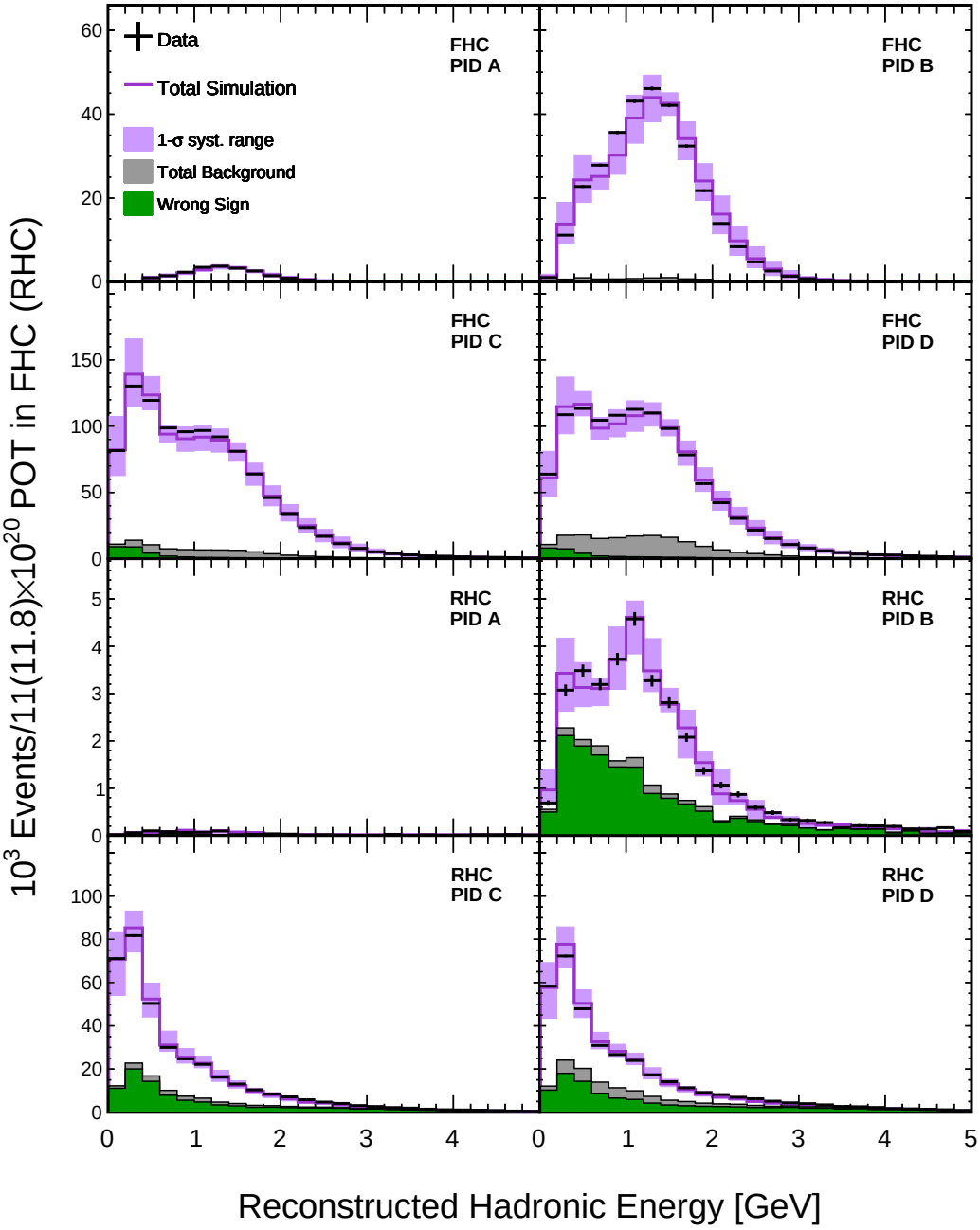

Figure 6.11: Distribution of the reconstructed hadronic energy in data (black) compared to the area-normalised MC total prediction (purple) with the systematic shape uncertainty band (purple shaded region) in the low PID ν_μ candidate sample at the ND. The wrong sign and total background are shown in green and grey respectively by stacked histograms.

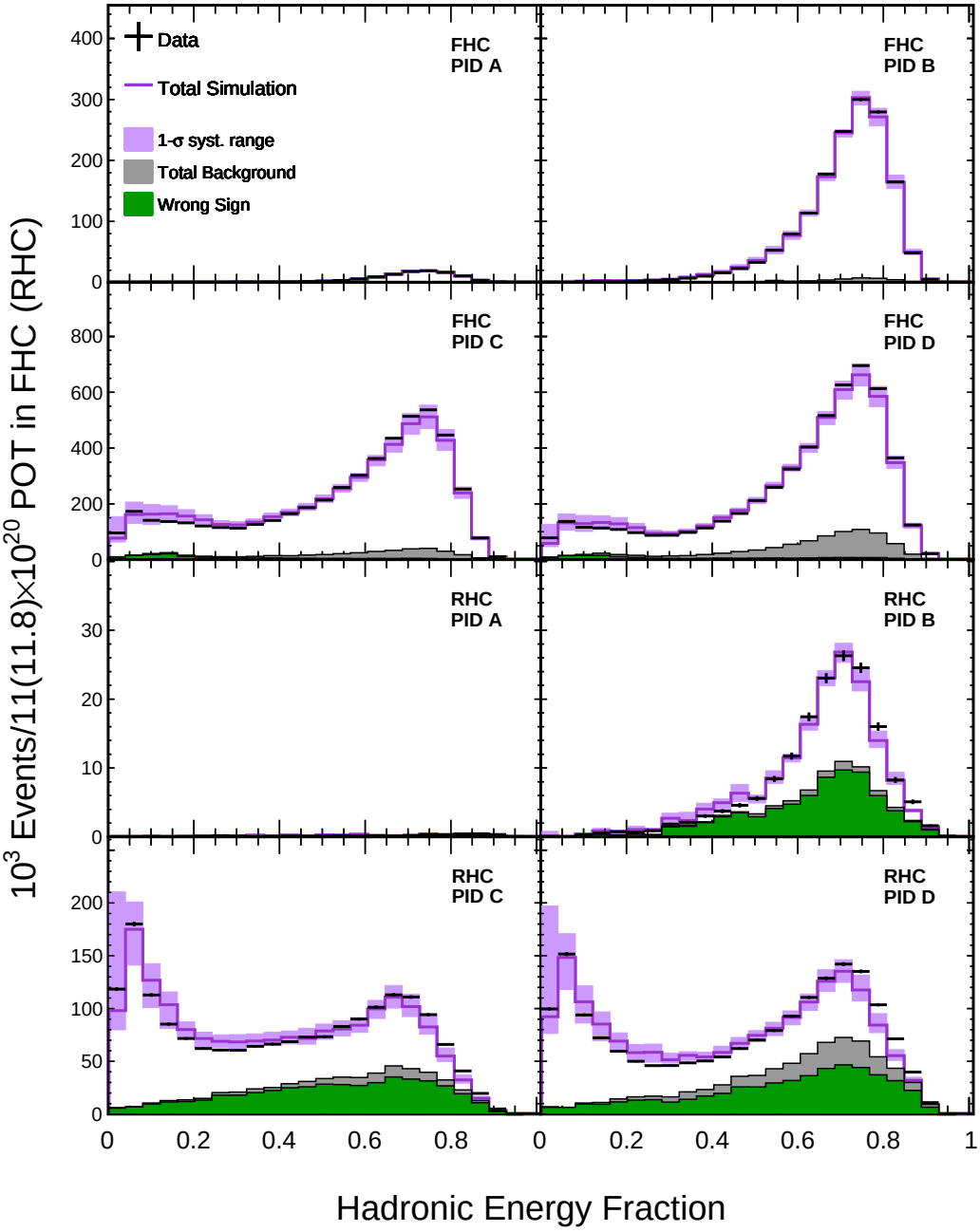

Figure 6.12: Distribution of the hadronic energy fraction in data (black) compared to the area-normalised MC total prediction (purple) with the systematic shape uncertainty band (purple shaded region) in the low PID ν_μ candidate sample at the ND. The wrong sign and total background are shown in green and grey respectively by stacked histograms.

6.2 Study at the FD

6.2.1 Best fit with the new analysis method

In the standard sample, there are 209 ν_μ-CC events observed in FHC data and 105 $\bar{\nu}_\mu$-CC candidate events observed in RHC data. For the low PID sample, 43 ν_μ-CC candidate events in FHC data and 16 $\bar{\nu}_\mu$-CC candidate events in RHC data are found, respectively. Table 6.1 and Table 6.2 show the predicted events in the FD simulation at the thesis best fit point and the observed data in the standard sample and low PID sample respectively. It can be seen that the predicted total number of events in simulation in general agrees to the observed data. A notable bin is the Quartile 3 PID 3 sample, where 3.6 (1.3) events are expected and 0 (5) events are observed in FHC (RHC). The best fit values of the oscillation parameters are found to be $\sin^2\theta_{23} = 0.568^{+0.025}_{-0.043}$ ($\sin^2\theta_{23} = 0.454^{+0.046}_{-0.026}$) and $\Delta m^2_{32} = 2.399^{+0.055}_{-0.070}\times10^{-3}$ eV^2 ($\Delta m^2_{32} = -2.427^{+0.055}_{-0.067}\times10^{-3}$ eV^2) for the normal (inverted) hierarchy with a χ^2 of 488.897 (488.813). The thesis best fit point is defined as the most favoured values of the oscillation parameters, which are obtained in the inverted hierarchy case. The new analysis uses 436 analysis bins (360 bins in the standard sample and 76 bins in the low PID sample), and the fit is implemented in the $\sin^2\theta_{23}$ vs. Δm^2_{32} space. Thus the best fit has a χ^2 with 434 degrees of freedom, corresponding to a Gaussian p-value of 0.035. NOvA's 2020 best fit point when only running the muon disappearance channels was found to be $\sin^2\theta_{23} = 0.569^{+0.026}_{-0.043}$ ($\sin^2\theta_{23} = 0.453^{+0.043}_{-0.026}$) and $\Delta m^2_{32} = 2.432^{+0.059}_{-0.077} \times 10^{-3}$ eV^2 ($\Delta m^2_{32} = -2.460^{+0.060}_{-0.067} \times 10^{-3}$ eV^2) for the normal (inverted) hierarchy. The difference of best fit point between the new analysis and NOvA's 2020 analysis is about 2% for $\sin^2\theta_{23}$ and 1.4% for Δm^2_{32}. The uncertainty range of the new analysis at 1 sigma for Δm^2_{32} decreases by 8% (4%) for the normal hierarchy (inverted hierarchy) compared to the standard analysis. The uncertainty range for $\sin^2\theta_{23}$ is close to the standard analysis.

6.2.2 Distributions at the FD

This section discusses comparisons between the FD data and the oscillated predictions at the thesis best fit point for various variables of interest. As mentioned in Chapter 4, the predicted spectra are generated using the extrapolation method which extrapolates the ND data and MC distributions to the FD. In all the plots, the total prediction at the thesis best fit point is shown by the purple line and the shaded purple region corresponds to the 1 σ systematic uncertainty in the prediction. The wrong-sign events, beam backgrounds, and cosmic backgrounds are shown by the green, grey, and the blue stacked histograms,

		Pred	Signal	Cosmic	Beam bkg.	Data
FHC	Quartile 1 PID 1	47.6	47.5	0.1	0.1	41
	Quartile 1 PID 2	3.7	3.5	0.1	0.0	4
	Quartile 1 PID 3	1.8	1.6	0.2	0.0	2
	Quartile 2 PID 1	44.9	44.7	0.1	0.1	45
	Quartile 2 PID 2	3.0	2.9	0.1	0.1	2
	Quartile 2 PID 3	2.0	1.7	0.2	0.1	1
	Quartile 3 PID 1	42.7	42.4	0.1	0.2	37
	Quartile 3 PID 2	5.7	5.4	0.1	0.2	4
	Quartile 3 PID 3	3.6	2.8	0.7	0.2	0
	Quartile 4 PID 1	30.1	29.7	0.2	0.2	31
	Quartile 4 PID 2	14.3	13.6	0.2	0.4	14
	Quartile 4 PID 3	20.3	15.7	3.0	1.6	28
	Total	**219.7**	**211.5**	**5.1**	**3.2**	**209**
RHC	Quartile 1 PID 1	22.8	22.8	0.0	0.0	21
	Quartile 1 PID 2	1.8	1.8	0.0	0.0	4
	Quartile 1 PID 3	0.7	0.7	0.0	0.0	1
	Quartile 2 PID 1	22.4	22.3	0.0	0.1	20
	Quartile 2 PID 2	1.5	1.5	0.0	0.0	2
	Quartile 2 PID 3	0.7	0.7	0.0	0.0	1
	Quartile 3 PID 1	21.3	21.2	0.0	0.1	20
	Quartile 3 PID 2	2.0	2.0	0.0	0.0	2
	Quartile 3 PID 3	1.3	1.1	0.1	0.0	5
	Quartile 4 PID 1	15.7	15.6	0.0	0.1	13
	Quartile 4 PID 2	6.4	6.1	0.1	0.2	7
	Quartile 4 PID 3	6.7	5.5	0.7	0.5	9
	Total	**103.3**	**101.3**	**0.9**	**1.0**	**105**

Table 6.1: Numbers of muon neutrino or antineutrino candidate events for the thesis best fit point in prediction and in data at the FD for the standard sample.

		Pred.	Signal	Cosmic	Beam bkg.	Data
FHC	PID A	1.9	1.5	0.4	0.0	1
	PID B	8.3	4.8	3.1	0.4	12
	PID C	13.3	7.9	3.0	2.4	14
	PID D	19.8	6.8	7.8	5.2	16
	Total	**43.3**	**21.0**	**14.3**	**8.0**	**43**
RHC	PID A	0.3	0.3	0.0	0.0	1
	PID B	1.8	1.2	0.5	0.1	3
	PID C	4.5	3.0	0.8	0.7	5
	PID D	5.3	2.3	1.6	1.4	7
	Total	**11.9**	**6.8**	**2.9**	**2.2**	**16**

Table 6.2: Numbers of muon neutrino or antineutrino candidate events for the thesis best fit point in prediction and in data at the FD for the low PID sample.

respectively. As described in Chapter 5, the standard sample is split into 12 subsamples with four hadronic fraction quartile bins divided into three particle identification bins. Figure 6.13 and Figure 6.14 show the reconstructed neutrino energy distribution in FHC and in RHC at the FD respectively. It can be seen the energy distributions show reasonable agreement but there are very low statistics in some bins. In addition, the PID binning is able to separate the signal and background well in hadronic quartile 3 and quartile 4, as the PID 2 and PID 3 bins have a larger background fraction in simulation. Figure 6.15 through Figure 6.20 show distributions of other variables including the reconstructed muon energy, reconstructed hadronic energy, and hadronic energy fraction. Other variables, CVN, ReMId, Cosmic Rejection, $\cos\theta_{\text{NuMI}}$ (where θ_{NuMI} is the angle of the muon track with respect to the beam direction), Kalman track length, transverse momentum and transverse momentum fraction, are shown in Figure B.25 to Figure B.38 in Appendix B. These plots also show a good agreement between the prediction and data. In the low PID sample, as described in Chapter 5, there are 4 PID bins defined using CVN and CosPID. Figure 6.21 shows the distributions of neutrino energy for each PID bin for each beam mode. It can be seen the background events increases from the PID A sample to PID D sample. Figure 6.22 shows the energy distribution with all PID bins combined in both FHC and RHC. Figure 6.23 through Figure 6.25 and Figure B.39 through Figure B.45 show the distributions of other variables, where all the 4 bins are combined in one. Again,

these distributions show reasonable agreement between the data and MC, albeit with large statistical uncertainties on the data.

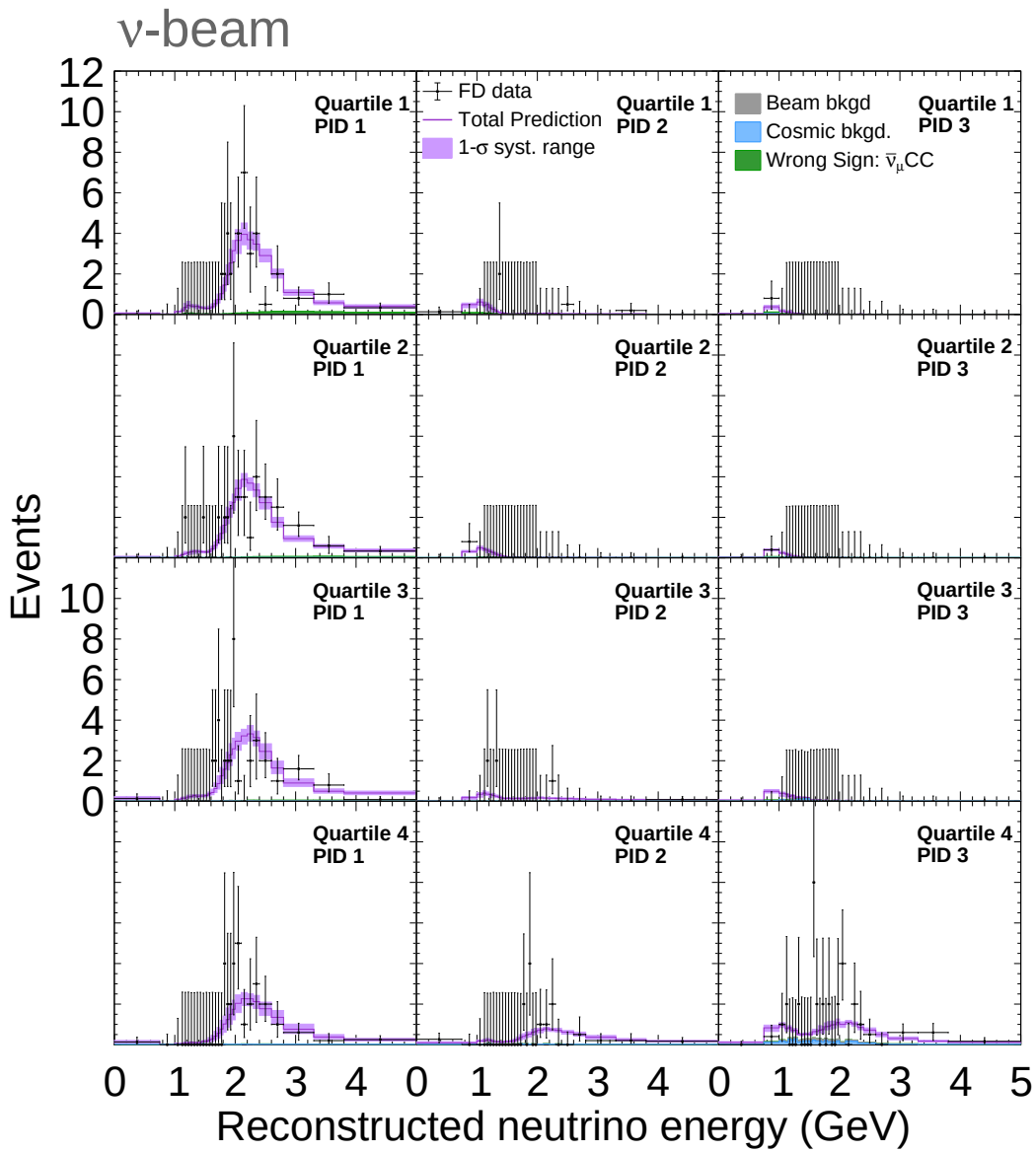

Figure 6.13: Reconstructed neutrino energy spectra for the ν_μ CC events in the standard sample at the FD in each selection bin in FHC. The selected ν_μ sample at the FD is split into 12 sub-samples (i.e. four quartile bins times three particle identification bins). Data is shown in black. The prediction at the thesis best fit point is shown by the purple line and the shaded purple region corresponds to the 1 σ systematic uncertainty in the simulation. The green, grey, and the blue stacked histograms show the wrong-sign ($\bar{\nu}_\mu$ CC), beam, and cosmic backgrounds, respectively.

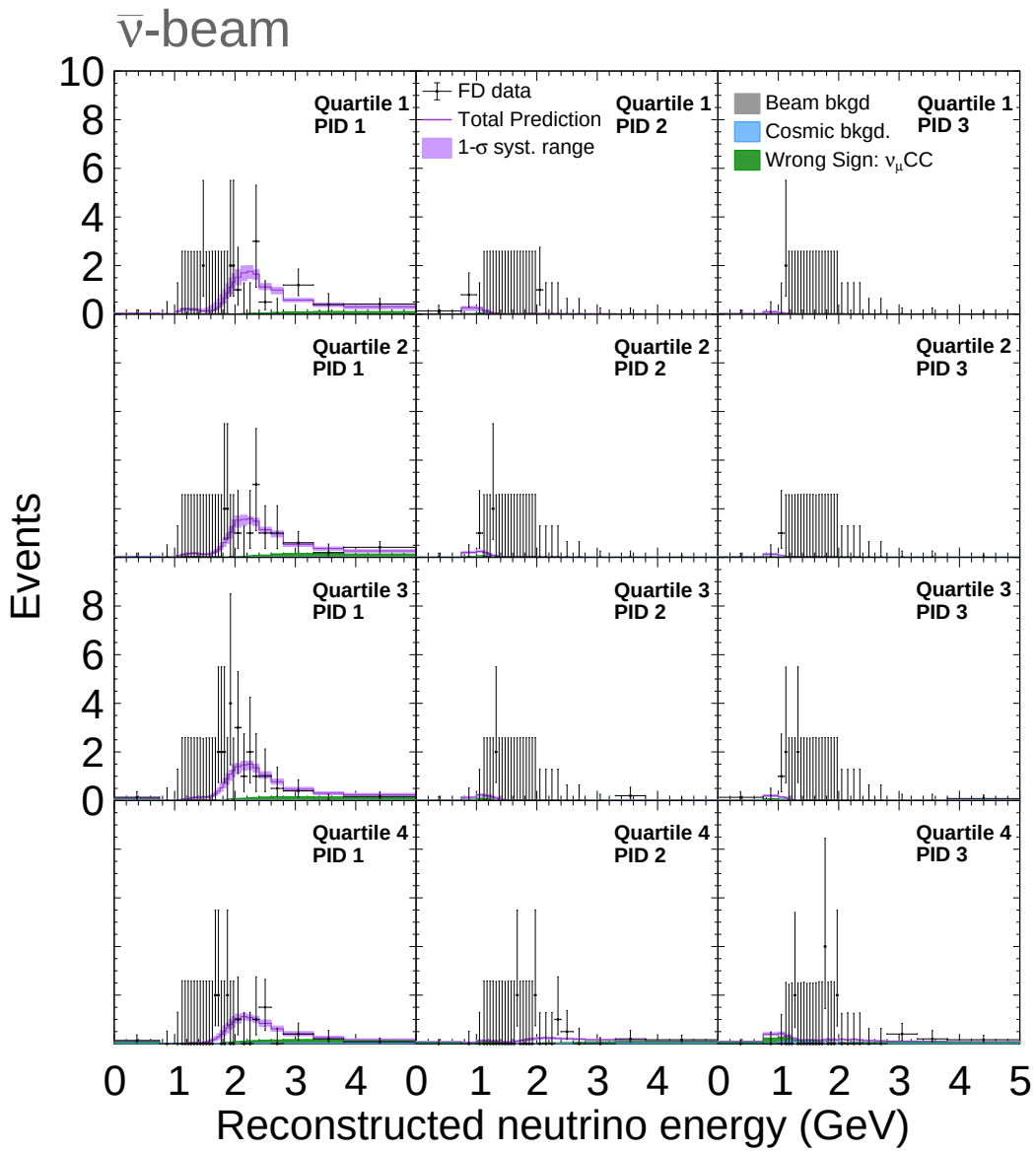

Figure 6.14: Reconstructed neutrino energy spectra for the ν_μ CC events in the standard sample at the FD in each selection bin in RHC. The selected ν_μ sample at the FD is split into 12 sub-samples (i.e. four quartile bins times three particle identification bins). Data is shown in black. The prediction at the thesis best fit point is shown by the purple line and the shaded purple region corresponds to the 1 σ systematic uncertainty in the simulation. The green, grey, and the blue stacked histograms show the wrong-sign (ν_μ CC), beam, and cosmic backgrounds, respectively.

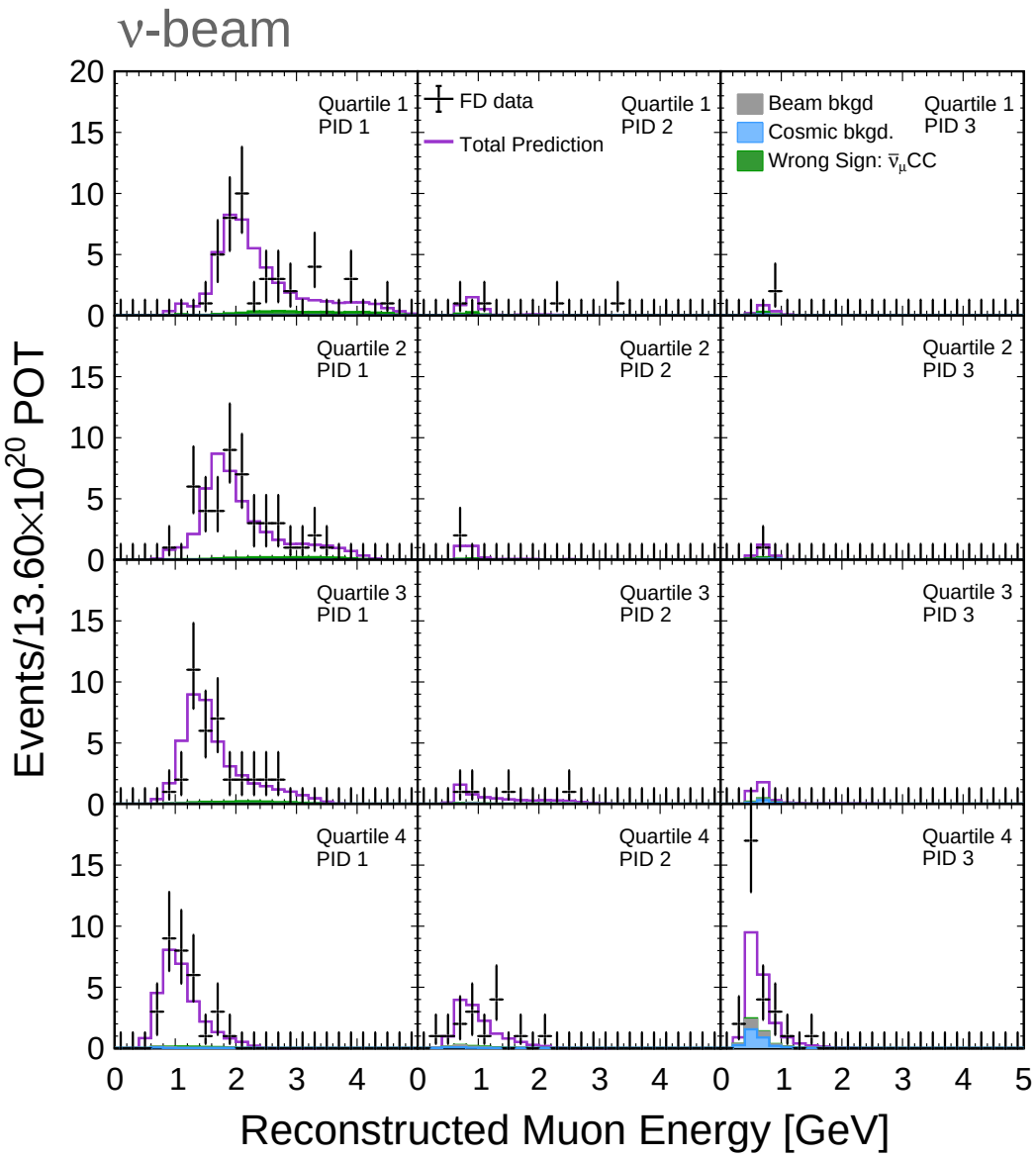

Figure 6.15: Reconstructed muon energy spectra for the ν_μ CC events in the standard sample at the FD in each selection bin in FHC. The selected ν_μ sample at the FD is split into 12 sub-samples (i.e. four quartile bins times three particle identification bins). Data is shown in black. The prediction at the thesis best fit point is shown by the purple line and the shaded purple region corresponds to the 1 σ systematic uncertainty in the simulation. The green, grey, and the blue stacked histograms show the wrong-sign ($\bar{\nu}_\mu$ CC), beam, and cosmic backgrounds, respectively.

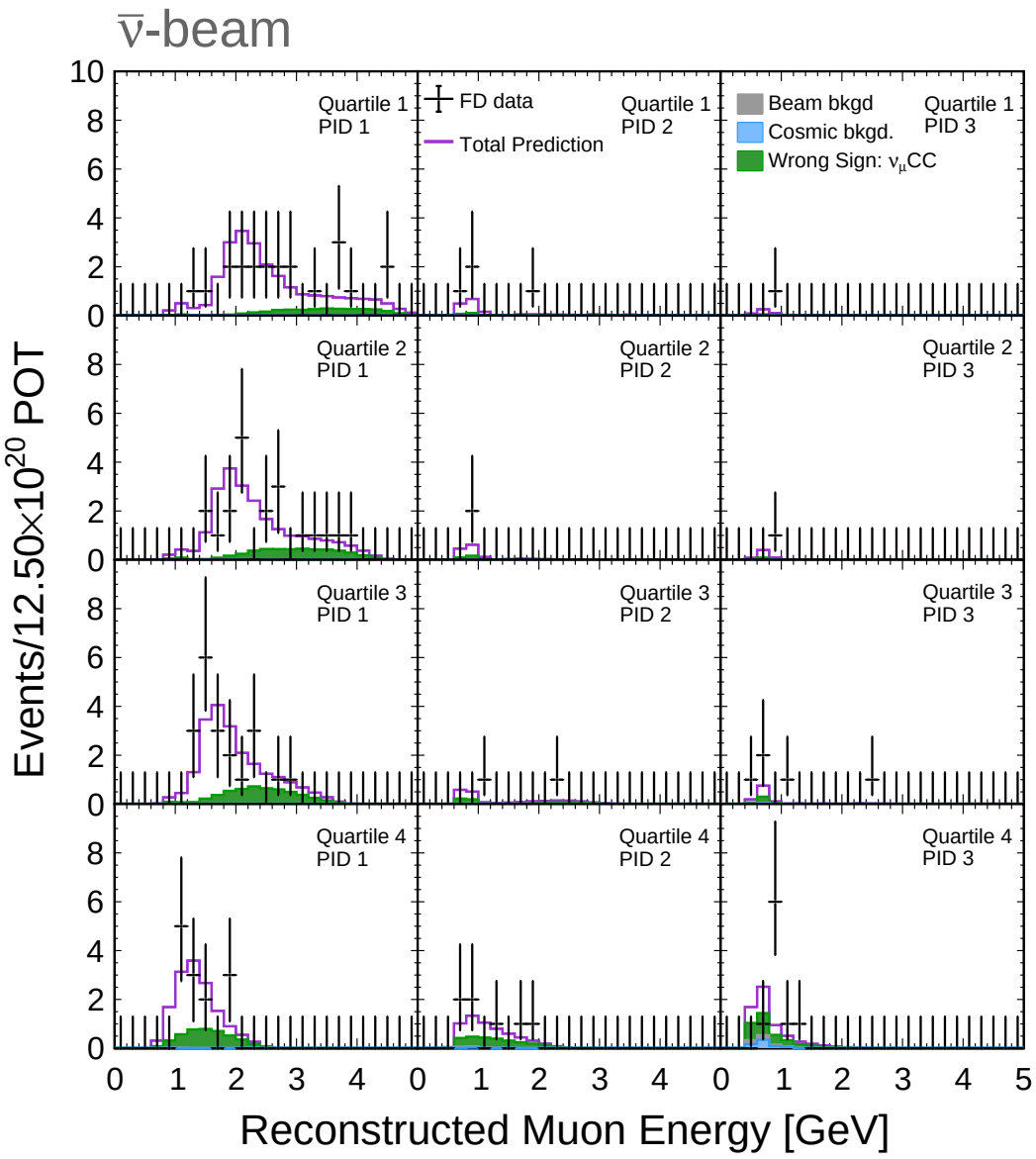

Figure 6.16: Reconstructed muon energy spectra for the ν_μ CC events in the standard sample at the FD in each selection bin in RHC. The selected ν_μ sample at the FD is split into 12 sub-samples (i.e. four quartile bins times three particle identification bins). Data is shown in black. The prediction at the thesis best fit point is shown by the purple line and the shaded purple region corresponds to the 1 σ systematic uncertainty in the simulation. The green, grey, and the blue stacked histograms show the wrong-sign (ν_μ CC), beam, and cosmic backgrounds, respectively.

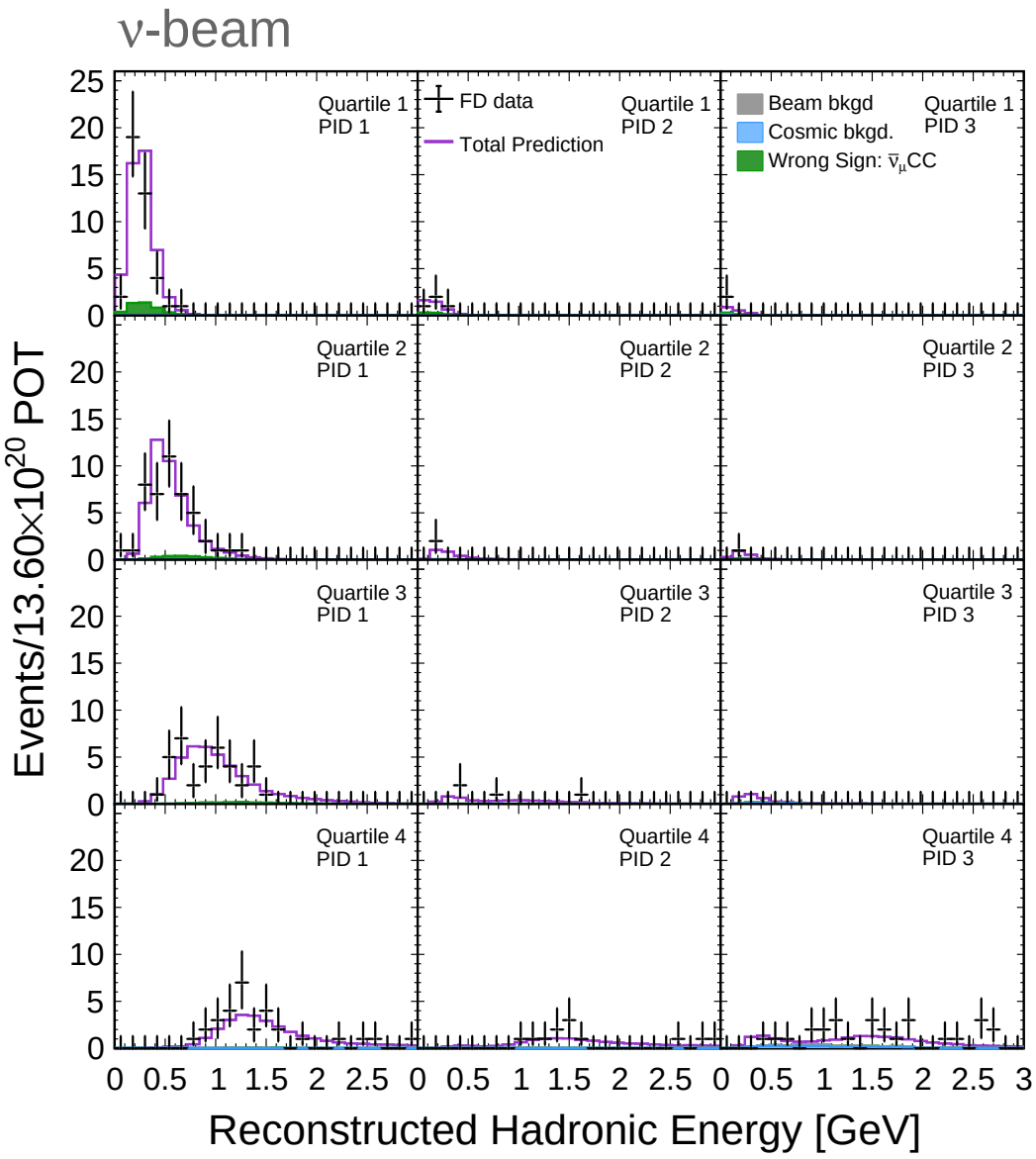

Figure 6.17: Reconstructed hadronic energy spectra for the ν_μ CC events in the standard sample at the FD in each selection bin in FHC. The selected ν_μ sample at the FD is split into 12 sub-samples (i.e. four quartile bins times three particle identification bins). Data is shown in black. The prediction at the thesis best fit point is shown by the purple line and the shaded purple region corresponds to the 1 σ systematic uncertainty in the simulation. The green, grey, and the blue stacked histograms show the wrong-sign ($\bar{\nu}_\mu$ CC), beam, and cosmic backgrounds, respectively.

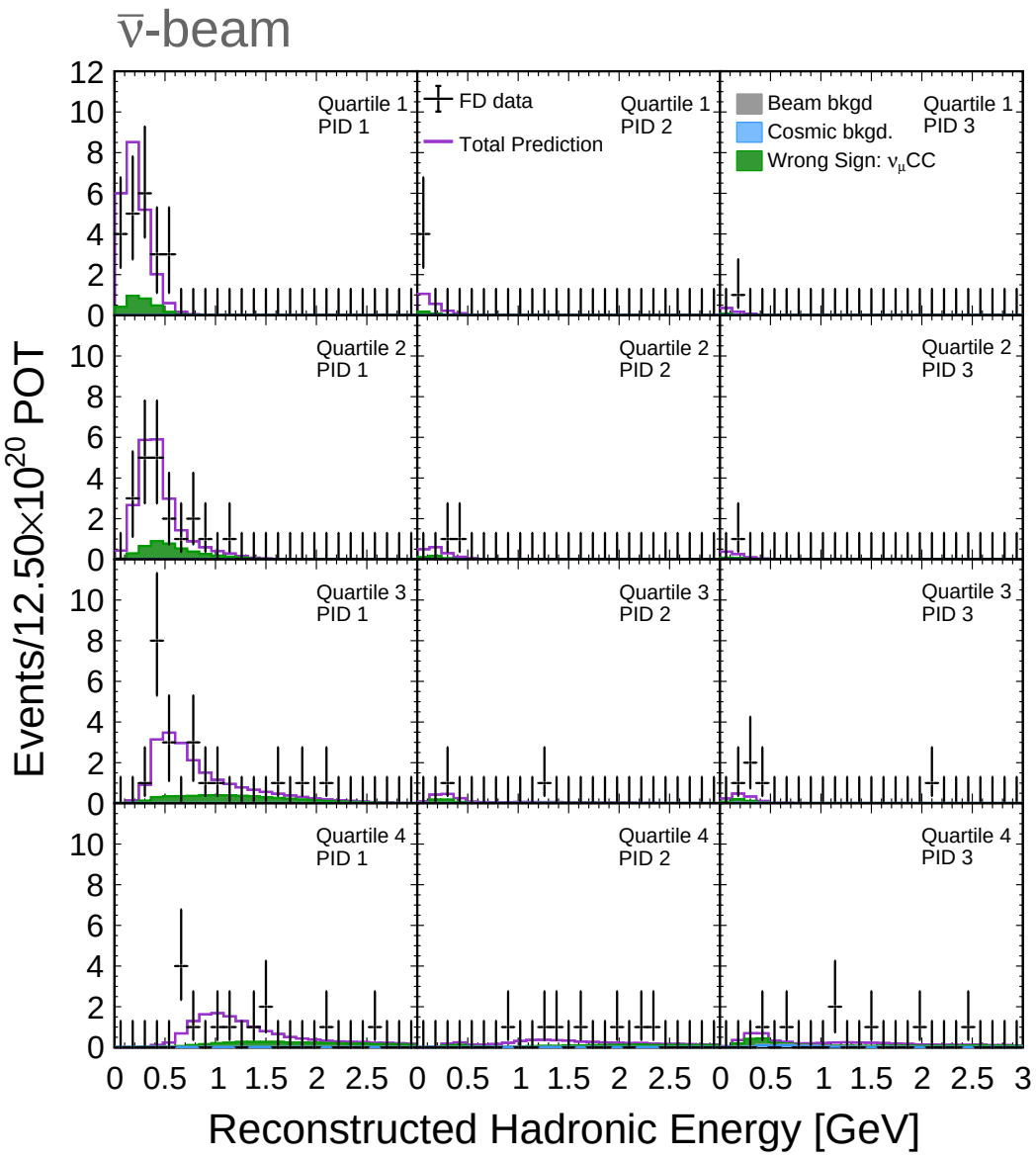

Figure 6.18: Reconstructed hadronic energy spectra for the ν_μ CC events in the standard sample at the FD in each selection bin in RHC. The selected ν_μ sample at the FD is split into 12 sub-samples (i.e. four quartile bins times three particle identification bins). Data is shown in black. The prediction at the thesis best fit point is shown by the purple line and the shaded purple region corresponds to the 1 σ systematic uncertainty in the simulation. The green, grey, and the blue stacked histograms show the wrong-sign (ν_μ CC), beam, and cosmic backgrounds, respectively.

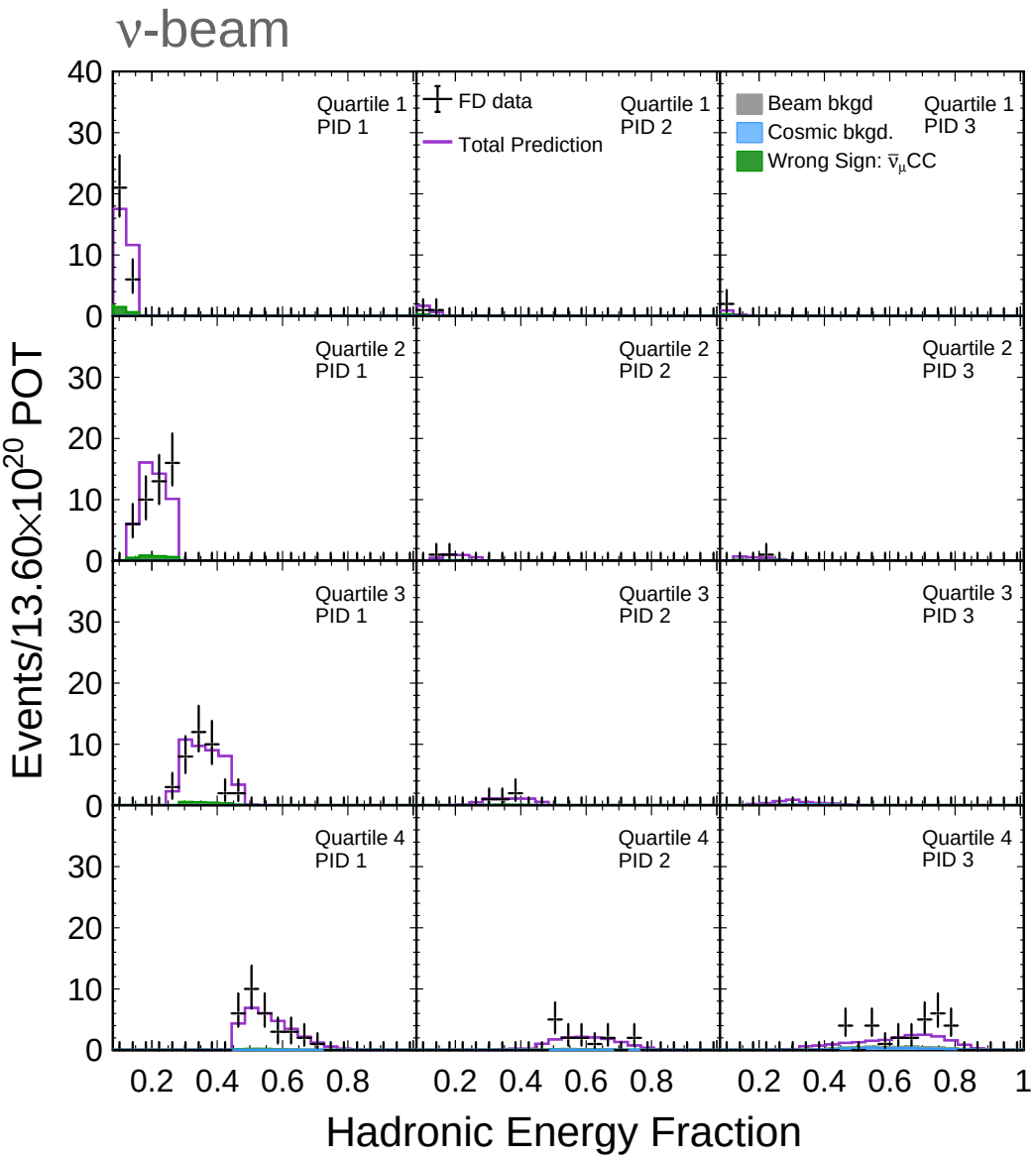

Figure 6.19: Distribution of hadronic energy fraction for the ν_μ CC events in the standard sample at the FD in each selection bin in FHC. The selected ν_μ sample at the FD is split into 12 sub-samples (i.e. four quartile bins times three particle identification bins). Data is shown in black. The prediction at the thesis best fit point is shown by the purple line and the shaded purple region corresponds to the 1 σ systematic uncertainty in the simulation. The green, grey, and the blue stacked histograms show the wrong-sign ($\bar{\nu}_\mu$ CC), beam, and cosmic backgrounds, respectively.

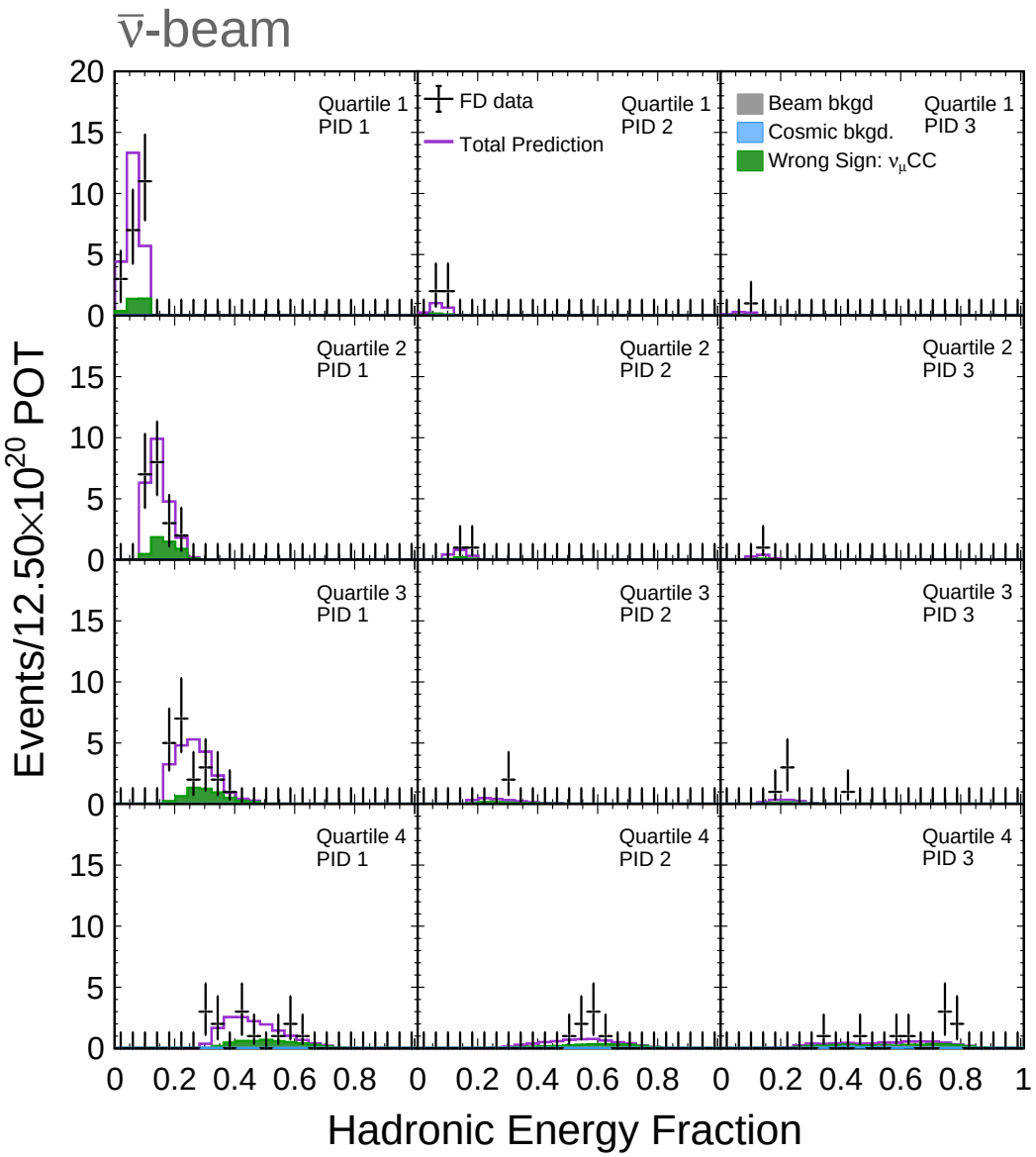

Figure 6.20: Distribution of hadronic energy fraction score for the ν_μ CC events in the standard sample at the FD in each selection bin in RHC. The selected ν_μ sample at the FD is split into 12 sub-samples (i.e. four quartile bins times three particle identification bins). Data is shown in black. The prediction at the thesis best fit point is shown by the purple line and the shaded purple region corresponds to the 1 σ systematic uncertainty in the simulation. The green, grey, and the blue stacked histograms show the wrong-sign (ν_μ CC), beam, and cosmic backgrounds, respectively.

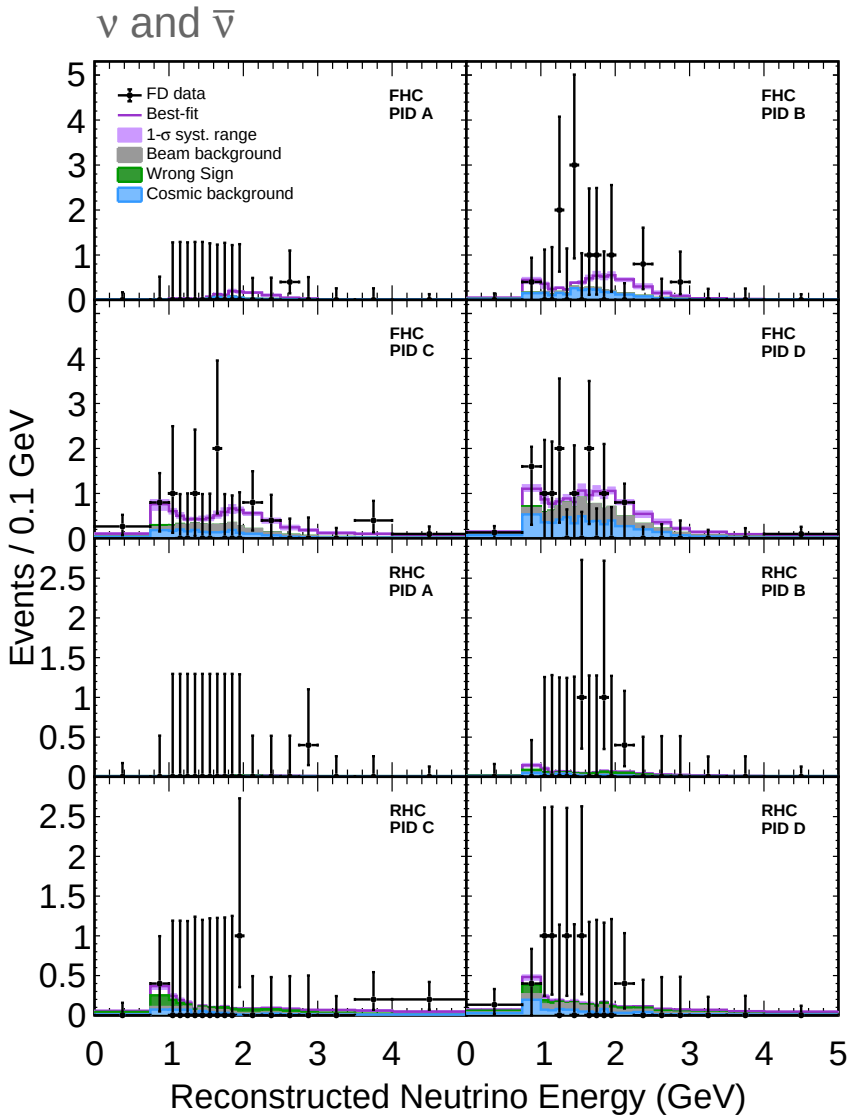

Figure 6.21: Reconstructed neutrino energy spectra for the ν_μ CC events in the low PID sample at the FD in each selection bin (PID A-PID D) in FHC (two upper rows) and RHC (two lower rows). Data is shown in black. The prediction at the thesis best fit point is shown by the purple line and the shaded purple region corresponds to the 1 σ systematic uncertainty in the simulation. The green, grey, and the blue stacked histograms show the wrong-sign ($\bar{\nu}_\mu$ for FHC and ν_μ for RHC), beam, and cosmic backgrounds, respectively.

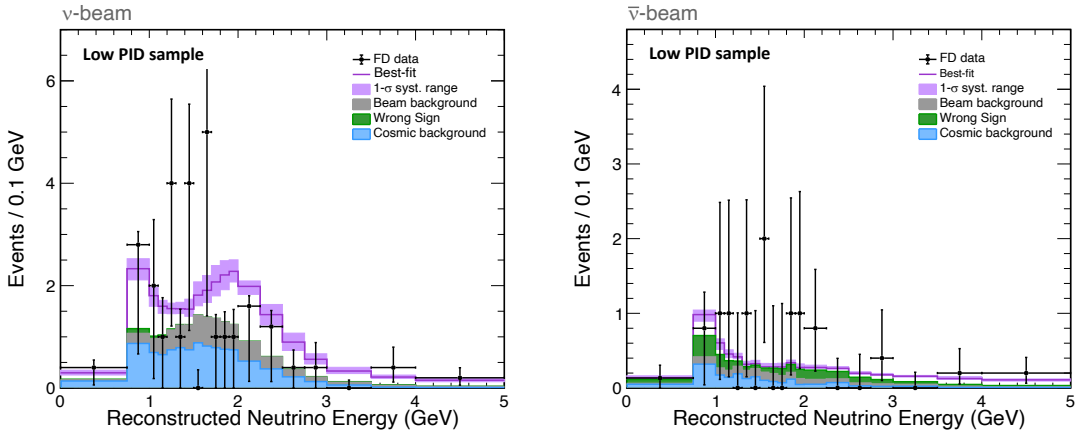

Figure 6.22: Reconstructed neutrino energy spectra for the ν_μ CC events in the low PID sample at the FD in FHC (left) and RHC (right). Data is shown in black. The prediction at the thesis best fit point is shown by the purple line and the shaded purple region corresponds to the 1 σ systematic uncertainty in the simulation. The green, grey, and the blue stacked histograms show the wrong-sign events, beam background and cosmic background, respectively.

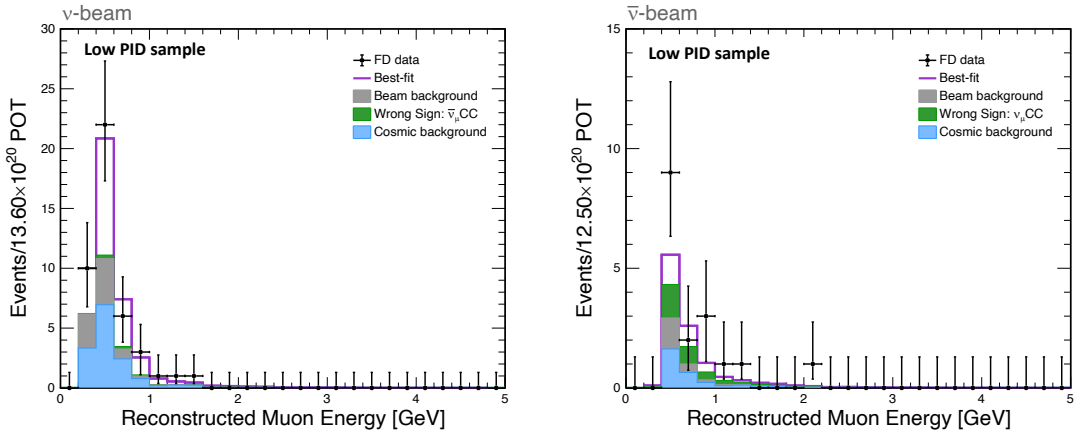

Figure 6.23: Distribution of the muon energy for the ν_μ CC events in the low PID sample at the FD in FHC (left) and RHC (right). Data is shown in black. The prediction at the thesis best fit point is shown by the purple line and the shaded purple region corresponds to the 1 σ systematic uncertainty in the simulation. The green, grey, and the blue stacked histograms show the wrong-sign events, beam background, and cosmic background, respectively.

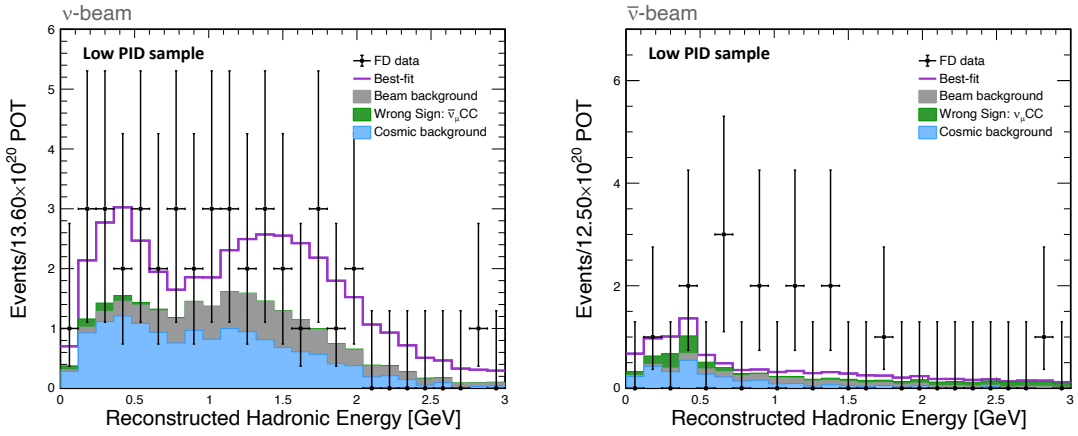

Figure 6.24: Distribution of the hadronic energy for the ν_μ CC events in the low PID sample at the FD in FHC (left) and RHC (right). Data is shown in black. The prediction at the thesis best fit point is shown by the purple line and the shaded purple region corresponds to the 1 σ systematic uncertainty in the simulation. The green, grey, and the blue stacked histograms show the wrong-sign events, beam background, and cosmic background, respectively.

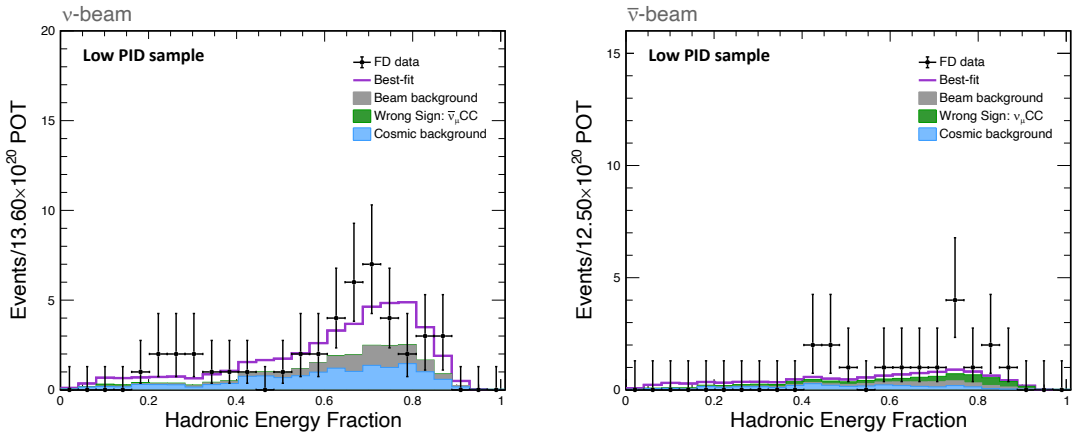

Figure 6.25: Distribution of the hadronic energy fraction for the ν_μ CC events in the low PID sample at the FD in FHC (left) and RHC (right). Data is shown in black. The prediction at the thesis best fit point is shown by the purple line and the shaded purple region corresponds to the 1 σ systematic uncertainty in the simulation. The green, grey, and the blue stacked histograms show the wrong-sign events, beam background, and cosmic background, respectively.

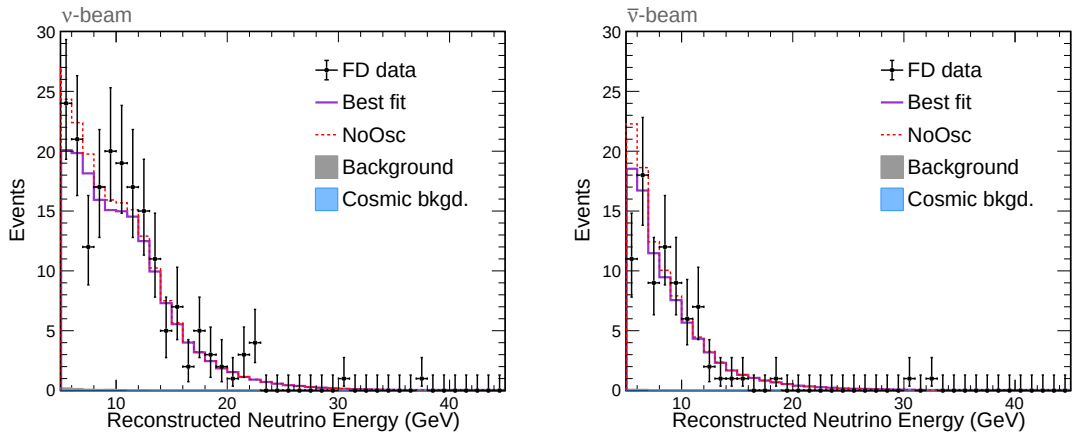

Figure 6.26: Distribution of the reconstructed neutrino energy for the ν_μ CC events in the high energy sample for all hadronic quartiles at the FD in FHC (left) and RHC (right). Data is shown in black. The prediction at the thesis best fit point is shown by the purple line. The grey and blue stacked histograms show the beam background and cosmic background, respectively.

6.2.2.1 High energy events

As is mentioned in Section 5.2.1, it is useful to compare the MC and the real data using the high energy events to verify the beam and detector perform as expected although this sample is not used in the oscillation parameter fits. The ND has few events in this energy range so extrapolation does not really make sense. Furthermore, the ND is too small to measure high energy events well it is hard to control the systematic uncertainties so well. Thus this section compares this to FD MC with a no-extrapolation (see Section 4.6) method. Figure 6.26 shows the energy distributions in 5-45 GeV for all hadronic quartiles for both RHC and FHC. Figure 6.27 and Figure 6.28 show the energy distributions for individual quartiles for FHC and RHC, respectively. From these plots, the prediction and data matches well. The spectra with no oscillations are also shown in these plots. It can be seen there is a small difference between the predictions with and without oscillations. Thus the high energy sample is not able to effectively improve the oscillation parameter measurements. The bottom plots are the cosmic background and beam background distributions. It can be seen there is only a tiny number of background events at high energies.

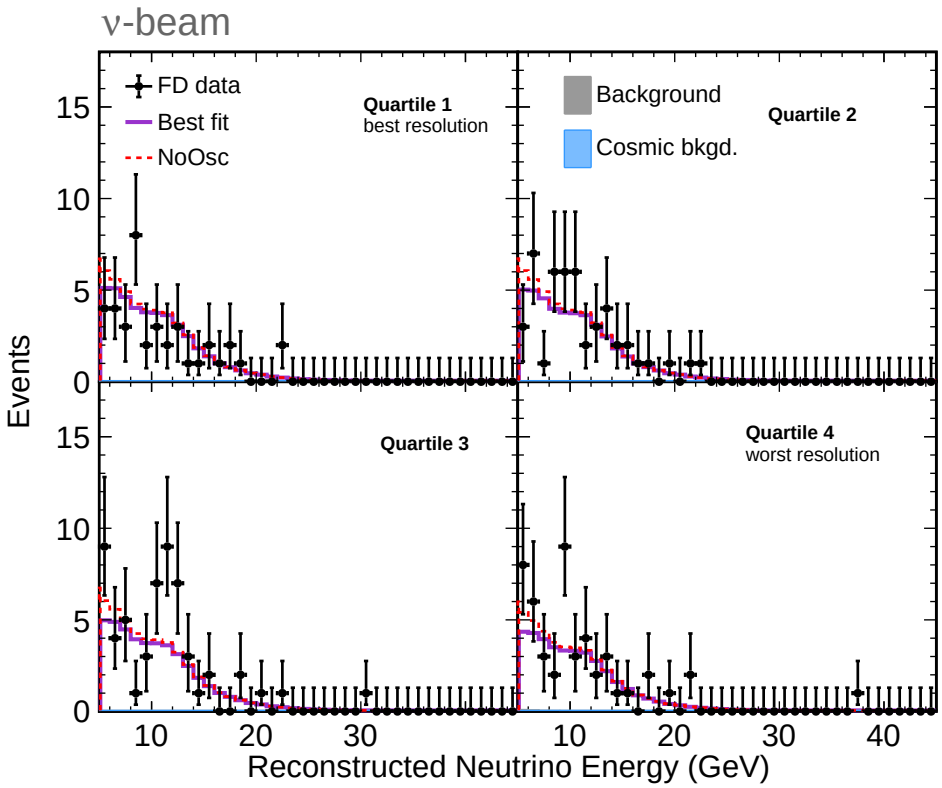

Figure 6.27: Distribution of the reconstructed neutrino energy for the ν_μ CC events in the high energy sample for individual hadronic quartiles at the FD in FHC. Data is shown in black. The prediction at the thesis best fit point is shown by the purple line, and the prediction without oscillations are shown in the dashed red line. The grey and blue stacked histograms show the and cosmic background, respectively.

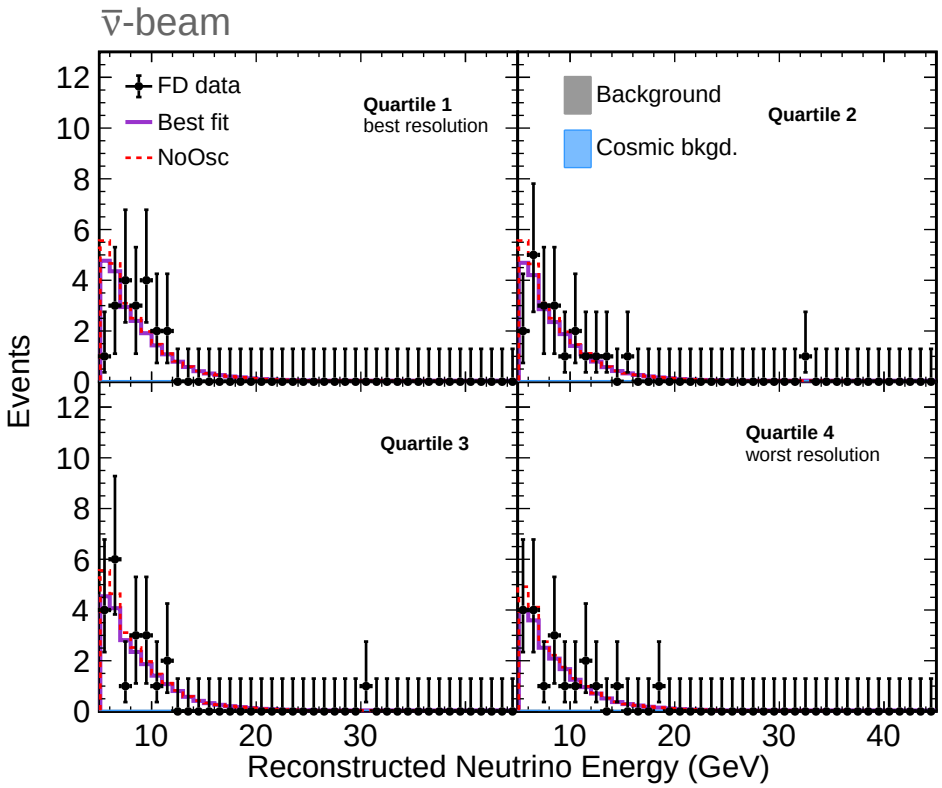

Figure 6.28: Distribution of the reconstructed neutrino energy for the ν_μ CC events in the high energy sample for individual hadronic quartiles at the FD in RHC. Data is shown in black. The prediction at the thesis best fit point is shown by the purple line, and the prediction without oscillations are shown in the dashed red line. The grey and blue stacked histograms show the beam background and cosmic background, respectively.

6.2.3 Results of Δm^2_{32} and $\sin^2\theta_{23}$ measurement

This section shows the plots of confidence intervals resulting from a fit to the data. Figures 6.29 through Figure 6.32 show the measurements of Δm^2_{32} and $\sin^2\theta_{23}$ when considering only the statistical errors. Figures 6.29 and Figures 6.30 show the comparison of contours between the new analysis and NOvA's 2020 analysis for constant $\Delta\chi^2$ (see Equation 4.12) in the Δm^2_{32} vs. $\sin^2\theta_{23}$ space in the normal hierarchy and inverted hierarchy, respectively. The $\Delta\chi^2$ for each point in the 2D surface is obtained by subtracting the global minimum χ^2 from the minimum χ^2 at that point. As described in Section 4.8, other oscillation parameters are profiled over. The 1 σ, 2 σ and 3 σ allowed regions are drawn in dark red (blue) through to light red (blue) using a Gaussian estimate in the new (standard) analysis. It can be seen that the new analysis cause the contours to shrink and move slightly in the direction of smaller Δm^2_{32} and thus the parameters are measured with a better precision. Figures 6.31 and Figure 6.32 show the comparison between the new analysis and NOvA's 2020 analysis for Gaussian significance $\sqrt{\Delta\chi^2}$ as a function of Δm^2_{32} and $\sin^2\theta_{23}$ individually, respectively. It can be seen that the new analysis improves the maximal disappearance significance from 1.16 to 1.36, corresponding to a 17% improvement. The uncertainty on Δm^2_{32} in the new analysis is smaller than the 2020 analysis, for both the normal and inverted hierarchy. Figure 6.33 through Figure 6.36 show the fitting results when considering the statistical and systematic uncertainties. In this case, all the systematic uncertainty parameters and other oscillation parameters are profiled over. The contours of Δm^2_{32} versus $\sin^2\theta_{23}$ show that the constraints with systematic uncertainties are not as tight as the case without systematic uncertainties. As with the statistics only results, it can be seen there is a shift to smaller values of Δm^2_{32} in the new analysis. Additionally, similar to the statistic only contours, the 1 σ, 2 σ and 3 σ allowed regions also shrink compared to the 2020 analysis. Like the description in Section 6.2.1, the uncertainty range of Δm^2_{32} is narrower than NOvA's 2020 analysis. For $\sin^2\theta_{23}$, Figure 6.36 shows that the systematic uncertainties make the maximal disappearance close the 2020 analysis. But the new analysis can still improve the rejection of the other octant more strongly. Figure 6.37 shows the comparison of the contours of Δm^2_{32} versus $\sin^2\theta_{23}$ for the fake data (evaluated at the thesis best fit) and real data. These plots verify that the simulation is consistent with the fit to the real data at the FD.

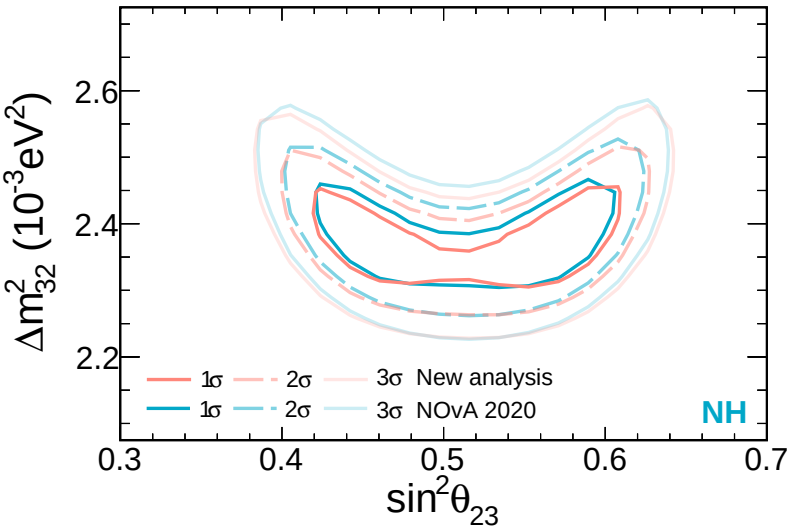

Figure 6.29: Comparison of constraints on the allowed regions as a function of Δm^2_{32} and $\sin^2\theta_{23}$ in the normal hierarchy scenario between the new analysis in this thesis and NOvA's 2020 standard analysis. The borders of the 1 σ, 2 σ and 3 σ allowed Gaussian regions of the new analysis (NOvA's 2020 standard analysis) are shown in dark orange (blue) through to light orange (blue) respectively. Only statistical uncertainty is included here.

6.2.4 Fit results with ν_μ disappearance and ν_e appearance

This section presents the combined fit results with the muon neutrino disappearance and electron neutrino appearance channels. Table 6.3 shows the best fit of oscillation parameters and the corresponding 1 σ range with the combined muon neutrino disappearance and electron appearance analysis, for the new analysis and NOvA's 2020 analysis. The table shows the uncertainty range at 1 σ for Δm^2_{32} is reduced by 3.7% using the new analysis. But there isn't an improvement for $\sin^2\theta_{23}$ uncertainty using the new analysis. Figure 6.38 and Figure 6.39 show the comparison of constraints on the allowed regions as a function of Δm^2_{32} and $\sin^2\theta_{23}$ for the normal hierarchy and inverted hierarchy, respectively. The 1 σ, 2 σ and 3 σ allowed regions of the combined analysis are smaller than the muon neutrino disappearance only analysis. Similar to the muon neutrino disappearance only analysis, the constraints from the new analysis are tighter, and there is a shift along the Δm^2_{32} direction, comparing to the 2020 analysis. Figure 6.40 and Figure 6.41 show the comparison between the new analysis and NOvA's 2020 analysis for Gaussian significance $\sqrt{\Delta\chi^2}$ as a function of $\sin^2\theta_{23}$ and Δm^2_{32}, respectively. It can be seen the new analysis can improve the rejection of the disfavoured octant. Similar to the muon neutrino only

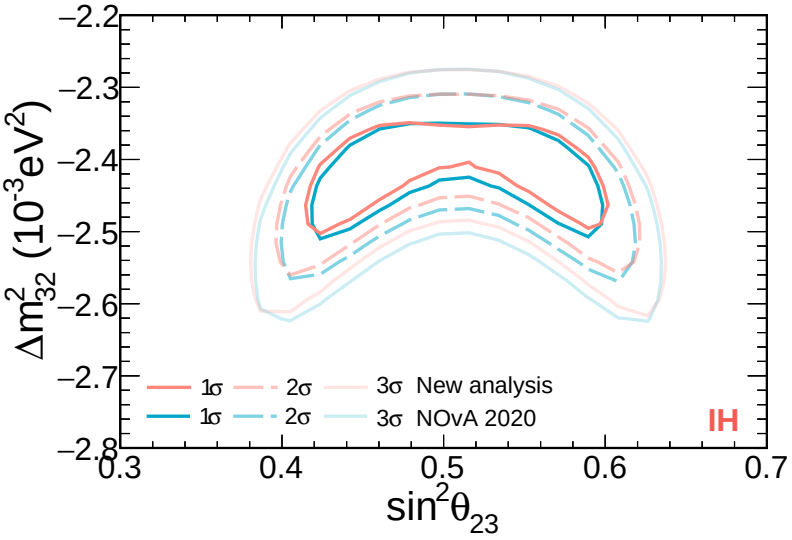

Figure 6.30: Comparison of constraints on the allowed regions as a function of Δm^2_{32} and $\sin^2\theta_{23}$ in the inverted hierarchy scenario between the new analysis in this thesis and NOvA's 2020 standard analysis. The borders of the 1 σ, 2 σ and 3 σ allowed Gaussian regions of the new analysis (NOvA's 2020 standard analysis) are shown in dark orange (blue) through to light orange (blue) respectively. Only statistical uncertainty is included here.

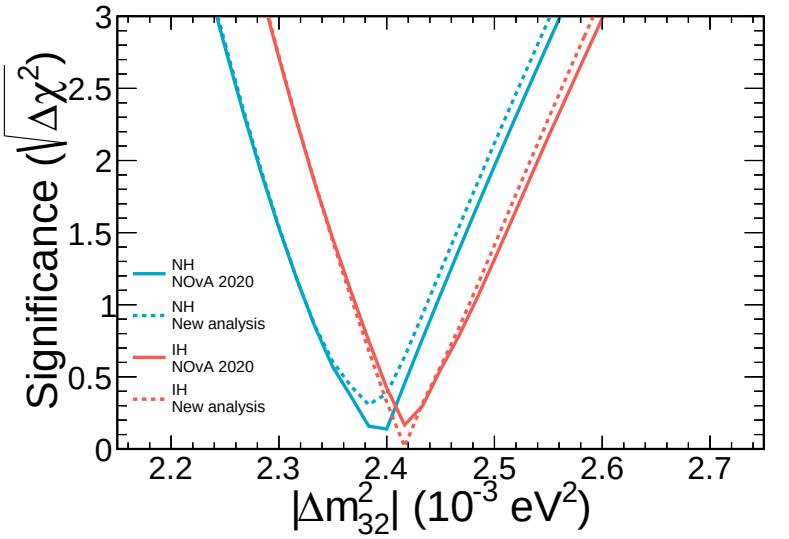

Figure 6.31: Comparison of significance on the measurement of Δm^2_{32} between the new analysis and NOvA's 2020 analysis. Only statistical uncertainty is included here.

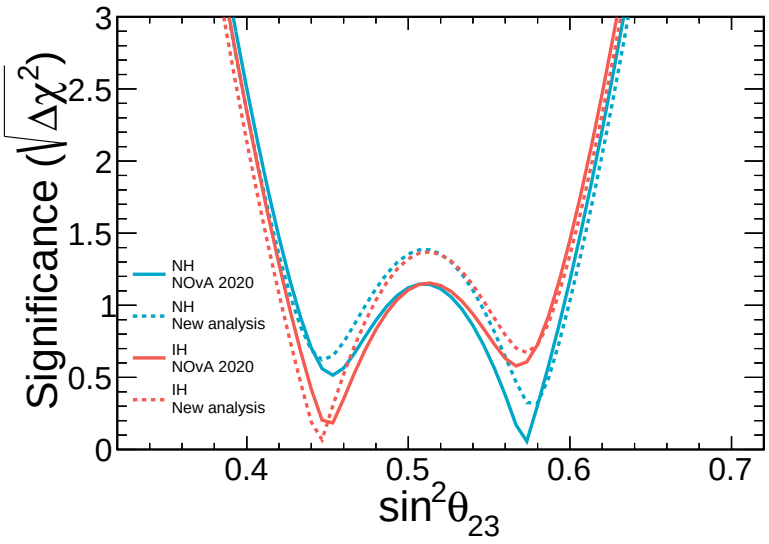

Figure 6.32: Comparison of significance on the measurement of $\sin^2\theta_{23}$ between the new analysis and NOvA's 2020 analysis. Only statistical uncertainty is included here.

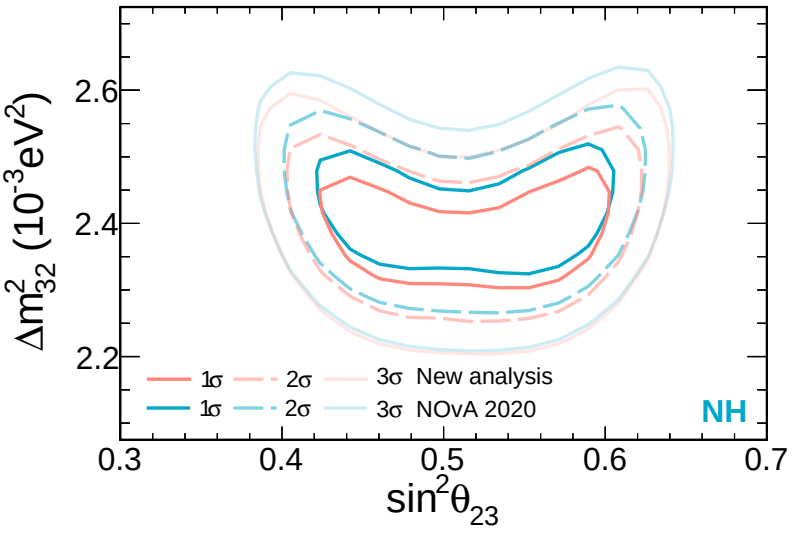

Figure 6.33: Comparison of constraints on the allowed regions as a function of Δm^2_{32} and $\sin^2\theta_{23}$ in the normal hierarchy scenario between the new analysis in this thesis and NOvA's 2020 standard analysis. The borders of the 1 σ, 2 σ and 3 σ allowed Gaussian regions of the new analysis (NOvA's 2020 standard analysis) are shown in dark orange (blue) through to light orange (blue) respectively. All systematic uncertainties are applied.

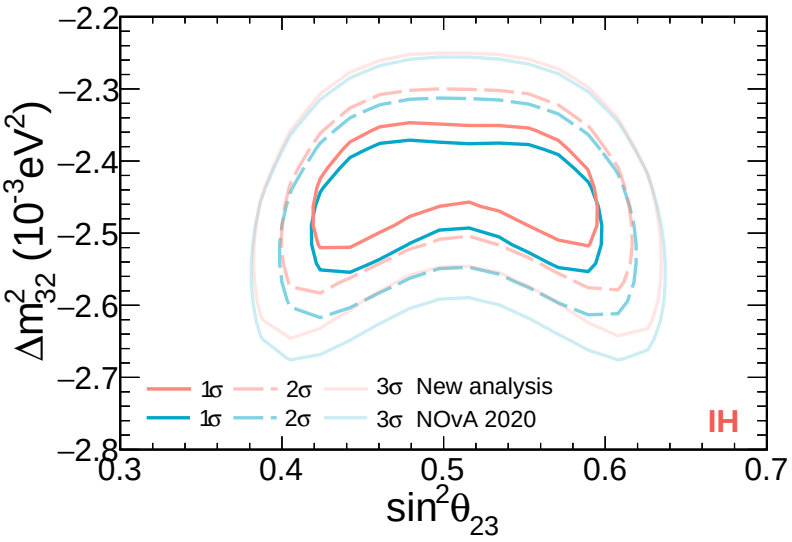

Figure 6.34: Comparison of constraints on the allowed regions as a function of Δm^2_{32} and $\sin^2\theta_{23}$ in the inverted hierarchy scenario between the new analysis in this thesis and the NOvA's 2020 standard analysis. The borders of the 1 σ, 2 σ and 3 σ allowed gaussian regions of the new analysis (NOvA's 2020 standard analysis) are shown in dark red (blue) through to light red (blue) respectively. All systematic uncertainties are applied.

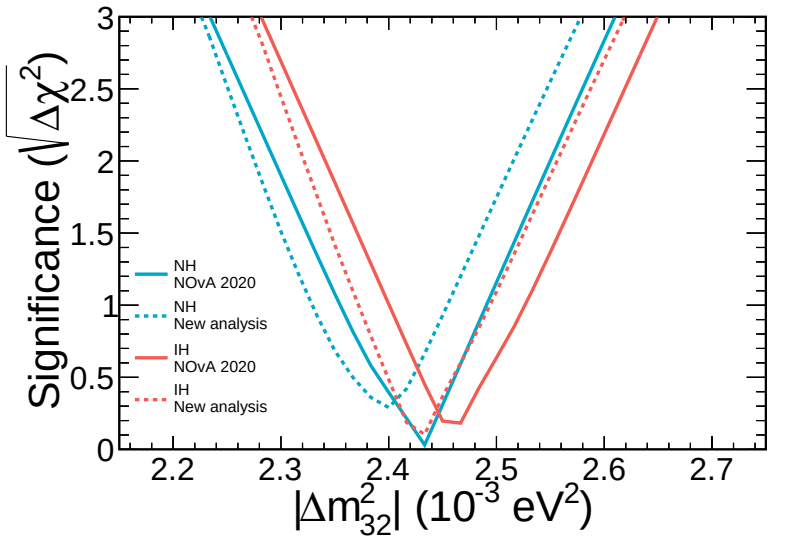

Figure 6.35: Comparison of significance on the measurement of Δm^2_{32} between the new analysis and NOvA's 2020 analysis. All systematic uncertainties are applied.

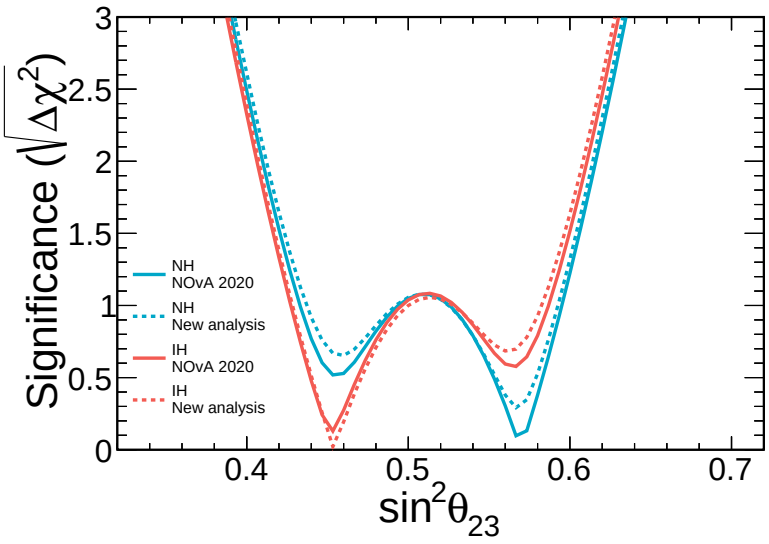

Figure 6.36: Comparison of significance on the measurement of $\sin^2\theta_{23}$ between the new analysis and NOvA's 2020 analysis. All systematic uncertainties are applied.

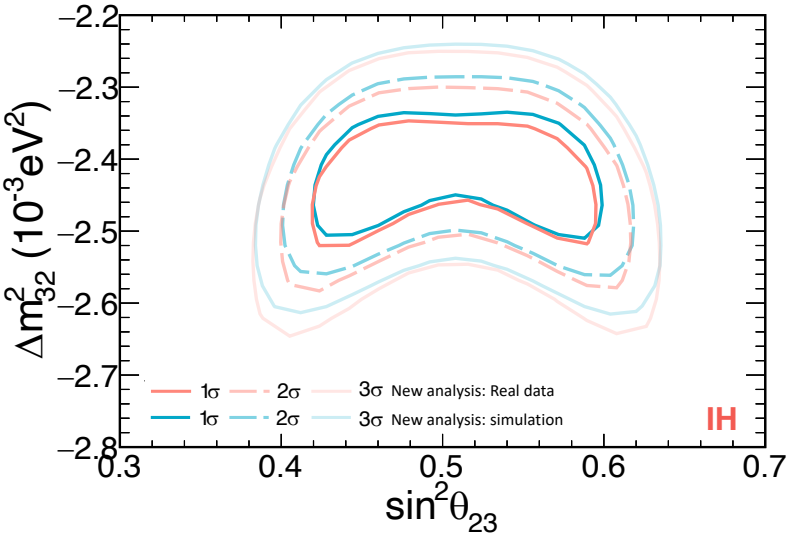

Figure 6.37: Comparison of constraints on the allowed regions as a function of Δm^2_{32} and $\sin^2\theta_{23}$ in the inverted hierarchy scenario between the real data and fake data with the new analysis. All systematic uncertainties are applied.

Parameter	Analysis	Best fit	1 σ range
$\sin^2\theta_{23}$	Standard analysis	0.567	[0.530, 0.592]
	New analysis	0.564	[0.523, 0.588]
Δm^2_{32} ($\times 10^{-3}$ eV^2)	Standard analysis	2.407	[2.354, 2.462]
	New analysis	2.398	[2.346, 2.450]

Table 6.3: Comparison of best fits for the new analysis and standard analysis with the combination of disappearance and appearance channels.

analysis, the Δm^2_{32} significance curve shifts to the left-handed side and the uncertainty range is narrower than the 2020 analysis. Figure 6.42 and Figure 6.43 show the estimated contribution of each category of systematic uncertainty and the statistical uncertainty on the measurements of Δm^2_{32} and $\sin^2\theta_{23}$, respectively, at the best fit point from the ν_e and ν_μ combined analysis. NOvA's 2020 analysis is also shown in the these plots. It can be seen the uncertainty of parameter measurement is still dominated by the statistical uncertainty, rather than the systematic uncertainty. It can be seen the largest category of systematic uncertainty is Detector Calibration for these two parameters. It also can be seen the new analysis reduces both the statistical and systematic uncertainties on Δm^2_{32} and $\sin^2\theta_{23}$.

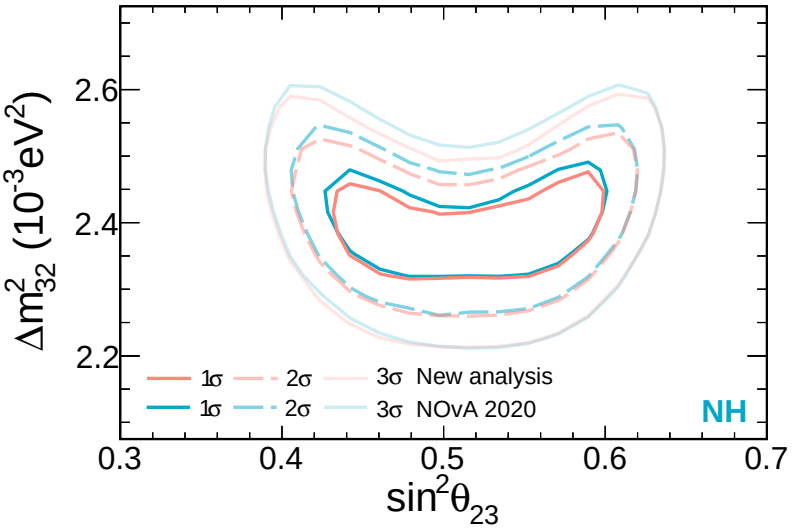

Figure 6.38: Comparison of constraints on the allowed regions as a function of Δm^2_{32} and $\sin^2\theta_{23}$ in the normal hierarchy scenario between the new analysis in this thesis and NOvA's 2020 standard analysis with the combined analysis. The borders of the 1 σ, 2 σ and 3 σ allowed Gaussian regions of the new analysis (NOvA's 2020 standard analysis) are shown in dark orange (blue) through to light orange (blue) respectively. All systematic uncertainties are applied.

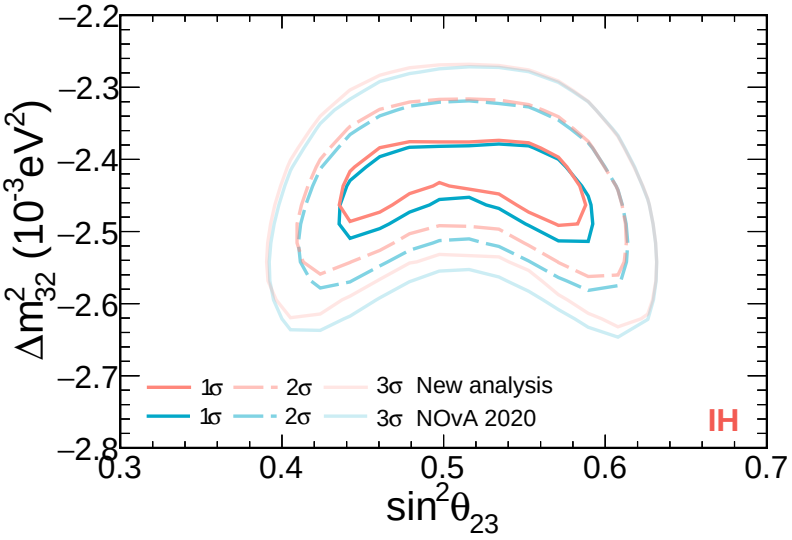

Figure 6.39: Comparison of constraints on the allowed regions as a function of Δm^2_{32} and $\sin^2\theta_{23}$ in the inverted hierarchy scenario between the new analysis in this thesis and NOvA's 2020 standard analysis with the combined analysis. The borders of the 1 σ, 2 σ and 3 σ allowed Gaussian regions of the new analysis (NOvA's 2020 standard analysis) are shown in dark orange (blue) through to light orange (blue) respectively. All systematic uncertainties are applied.

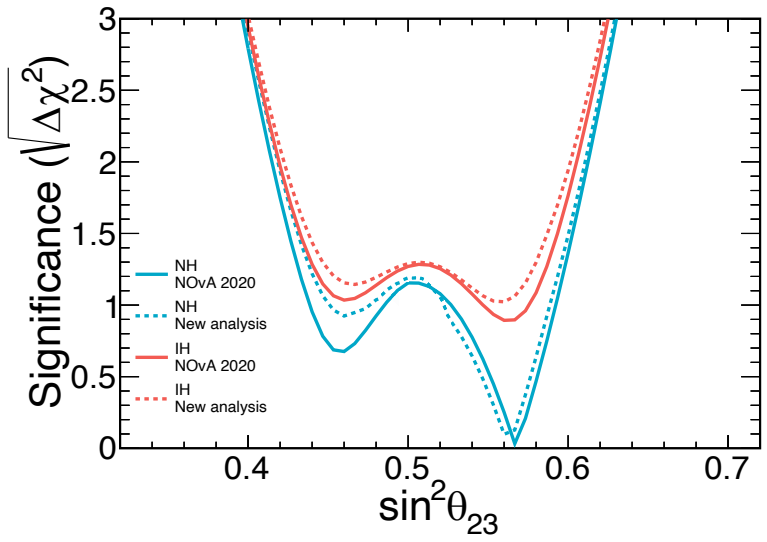

Figure 6.40: Comparison of significance on the measurement of $\sin^2\theta_{23}$ between the new analysis and NOvA's 2020 analysis with the combined analysis. All systematic uncertainties are applied.

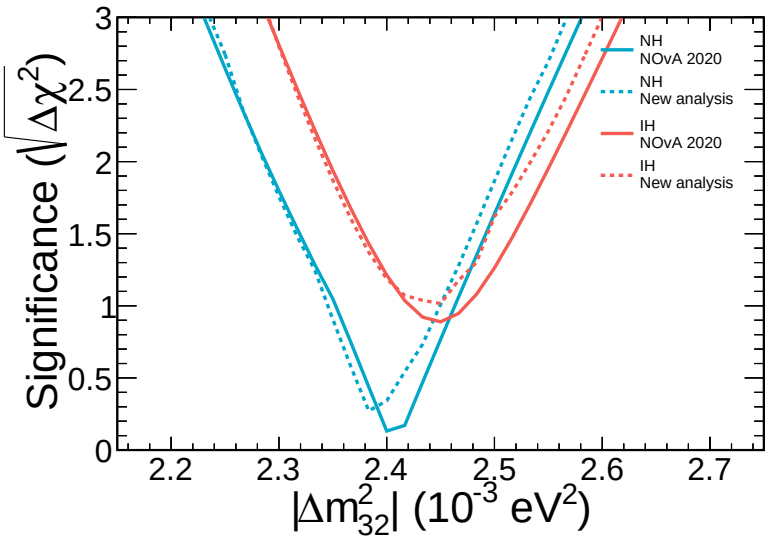

Figure 6.41: Comparison of significance on the measurement of $|\Delta m^2_{32}|$ between the new analysis and NOvA's 2020 analysis with the combined analysis. All systematic uncertainties are applied.

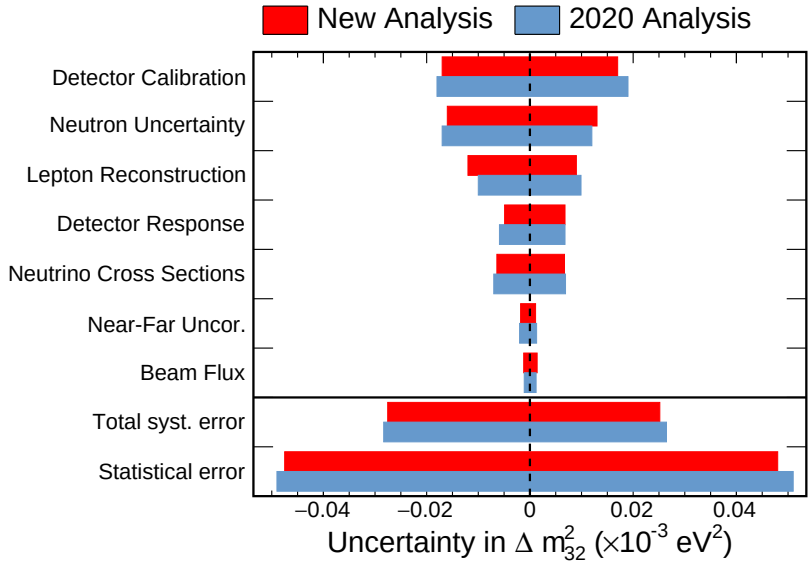

Figure 6.42: The simulated contribution of each category of systematic uncertainty and statistical uncertainty on Δm^2_{32} at the thesis best fit in the ν_μ and ν_e combined analysis. The new analysis (red) is compared to the standard analysis (blue).

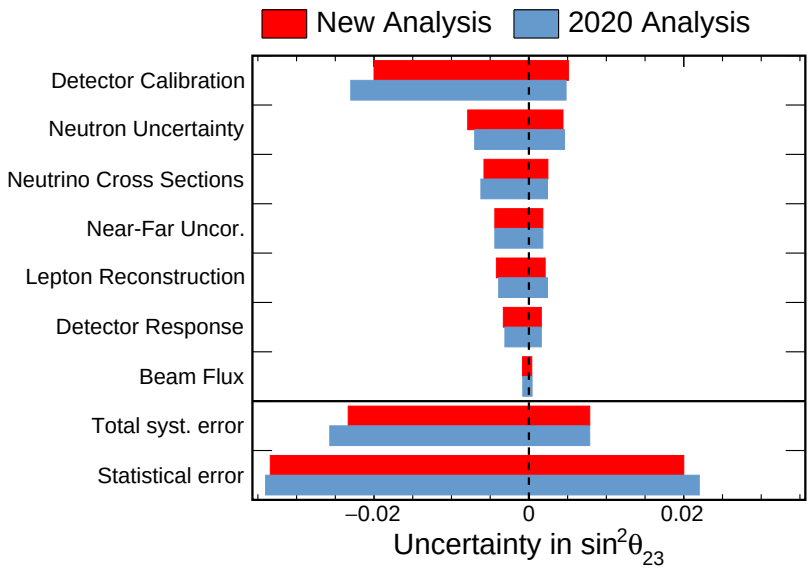

Figure 6.43: The simulated contribution of each category of systematic uncertainty and statistical uncertainty on $\sin^2\theta_{23}$ at the thesis best fit in the ν_μ and ν_e combined analysis. The new analysis (red) is compared to the standard analysis (blue).

Chapter 7

Conclusion

This thesis has presented a new analysis method aimed to improved sensitivity to the parameters $|\Delta m^2_{32}|$ and θ_{23} in the ν_μ disappearance using the NOvA data collected during 2014 to 2020, which corresponds an exposure of 12.50×10^{20} protons on target (POT) in the antineutrino beam mode and 13.60×10^{20} protons on target (POT) in the neutrino beam mode.

Several methodologies have been found to improve the muon neutrino disappearance analysis. First, adding in an additional low PID sample and binning this sample with two particle identifiers, CosPID and CVN bins. Second, the new analysis in this thesis has introduced a new energy estimator developed by the NOvA collaboration. This energy estimator uses both slice and prong level inputs to a LSTM neural network and has shown better performance in energy resolution compared to the standard energy estimator. Third, for the standard sample, in order to separate backgrounds from signals, this thesis has introduced a PID binning which involves three particle identifiers: CVN, ReMId and CosPID. Finally, a finer energy binning that can improve the sensitivity of the standard sample has been used. This fine energy binning was shown not to improve the sensitivity effectively in the low PID sample, and so it is not used there.

Chapter 5 has implemented a fit to Asimov fake data, generated where $\sin^2\theta_{23} = 0.59$ and $\Delta m^2_{32} = 2.5 \times 10^{-3}$ eV^2. The fake data is fit assuming the normal hierarchy. These sensitivity studies show that the uncertainty range of $|\Delta m^2_{32}|$ at 1 σ for the new analysis is reduced by 6.1% (5.5%) compared to the standard analysis, and the significance of maximal disappearance rejection improves by 9.7% (7.7%), when only statistics (all systematic uncertainties) is (are) considered. The best fit values of the oscillation parameters from fitting to FD data with the new analysis are found to be $\sin^2\theta_{23} = 0.568^{+0.025}_{-0.043}$ ($\sin^2\theta_{23} = 0.454^{+0.046}_{-0.026}$) and $\Delta m^2_{32} = 2.399^{+0.055}_{-0.070} \times 10^{-3}$ eV^2($\Delta m^2_{32} = -2.427^{+0.055}_{-0.067} \times 10^{-3}$ eV^2) for

the normal (inverted) hierarchy with a χ^2 of 488.9 (488.8). The difference for $\sin^2\theta_{23}$ (Δm^2_{32}) between the new analysis and NOvA's 2020 analysis is around 2% (1.35%). The uncertainty range at 1 σ for Δm^2_{32} decrease by 8% (4%) for the normal hierarchy (inverted hierarchy) compared to the standard analysis. The uncertainty range for $\sin^2\theta_{23}$ is close to the standard analysis, due to the systematic uncertainties. This thesis also produces new results from combining electron neutrino appearance and muon neutrino disappearance. The combined fit shows that the best fit values are very close to the standard analysis. However, the uncertainty range of Δm^2_{32} at 1 σ is reduced by 3.7% using the new analysis. Similar to the muon neutrino only analysis, the maximal disappearance significance is not improved in the new analysis, but the new analysis slightly improves the rejection of the disfavoured octant.

If I had more time to improve the analysis, I would optimise the new analysis from three directions. First, I would optimise the PID binning in the standard sample. In this thesis, the four hadronic quartile samples use the same PID binning to separate signals from backgrounds. The Quartile 1 and Quartile 2 samples include a small number of background events, therefore it is probably reasonable to develop less (1 or 2) PID bins for Quartile 1 and Quartile 2 samples to reduce the amount of computing resources and time. Second, I would return to study the HadNHits binning further, since it has a good performance in improving the maximal mixing rejection. Third, I would try to implement a more reasonable systematic uncertainty of muon energy. In this thesis, I applied a correlated 1% muon energy uncertainty. But that is an approximated and conservative way. It is reasonable to also try both correlated and uncorrelated uncertainties. It is also reasonable to adjust the shift size to make this systematic uncertainty more closer to the official muon energy uncertainty.

In the future, NOvA aims to collect the data in both horn currents into 2027. The current projection of the ultimate exposure delivered to NuMI is between 60 and 70 $\times 10^{20}$ protons on target [113]. Since more data will be gathered, the parameter measurements will become more affected by systematic uncertainty. As is shown in Figure 6.42 and Figure 6.43, the measurement of $\sin^2\theta_{23}$ and Δm^2_{32} are still statistics limited. The reduction of statistical uncertainty can be roughly calculated by the improvement of square root of exposure. In the new analysis, the statistical uncertainty of Δm^2_{32} will become [-0.018, +0.018], which is smaller than the systematic uncertainty [-0.027, +0.025], when assuming an an exposure of 70×10^{20} protons on target and assuming the systematic uncertainties remain the same. In a similar way, NOvA's future measurement of $\sin^2\theta_{23}$ will become

[-0.012, +0.007], which is smaller than the systematic uncertainty [-0.023, +0.007].

Future long-baseline experiments, such as DUNE [53] and Hyper-K [54], with more powerful beams and detectors, will be able to make far more sensitive measurements. Hyper-K has the ability to exclude the CP conserved case with more than 5-σ significance for 57% of the possible values of δ_{CP} when the normal hierarchy is assumed after 10 years of running. Hyper-K will have significant sensitivity to the θ_{23} octant for values of $\sin^2\theta_{23}$ less than about 0.46 and greater than about 0.57 and precisely determine $\sin^2\theta_{23}$ with a 1-σ uncertainty less than 0.01. The uncertainty of Δm^2_{32} by Hyper-K is expected to reach 0.6%, while reactor neutrino experiments are expected to achieve $< 1\%$ precision. DUNE will be able to the determine neutrino mass hierarchy at the 5-σ level for 100% of δ_{CP} values within three years. With 10 years of running, DUNE has the ability to exclude the CP conserved case at 5-σ for greater than 50% of δ_{CP}'s range. With 15 years of running, DUNE will have significant sensitivity to the θ_{23} octant for values of $\sin^2\theta_{23}$ less than about 0.47 and greater than about 0.55. These future experiments aim to take data towards 2030. Before 2027, with an upgraded beam facility, NOvA will collect more data and give more precise results of neutrino oscillations.

Appendices

Appendix A

Definitions of Variables

HadNHit Number of Hadronic Hits

KalPtP Transverse momentum fraction of the muon

KalCosNumi Kalman track $\cos\theta_{\mathrm{NuMI}}$ (θ_{NuMI} is the angle of the muon track with respect to the beam direction)

HadEPerNHit Average Hadronic Energy per Hit

KalTrkNPlaneGapFrac Fraction of Missing Planes in Track

NPng2d Number of 2D Prongs

NCellsEdge Number of Cells from detector Edge in a slice

kBPFBestMuonStartX BPF track start X [m]

KalmanTrkStartX Kalman Track Start X [m]

CVN ConVolutional Network score

KalmanTrkStartY Kalman Track Start Y [m]

kBPFBestMuonStartY BPF track start Y [m]

kBPFBestMuonStopX BPF track stop X [m]

kBPFBestMuonStopY BPF track stop Y [m]

KalmanTrkEndX Kalman Track End X [m]

KalNPlaneGapLength Track missing planes/length

KalmanTrkEndY Kalman Track End Y [m]

NumuHadCalE Off Track Calorimetric Hadronic Energy [GeV]

kBPFBestMuonStopZ BPF track stop Z [m]

KalmanTrkEndZ Kalman Track End Z [m]

kBPFBestMuonStartZ BPF track start Z [m]

KalmanTrkStartZ Kalman Track Start Z [m]

ReMId Reconstruction Muon Identification score

CosPID ν_μ Cosmic rejection BDT

MuEPerNHit Average Reconstructed Muon Energy Per Hit [GeV]

KalNhitLength Ratio of Number of hits Kalman Track to the track length

KalTrkCalE Calorimetric Energy of Kalman Track [GeV]

NumuHadTrkE Calorimetric Hadronic Energy [GeV] on Track

KalTrkOverlapE Hadronic Energy Overlap on Kalman Track

KalTrkNPlaneGap Missing Planes in Tracks

scatLL ReMId Input: Scattering Log-likelihood

HadEFrac Hadronic Energy Fraction

KalTrkLength Kalman Track Length

nonHadPlaneFrac ReMId Input: Non-hadronic Plane Fract

KalTrkCalEPerNHit Average Calorimetric Energy on Kalman Track Per Hit [GeV]

MuE Muon Energy

NumuHadVisE Visible Hadronic Energy [GeV]

NPng3d Number of 3D Prongs

dedxLL ReMId Input: dE/dx Log-likelihood

HadE Reconstructed Hadronic Energy [GeV]

kNKalman Number of Kalman Tracks in Slice

Appendix B

Supplementary Comparison Plots of Data versus Simulation

This appendix presents some distributions of the reconstructed variables at the ND and FD. These plots are mentioned and discussed in Chapter 6.

B.0.1 Distributions of variables in the standard sample at the ND

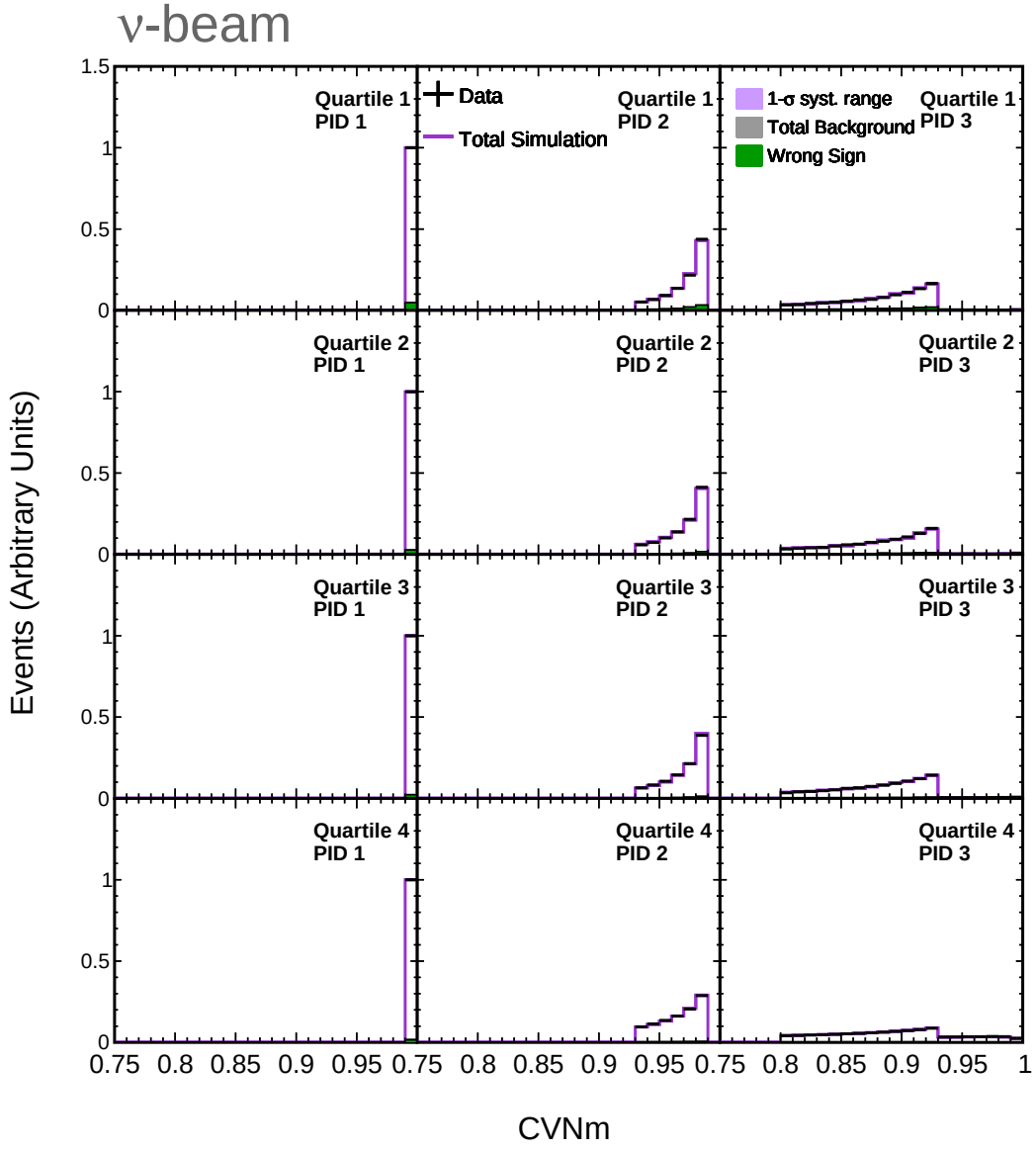

Figure B.1: Distribution of the CVN muon identification score in data (black) compared to the MC total prediction (purple) with the systematic shape uncertainty band (purple shaded region) in the standard ν_μ candidate sample at the ND in FHC. The wrong sign and total background are shown in green and grey respectively by stacked histograms. Both data and MC are normalised to one.

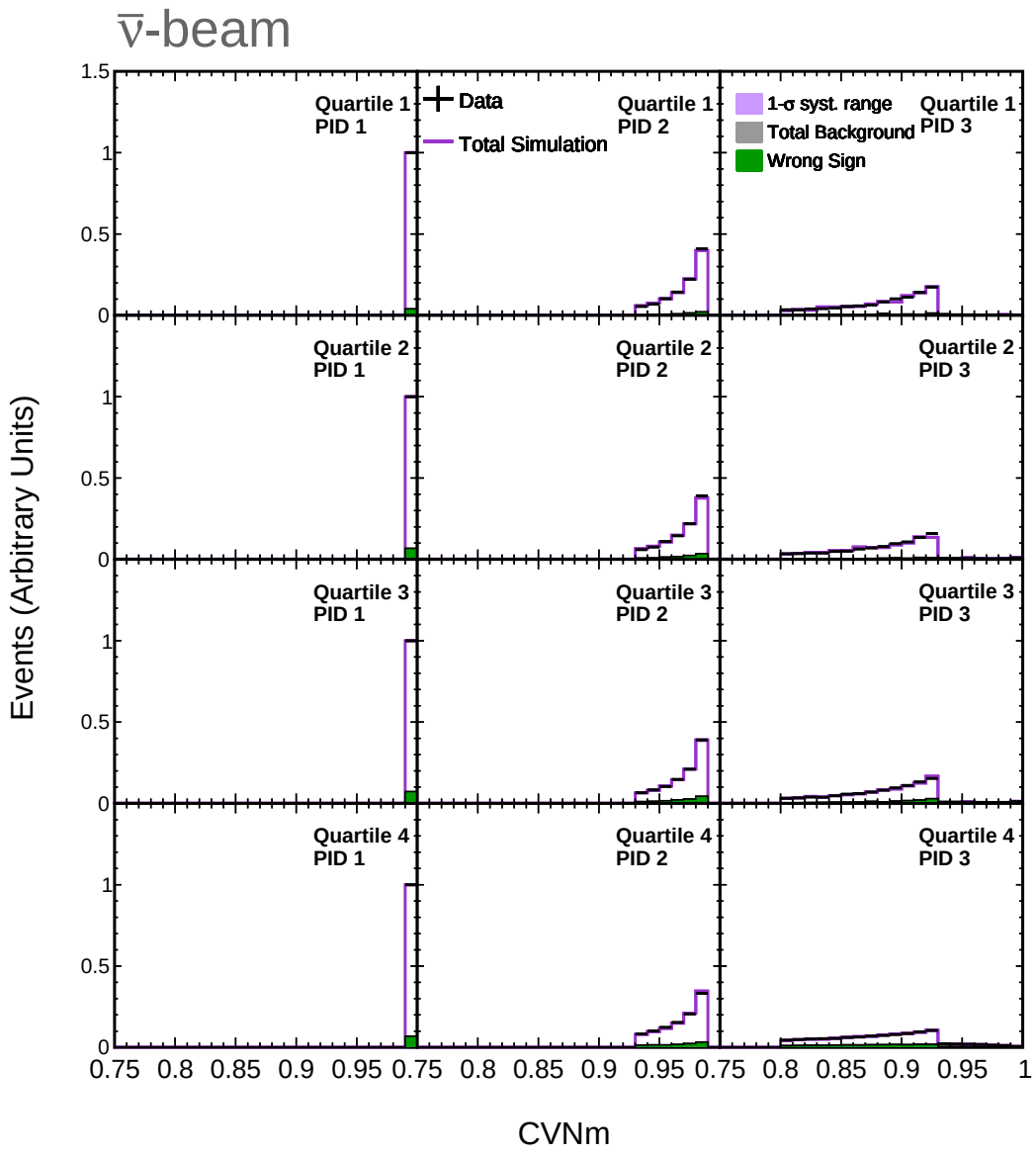

Figure B.2: Distribution of the CVN muon identification score in data (black) compared to the MC total prediction (purple) with the systematic shape uncertainty band (purple shaded region) in the standard ν_μ candidate sample at the ND in RHC. The wrong sign and total background are shown in green and grey respectively by stacked histograms. Both data and MC are normalised to one.

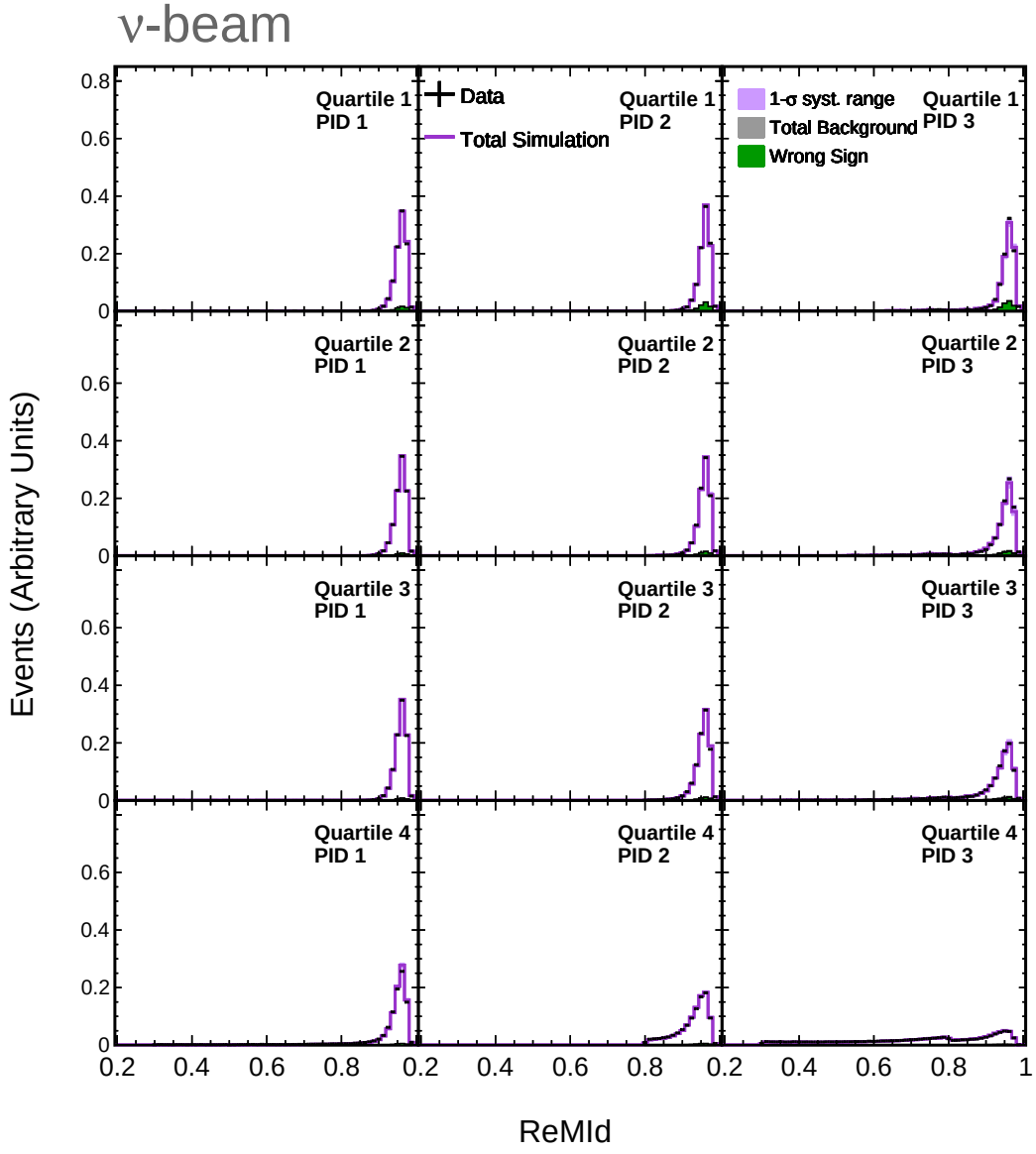

Figure B.3: Distribution of the ReMId muon identification score in data (black) compared to the MC total prediction (purple) with the systematic shape uncertainty band (purple shaded region) in the standard ν_μ candidate sample at the ND in FHC. The wrong sign and total background are shown in green and grey respectively by stacked histograms. Both data and MC are normalised to one.

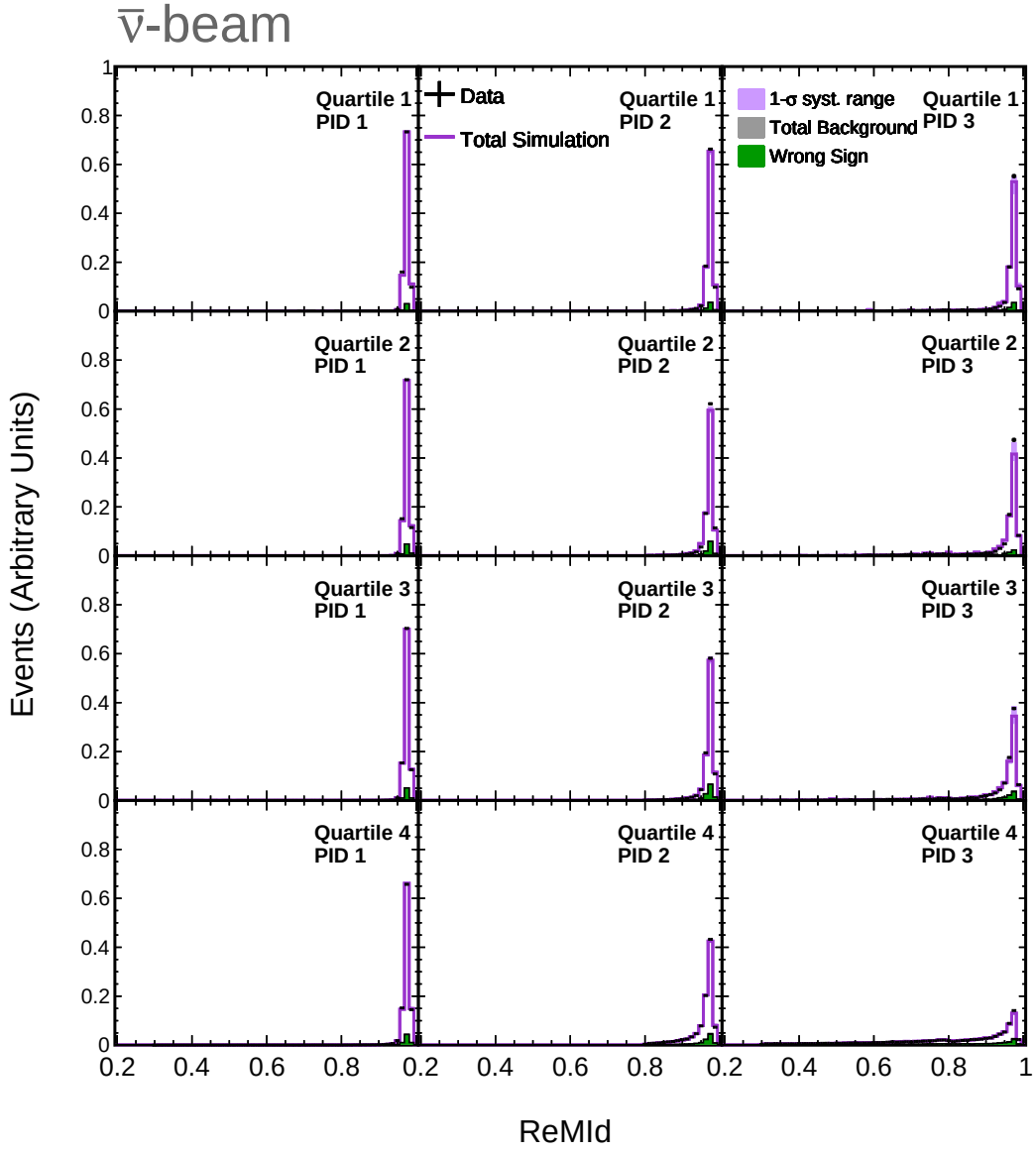

Figure B.4: Distribution of the ReMId muon identification score in data (black) compared to the MC total prediction (purple) with the systematic shape uncertainty band (purple shaded region) in the standard ν_μ candidate sample at the ND in RHC. The wrong sign and total background are shown in green and grey respectively by stacked histograms. Both data and MC are normalised to one.

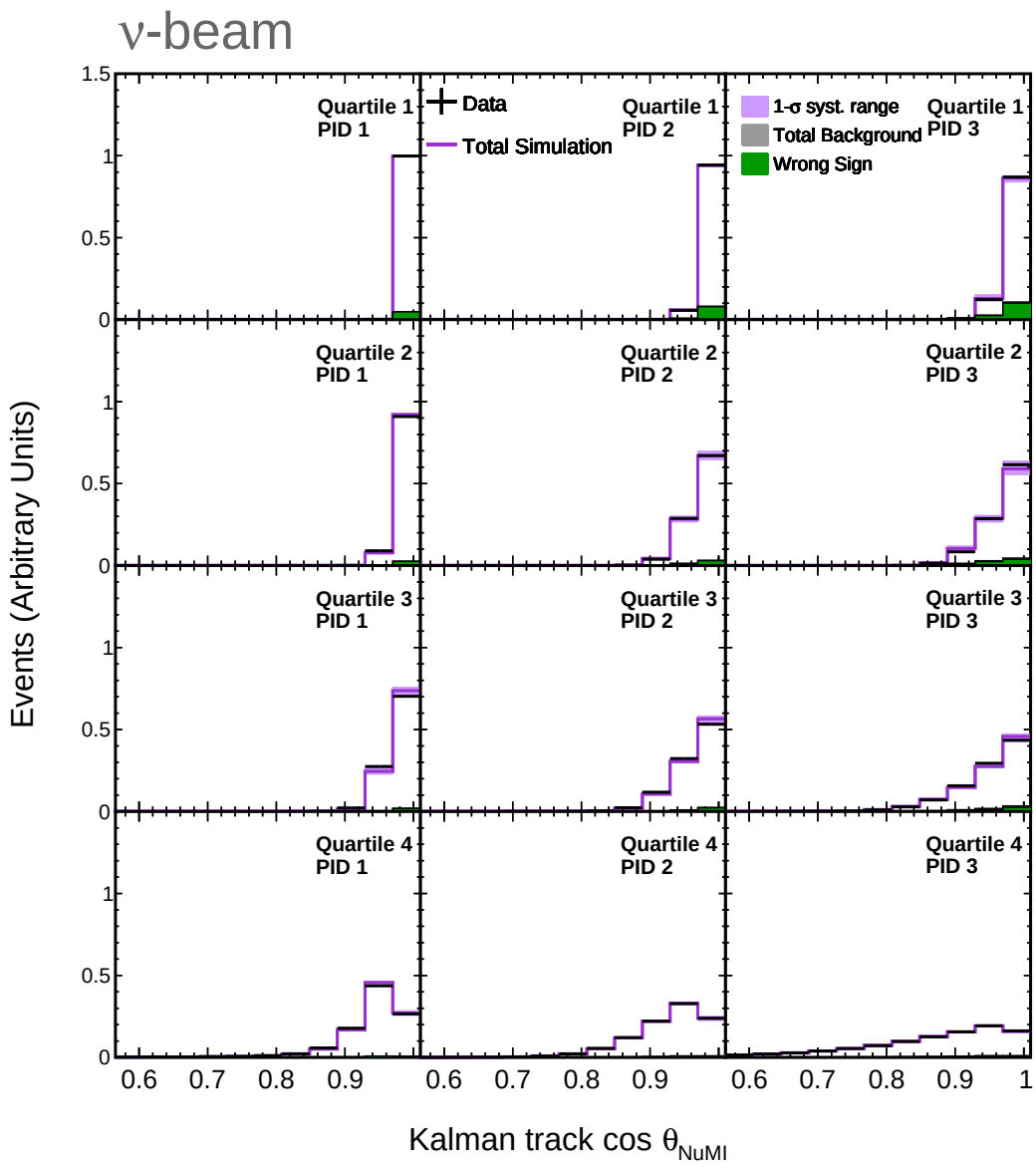

Figure B.5: Distribution of the $\cos\theta_{\mathrm{NuMI}}$ (where θ_{NuMI} is the angle of the muon track with respect to the beam direction) in data (black) compared to the MC total prediction (purple) with the systematic shape uncertainty band (purple shaded region) in the standard ν_μ candidate sample at the ND in FHC. The wrong sign and total background are shown in green and grey respectively by stacked histograms. Both data and MC are normalised to one.

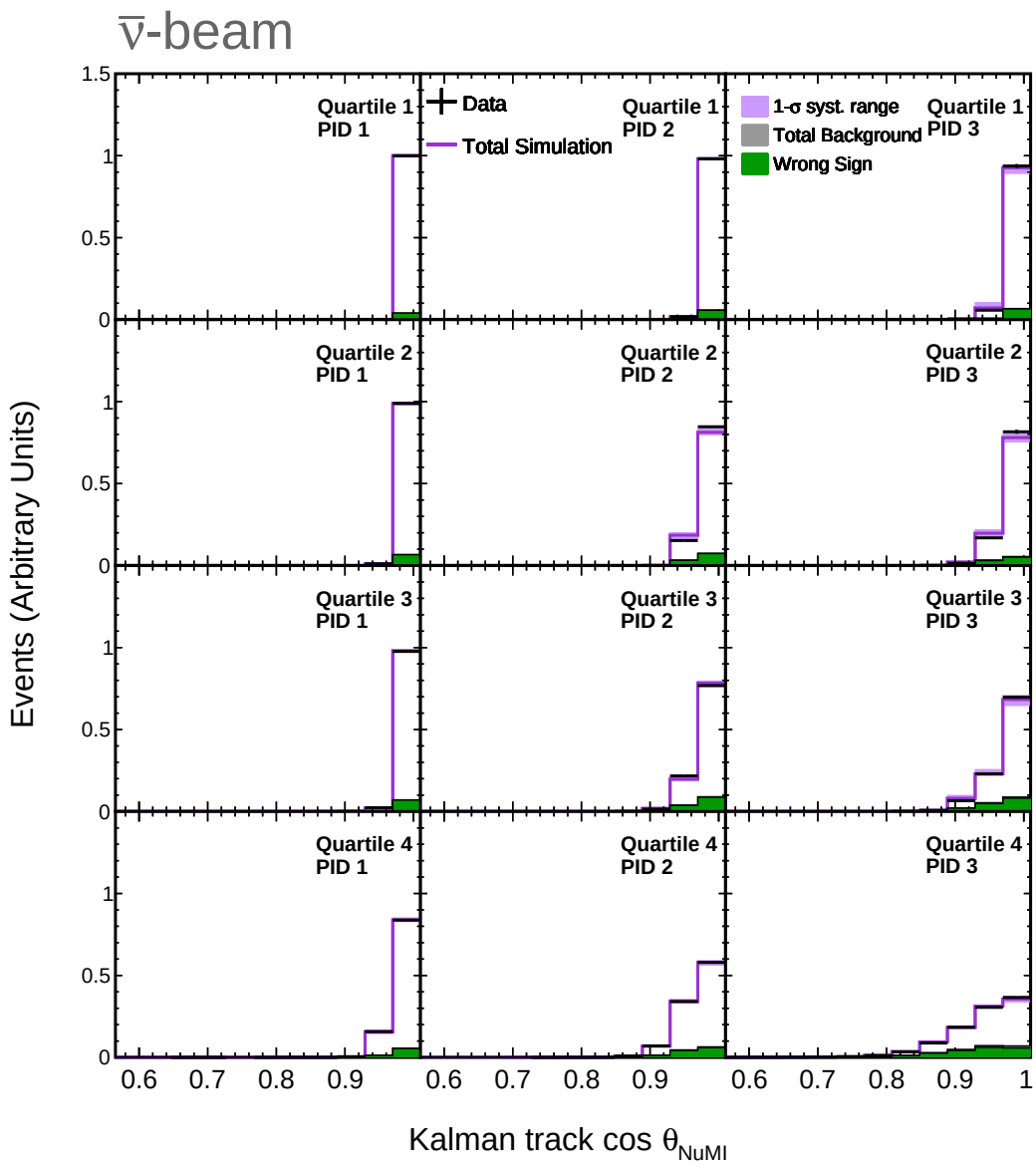

Figure B.6: Distribution of the $\cos\theta_{\mathrm{NuMI}}$ (where θ_{NuMI} is the angle of the muon track with respect to the beam direction) in data (black) compared to the MC total prediction (purple) with the systematic shape uncertainty band (purple shaded region) in the standard ν_μ candidate sample at the ND in RHC. The wrong sign and total background are shown in green and grey respectively by stacked histograms. Both data and MC are normalised to one.

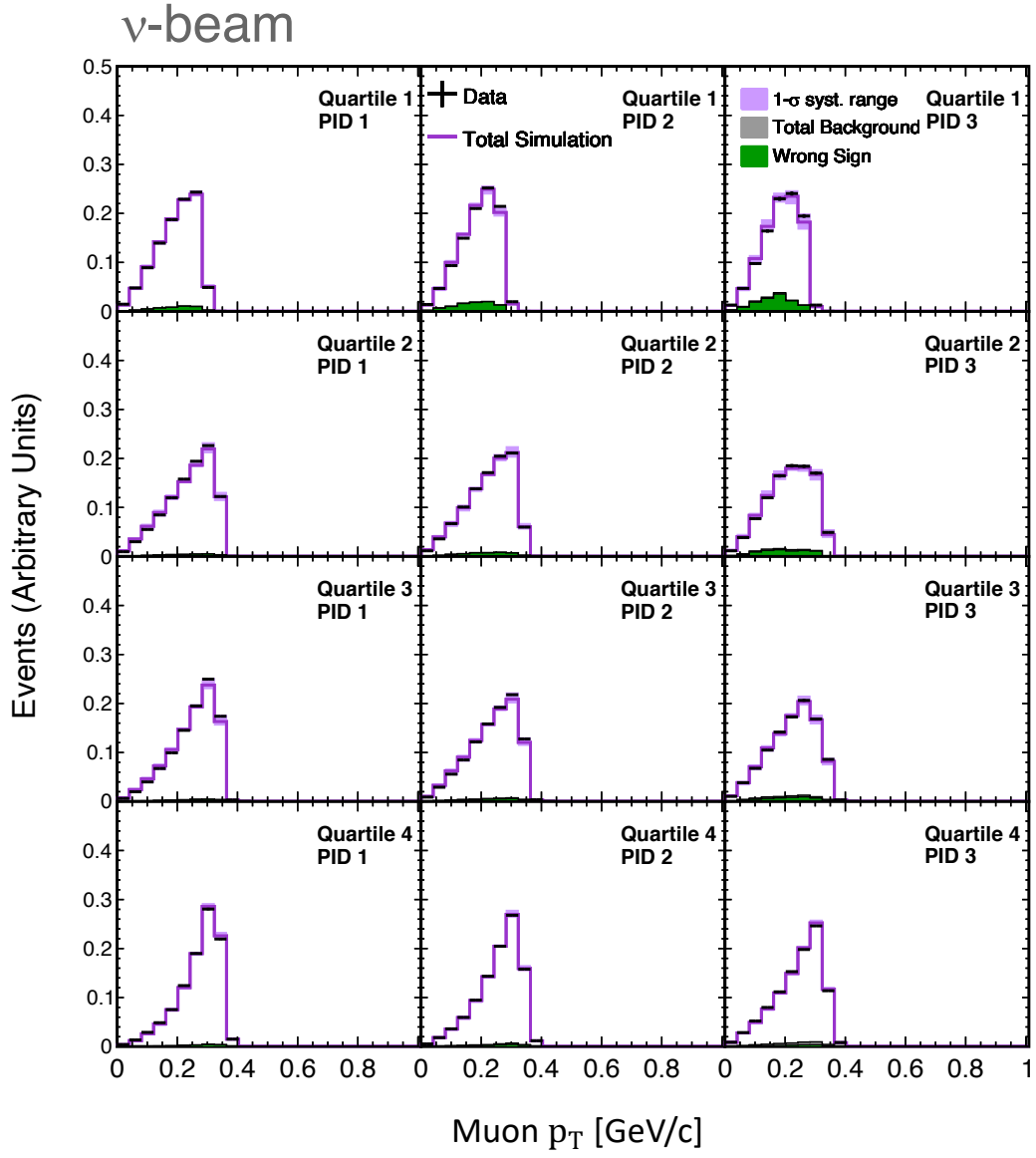

Figure B.7: Distribution of the transverse momentum in data (black) compared to the MC total prediction (purple) with the systematic shape uncertainty band (purple shaded region) in the standard ν_μ candidate sample at the ND in FHC. The wrong sign and total background are shown in green and grey respectively by stacked histograms. Both data and MC are normalised to one.

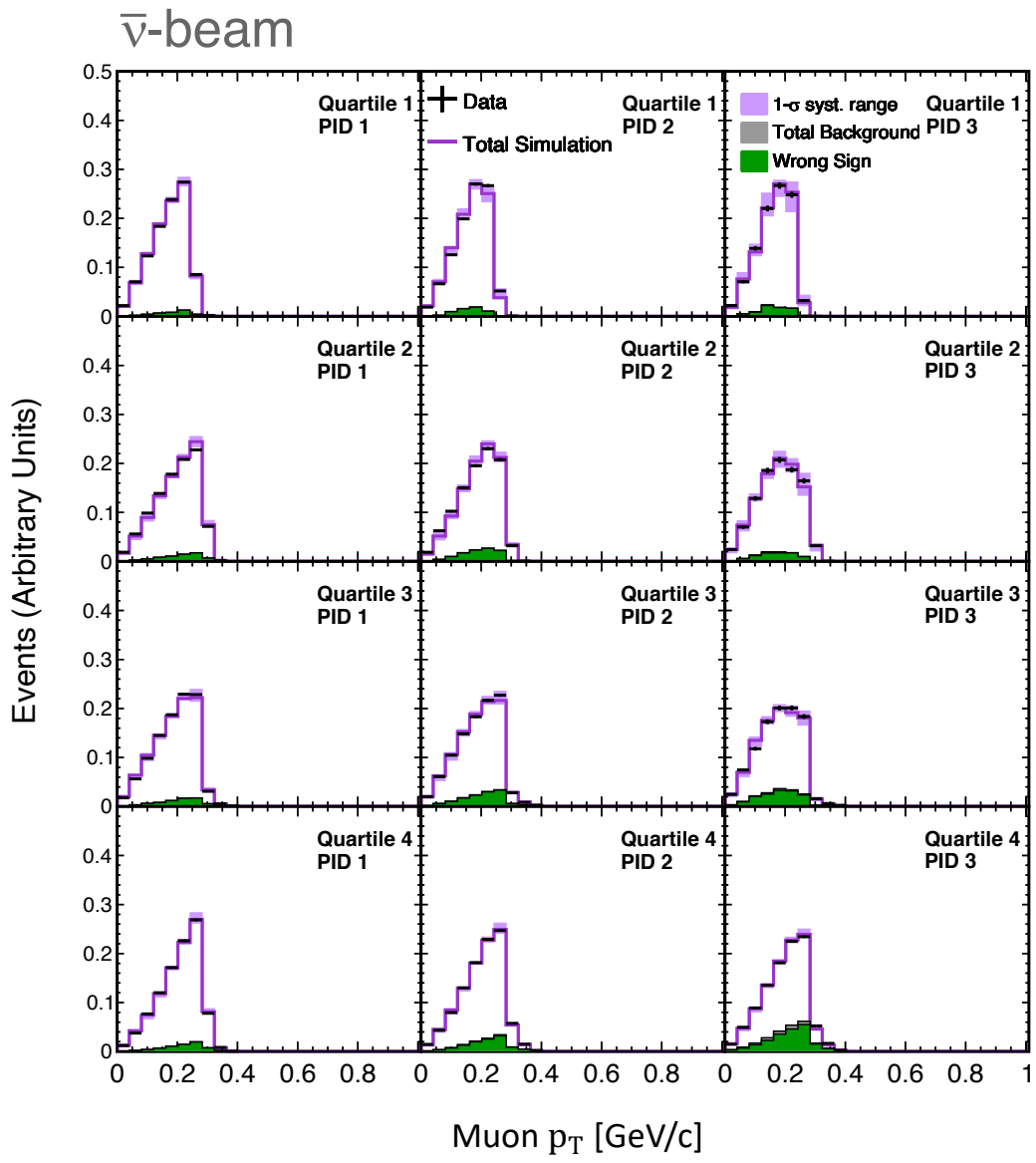

Figure B.8: Distribution of the transverse momentum in data (black) compared to the MC total prediction (purple) with the systematic shape uncertainty band (purple shaded region) in the standard ν_μ candidate sample at the ND in RHC. The wrong sign and total background are shown in green and grey respectively by stacked histograms. Both data and MC are normalised to one.

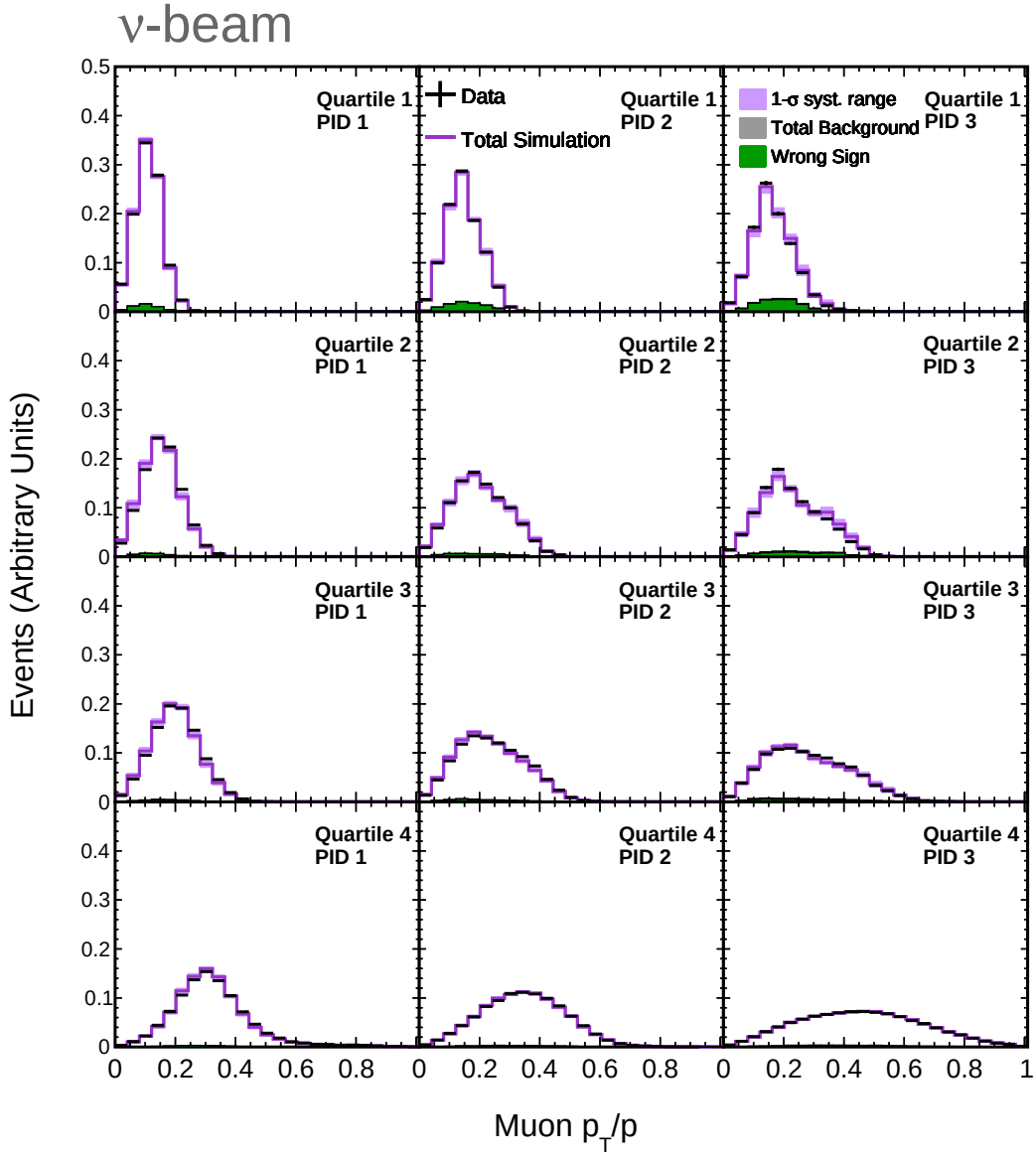

Figure B.9: Distribution of the transverse momentum fraction in data (black) compared to the MC total prediction (purple) with the systematic shape uncertainty band (purple shaded region) in the standard ν_μ candidate sample at the ND in FHC. The wrong sign and total background are shown in green and grey respectively by stacked histograms. Both data and MC are normalised to one.

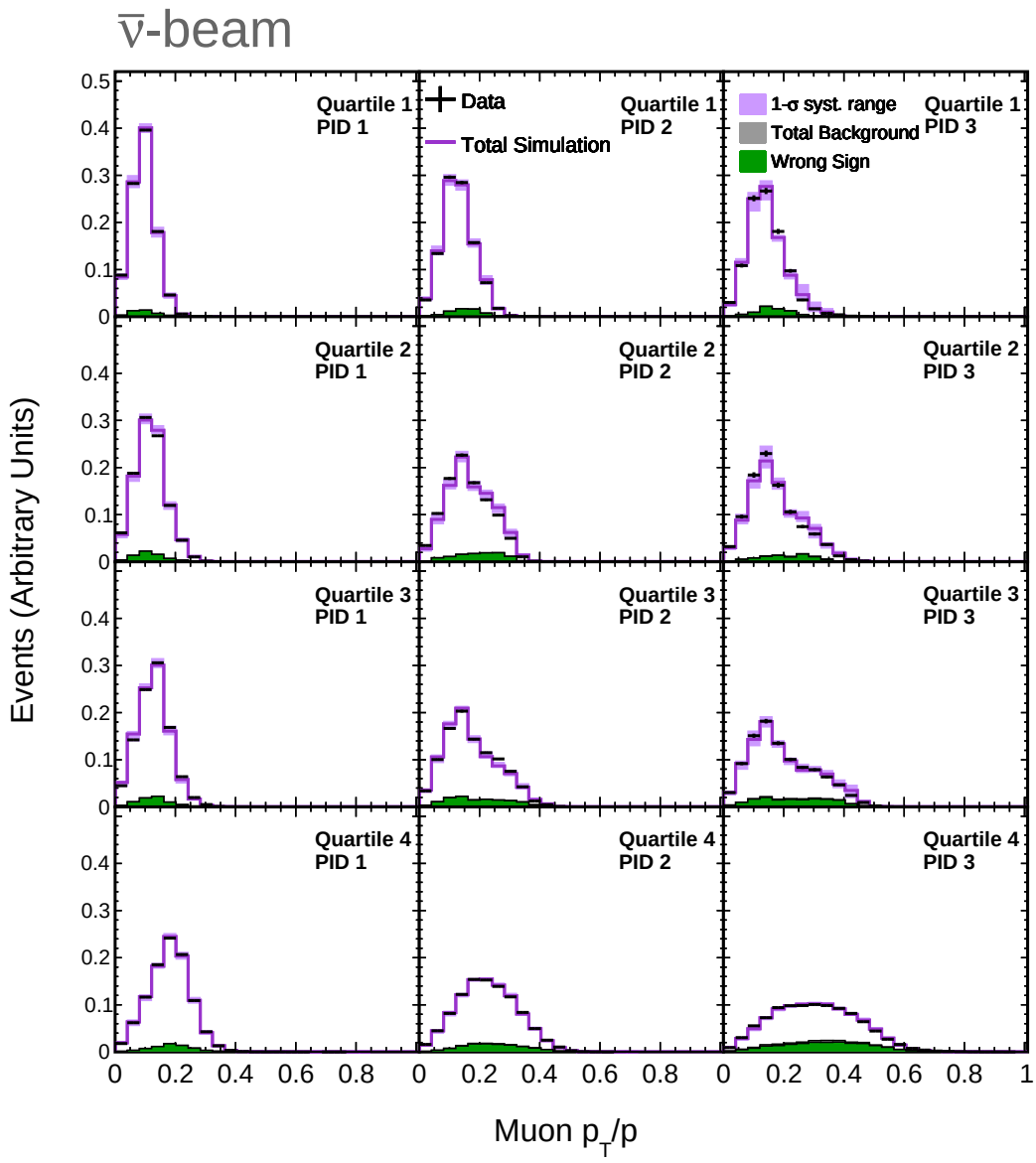

Figure B.10: Distribution of the transverse momentum fraction in data (black) compared to the MC total prediction (purple) with the systematic shape uncertainty band (purple shaded region) in the standard ν_μ candidate sample at the ND in RHC. The wrong sign and total background are shown in green and grey respectively by stacked histograms. Both data and MC are normalised to one.

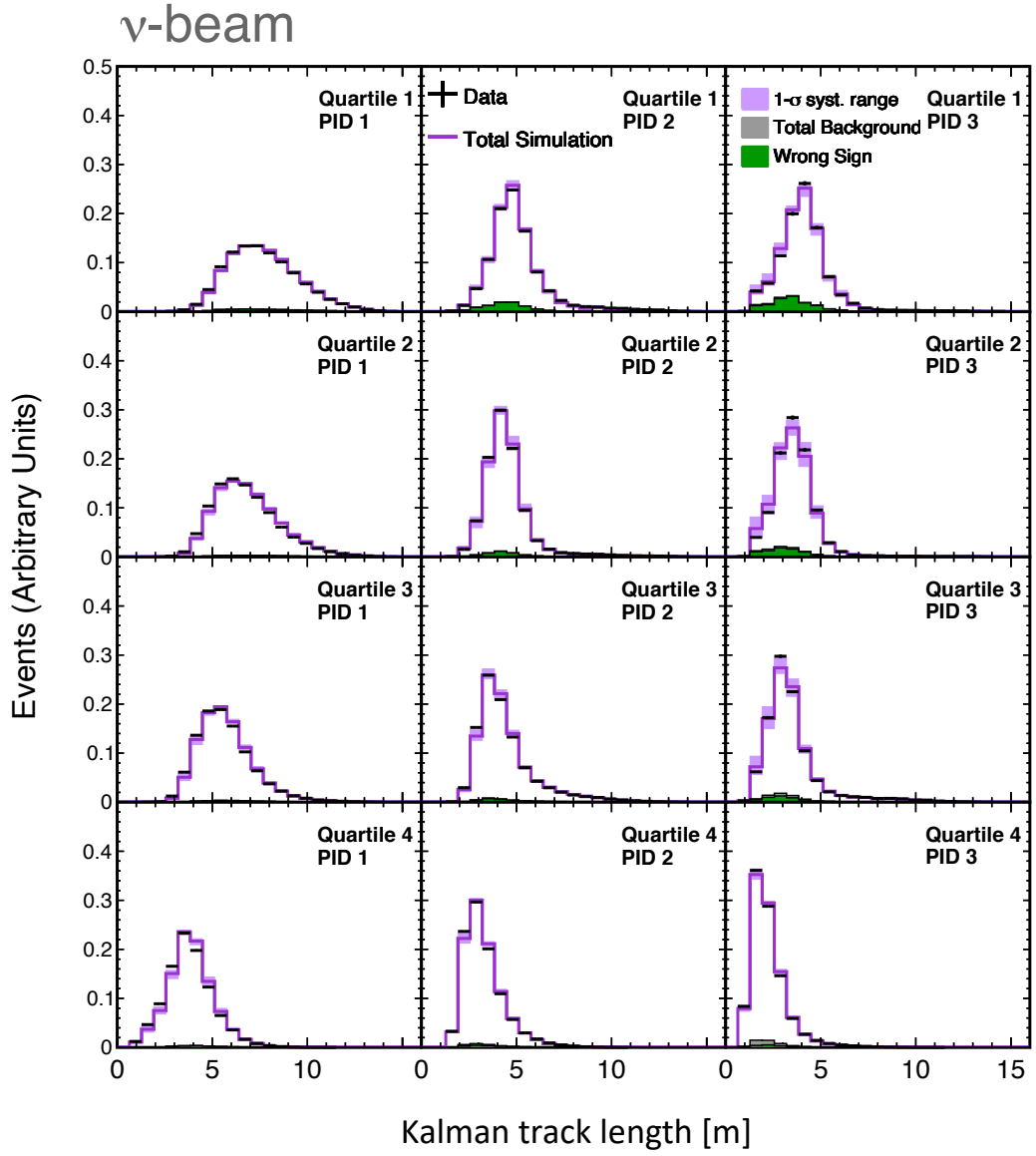

Figure B.11: Distribution of the length of Kalman tracks in data (black) compared to the MC total prediction (purple) with the systematic shape uncertainty band (purple shaded region) in the standard ν_μ candidate sample at the ND in FHC. The wrong sign and total background are shown in green and grey respectively by stacked histograms. Both data and MC are normalised to one.

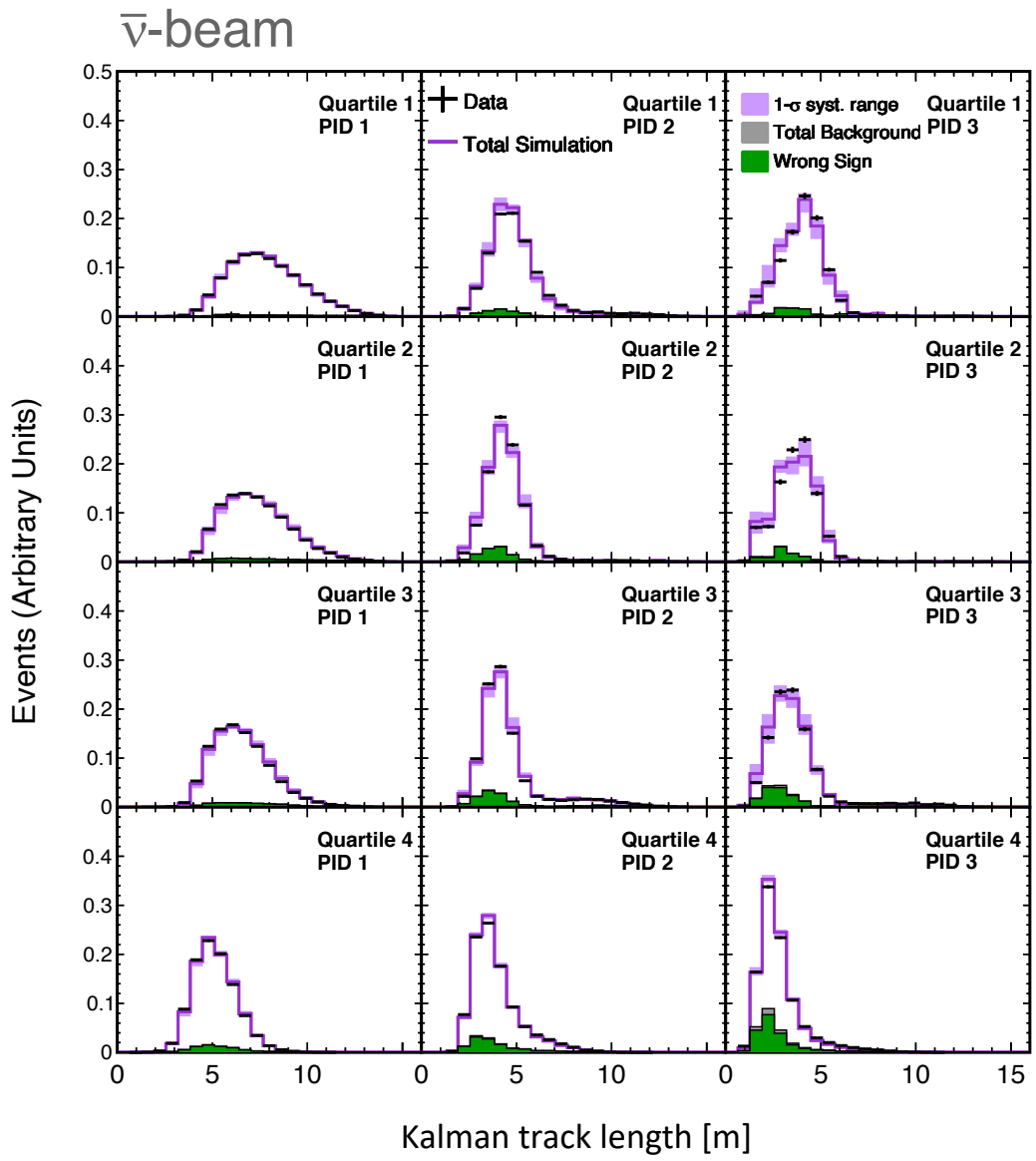

Figure B.12: Distribution of the length of Kalman tracks in data (black) compared to the MC total prediction (purple) with the systematic shape uncertainty band (purple shaded region) in the standard ν_μ candidate sample at the ND in RHC. The wrong sign and total background are shown in green and grey respectively by stacked histograms. Both data and MC are normalised to one.

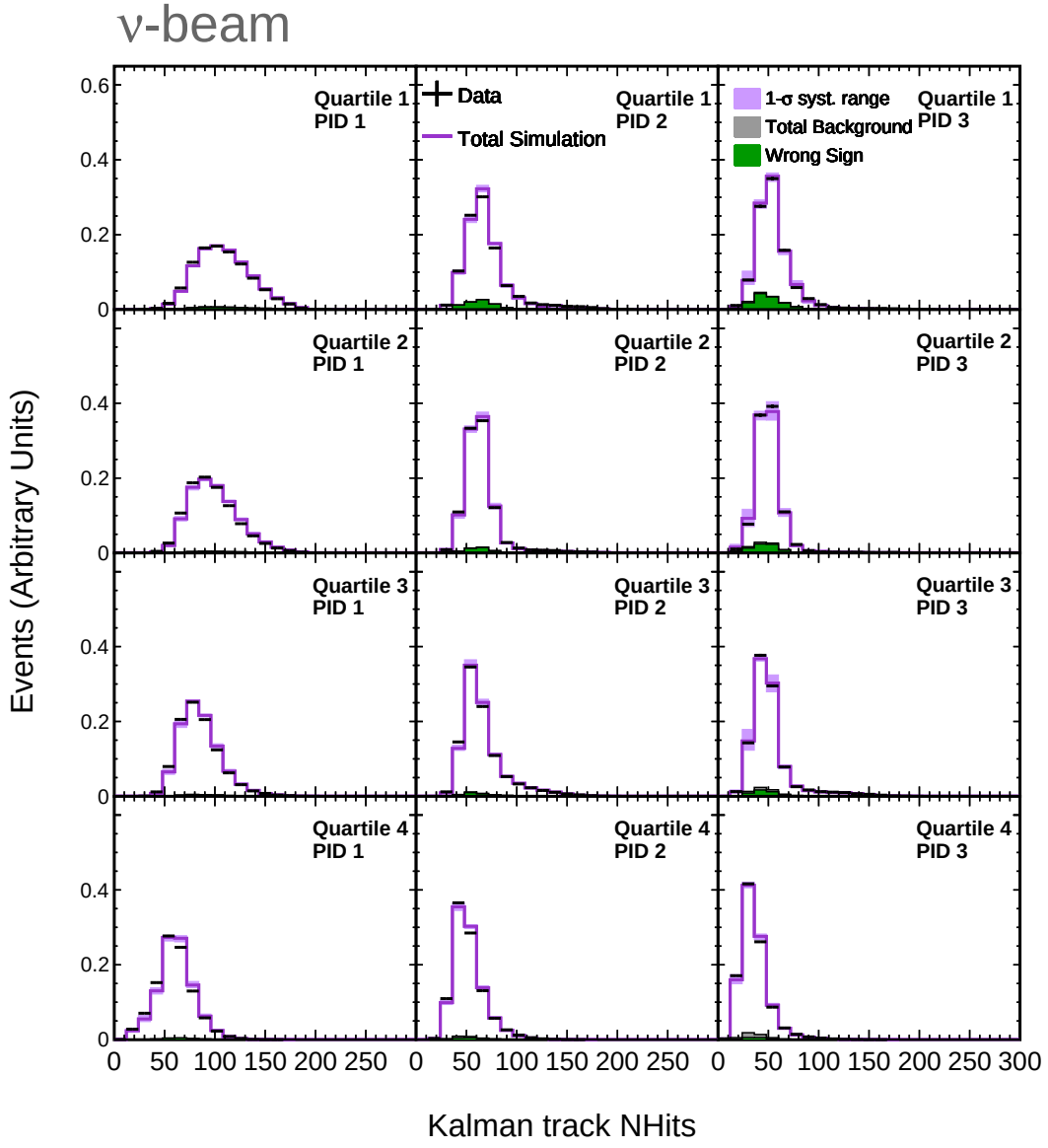

Figure B.13: Distribution of the number of hits of Kalman tracks in data (black) compared to the MC total prediction (purple) with the systematic shape uncertainty band (purple shaded region) in the standard ν_μ candidate sample at the ND in FHC. The wrong sign and total background are shown in green and grey respectively by stacked histograms. Both data and MC are normalised to one.

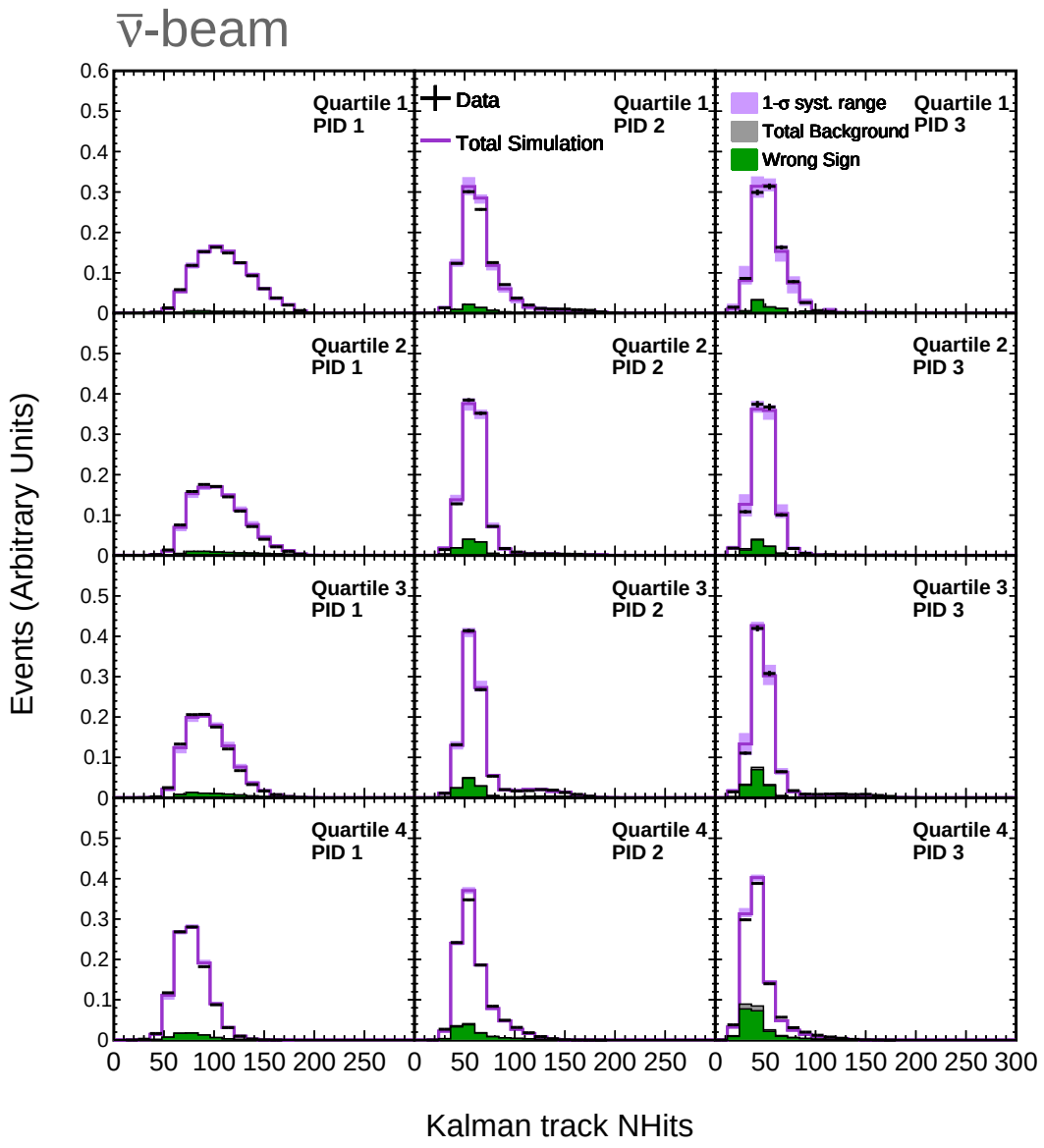

Figure B.14: Distribution of the number of hits of Kalman tracks in data (black) compared to the MC total prediction (purple) with the systematic shape uncertainty band (purple shaded region) in the standard ν_μ candidate sample at the ND in RHC. The wrong sign and total background are shown in green and grey respectively by stacked histograms. Both data and MC are normalised to one.

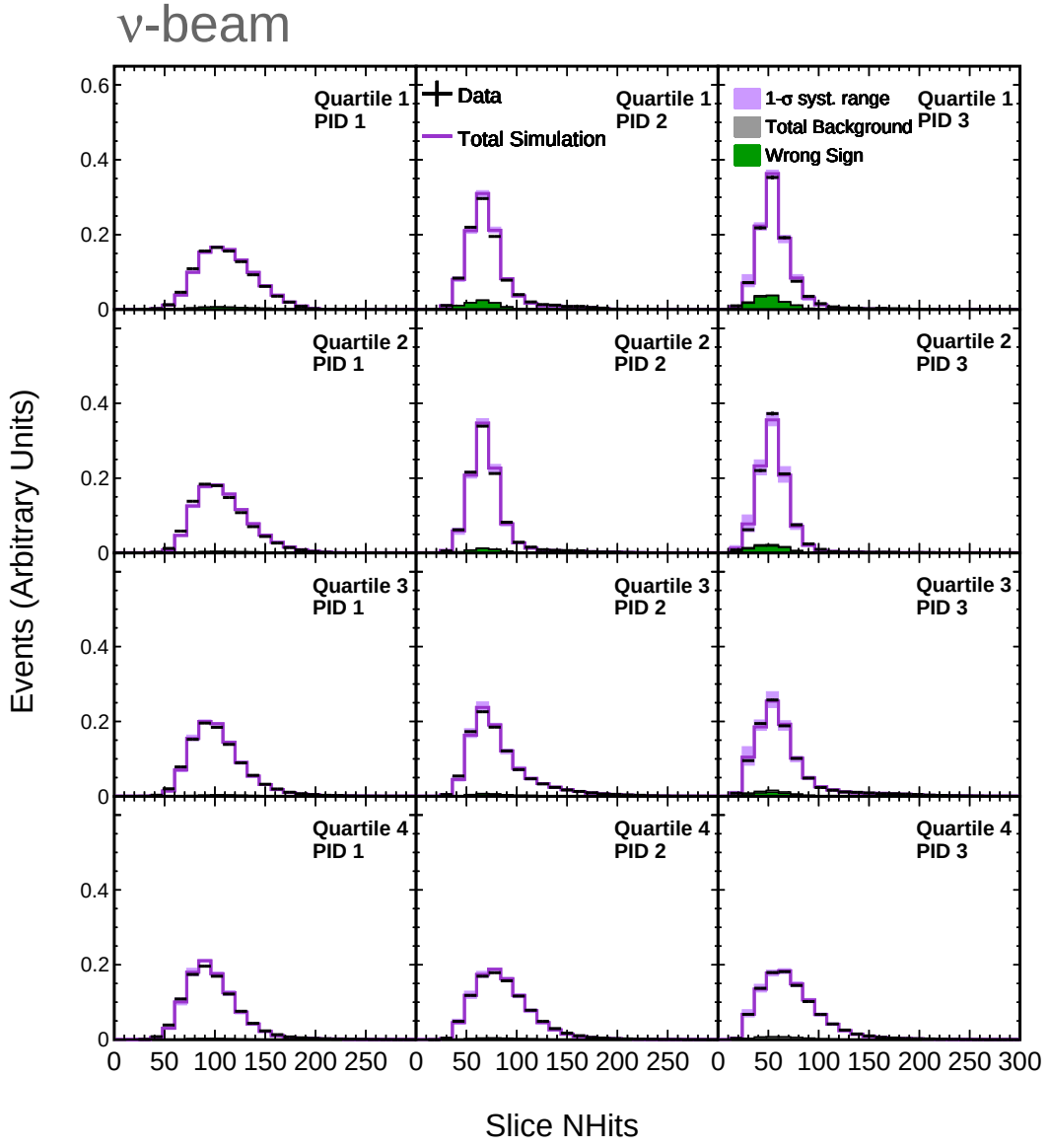

Figure B.15: Distribution of the number of hits in slice in data (black) compared to the MC total prediction (purple) with the systematic shape uncertainty band (purple shaded region) in the standard ν_μ candidate sample at the ND in FHC. The wrong sign and total background are shown in green and grey respectively by stacked histograms. Both data and MC are normalised to one.

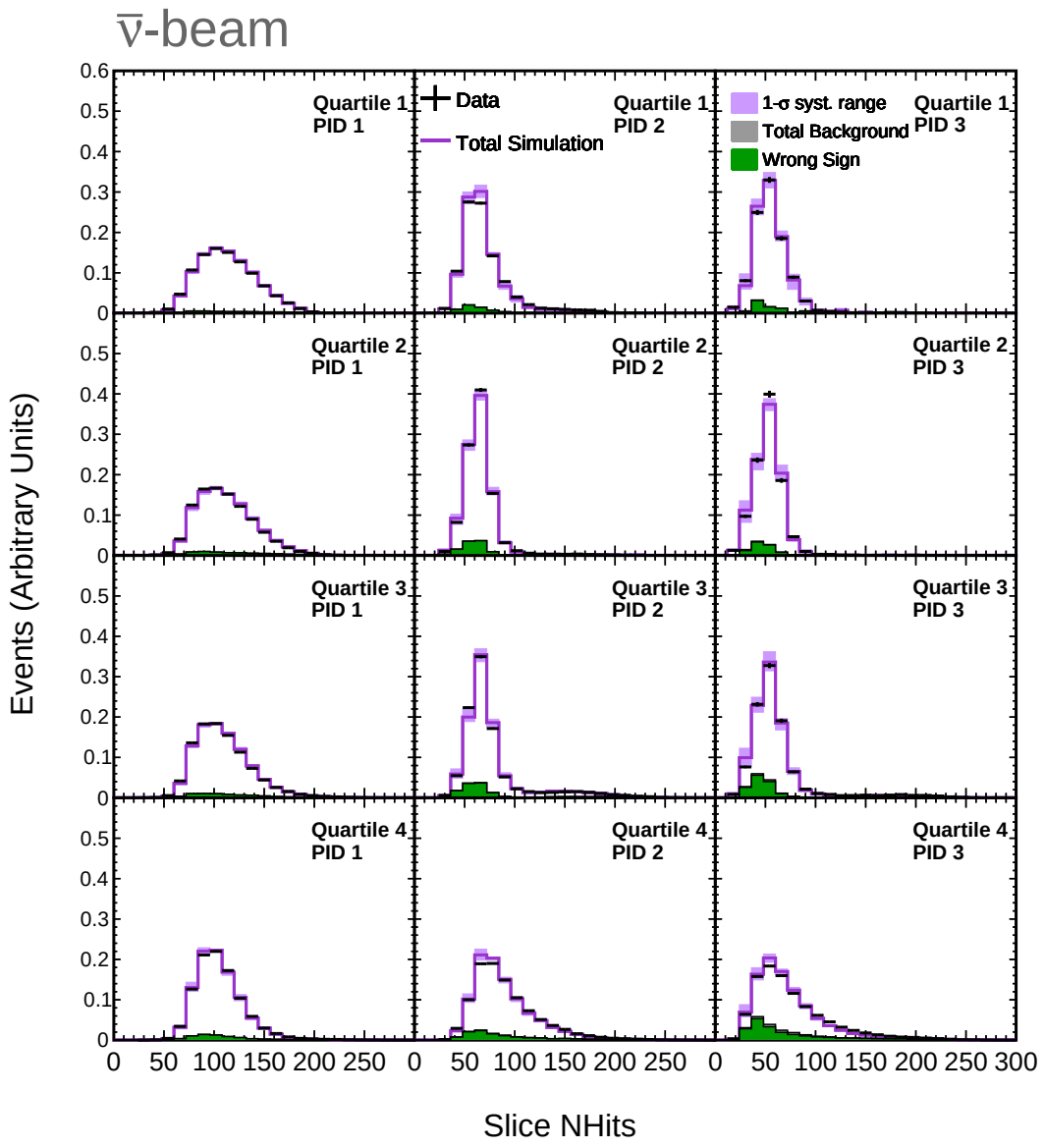

Figure B.16: Distribution of the distribution of the number of hits in slice in data (black) compared to the MC total prediction (purple) with the systematic shape uncertainty band (purple shaded region) in the standard ν_μ candidate sample at the ND in RHC. The wrong sign and total background are shown in green and grey respectively by stacked histograms. Both data and MC are normalised to one.

B.0.2 Distributions of variables in the low-PID sample at the ND

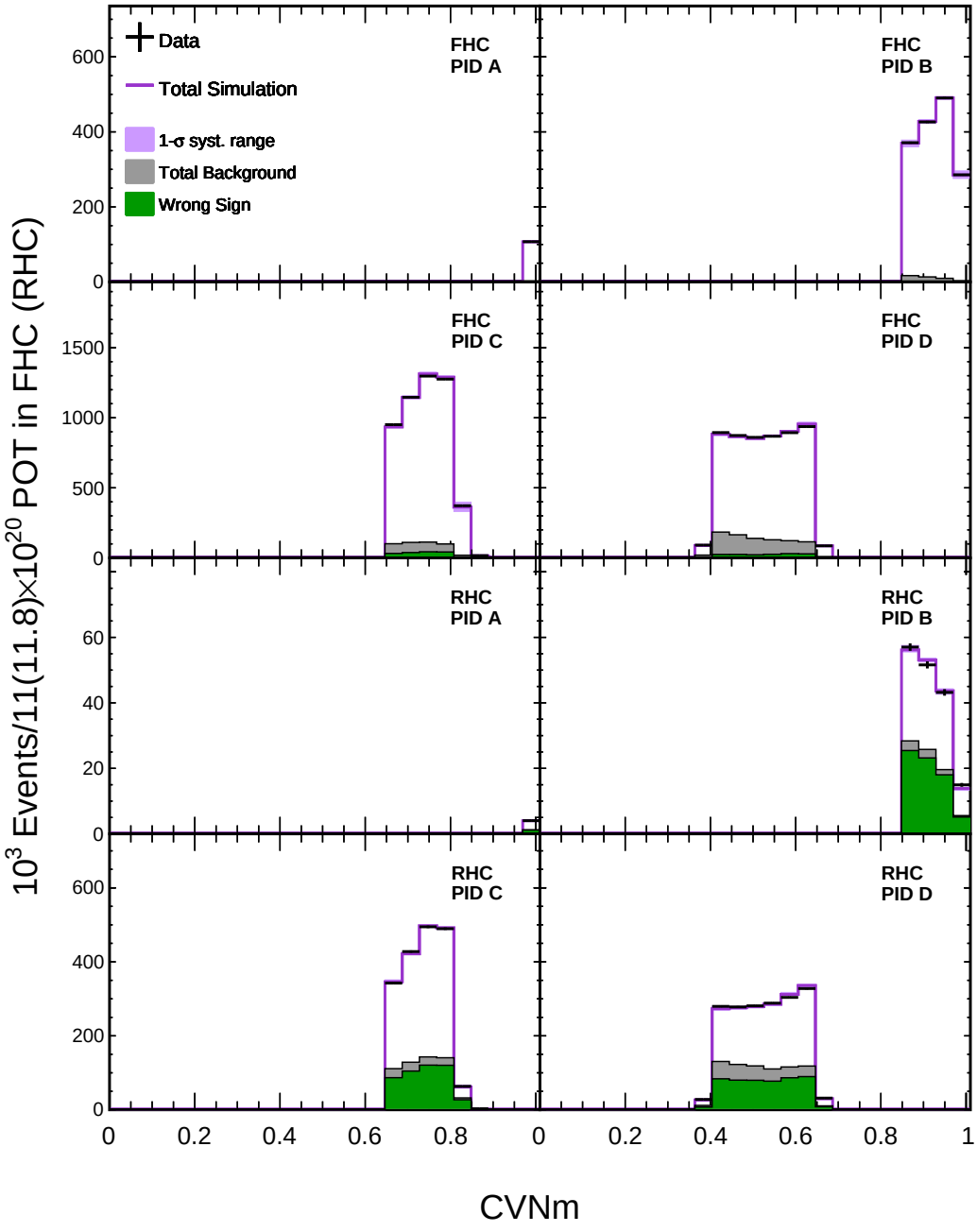

Figure B.17: Distribution of the CVN muon identification score in data (black) compared to the area-normalised MC total prediction (purple) with the systematic shape uncertainty band (purple shaded region) in the low PID ν_μ candidate sample at the ND. The wrong sign and total background are shown in green and grey respectively by stacked histograms.

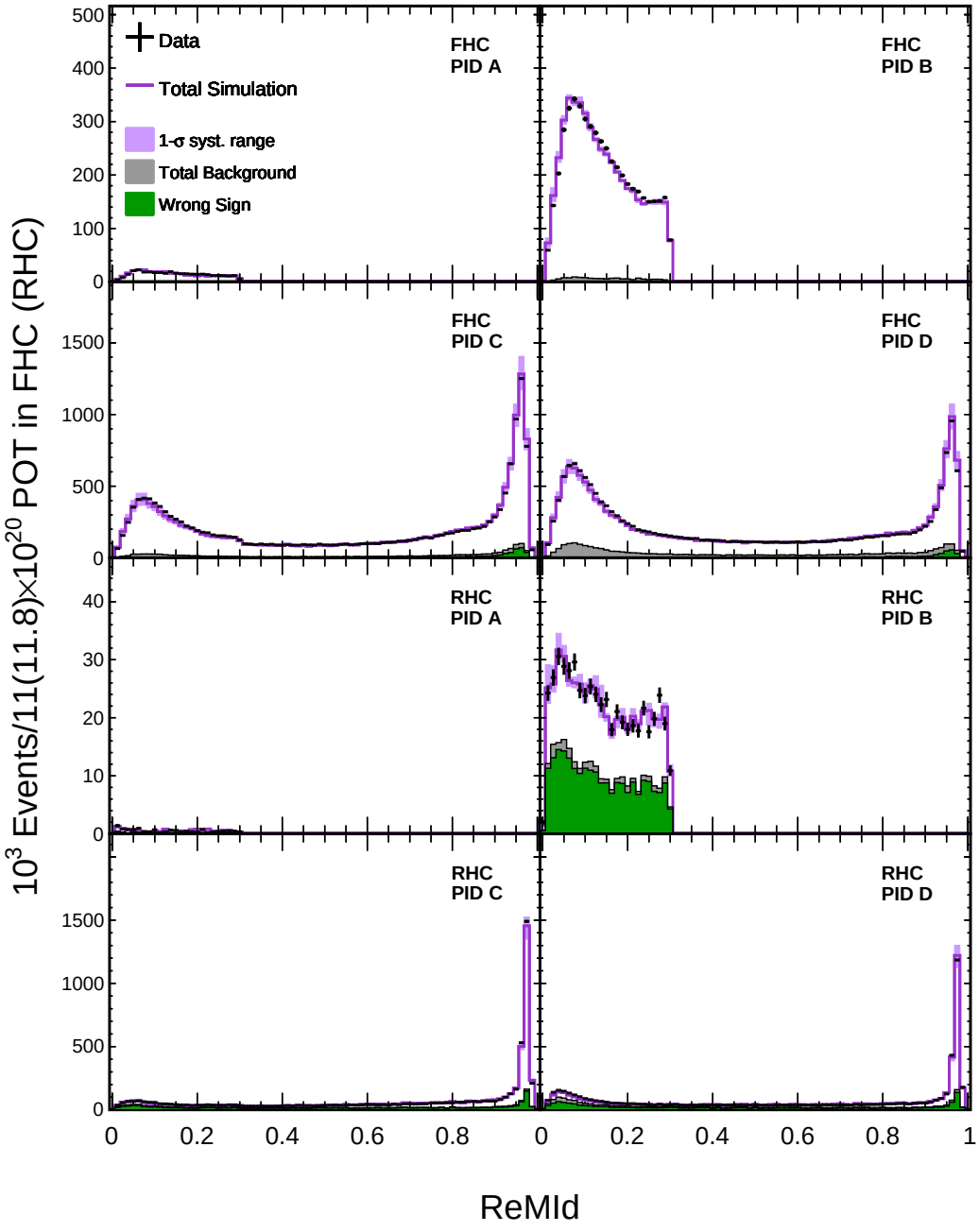

Figure B.18: Distribution of the ReMId muon identification score in data (black) compared to the area-normalised MC total prediction (purple) with the systematic shape uncertainty band (purple shaded region) in the low PID ν_μ candidate sample at the ND. The wrong sign and total background are shown in green and grey respectively by stacked histograms.

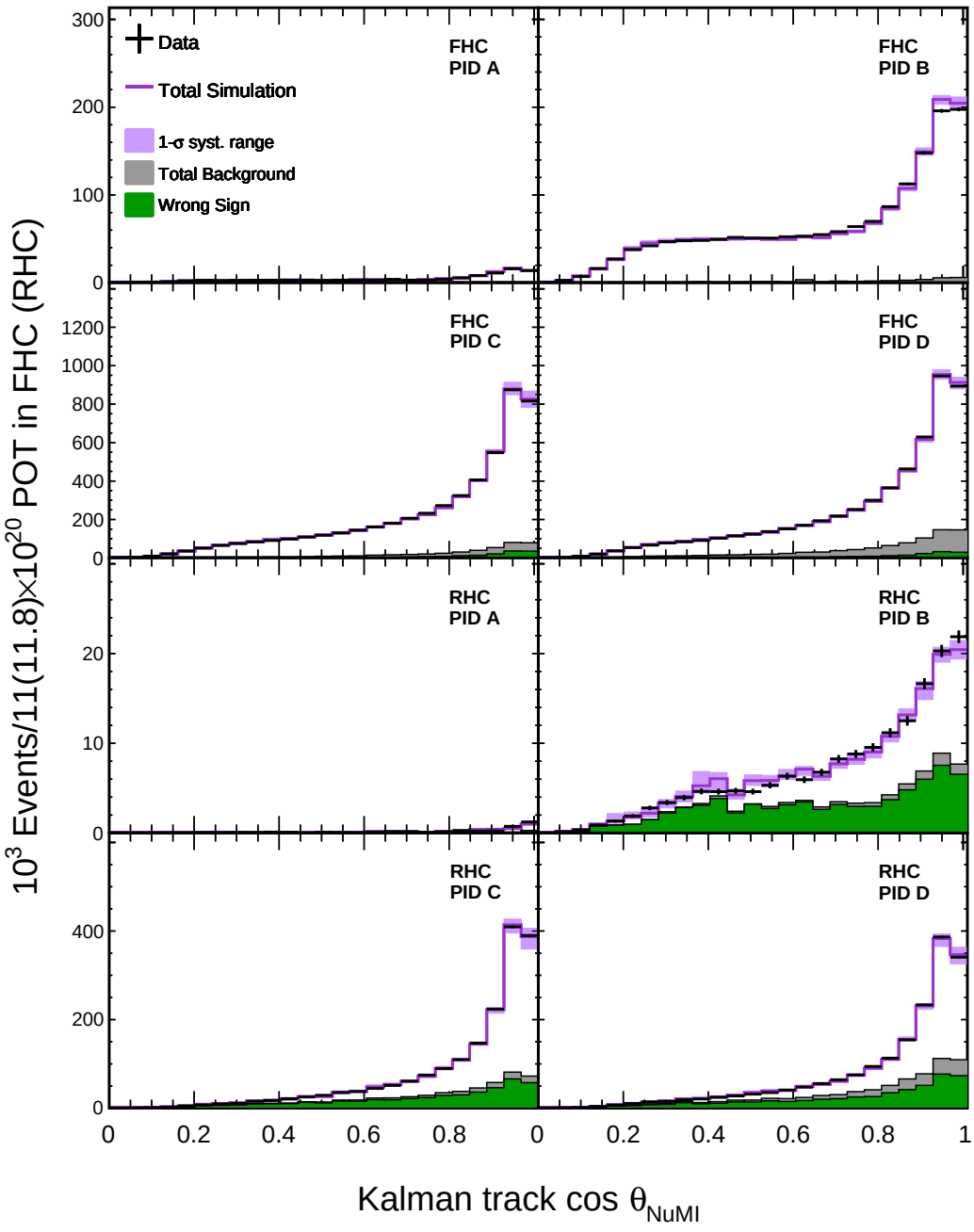

Figure B.19: Distribution of the cosθ_{NuMI} (where θ_{NuMI} is the angle of the muon track with respect to the beam direction) in data (black) compared to the area-normalised MC total prediction (purple) with the systematic shape uncertainty band (purple shaded region) in the low PID ν_μ candidate sample at the ND. The wrong sign and total background are shown in green and grey respectively by stacked histograms.

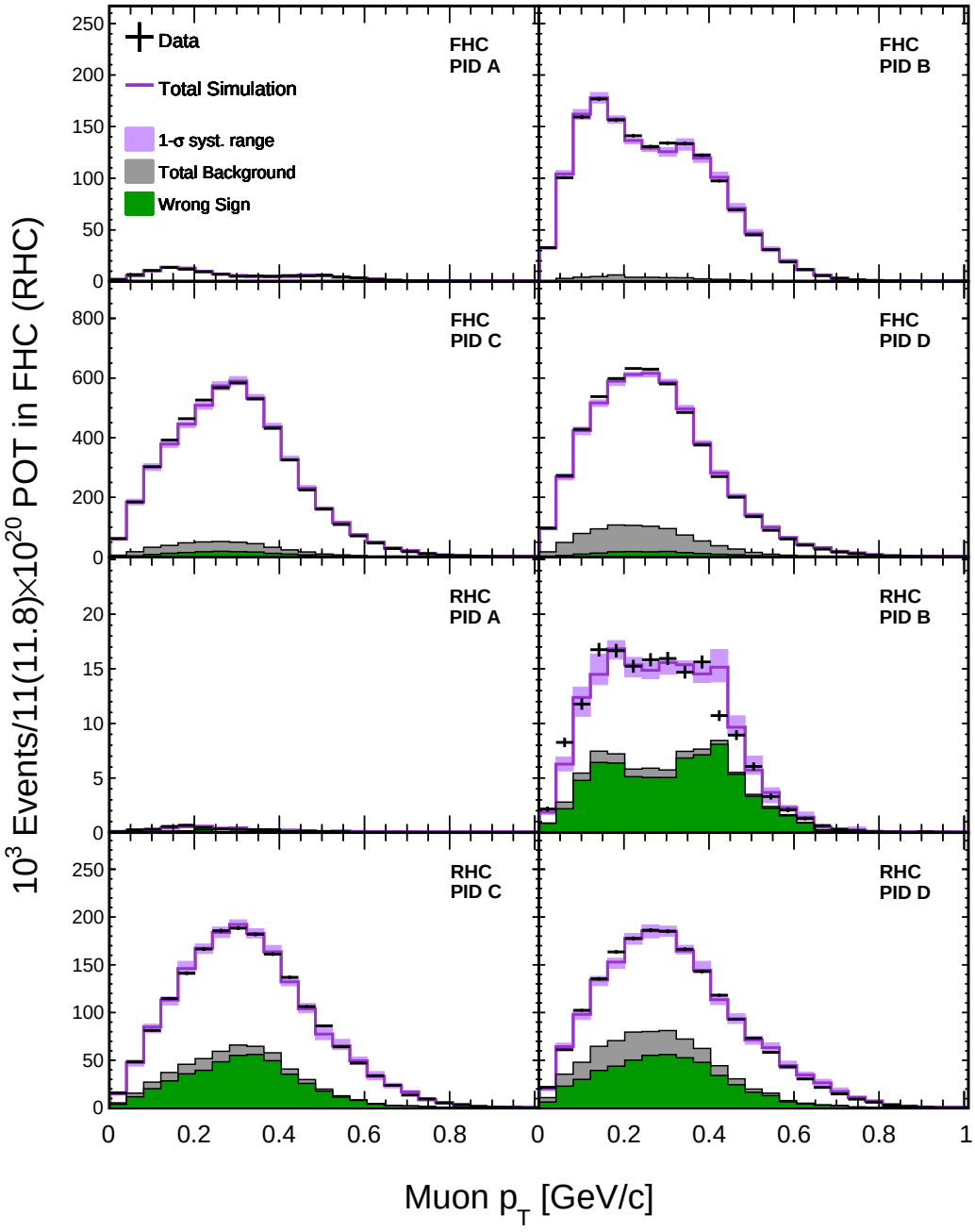

Figure B.20: Distribution of the transverse momentum in data (black) compared to the area-normalised MC total prediction (purple) with the systematic shape uncertainty band (purple shaded region) in the low PID ν_μ candidate sample at the ND. The wrong sign and total background are shown in green and grey respectively by stacked histograms.

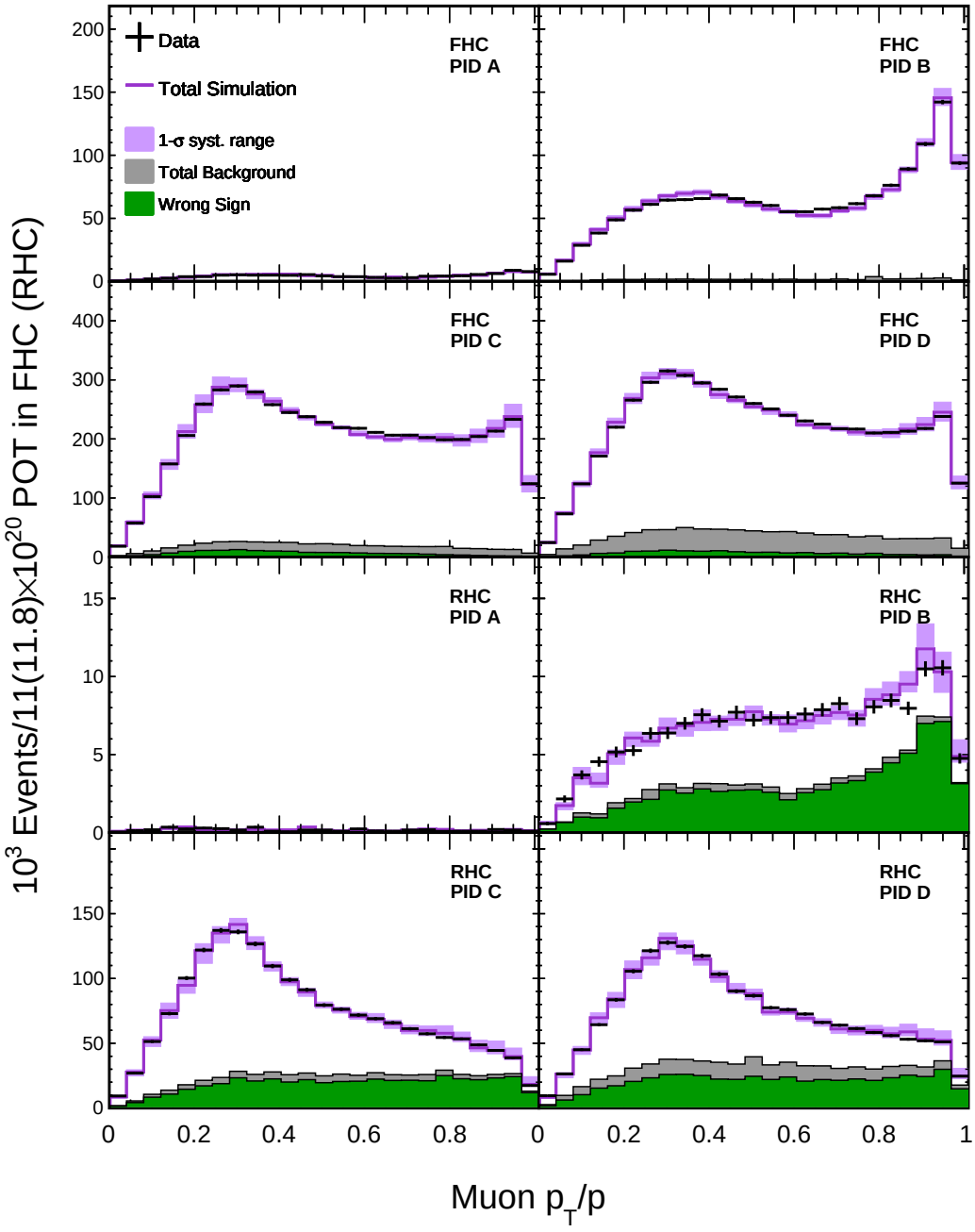

Figure B.21: Distribution of the transverse momentum fraction in data (black) compared to the area-normalised MC total prediction (purple) with the systematic shape uncertainty band (purple shaded region) in the low PID ν_μ candidate sample at the ND. The wrong sign and total background are shown in green and grey respectively by stacked histograms.

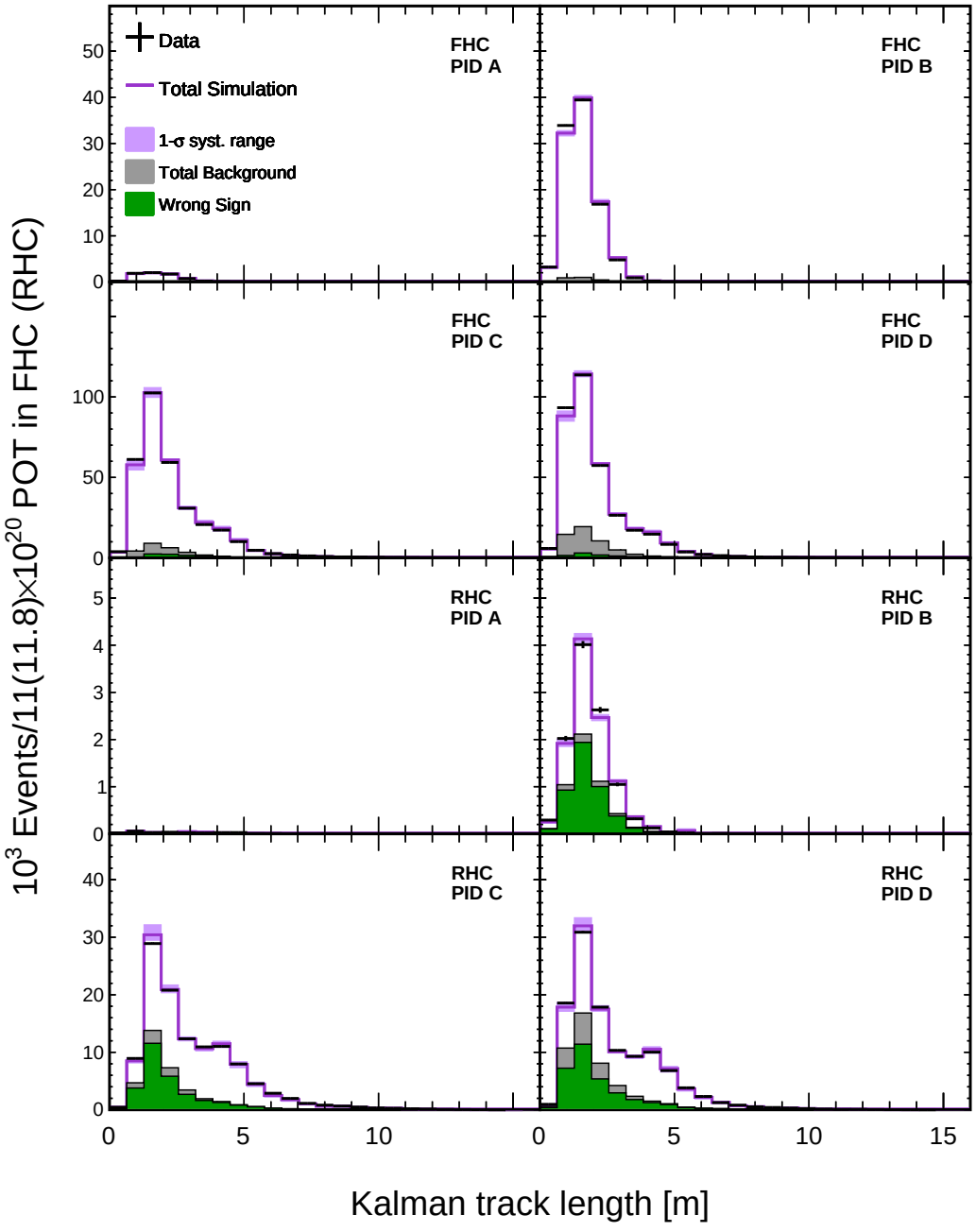

Figure B.22: Distribution of the length of Kalman tracks in data (black) compared to the area-normalised MC total prediction (purple) with the systematic shape uncertainty band (purple shaded region) in the low PID ν_μ candidate sample at the ND. The wrong sign and total background are shown in green and grey respectively by stacked histograms.

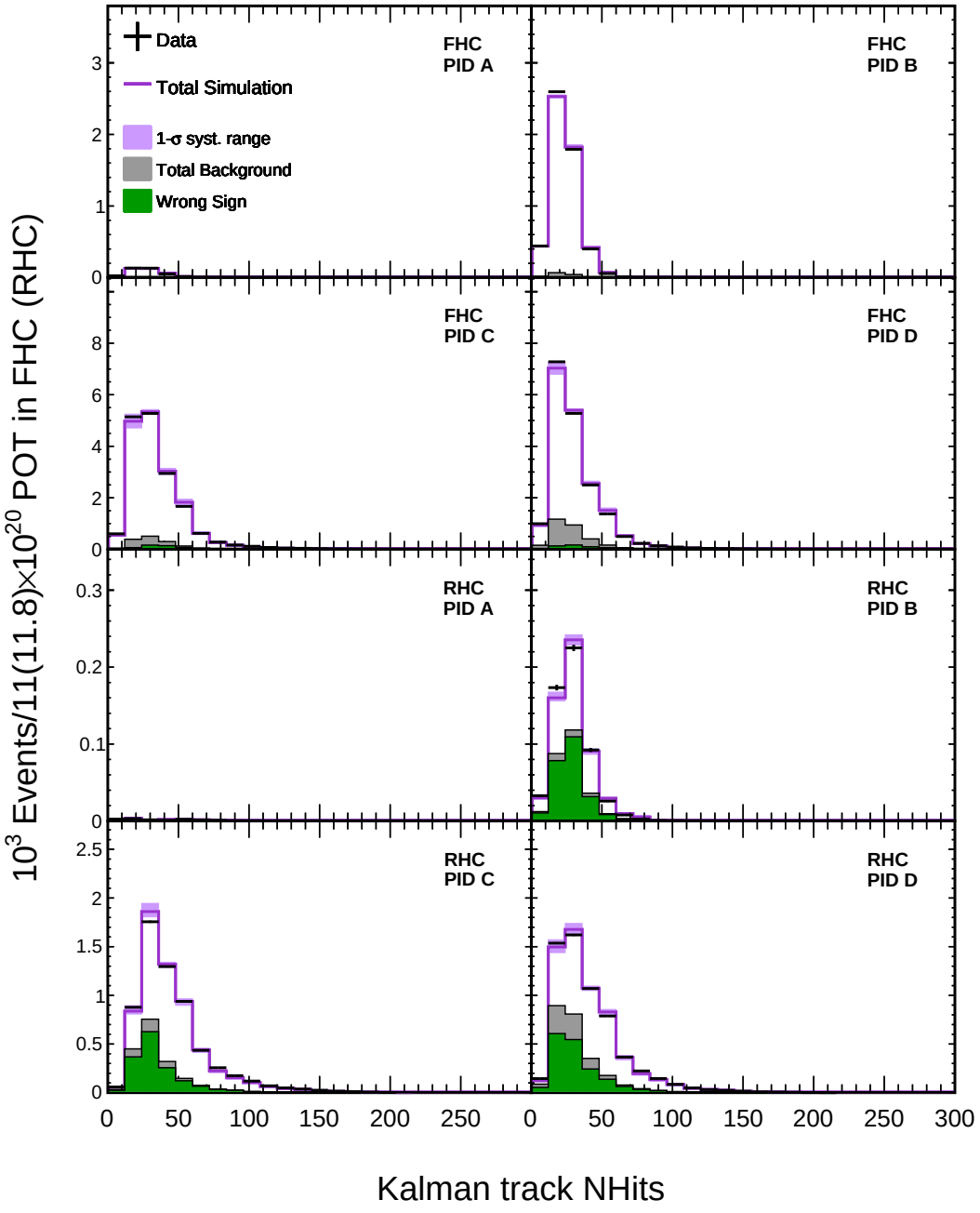

Figure B.23: Distribution of the number of hits of Kalman tracks in data (black) compared to the area-normalised MC total prediction (purple) with the systematic shape uncertainty band (purple shaded region) in the low PID ν_μ candidate sample at the ND. The wrong sign and total background are shown in green and grey respectively by stacked histograms.

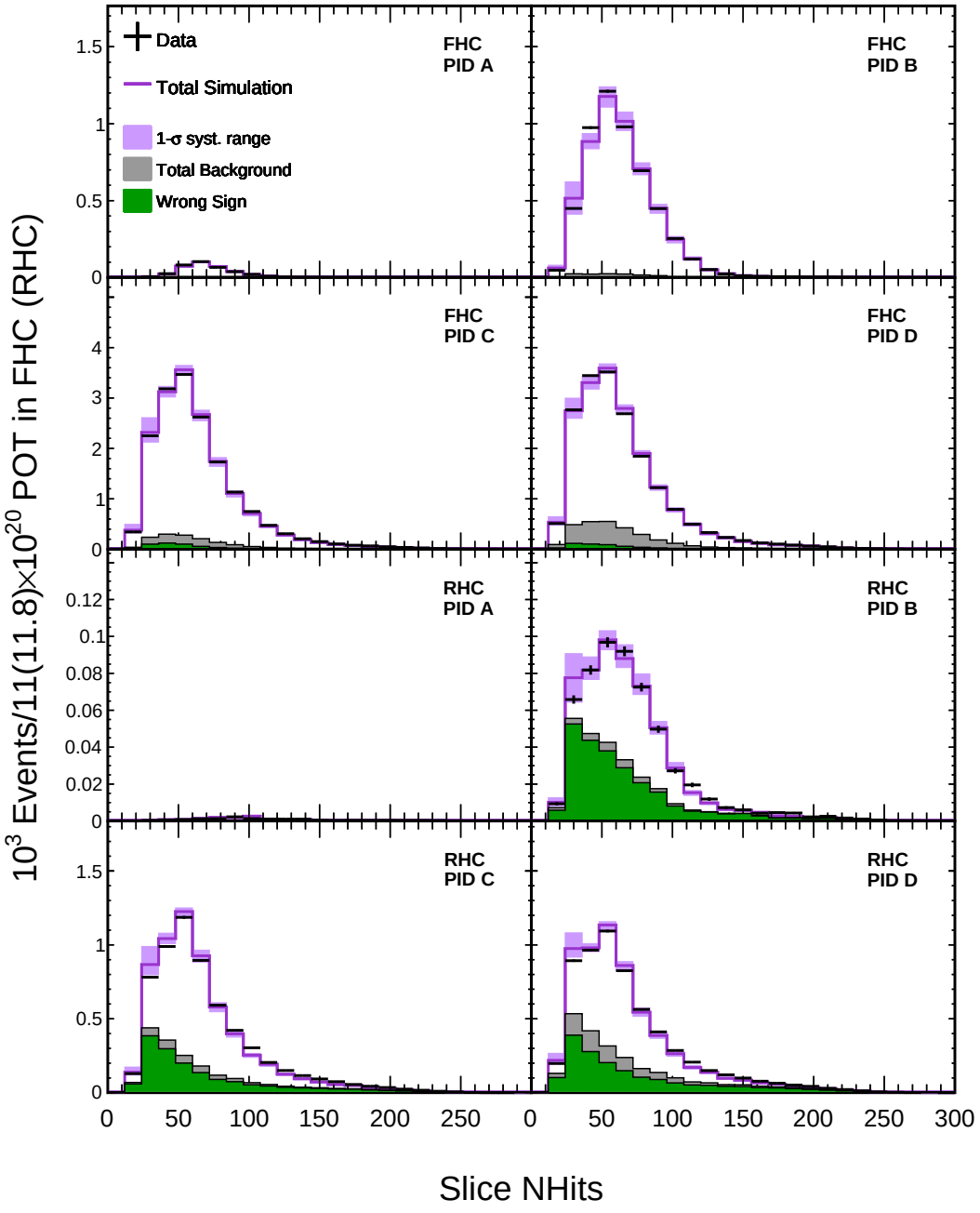

Figure B.24: Distribution of the number of hits in slice in data (black) compared to the area-normalised MC total prediction (purple) with the systematic shape uncertainty band (purple shaded region) in the low PID ν_μ candidate sample at the ND. The wrong sign and total background are shown in green and grey respectively by stacked histograms.

B.0.3 Distributions of variables in the standard sample at the FD

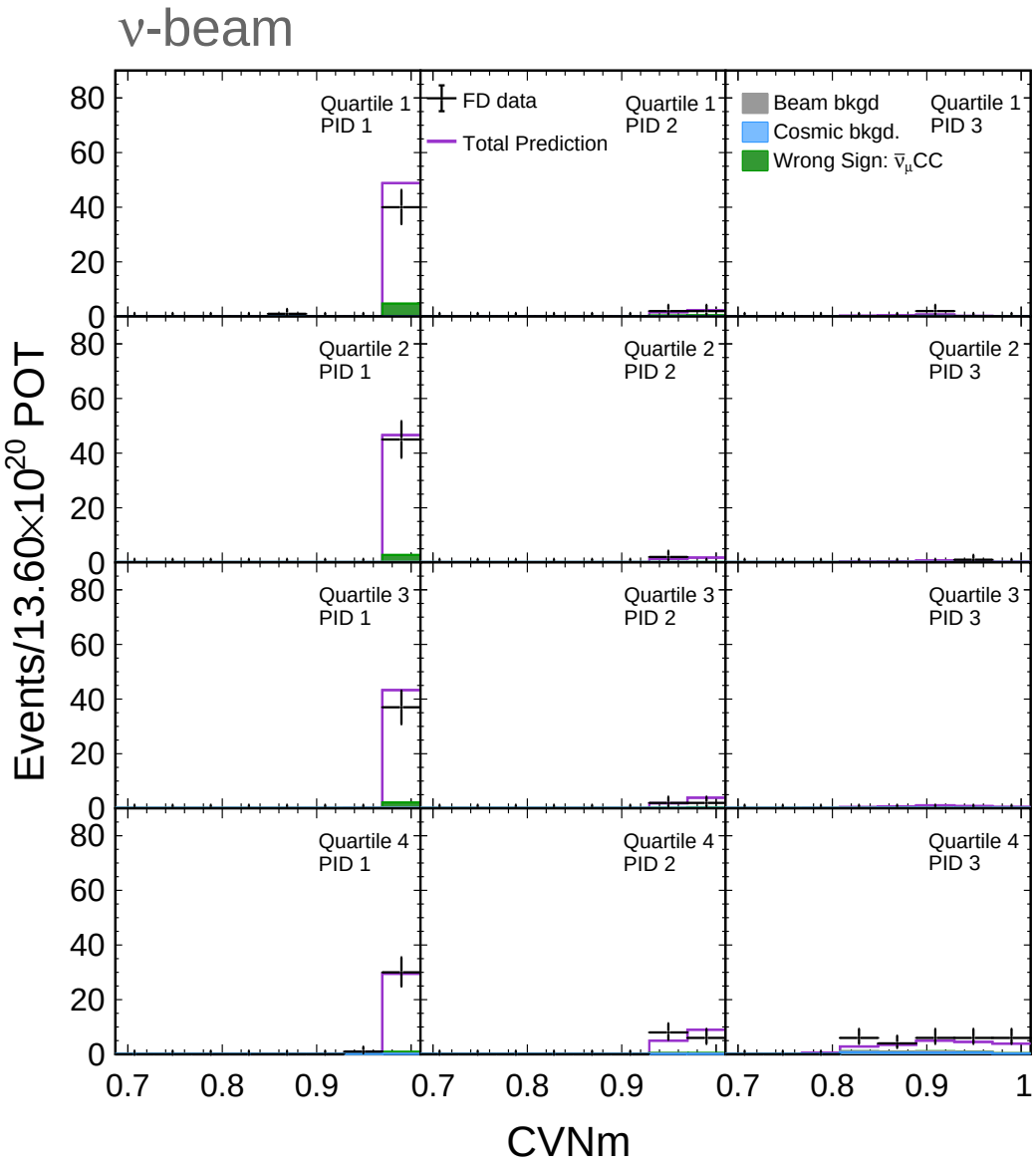

Figure B.25: Distribution of CVN score for the ν_μ CC events in the standard sample at the FD in each selection bin in FHC. The selected ν_μ sample at the FD is split into 12 sub-samples (i.e. four quartile bins times three particle identification bins). Data is shown in black. The prediction at the thesis best fit point is shown by the purple line and the shaded purple region corresponds to the 1 σ systematic uncertainty in the simulation. The green, grey, and the blue stacked histograms show the wrong-sign ($\bar{\nu}_\mu$ CC), beam, and cosmic backgrounds, respectively.

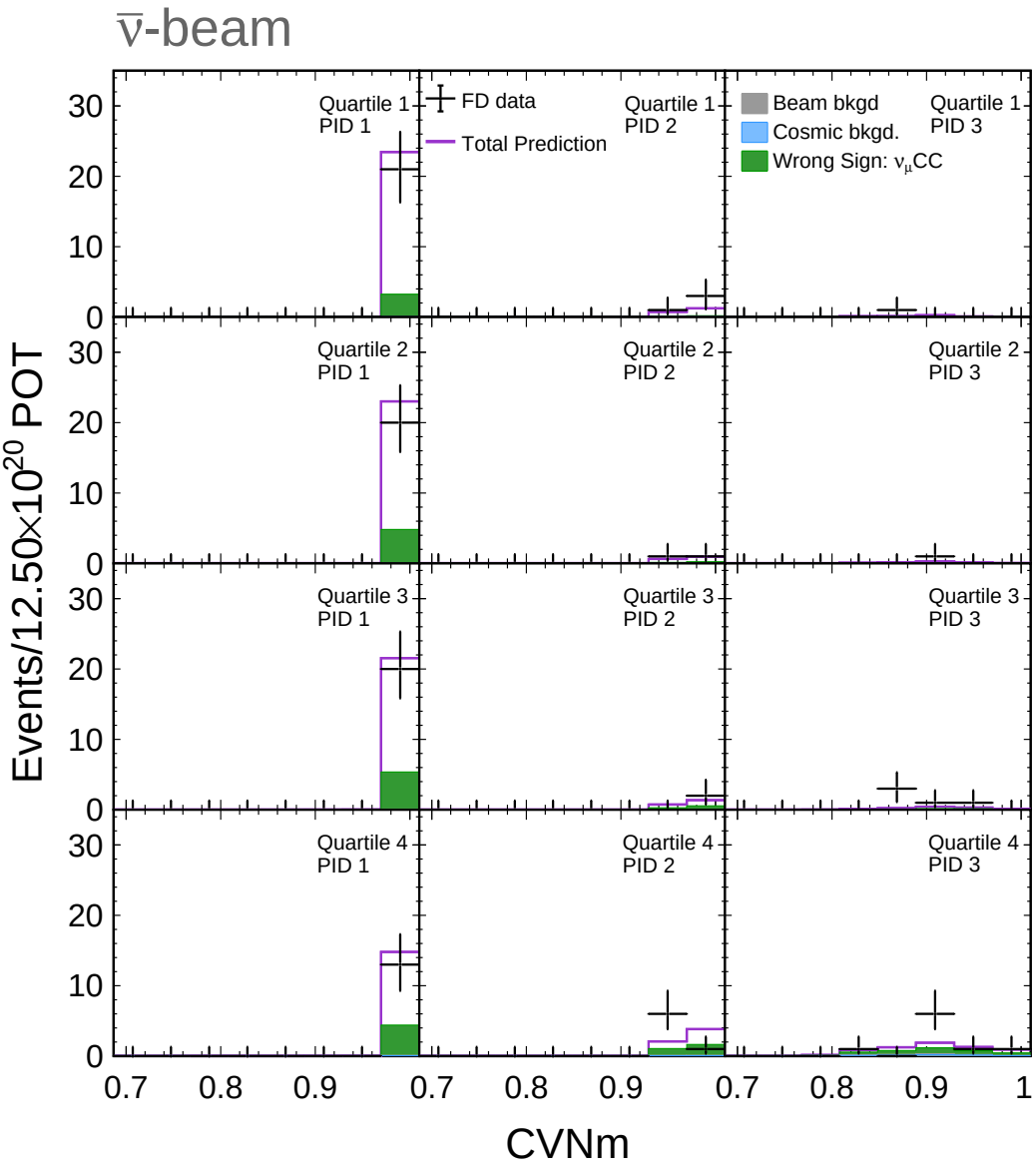

Figure B.26: Distribution of CVN score for the ν_μ CC events in the standard sample at the FD in each selection bin in RHC. The selected ν_μ sample at the FD is split into 12 sub-samples (i.e. four quartile bins times three particle identification bins). Data is shown in black. The prediction at the thesis best fit point is shown by the purple line and the shaded purple region corresponds to the 1 σ systematic uncertainty in the simulation. The green, grey, and the blue stacked histograms show the wrong-sign (ν_μ CC), beam, and cosmic backgrounds, respectively.

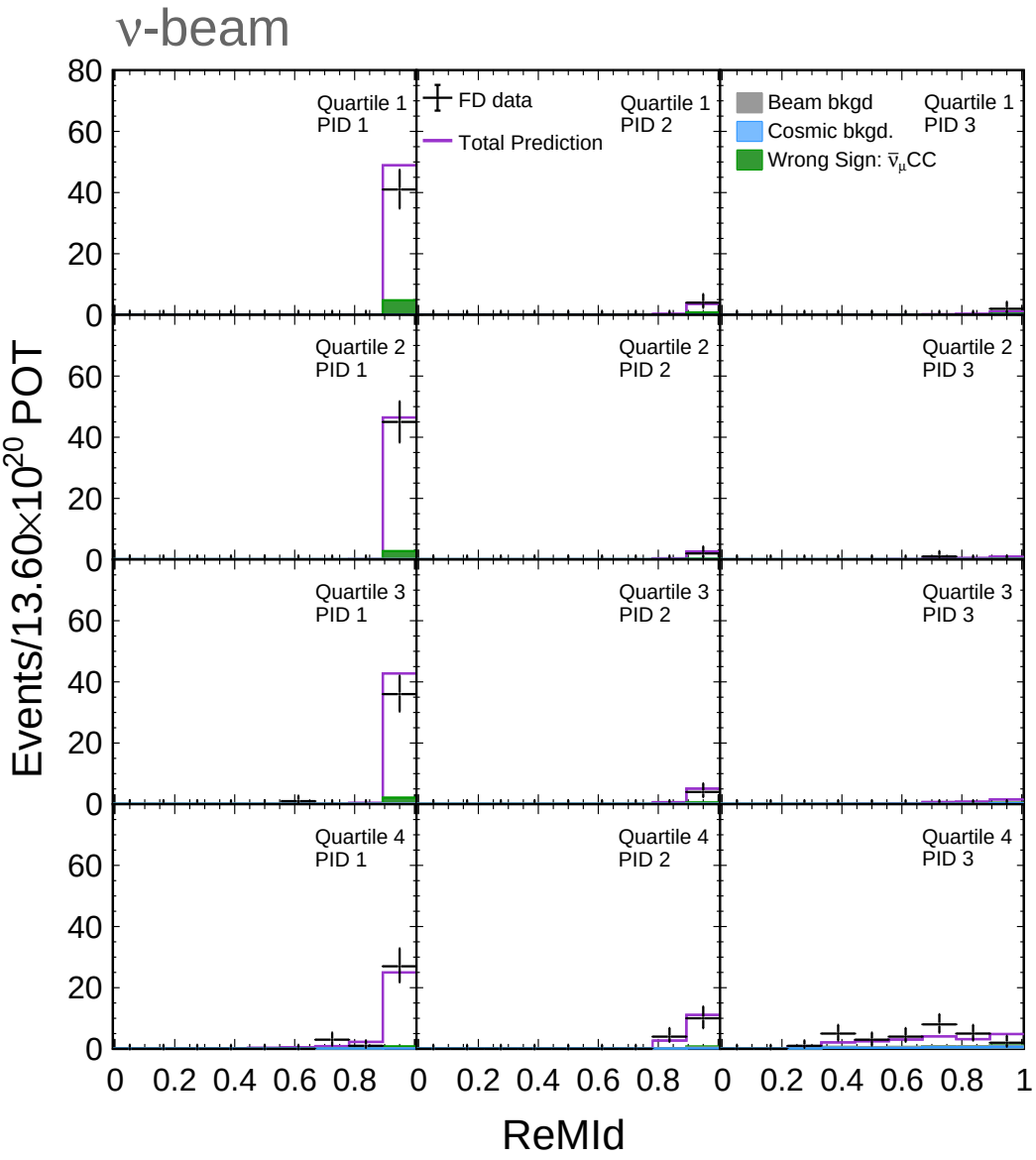

Figure B.27: Distribution of ReMId score for the ν_μ CC events in the standard sample at the FD in each selection bin in FHC. The selected ν_μ sample at the FD is split into 12 sub-samples (i.e. four quartile bins times three particle identification bins). Data is shown in black. The prediction at the thesis best fit point is shown by the purple line and the shaded purple region corresponds to the 1 σ systematic uncertainty in the simulation. The green, grey, and the blue stacked histograms show the wrong-sign ($\bar{\nu}_\mu$ CC), beam, and cosmic backgrounds, respectively.

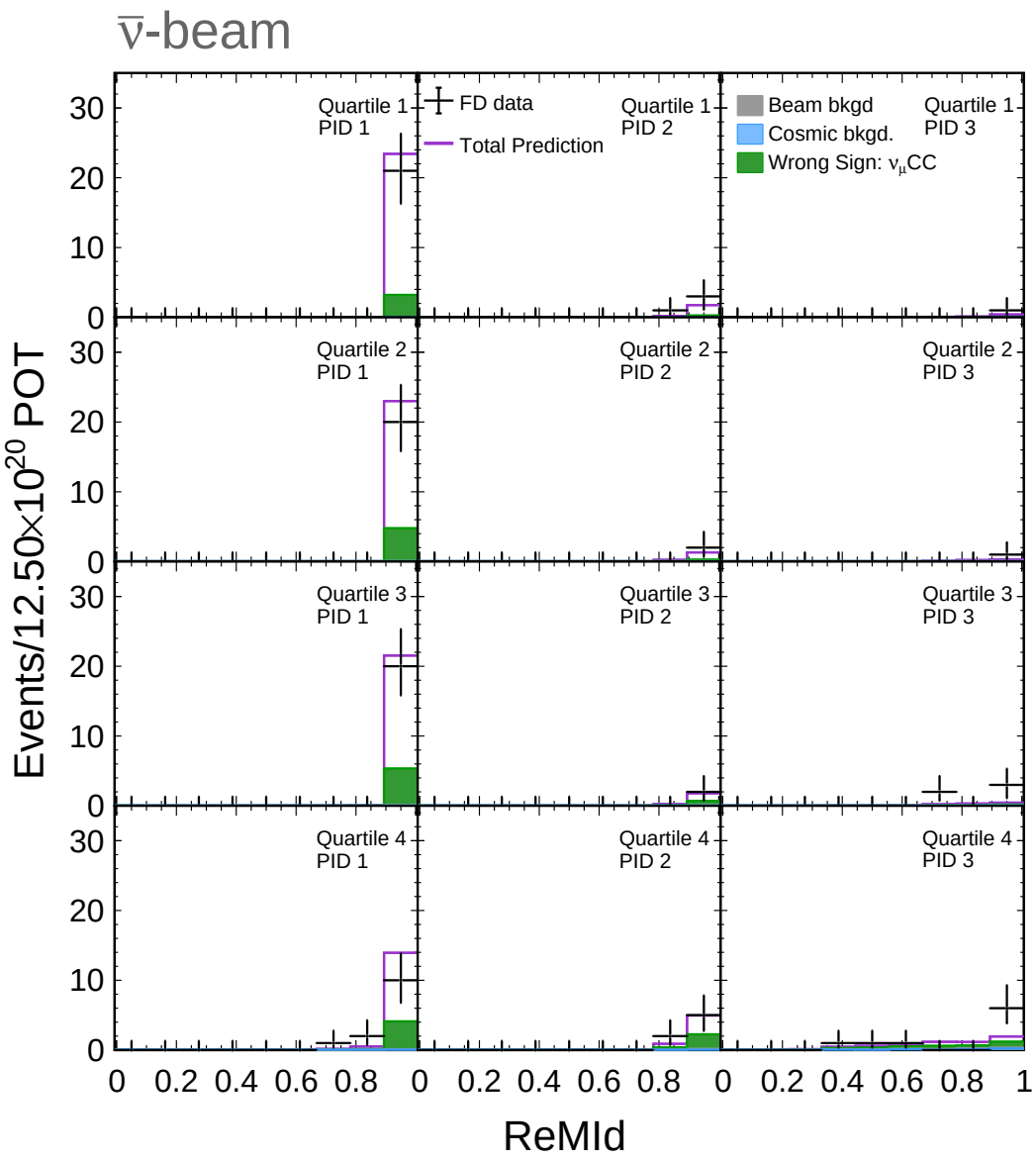

Figure B.28: Distribution of ReMId score for the ν_μ CC events in the standard sample at the FD in each selection bin in RHC. The selected ν_μ sample at the FD is split into 12 sub-samples (i.e. four quartile bins times three particle identification bins). Data is shown in black. The prediction at the thesis best fit point is shown by the purple line and the shaded purple region corresponds to the 1 σ systematic uncertainty in the simulation. The green, grey, and the blue stacked histograms show the wrong-sign (ν_μ CC), beam, and cosmic backgrounds, respectively.

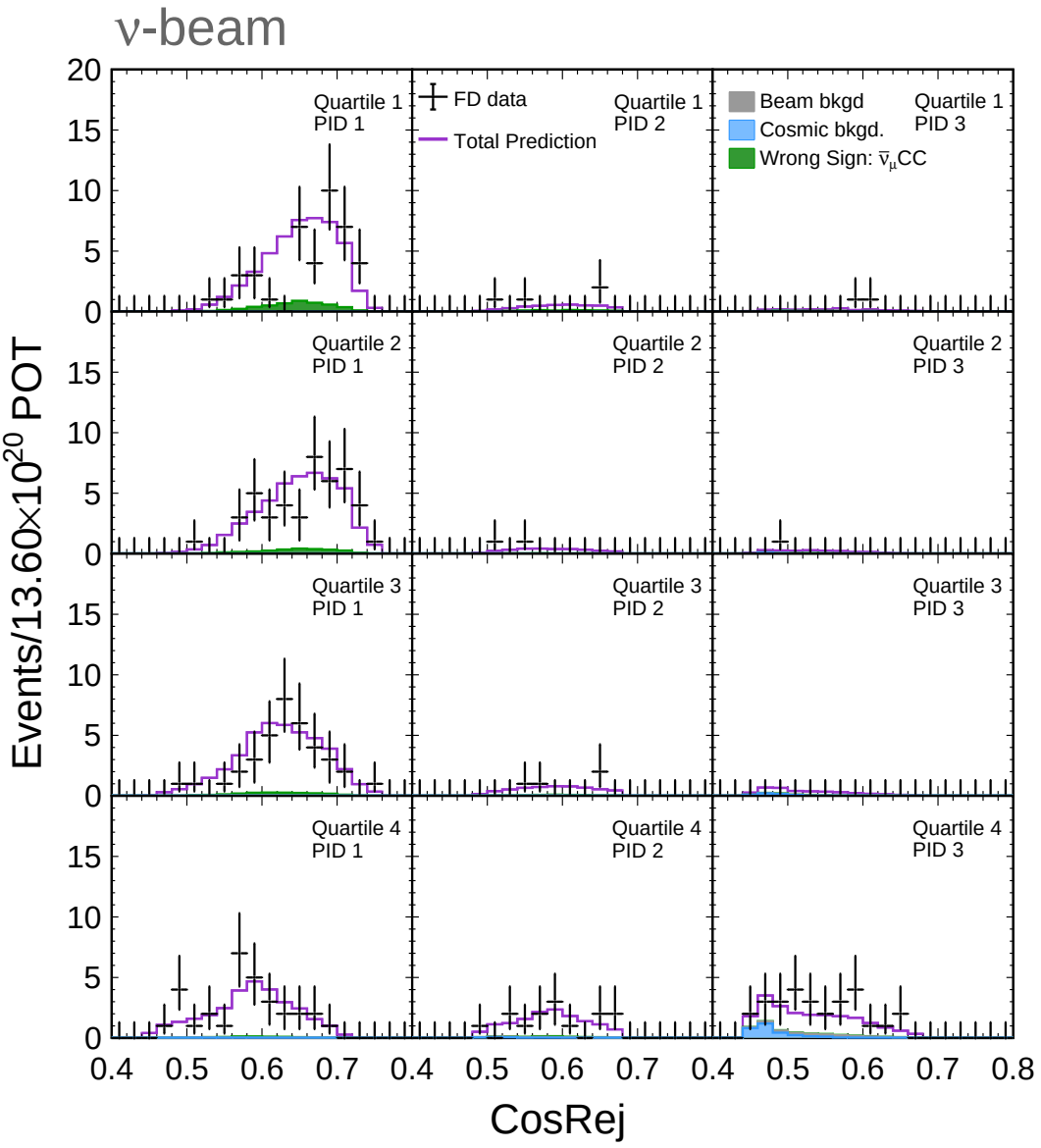

Figure B.29: Distribution of the cosmic rejection score for the ν_μ CC events in the standard sample at the FD in each selection bin in FHC. The selected ν_μ sample at the FD is split into 12 sub-samples (i.e. four quartile bins times three particle identification bins). Data is shown in black. The prediction at the thesis best fit point is shown by the purple line and the shaded purple region corresponds to the 1 σ systematic uncertainty in the simulation. The green, grey, and the blue stacked histograms show the wrong-sign ($\bar{\nu}_\mu$ CC), beam, and cosmic backgrounds, respectively.

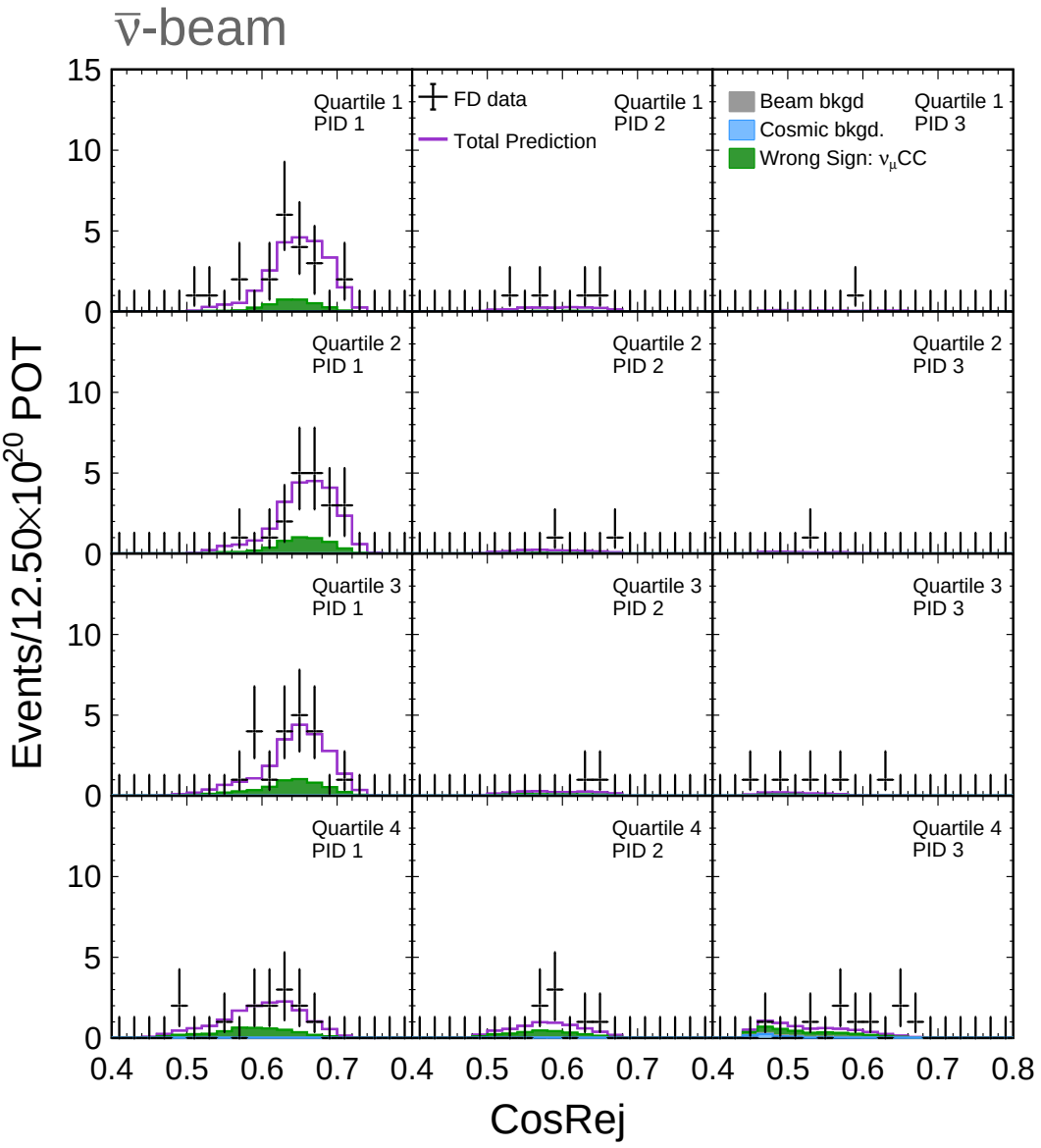

Figure B.30: Distribution of the cosmic rejection score for the ν_μ CC events in the standard sample at the FD in each selection bin in RHC. The selected ν_μ sample at the FD is split into 12 sub-samples (i.e. four quartile bins times three particle identification bins). Data is shown in black. The prediction at the thesis best fit point is shown by the purple line and the shaded purple region corresponds to the 1 σ systematic uncertainty in the simulation. The green, grey, and the blue stacked histograms show the wrong-sign (ν_μ CC), beam, and cosmic backgrounds, respectively.

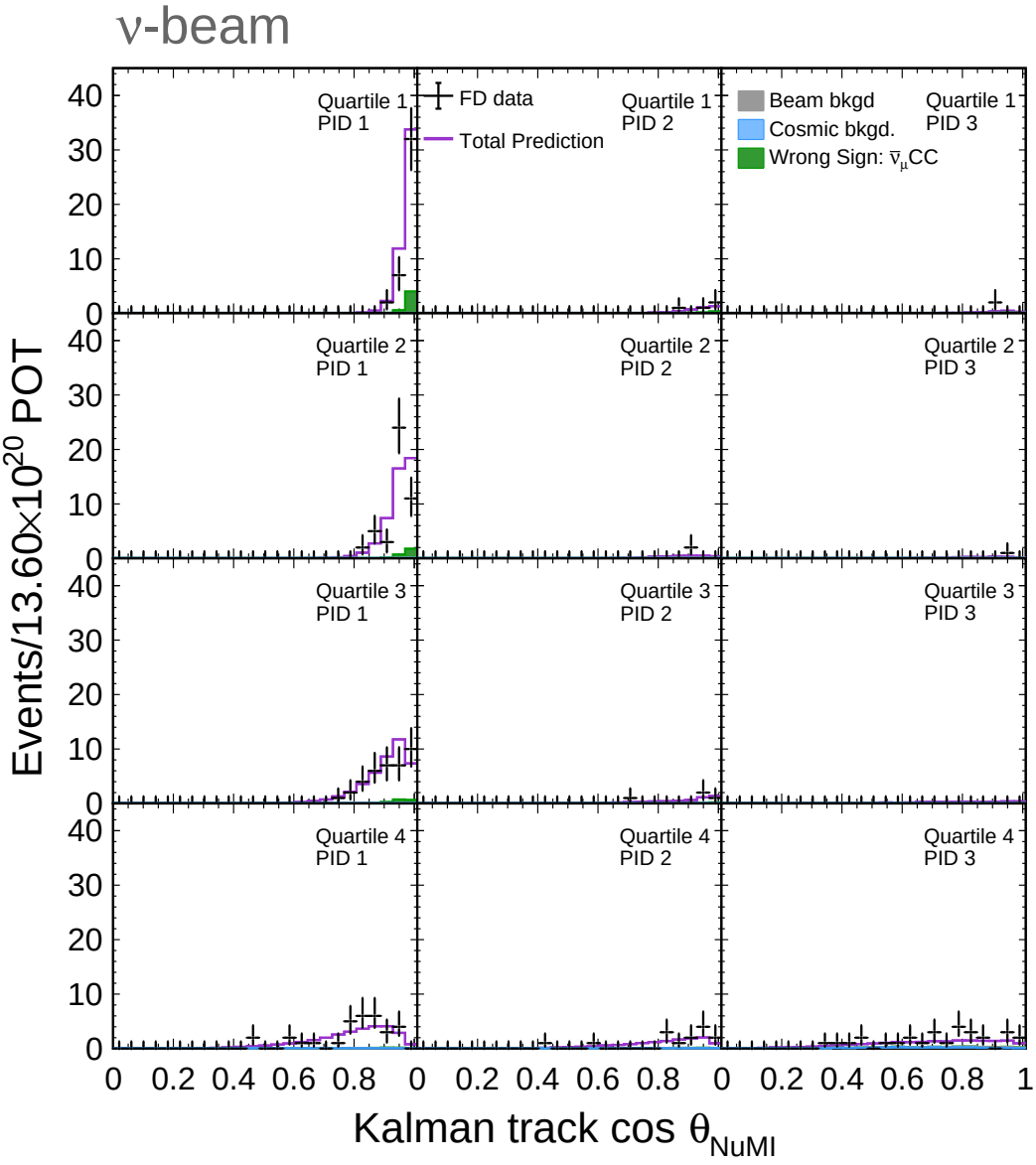

Figure B.31: Distribution of the cosθ_{NuMI} (where θ_{NuMI} is the angle of the muon track with respect to the beam direction) for the ν_μ CC events in the standard sample at the FD in each selection bin in FHC. The selected ν_μ sample at the FD is split into 12 sub-samples (i.e. four quartile bins times three particle identification bins). Data is shown in black. The prediction at the thesis best fit point is shown by the purple line and the shaded purple region corresponds to the 1 σ systematic uncertainty in the simulation. The green, grey, and the blue stacked histograms show the wrong-sign ($\bar{\nu}_\mu$ CC), beam, and cosmic backgrounds, respectively.

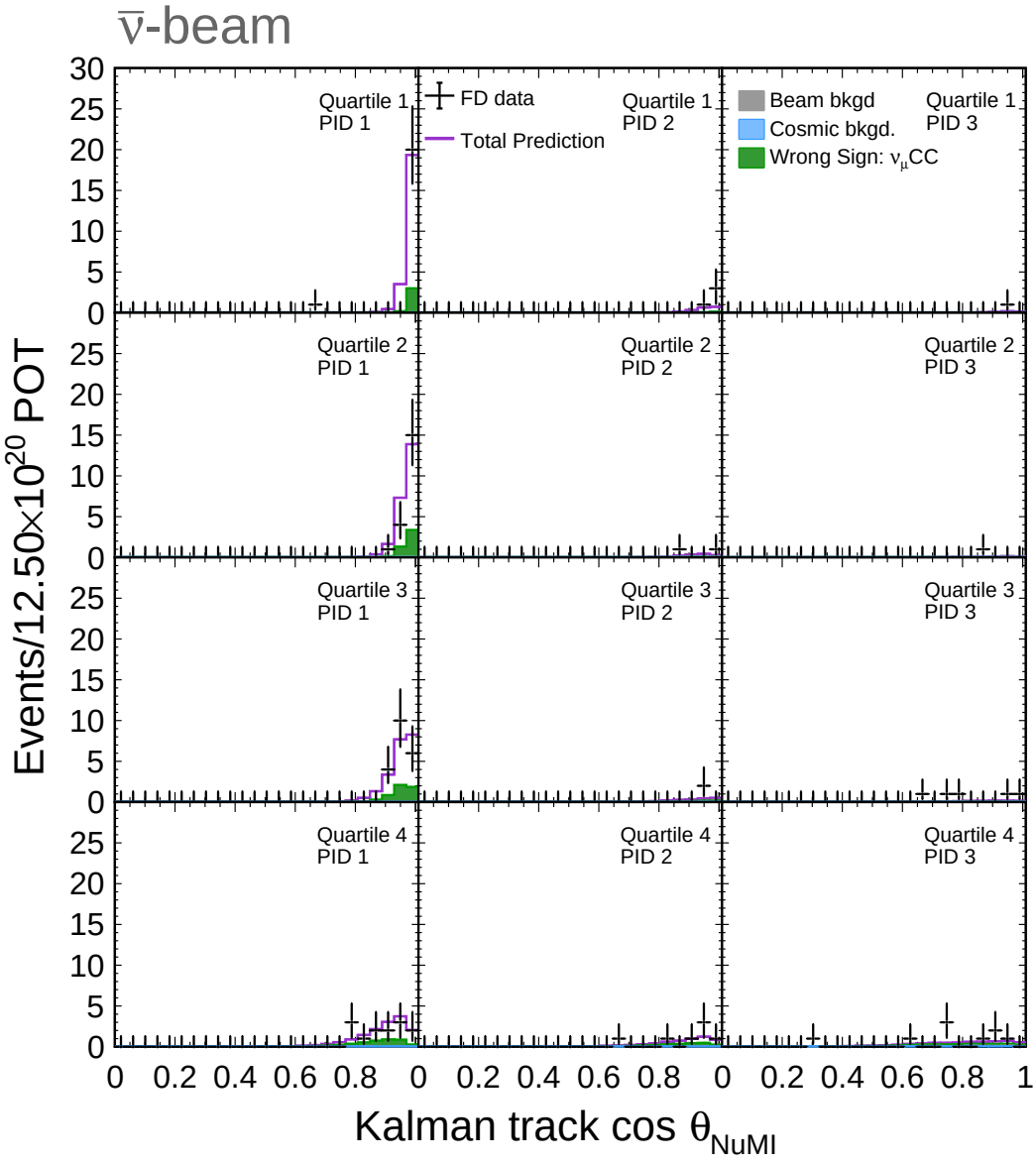

Figure B.32: Distribution of the cosθ_{NuMI} (where θ_{NuMI} is the angle of the muon track with respect to the beam direction) for the ν_μ CC events in the standard sample at the FD in each selection bin in RHC. The selected ν_μ sample at the FD is split into 12 sub-samples (i.e. four quartile bins times three particle identification bins). Data is shown in black. The prediction at the thesis best fit point is shown by the purple line and the shaded purple region corresponds to the 1 σ systematic uncertainty in the simulation. The green, grey, and the blue stacked histograms show the wrong-sign (ν_μ CC), beam, and cosmic backgrounds, respectively.

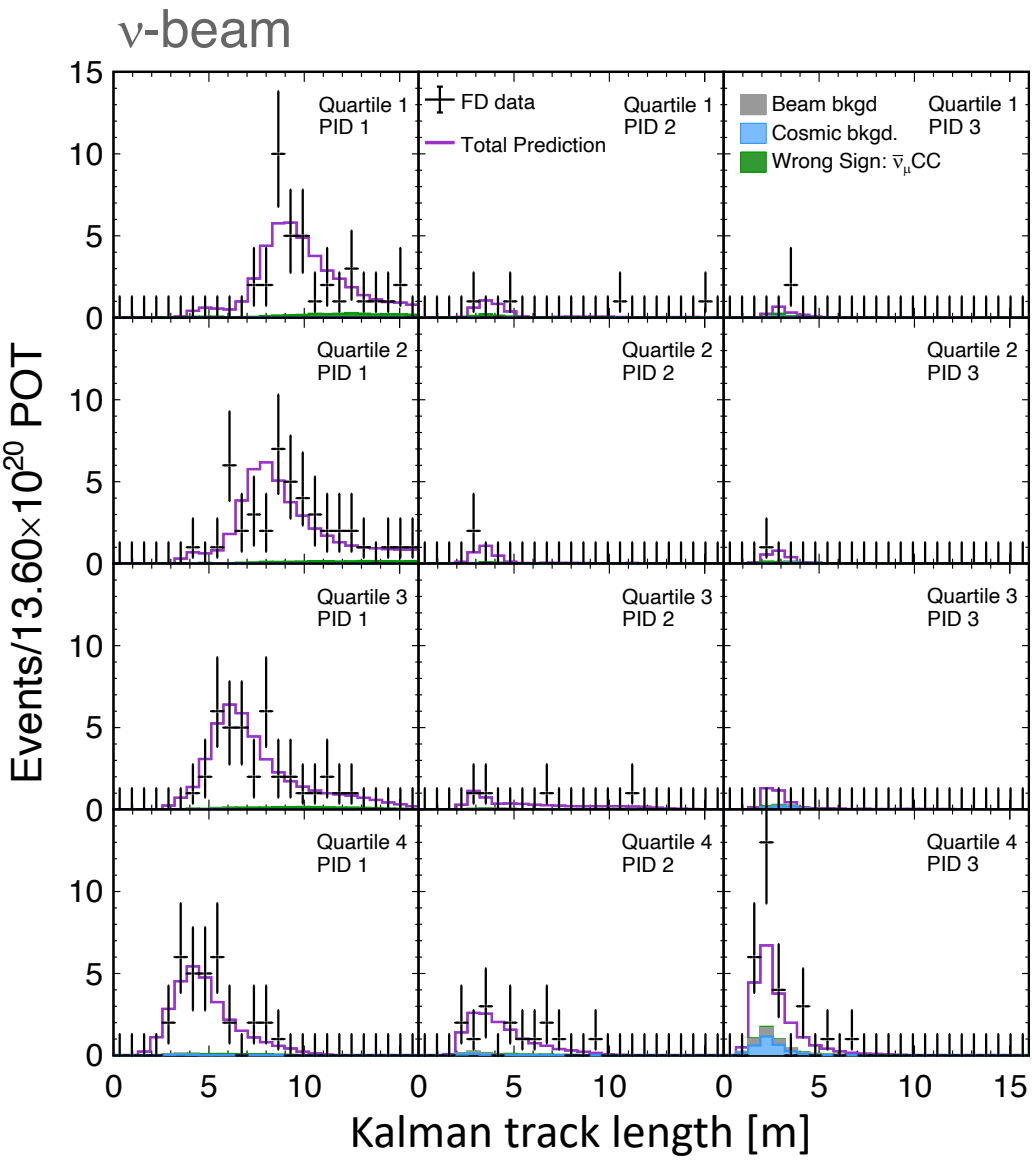

Figure B.33: Distribution of Kalman track length for the ν_μ CC events in the standard sample at the FD in each selection bin in FHC. The selected ν_μ sample at the FD is split into 12 sub-samples (i.e., four quartile bins times three particle identification bins). Data is shown in black. The prediction at the thesis best fit point is shown by the purple line and the shaded purple region corresponds to the 1 σ systematic uncertainty in the simulation. The green, grey, and the blue stacked histograms show the wrong-sign ($\bar{\nu}_\mu$ CC), beam, and cosmic backgrounds, respectively.

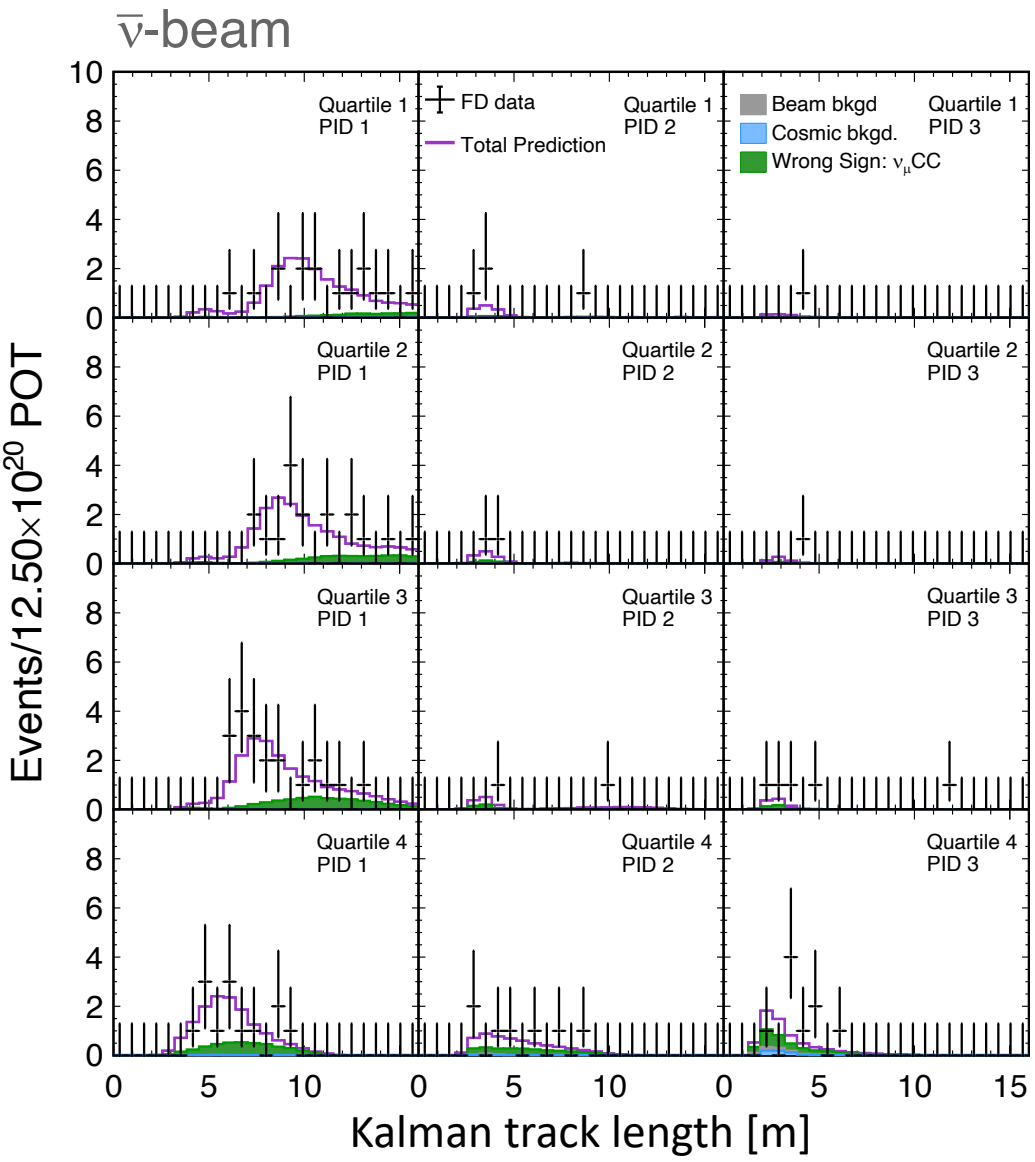

Figure B.34: Distribution of Kalman track length for the ν_μ CC events in the standard sample at the FD in each selection bin in RHC. The selected ν_μ sample at the FD is split into 12 sub-samples (i.e. four quartile bins times three particle identification bins). Data is shown in black. The prediction at the thesis best fit point is shown by the purple line and the shaded purple region corresponds to the 1 σ systematic uncertainty in the simulation. The green, grey, and the blue stacked histograms show the wrong-sign (ν_μ CC), beam, and cosmic backgrounds, respectively.

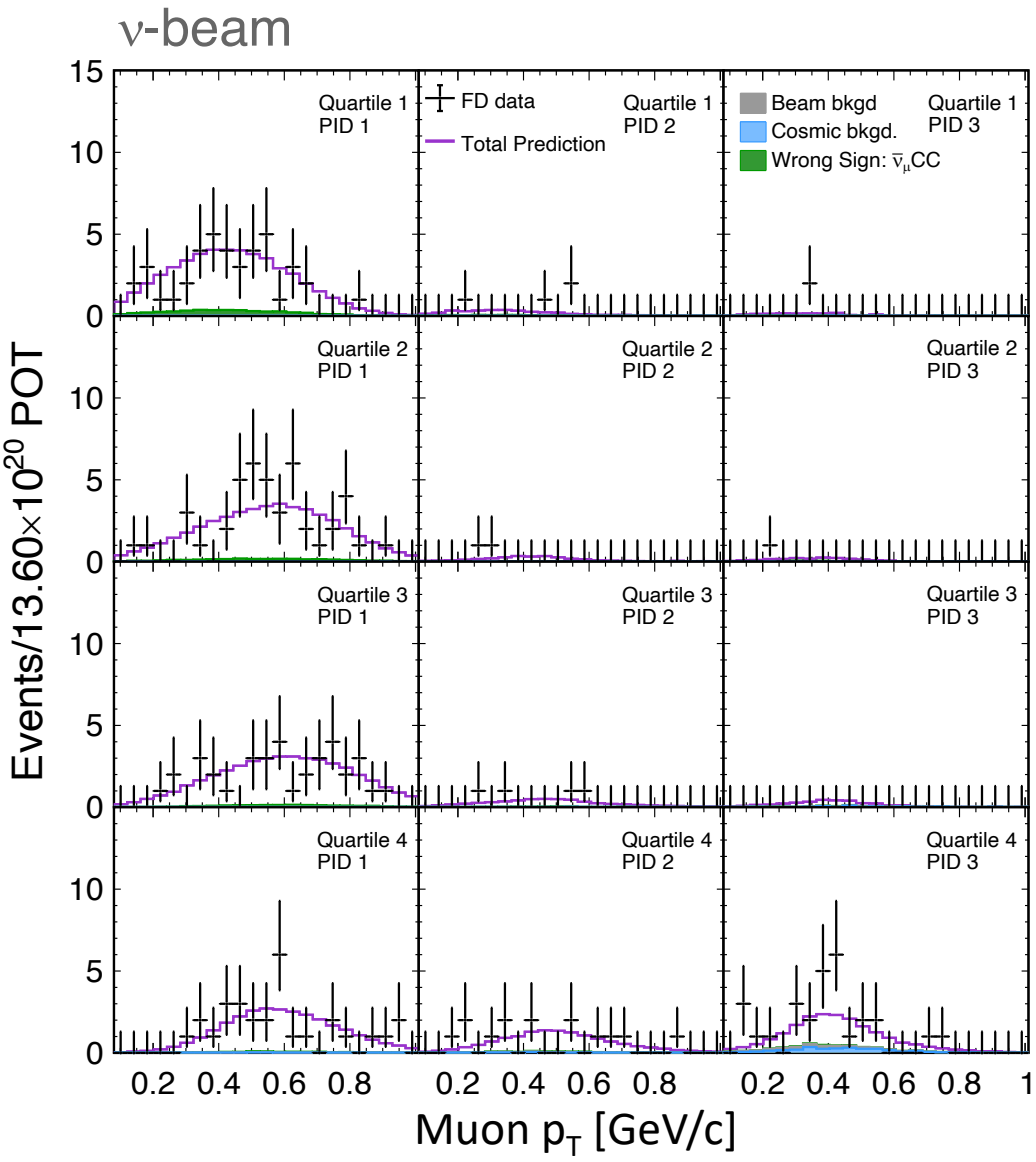

Figure B.35: Distribution of the transverse momentum for the ν_μ CC events in the standard sample at the FD in each selection bin in FHC. The selected ν_μ sample at the FD is split into 12 sub-samples (i.e. four quartile bins times three particle identification bins). Data is shown in black. The prediction at the thesis best fit point is shown by the purple line and the shaded purple region corresponds to the 1 σ systematic uncertainty in the simulation. The green, grey, and the blue stacked histograms show the wrong-sign ($\bar{\nu}_\mu$ CC), beam, and cosmic backgrounds, respectively.

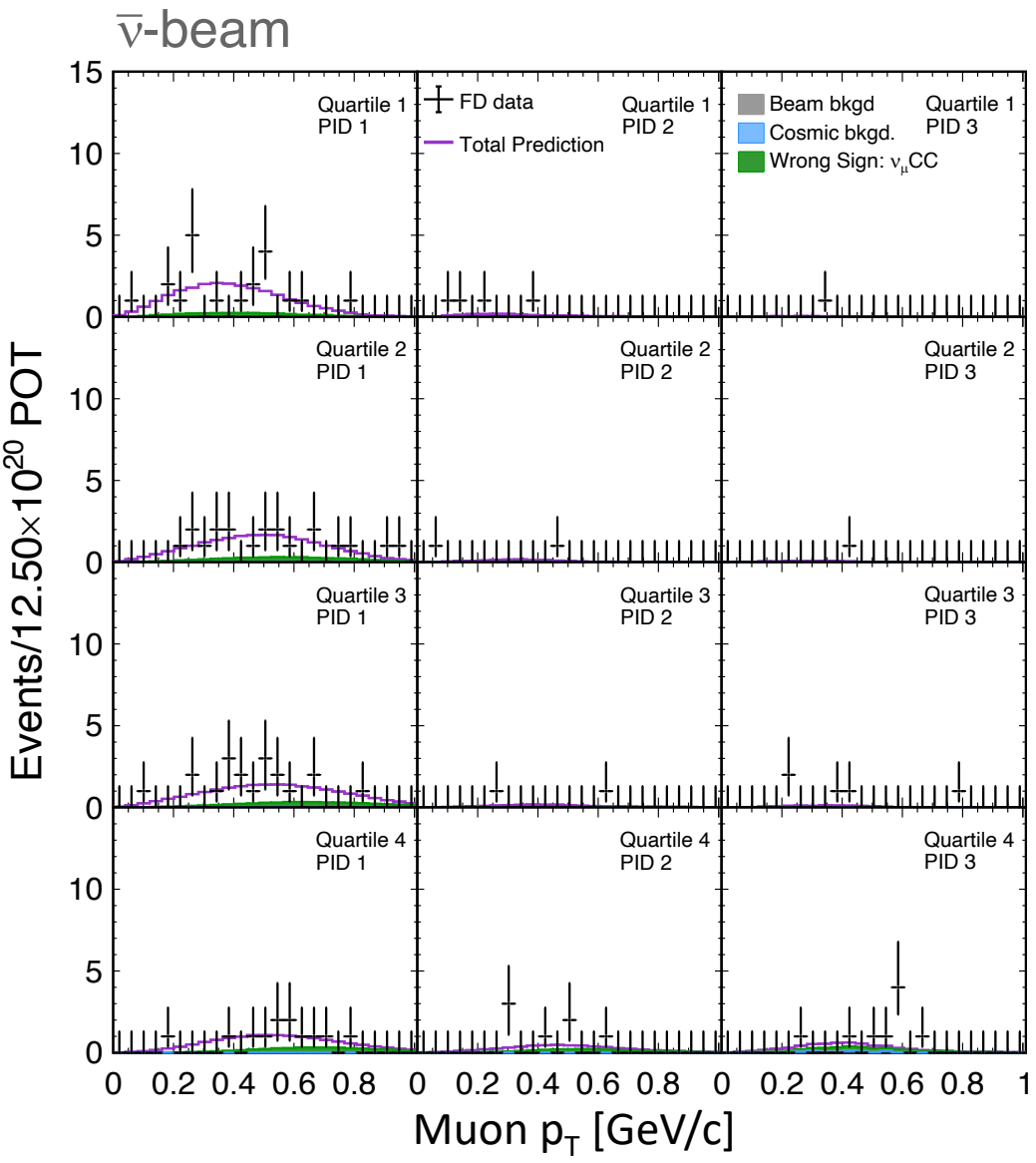

Figure B.36: Distribution of the transverse momentum for the ν_μ CC events in the standard sample at the FD in each selection bin in RHC. The selected ν_μ sample at the FD is split into 12 sub-samples (i.e. four quartile bins times three particle identification bins). Data is shown in black. The prediction at the thesis best fit point is shown by the purple line and the shaded purple region corresponds to the 1 σ systematic uncertainty in the simulation. The green, grey, and the blue stacked histograms show the wrong-sign (ν_μ CC), beam, and cosmic backgrounds, respectively.

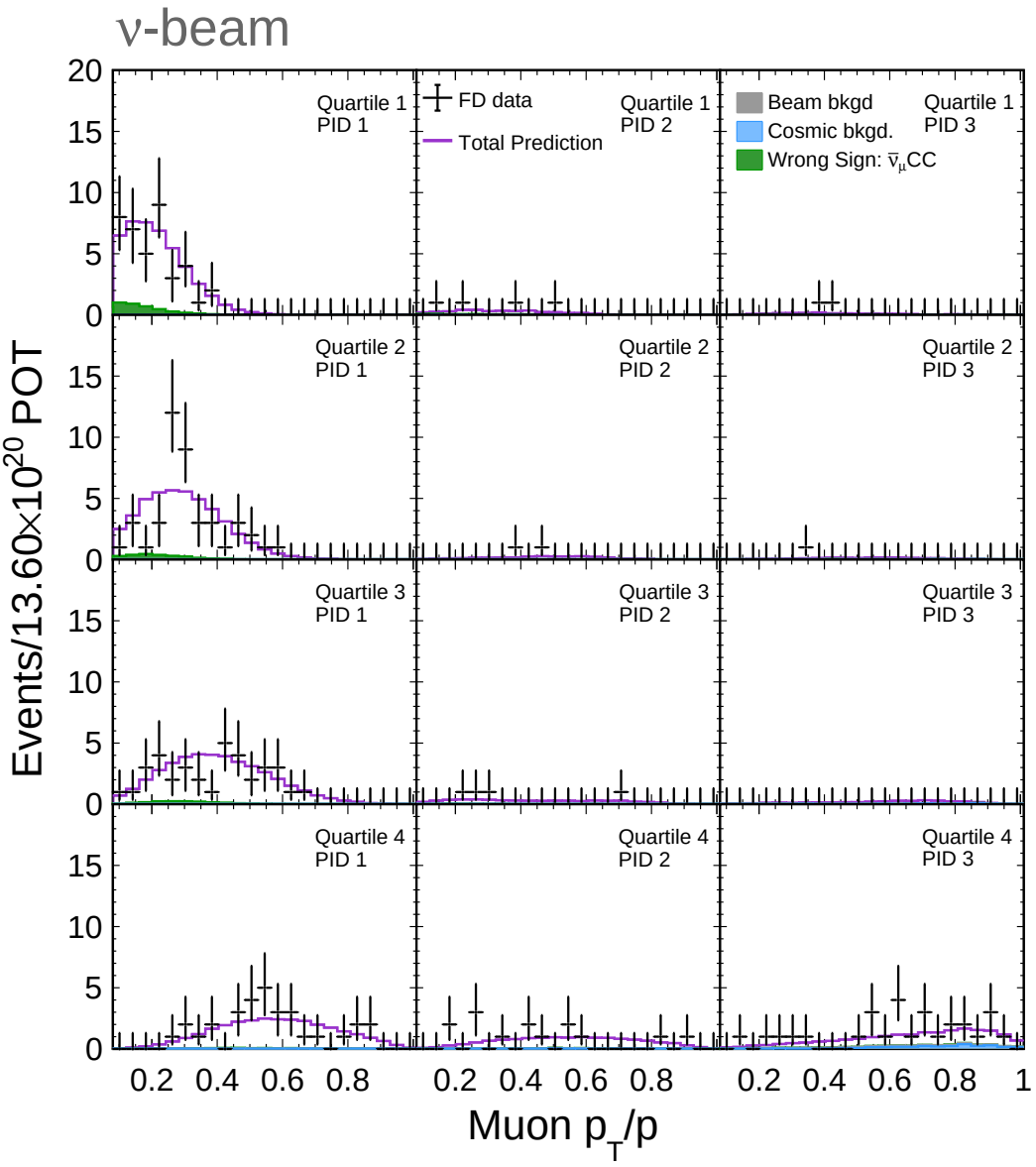

Figure B.37: Distribution of the transverse momentum fraction for the ν_μ CC events in the standard sample at the FD in each selection bin in FHC. The selected ν_μ sample at the FD is split into 12 sub-samples (i.e. four quartile bins times three particle identification bins). Data is shown in black. The prediction at the thesis best fit point is shown by the purple line and the shaded purple region corresponds to the 1 σ systematic uncertainty in the simulation. The green, grey, and the blue stacked histograms show the wrong-sign ($\bar{\nu}_\mu$ CC), beam, and cosmic backgrounds, respectively.

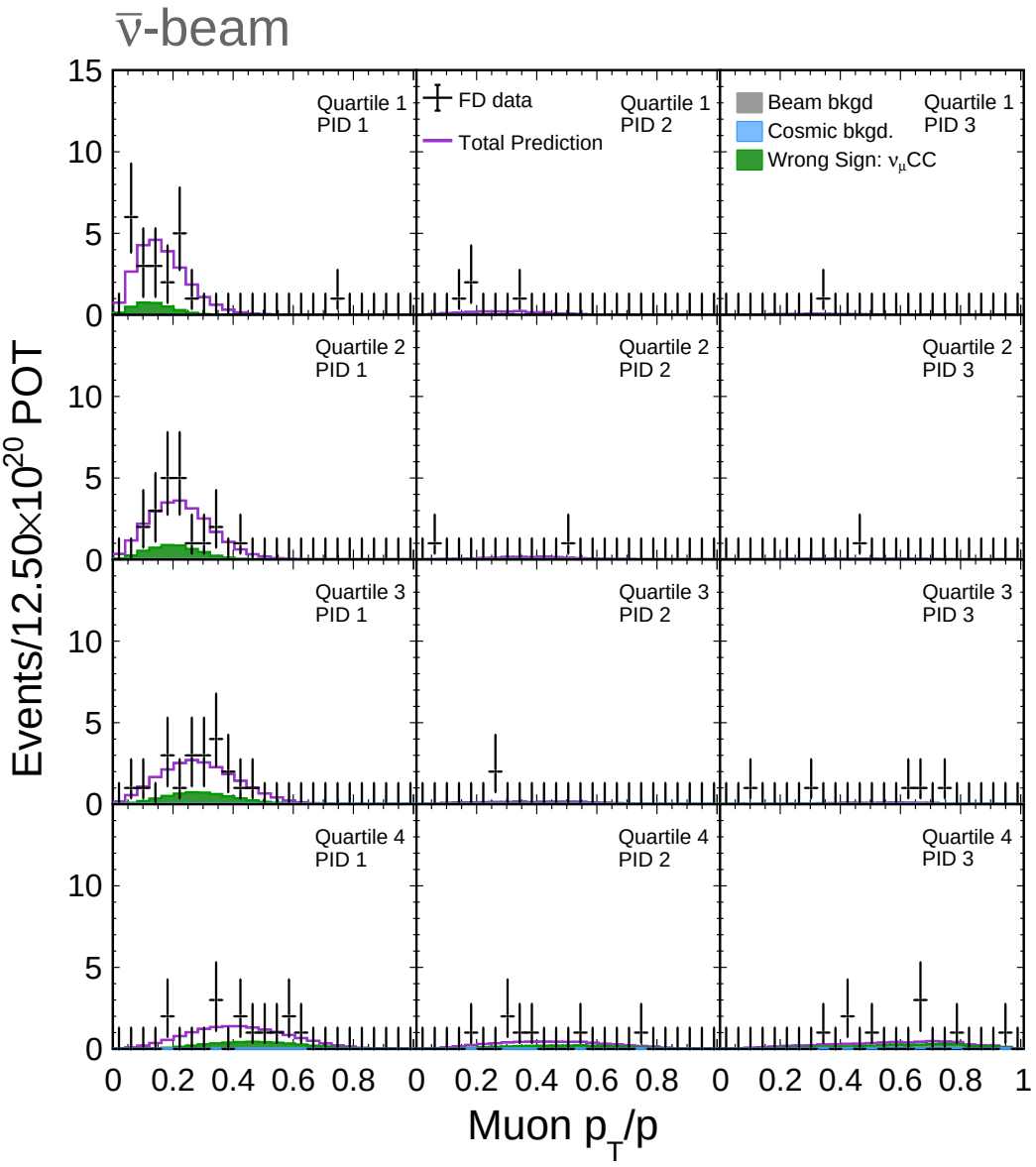

Figure B.38: Distribution of the transverse momentum fraction for the ν_μ CC events in the standard sample at the FD in each selection bin in RHC. The selected ν_μ sample at the FD is split into 12 sub-samples (i.e. four quartile bins times three particle identification bins). Data is shown in black. The prediction at the thesis best fit point is shown by the purple line and the shaded purple region corresponds to the 1 σ systematic uncertainty in the simulation. The green, grey, and the blue stacked histograms show the wrong-sign (ν_μ CC), beam, and cosmic backgrounds, respectively.

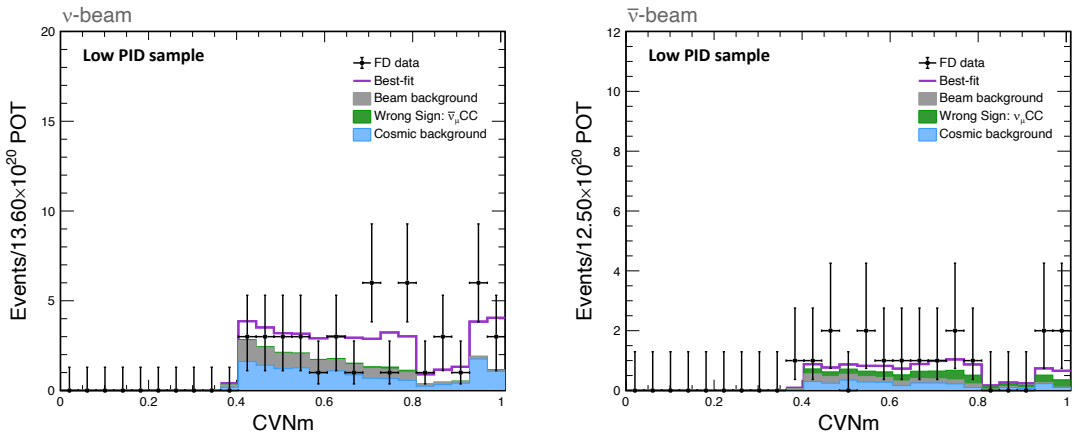

Figure B.39: Distribution of CVN for the ν_μ CC events in the low PID sample at the FD in FHC (left) and RHC (right). Data is shown in black. The prediction at the thesis best fit point is shown by the purple line and the shaded purple region corresponds to the 1 σ systematic uncertainty in the simulation. The green, grey, and the blue stacked histograms show the wrong-sign events, beam background, and cosmic background, respectively.

B.0.4 Distributions of variables in the low-PID sample at the FD

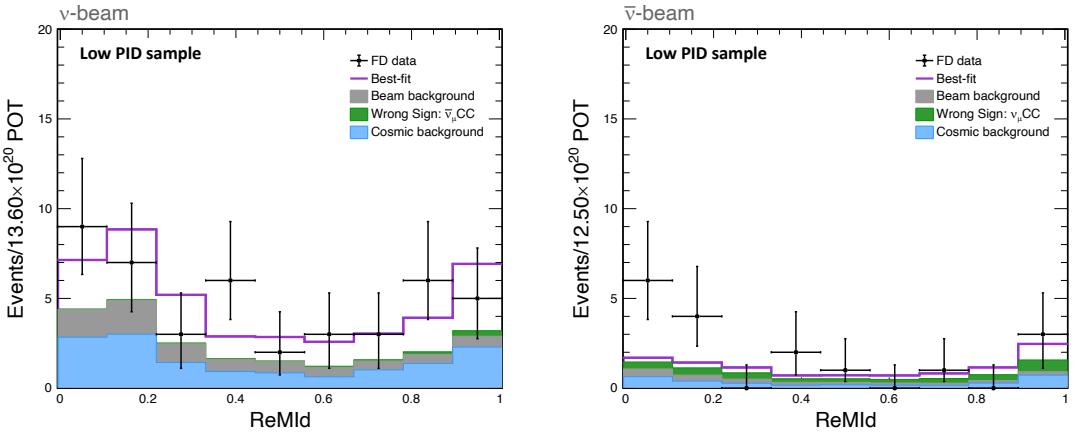

Figure B.40: Distribution of ReMId for the ν_μ CC events in the low PID sample at the FD in FHC (left) and RHC (right). Data is shown in black. The prediction at the thesis best fit point is shown by the purple line and the shaded purple region corresponds to the 1 σ systematic uncertainty in the simulation. The green, grey, and the blue stacked histograms show the wrong-sign events, beam background, and cosmic background, respectively.

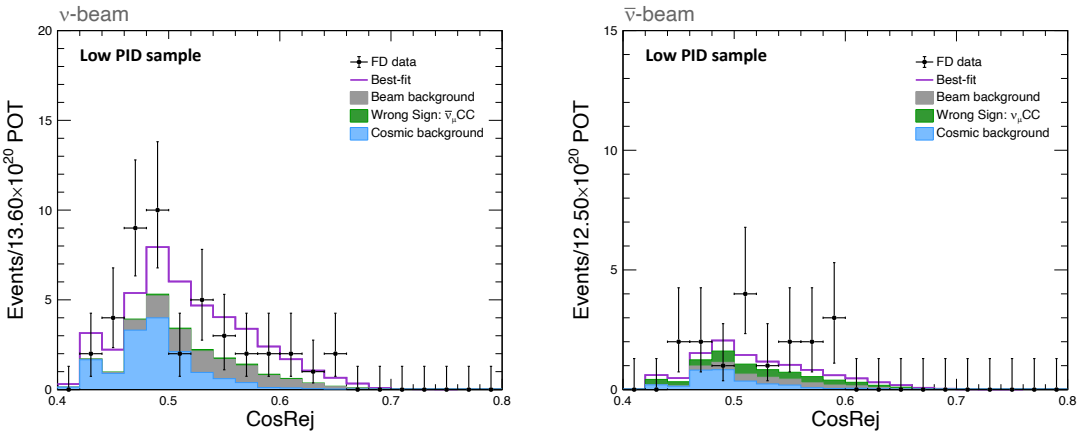

Figure B.41: Distribution of the cosmic rejection score for the ν_μ CC events in the low PID sample at the FD in FHC (left) and RHC (right). Data is shown in black. The prediction at the thesis best fit point is shown by the purple line and the shaded purple region corresponds to the 1 σ systematic uncertainty in the simulation. The green, grey, and the blue stacked histograms show the wrong-sign events, beam background, and cosmic background, respectively.

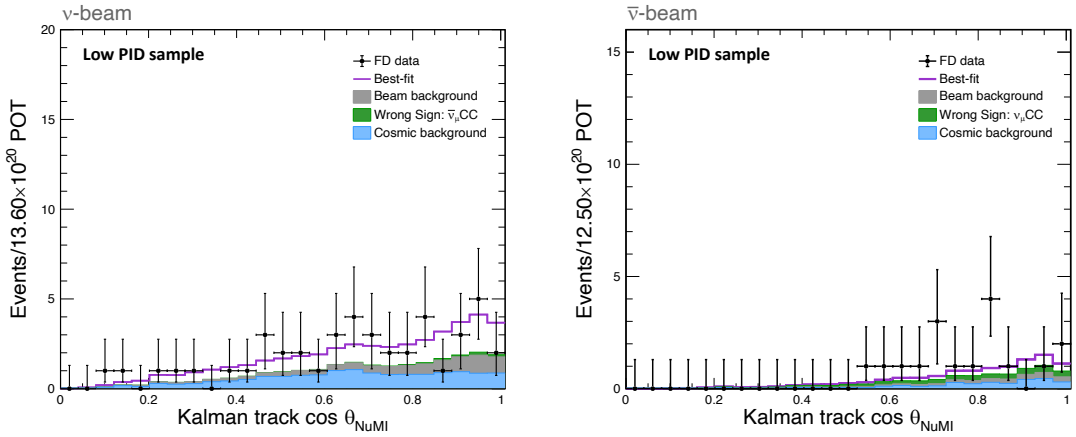

Figure B.42: Distribution of the cosθ_{NuMI} (where θ_{NuMI} is the angle of the muon track with respect to the beam direction) for the ν_μ CC events in the low PID sample at the FD in FHC (left) and RHC (right). Data is shown in black. The prediction at the thesis best fit point is shown by the purple line and the shaded purple region corresponds to the 1 σ systematic uncertainty in the simulation. The green, grey, and the blue stacked histograms show the wrong-sign events, beam background, and cosmic background, respectively.

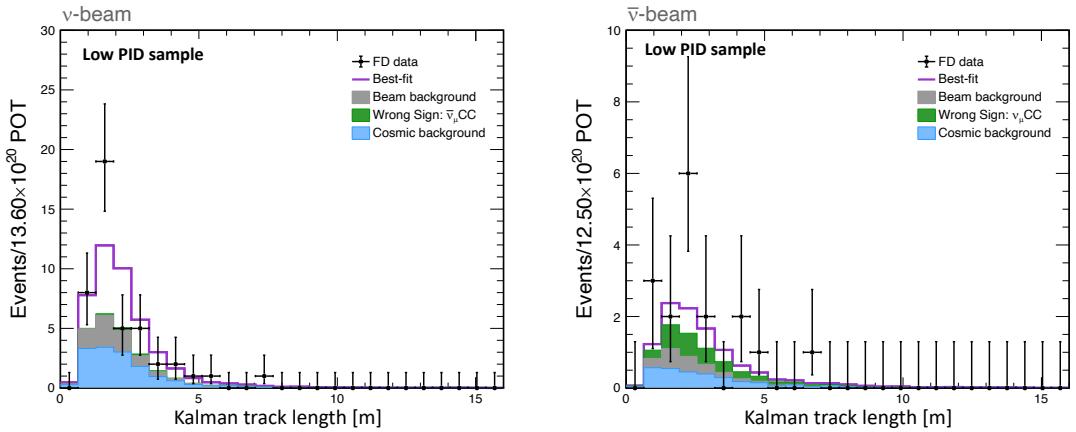

Figure B.43: Distribution of Kalman track length for the ν_μ CC events in the low PID sample at the FD in FHC (left) and RHC (right). Data is shown in black. The prediction at the thesis best fit point is shown by the purple line and the shaded purple region corresponds to the 1 σ systematic uncertainty in the simulation. The green, grey, and the blue stacked histograms show the wrong-sign events, beam background, and cosmic background, respectively.

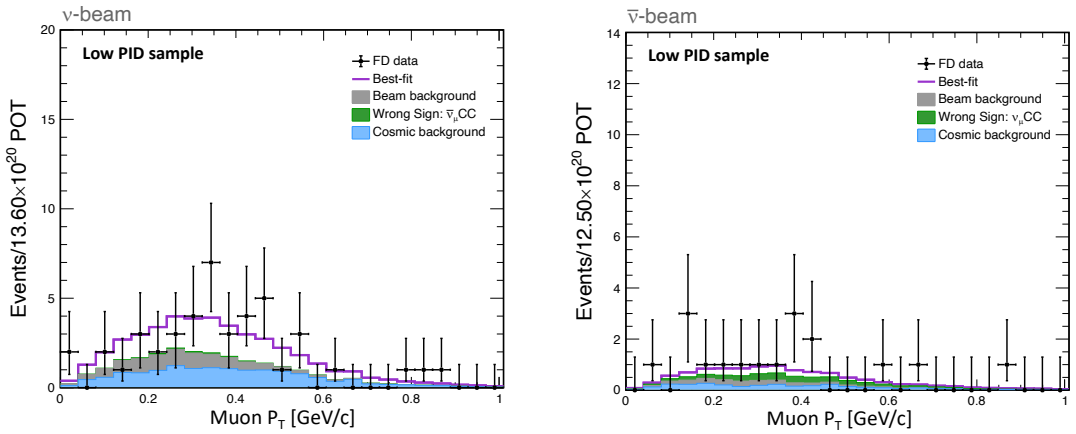

Figure B.44: Distribution of the transverse momentum fraction for the ν_μ CC events in the low PID sample at the FD in FHC (left) and RHC (right). Data is shown in black. The prediction at the thesis best fit point is shown by the purple line and the shaded purple region corresponds to the 1 σ systematic uncertainty in the simulation. The green, grey, and the blue stacked histograms show the wrong-sign events, beam background, and cosmic background, respectively.

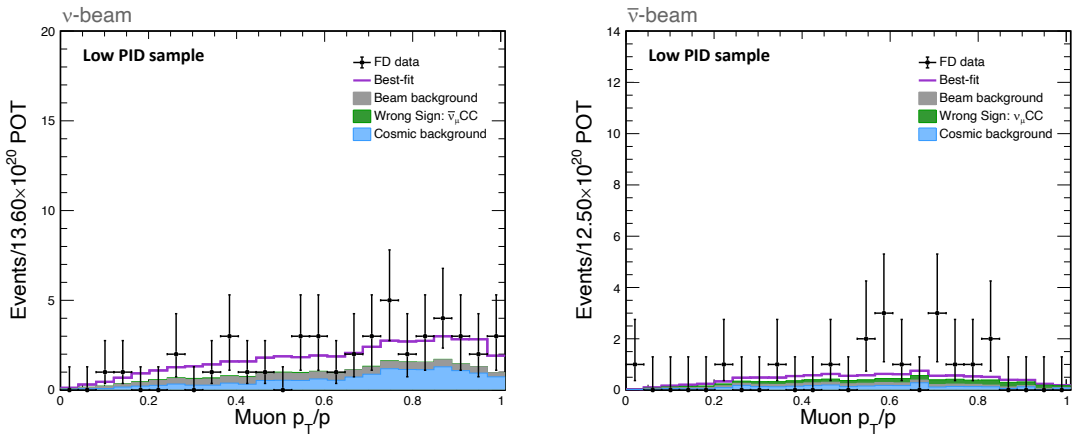

Figure B.45: Distribution of the transverse momentum fraction for the ν_μ CC events in the low PID sample at the FD in FHC (left) and RHC (right). Data is shown in black. The prediction at the thesis best fit point is shown by the purple line and the shaded purple region corresponds to the 1 σ systematic uncertainty in the simulation. The green, grey, and the blue stacked histograms show the wrong-sign events, beam background, and cosmic background, respectively.

Bibliography

[1] Frederick Reines and Clyde L. Cowan. The neutrino. *Nature*, 178:446–449, 1956. 1

[2] Carlo Giunti and Chung W.Kim. Fundamentals of Neutrino Physics and Astrophysics. 1, 10, 16

[3] C. P. Burgess and Guy D. Moore. The Standard Model: A Primer. 1

[4] Y. Fukuda et al. Evidence for oscillation of atmospheric neutrinos. *Phys. Rev. Lett.*, 81:1562–1567, 1998. 1, 5

[5] Q. R. Ahmad et al. Direct evidence for neutrino flavor transformation from neutral current interactions in the Sudbury Neutrino Observatory. *Phys. Rev. Lett.*, 89:011301, 2002. 1, 5, 19

[6] Ivan Esteban, M. C. Gonzalez-Garcia, Michele Maltoni, Thomas Schwetz, and Albert Zhou. The fate of hints: updated global analysis of three-flavor neutrino oscillations. *JHEP*, 09:178, 2020. 1, 26

[7] R. B. Patterson. Prospects for Measurement of the Neutrino Mass Hierarchy. *Ann. Rev. Nucl. Part. Sci.*, 65:177–192, 2015. 2

[8] Kenichi Fuki and Masaki Yasue. What does mu-tau symmetry imply in neutrino mixings? *Phys. Rev. D*, 73:055014, 2006. 2, 12

[9] D. S. Ayres et al. The NOvA Technical Design Report. 10 2007. 2, 30, 33, 37, 38

[10] Wolfgang Pauli. Open Letter to the Gauverein meeting in Tubingen. 1930. 3

[11] J.Chadwick. Possible existence of a neutron. *Nature*, 129:312, 1932. 3

[12] E. Fermi. An attempt of a theory of beta radiation. 1. *Z. Phys.*, 88:161–177, 1934. 3

[13] M. Goldhaber, L. Grodzins, and A. W. Sunyar. Helicity of Neutrinos. *Phys. Rev.*, 109:1015–1017, 1958. 4

[14] G. Danby, J. M. Gaillard, Konstantin A. Goulianos, L. M. Lederman, Nari B. Mistry, M. Schwartz, and J. Steinberger. Observation of High-Energy Neutrino Reactions and the Existence of Two Kinds of Neutrinos. *Phys. Rev. Lett.*, 9:36–44, 1962. 4

[15] F. J. Hasert et al. F. J. Hasert et al., Phys. Lett. B46, 138 (1973). 4

[16] F. J. Hasert et al. F. J. Hasert et al., Nucl. Phys. B73, 1 (1974). 4

[17] F. J. Hasert et al. Phys. Lett. B46, 121 (1973). 4

[18] Martin L. Perl et al. Evidence for Anomalous Lepton Production in e+ - e- Annihilation. *Phys. Rev. Lett.*, 35:1489–1492, 1975. 4

[19] K. Kodama et al. Observation of tau neutrino interactions. *Phys. Lett. B*, 504:218–224, 2001. 4

[20] B. T. Cleveland, Timothy Daily, Raymond Davis, Jr., James R. Distel, Kenneth Lande, C. K. Lee, Paul S. Wildenhain, and Jack Ullman. Measurement of the solar electron neutrino flux with the Homestake chlorine detector. *Astrophys. J.*, 496:505–526, 1998. 4

[21] John N. Bahcall. Solar neutrinos. I: Theoretical. *Phys. Rev. Lett.*, 12:300–302, 1964. 4

[22] P. Anselmann et al. Solar neutrinos observed by GALLEX at Gran Sasso. *Phys. Lett. B*, 285:376–389, 1992. 5

[23] A. I. Abazov et al. Search for neutrinos from sun using the reaction Ga-71 (electron-neutrino e-) Ge-71. *Phys. Rev. Lett.*, 67:3332–3335, 1991. 5

[24] K. S. Hirata et al. Observation of B-8 Solar Neutrinos in the Kamiokande-II Detector. *Phys. Rev. Lett.*, 63:16, 1989. 5

[25] K. S. Hirata et al. Experimental Study of the Atmospheric Neutrino Flux. *Phys. Lett. B*, 205:416, 1988. 5

[26] M. H. Ahn et al. Measurement of Neutrino Oscillation by the K2K Experiment. *Phys. Rev. D*, 74:072003, 2006. 5, 21

[27] P. Adamson et al. Measurement of Neutrino and Antineutrino Oscillations Using Beam and Atmospheric Data in MINOS. *Phys. Rev. Lett.*, 110(25):251801, 2013. 5

[28] URL. https://www.thinglink.com/scene/682607679780159489. 6

[29] S. L. Glashow. *Nucl. Phys.*, 22, 579–588, 1961. 5

[30] S. Weinberg. *Phys. Rev. Lett.*, 19, 1264–1266, 1967. 5

[31] A. Salam. *1969, Proc. of the 8th Nobel Symposium on 'Elementary Particle Theory, Relativistic Groups and Analyticity'*, Stockholm, Sweden, 1968, edited by N. Svartholm, p. 367-377. 5

[32] Georges Aad et al. Observation of a new particle in the search for the Standard Model Higgs boson with the ATLAS detector at the LHC. *Phys. Lett. B*, 716:1–29, 2012. 6

[33] *Fundamental Physics at the Intensity Frontier*, 5 2012. 7

[34] M. Martini, M. Ericson, G. Chanfray, and J. Marteau. A Unified approach for nucleon knock-out, coherent and incoherent pion production in neutrino interactions with nuclei. *Phys. Rev. C*, 80:065501, 2009. 9

[35] Hiroshi Nunokawa, Stephen J. Parke, and Jose W. F. Valle. CP Violation and Neutrino Oscillations. *Prog. Part. Nucl. Phys.*, 60:338–402, 2008. 15, 16

[36] L. Wolfenstein. Neutrino oscillations in matter, Phys. Rev. D17 (1978),2369. 16

[37] S. P. Mikheyev and A. Y. Smirnov. Resonance enhancement of oscillations in matter and solar neutrino spectroscopy, Sov. J. Nucl. Phys. 42 (1985), 913–917. 16

[38] S. P. Mikheyev and A. Y. Smirnov. Resonant amplification of neutrino oscillations in matter and solar neutrino spectroscopy, Nuovo Cim. C9 (1986), 17–26. 16

[39] B. Aharmim et al. Electron energy spectra, fluxes, and day-night asymmetries of B-8 solar neutrinos from measurements with NaCl dissolved in the heavy-water detector at the Sudbury Neutrino Observatory. *Phys. Rev. C*, 72:055502, 2005. 17

[40] S. Fukuda et al. Determination of solar neutrino oscillation parameters using 1496 days of Super-Kamiokande I data. *Phys. Lett. B*, 539:179–187, 2002. 17

[41] A. Gando et al. Reactor On-Off Antineutrino Measurement with KamLAND. *Phys. Rev. D*, 88(3):033001, 2013. 17, 18

[42] Y. Fukuda et al. Evidence for oscillation of atmospheric neutrinos. *Phys. Rev. Lett.*, 81:1562–1567, 1998. 20

[43] P. Adamson et al. Precision constraints for three-flavor neutrino oscillations from the full minos+ and minos dataset," Phys. Rev. Lett., vol. 125, no. 13, p. 131802, 2020. 21

[44] PY. Nakajima et al. Recent results and future prospects from super-kamiokande." The XXIX International Conference on Neutrino Physics and Astrophysics. indico.fnal.gov/event/43209, 2020. 21

[45] R. Acciarri et al. Long-Baseline Neutrino Facility (LBNF) and Deep Underground Neutrino Experiment (DUNE): Conceptual Design Report, Volume 2: The Physics Program for DUNE at LBNF. 12 2015. 21

[46] F. P. An et al. Observation of electron-antineutrino disappearance at Daya Bay. *Phys. Rev. Lett.*, 108:171803, 2012. 21, 22

[47] Y. Abe et al. Indication of Reactor $\bar{\nu}_e$ Disappearance in the Double Chooz Experiment. *Phys. Rev. Lett.*, 108:131801, 2012. 22

[48] J. K. Ahn et al. Observation of Reactor Electron Antineutrino Disappearance in the RENO Experiment. *Phys. Rev. Lett.*, 108:191802, 2012. 22

[49] D. Adey et al. Measurement of the Electron Antineutrino Oscillation with 1958 Days of Operation at Daya Bay. *Phys. Rev. Lett.*, 121(24):241805, 2018. 23

[50] K. Abe et al. Indication of Electron Neutrino Appearance from an Accelerator-produced Off-axis Muon Neutrino Beam. *Phys. Rev. Lett.*, 107:041801, 2011. 23

[51] J. G. Walsh. CP-violation search with T2K data. In *20th Conference on Flavor Physics and CP Violation* , 8 2022. 23

[52] Ajmi Ali. Precision Measurements of the PMNS Parameters with T2K Data. In *20th Conference on Flavor Physics and CP Violation* , 7 2022. 23

[53] Babak Abi et al. Deep Underground Neutrino Experiment (DUNE), Far Detector Technical Design Report, Volume II: DUNE Physics. 2 2020. 23, 149

[54] K. Abe et al. Hyper-Kamiokande Design Report. 5 2018. 23, 149

[55] P. Adamson et al. The NuMI Neutrino Beam. *Nucl. Instrum. Meth. A*, 806:279–306, 2016. 29, 30

[56] P. Adamson et al. (NOvA). NOvA Official Plot Database. *NOvA Internal Document*, (2014–2018). 33

[57] Tian Xin. *Observing Muon Neutrino to Electron Neutrino Oscillations in the NOνA Experiment*. PhD thesis, Iowa State U., 2016. 34

[58] Hayes D Merritt. DAQChannelMap Terms and Definitions. *NOvA Internal Document*, DocDB-11570, 2014. 34

[59] Fermilab Creative Services. https://vms.fnal.gov. 35, 36

[60] S. Mufson et al. Liquid scintillator production for the NOvA experiment. *Nucl. Instrum. Meth. A*, 799:1–9, 2015. 37

[61] Louise Suter. Introduction to NOvA and data taking. *NOvA Internal Document*, DocDB-15021, 2016. 38, 39

[62] Jose Andres Sepulveda-Quiroz. *Measurement of the Kaon Production Normalization in the NuMI Target Using Uncontained Charged-Current Muon Neutrino Interactions in the NOvA Far Detector*. PhD thesis, Iowas State U., 2018. 40

[63] A. Norman, R. Kwarciany, G. Deuerling, and N. Wilcer. The NOvA Timing System: A System for Synchronizing a Long Baseline Neutrino Experiment. *J. Phys. Conf. Ser.*, 396:012034, 2012. 41

[64] F. Psihas. Measurement of Long Baseline Neutrino Oscillations and Improvements from Deep Learning. PhD thesis, Indiana University, 2018. 41

[65] Pietro Antonioli et al. SNEWS: The Supernova Early Warning System. *New J. Phys.*, 6:114, 2004. 42

[66] Robert Hatcher. Simulation Tools in Neutrino Experiments. *NOvA Internal Document*, DocDB-14441, 2015. 42

[67] L. Aliaga. 2017-2018 beam plots. *NOvA Internal Document*, DocDB-20843, 2018. 43

[68] Giuseppe Battistoni, S. Muraro, Paola R. Sala, Fabio Cerutti, A. Ferrari, Stefan Roesler, A. Fasso, and J. Ranft. The FLUKA code: Description and benchmarking. *AIP Conf. Proc.*, 896(1):31–49, 2007. 42

[69] S. Agostinelli et al. GEANT4–a simulation toolkit. *Nucl. Instrum. Meth. A*, 506:250–303, 2003. 42

[70] L. Aliaga et al. Neutrino Flux Predictions for the NuMI Beam. *Phys. Rev. D*, 94(9):092005, 2016. [Addendum: Phys.Rev.D 95, 039903 (2017)]. 44

[71] M. Martinez-Casales. Cross section tuning 2020 blessing package. *NOvA Internal Document*, DocDB-45359, 2020. 44

[72] C. Andreopoulos et al. The GENIE Neutrino Monte Carlo Generator. *Nucl. Instrum. Meth. A*, 614:87–104, 2010. 44

[73] Costas Andreopoulos, Christopher Barry, Steve Dytman, Hugh Gallagher, Tomasz Golan, Robert Hatcher, Gabriel Perdue, and Julia Yarba. The GENIE Neutrino Monte Carlo Generator: Physics and User Manual. 10 2015. 44

[74] R. Gran, J. Nieves, F. Sanchez, and M. J. Vicente Vacas. Neutrino-nucleus quasi-elastic and 2p2h interactions up to 10 GeV. *Phys. Rev. D*, 88(11):113007, 2013. 45

[75] J. Nieves, Jose Enrique Amaro, and M. Valverde. Inclusive quasi-elastic neutrino reactions. *Phys. Rev. C*, 70:055503, 2004. [Erratum: Phys.Rev.C 72, 019902 (2005)]. 45

[76] Richard Gran. Model Uncertainties for Valencia RPA Effect for MINERvA. 5 2017. 45

[77] Chris Hagmann, David Lange, and Douglas Wright. Cosmic-ray shower generator (cry) for monte carlo transport codes. In *2007 IEEE Nuclear Science Symposium Conference Record*, volume 2, pages 1143–1146, 2007. 45

[78] Christopher Backhouse. The CAFAna Framework. *NOvA Internal Document*, DocDB-9222, 2014. 46

[79] ROOT Data Analysis Framework. http://root.cern. 46

[80] Evan Niner. CAFAna Tutorial. *NOvA Internal Document*, DocDB-15025, 2016. 46

[81] Fermilab Creative Services. https://vms.fnal.gov/index/vms-home. 47

[82] M. Baird, J. Bian, M. Messier, E. Niner, D. Rocco, and K. Sachdev. Event Reconstruction Techniques in NOvA. *J. Phys. Conf. Ser.*, 664(7):072035, 2015. 47

[83] N. Raddatz. KalmanTrack Technical Note. *NOvA Internal Document: DocDB-13545*. 48, 49

[84] R. E. Kalman. A new approach to linear filtering and prediction problems. *Journal of basic Engineering*, 82:35–45, 1960. 49

[85] B. Rebel. A window tracking algorithm for cosmic ray muons. *NOvA Internal Document*, DocDB-15977, 2016. 49

[86] W. Mu. Blessed Package: NuMu Energy Spline Plots 2020. *NOvA Internal Document*, DocDB-46283, 2020. 50, 51

[87] D. Mendez. Second Analysis Calorimetric energy scale calibration of the nova detectors. *NOvA Internal Document*, 13579. 50

[88] P. Singh C. Backhouse, A. Radovic and M. Campbell. The attenuation and threshold calibration of the NOvA detectors. *NOvA Internal Document*, DocDB-13579, 2017. 52

[89] Tyler Alion. Third Analysis Calorimetric Energy Scale in the NOVA Detectors. *NOvA Internal Document*, 23372. 52

[90] Jeremy Wolcott Michael Baird, Louise Suter. Summary of the 2020 FHC+RHC 3-Flavor oscillation analysis. *NOvA Internal Document*, 44422. 54

[91] A. Aurisano, A. Radovic, D. Rocco, A. Himmel, M. D. Messier, E. Niner, G. Pawloski, F. Psihas, A. Sousa, and P. Vahle. A Convolutional Neural Network Neutrino Event Classifier. *JINST*, 11(09):P09001, 2016. 56

[92] T. Cover and P. Hart. Nearest neighbor pattern classification. IEEE transactions on information theory 13, 21–27 (1967). 55

[93] J. Donahue S. Karayev J. Long R. Girshick et al Y. Jia, E. Shelhamer. Caffe: Convolutional architecture for fast feature embedding. arxiv:1408.5093. 57

[94] Christian Szegedy, Wei Liu, Yangqing Jia, Pierre Sermanet, Scott Reed, Dragomir Anguelov, Dumitru Erhan, Vincent Vanhoucke, and Andrew Rabinovich. Going Deeper with Convolutions. 9 2014. 57

[95] T. Warburton. Ana 20 numu quantile plots. Internal Document NOvA DocDB 47242, May 2021. 57

[96] L. Vinton. Measurement of Muon Neutrino Disappearance with the NOvA Experiment. PhD thesis, U. of Sussex, 2018. 58

[97] Shiqi Yu. Blessing package: Extrapolation Cartoon. *NOvA Internal Document*, 29612. 59

[98] Michael Baird. 2019 Analysis Workshop Intro. *NOvA Internal Document*, 2019. 60

[99] N. Nayak. Pca flux systematics for the 2020 oscillation analysis. NOvA Internal Document DocDB: 44049, March 2020. 63

[100] T. Alion. Absolute calibration and shape systematics for 3a. *NOvA Internal Document*, DocDB-20318, 2017. 65

[101] Michael Baird and Alexander Booth. Summary of pre/post 2018-shutdown ND data studies. *NOvA Internal Document*, DocDB-36882, 2019. 65

[102] Anna Maureen Hall. Light Level Down/FD Aging Comparison. *NOvA Internal Document*, DocDB-41070, 2019. 65

[103] Ryan B. Patterson and Matthew J. Wetstein. NOvA Neutron Systematic for 3-Flavor Analysis. *NOvA Internal Document*, DocDB-43811, 2020. 65

[104] Matthew Strait. Muon Energy Scale Systematic. *NOvA Internal Document*, DocDB-20816, 2020. 65

[105] N. V. Mokhov D. E. Groom and S. I. Striganov. Muon stopping power and range tables 10-MeV to 100-TeV. *Atom. Data Nucl. Data Tabl*, vol. 78, pp. 183–356, 2001. 66

[106] Michael Baird and Thomas Warburton. Neutrons Within Beam Spill. *NOvA Internal Document*, DocDB-31144, 2018. 66

[107] S. MacDonald M. Casales A. Mislivec G. Pawloski K. Bays, M. Dolce and J. Wal-cott. Nova 2020 cross-section tune tech note. *NOvA Internal Document*, DocDB-43962, 2020. 66

[108] M. Baird. Update on gg-mismatch problem and other normalization issues for the 3f group. *NOvA Internal Document*, DocDB-44238, 2020. 67

[109] S. Baker and R. D. Cousins. Nucl. instrum. meth. 221, 437 (1984). 1984. 68

[110] L. Kolupaeva. Recent three-flavor neutrino oscillation results from the NOvA experiment. *J. Phys. Conf. Ser.*, 1690(1):012172, 2020. 69

[111] C. Patrignani et al. Chin. Phys. C, 40, 100001. *Particle Data Group, 2016*, pages 6, 8, 9, 11, 29, 54, 66, 67, 68. 69

[112] Dmitrii Torbunov. LSTM NuMu Energy Estimator Technote for Prod5. *NOvA Internal Document*, DocDB-42304-v2, 2020. 79

[113] Peter N. Shanahan and Patricia LaVern Vahle. Physics with NOvA: a half-time review. *Eur. Phys. J. ST*, 230(24):4259–4273, 2021. 148